Development of Evanescent Wave pH Sensors Based on Coated Optical Fibres

By

Thomas M. Butler B.Sc. (Hons)

Submitted for the degree of Doctor of Philosophy

Presented to

Dublin City University

Research Supervisor

Dr. Brian MacCraith,

School of Physical Sciences,

Dublin City University.

September 1996

I hereby certify that this material, which I now submit for assessment on the programme of study leading to the award of Doctor of Philosophy is entirely my own work and has not been taken from the work of others save and to the extent that such work has been cited and acknowledged within the text of my work.

Signed: Thomas Butler ID No.: 92700896

Candidate

Date: 27/11/96

ACKNOWLEDGEMENTS

I want to take this opportunity to thank all those people who helped to make this thesis possible. First, I want to thank my parents and family for all their help and support throughout my post graduate years.

A special thanks to all the physics staff for their willingness to help with queries, especially Dr. Colette McDonagh and Dr. Brian Lawless. A big thanks also to all the physics technicians, especially Des Lavelle and Al Devine. For the calixarene compound, I would like to thank Theresa Grady and Dr. Dermot Diamond of the chemistry department.

To all my fellow postgrads, past and present, a big thank you. In particular, I want to thank Aisling McEvoy, Vincent Murphy, and also Penny, Antonette, Aidan and Mick. The help of past postgrads, Ger, Fidlema, Fergal and Kieran is greatly appreciated.

Finally, but certainly not in order of importance, I would like to thank my supervisor Dr. Brain MacCraith for all his patience, suggestions and help over the last 4 years.

TABLE OF CONTENTS

ABSTRACT

The development of fibre optic ammonia and pH sensors using analyte-sensitive reagents entrapped in a sol-gel-derived silica film is presented. These sensors are based on evanescent wave absorption using unclad fibres dipcoated with the chemically-sensitive coating. A detailed characterisation of film properties was carried out. Film properties were monitored as a function of various processing parameters, and the results are interpreted in terms of the chemical reactions involved in the sol-gel process. A pH sensor was constructed using sulfonephthalein dyes immobilised in sol-gel-derived coatings. Its range was extended by co-immobilisation of two indicators. A detailed study of the parameters affecting the leaching of reagents from sol-gel films is presented. Ammonia sensing using pH and ammonia-specific reagents, immobilised in sol-gel silica and polymer coatings is detailed. The issues involved in choosing a pH indicator for ammonia sensing is discussed. Issues affecting the response time and sensitivity of these ammonia sensors are highlighted. These include the choice of sol-gel film, dye concentration and humidity dependence. Ammonia sensing using novel near-infrared absorbing reagents is discussed. In addition the issues affecting the diffusion of metal ions into sol-gel films is discussed. The reaction of xylenol orange with Pb^{2+} in solution is used as an example. A number of characterisation systems have been employed, and these are described in detail.

Chapter 1 Introduction

1.1 Introduction

A sensor is a device capable of continuously and reversibly recording a physical parameter or the concentration of a chemical or biochemical species. Typical examples of a mechanical, electrochemical, and optical sensor, respectively, are the mercury thermometer, the pH glass electrode and the pH indicator strip. Ideally, such a sensor can be brought directly into contact with the sample, and the result of the measurement is displayed within a few seconds. No sampling, addition of reagent, or dilution is required.

Industry has always been dependent on measuring instruments for the registration of physical parameters. For this reason, the technology of sensors and transducers has a long tradition. Today, the continuous sensing of chemical analytes is a matter of growing interest by virtue of the real-time nature of most sensors. Tremendous effort has been devoted to the development of various sensing devices for use in product and food control, in environmental monitoring, and in many other fields of routine analysis. The history of optical sensors can be traced back to when pH indicator strips were developed by immobilising pH-sensitive indicators on cellulose. Optical sensor methodologies are based on the change of optical properties through measurement of reflection, scattering, interference, fluorescence, absorption and refraction. When one or more of these phenomena takes place, the change in the optical properties will be reflected in the modulation of either one or more of the following properties: wavelength (colour), amplitude, phase or polarization. Amplitude and colour modulation are the most widely used phenomena.

1.2 Optical fibre sensors

Over the past 20 years major developments have taken place in the optoelectronics and fibre-optic communications industries. The fibre-optic communication industry has revolutionised the telecommunications industry by providing higher performance, more reliable telecommunications links with ever decreasing bandwidth costs. In parallel with these developments, fibre-optic sensor

technology has been a major user of technology associated with the optoelectronic and fibre-optic communications industry. Fibre-optic sensor technology has often been driven by the development and subsequent mass production of components in these industries. As component prices have fallen and quality improvements have been made, the ability of fibre-optic sensors to displace traditional sensors for temperature, pressure, rotation, humidity, chemical measurements, and a host of other sensor applications has been enhanced. Optical fibre sensors measure the modulation, caused by a parameter to be measured, which is impressed on the optical signal transmitted by the fibre.

Optical fibre chemical sensors, in which a chemical variable causes a change in the optical properties of the sensor, combine the advantages of optical fibres with, in many cases, specificity due to the chemical reaction of the analyte under test with a reagent. In general, optical fibre sensors can be divided into two main categories [1,2,3], i.e. intrinsic sensors where the measurand directly interacts with the light in the optical fibre, and extrinsic sensors where the measurand affects the light properties through a medium external to the fibre while the fibre acts only as a waveguide to transmit light to and from the sensing device. Figure 1.1 illustrates these two classes of sensor. In a typical extrinsic optical fibre sensor the sensing head or probe is attached to the end of the fibre tip. Extrinsic sensors have been used to measure pH [4] and temperature [5]. In an intrinsic optical fibre sensor the light is modulated within the fibre by the parameter to be measured. Examples of intrinsic optical fibre sensors include evanescent wave sensors [3,6,7], the method used in the work described in this thesis, and core-based sensing [8].

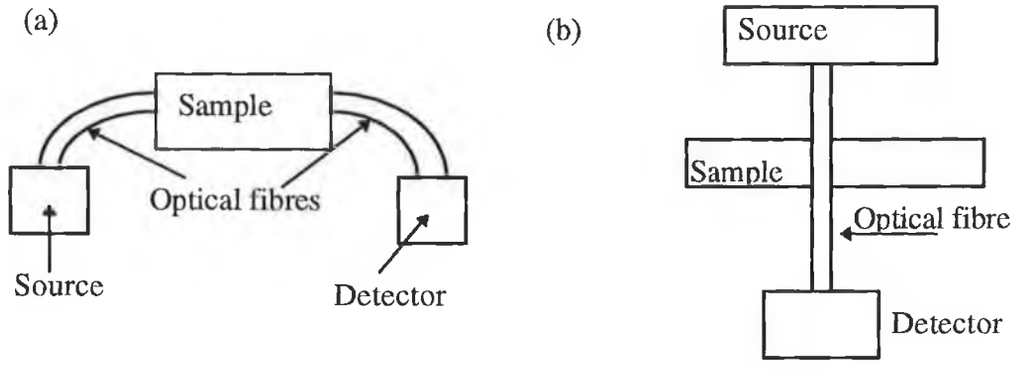

Figure 1.1 Optical fibre sensor types (a) extrinsic (b) intrinsic

Depending on the field of application, optical fibre sensing can offer one or more of the following advantages over other sensing types [3]:

(1) Because the primary signal is optical, it is not subject to strong magnetic fields, surface potentials of the sensor head, or electrical interference by static electricity.

(2) Low-loss optical fibres allow transmission of optical signals over long distances, making remote sensing possible.

(3) The ease of miniaturisation allows the development of very small, light, and flexible fibre sensors.

(4) Optical sensors do not present a significant risk of sparking, and are therefore suitable for use in potentially explosive areas e.g. mining and petroleum industries.

(5) Optical fibre sensing is a non-destructive analytical method.

(6) Optical sensors have been developed which respond to chemical analytes or physical parameters for which electrodes are not available.

There is however a number of potential disadvantages associated with optical fibre sensors [3]:

(1) Ambient light can interfere. Therefore, optical sensors must either be used in dim or dark surroundings, or the optical signal must be encoded so that it can be resolved from ambient background light.

(2) There is a lack of suitable LED and laser sources, especially in the blue spectrum range, and the expense of certain optical components prevents the commercialisation of some sensor designs.

(3) Sensors with indicator phases may have limited long-term stability because of photobleaching or washout.

(4) More selective indicators have to be found for various important analytes, and the immobilisation chemistry has to be improved so as to achieve both better selectivity and sensitivity.

(5) There is a need for referencing to compensate for fibre disturbances in the system.

Despite the above limitations, optical sensors are an attractive alternative to other sensing methods.

1.3 Evanescent wave sensing

When light propagates in an optical fibre or waveguide, a fraction of the radiation extends a short distance from the guiding region into the medium of low refractive index which surrounds it [6]. This evanescent field, which decays exponentially with distance from the waveguide interface, has been used in two distinct approaches in optical fibre sensor design. First, the evanescent wave can interact directly with the analyte if the interrogating wavelength coincides with an absorption band of the species. Such direct spectroscopic evanescent wave sensors are of particular interest in the infrared spectral region, where many species absorb strongly [9]. Alternatively, an intermediate reagent, which responds optically, e.g. by fluorescence or absorption change, to the analyte, may be attached to the waveguide. Often reagent mediated evanescent wave sensors provide greater sensitivity than direct spectroscopic devices. The work described in this thesis uses a reagent-mediated evanescent wave sensor for ammonia and pH sensing using coated optical fibres. The reagent is attached to the fibre core using either sol-gel-derived silica coatings or polymer coatings.

The evanescent wave is not unique to optical fibres. It is a consequence of total internal reflection and can be generated at the interface between any two dielectric materials. The phenomenon, under the name 'total internal reflection' (TIR) or 'attenuated total reflection' (ATR) spectroscopy has been used as a spectroscopic tool to investigate the optical spectra of thin films and highly absorbing materials [10,11]. Chapter 2 outlines the theory of evanescent wave sensing using multimode fibres.

The motivation of using the evanescent wave approach in fibre-optic sensing, is derived from a number of advantages offered by the technique in particular applications [6]:

(1) No coupling optics is required in the sensing region, because the interrogating light remains guided.

(2) It is possible, by varying the launch optics, to confine the evanescent field to a short distance from the guiding interface and thereby discriminate to a large extent between surface and bulk effects.

(3) The technique can provide enhanced sensitivity over conventional bulk-optic approaches. For example, fibre based evanescent wave absorption devices are more

sensitive than bulk-optic ATR crystals by virtue of the greater number of reflections per unit length.

(4) By coating discrete areas of the optical fibre, there is the possibility of carrying out fully-or quasi-distributed sensing.

(5) Greater control over interaction parameters such as interaction length, sensing volume and response time is possible than with distal-face fibre sensors.

A number of disadvantages of evanescent field sensors exist and these include the following:

(1) Careful control of launch is required to ensure repeatable behaviour.

(2) In coated optical fibre sensors fouling of the sensor may be a problem if the evanescent field is not fully contained within the coating.

(3) The relative sensitivity compared to bulk absorption is lower due to the small fraction of power typically carried in the evanescent field.

1.4 The sol-gel process

The sol-gel process is a method of preparing glasses and ceramics at low temperatures by hydrolysis and polymerisation of organic precursors [12]. The process is adaptable to producing bulk pieces as well as films and fibres [13]. The preparation of materials generally involve the use of metal alkoxides which undergo hydrolysis and polymerisation reactions to give gels. Chapter 3 describes in detail these reactions and how they are influenced by different processing parameters.

In the area of optical sensors the primary use of sol-gel materials is as a method of immobilisation of reagents for reagent-mediated sensing. When appropriate process parameters are employed the reagent cannot be leached out, but smaller analyte molecules can still permeate the interconnected microporous structure of the sol-gel material. Sol-gel materials used as sensing substrates can take many forms e.g. monoliths or thin films. For instance, the sol-gel process provides a means of coating an unclad optical fibre with a porous cladding within which the analyte-sensitive reagent is entrapped [14]. A wide range of chemical sensing materials using the sol-gel process has been reported. These include sensors for metal ions [18,19] and biomolecules

[20,21]. The sol-gel process has also been used to enhance the sensitivity of direct spectroscopic evanescent wave sensors [6,15] and to fabricate planar waveguide substrates for chemical sensing [16,17].

The sol-gel technique offers many advantages over other immobilisation techniques for the fabrication of chemically sensitive supports [6,18]:

(1) The glasses are chemically inert, photostable and thermally stable, compared with a plastic matrix, making then highly suitable for applications in harsh environments.

(2) The preparation of doped glass is technically simple. The trapping procedure is straightforward and non-specific as compared with, for example, covalent binding of a reagent to a solid support.

(3) Glass blocks of various shapes, as well as thin films, are easily prepared.

(4) Sensor fabrication using optical fibres is simple, involving straight-forward dip-coating of the unclad fibre followed by curing at low temperature.

(5) The flexibility of the process enables a range of critical sensor parameters to be optimised. For example, film thickness, which has a large effect on sensor response time, can be controlled by varying the coating rate [12,22].

(6) The technique is particularly suited to indicator based gas sensing because the high specific area (e.g. 100 m^2/g) of the microporous structure enhances the sensitivity considerably.

The applications of the sol-gel process to optical fibre chemical sensing was first proposed by Badini et al. in 1989 [23]. In their work, silica gels incorporating fluorescein isothiocyanate were prepared and coated on a glass slide. Cracks developed for most of the coatings and difficulties in the detection of spectral changes were also reported in their work due to very low sensitivity. In 1991, MacCraith et al. [24] developed a fibre optic pH sensor which was the first fibre optic chemical sensor prepared by sol-gel thin film coating. This was followed shortly afterwards by another fibre optic pH sensor by Ding et al. [25]. In each case, pH indicators were immobilised in a silica gel matrix before they were coated onto optical fibres. The pH sensor reported by MacCraith et al. was prepared by coating an unclad silica fibre with a thin layer of porous silica cladding within which a pH-sensitive fluorescence dye, fluorescein,

was entrapped. In the approach reported by Ding et al., a pH sensor was prepared by co-immobilising absorption-type pH indicators, bromocresol green and bromocresol purple, into sol-gel which was coated as a thin film onto a porous core silica glass fibre. Since these first reports, optical fibre sensing using sol-gel films has been reported by many groups for the sensing of a wide range of analytes [26,27,28]. The work in this thesis uses the sol-gel process to produce pH and ammonia-sensitive films for use in evanescent wave absorption-based sensors.

1.5 Objectives and structure of thesis

The primary objectives of this project were as follows:

- Investigation of the sol-gel process for the fabrication of porous silica films.
- Development of an evanescent-wave absorption-based characterisation system for coated optical fibres.
- Optimisation of doped sol-gel coated fibres for optical chemical sensing applications (pH, ammonia).

The investigation of the sol-gel process envisaged a detailed characterisation of the parameters affecting the thickness and refractive index of sol-gel-derived silica films. This was later expanded to include issues of film stability, dye leachability, analyte-diffusion in the sol-gel film and sensor response. In order to investigate doped sol-gel films in sensor applications, a characterisation system would be required. The use of evanescent wave absorption on coated optical fibres was proposed for this function. The initial objective was the use of doped sol-gel films for pH sensing. This was expanded to include ammonia sensing. For any sensor, the issues affecting its response time and sensitivity would need to be investigated in detail. The work on ammonia sensing was part of a European COPERNICUS project, whose aim is the construction of an optical fibre sensor for the rapid detection and location of ammonia leaks.

Chapter 2 of this thesis deals with evanescent wave sensing, with an outline of the theory for multimode fibres. The sol-gel process and the factors affecting the different chemical reactions are outlined in Chapter 3, while Chapter 5 outlines the results of the characterisation of sol-gel films. The factors affecting the sol-gel hydrolysis and condensation reactions include pH, water / alkoxide ratio, type of catalyst

and type of silicon alkoxide precursor and these are investigated in detail. A number of different film parameters (thickness, refractive index, temporal stability and film quality) were monitored as a function of dip-speed, water : silicon alkoxide ratio (R), sol aging time and time after drying. The effects of sol aging time, R value and dip-speed on film thickness are presented. A number of characterisation systems have been employed in this work and these are described in detail in Chapter 4. Three systems were used for characterisation, based on either broad-band white light sources or LED sources. A method for enhancement of the sensitivity of these evanescent wave sensors by the use of an annular beam mask to block low order modes in the fibre is demonstrated.

Chapters 6 and 7 deal with the application of doped sol-gel films to pH and ammonia gas sensing, respectively. The difference between the properties of the immobilised indicators and those in solution are illustrated, with a shift in pK and a broadening of the pH range the most distinct features. Methods for extending the operational range of a pH sensor by this broadening or by co-immobilisation of indicators are examined. The problem of leaching is the most important consideration in determining the suitability of sol-gel films for pH sensing applications and this was studied in detail. The influence of RH on ammonia sensing is investigated and in particular the contrasting behaviour of ormosil films are illustrated. In Chapter 8 the issues affecting the diffusion of metal ions into sol-gel films are discussed. The nature of the sol-gel surface is shown to be of critical importance. This is demonstrated here for the reaction of lead ions (Pb^{2+}) with xylenol orange in different sol-gel films.

References

1. E. Udd, 'An overview of fibre-optic sensors', Rev. Sci. Instrum., Vol. 66, No. 8, 1995, 4015-4030.

2. N.U. Taib and R. Narayanaswamy, 'Solid-state instruments for optical fibre chemical sensors: a review', Analyst, Vol. 120, 1995, pp. 1617-1625.

3. O.S. Wolfbeis, 'Fibre Optic Chemical Sensors and Biosensors', Vol. 1, CRC Press, Boca Raton, Fl., 1991.

4. J.I. Peterson, S.R. Goldstein, R.V. Fitzgerald and D.K. Buckhold, 'Fibre optic pH probe for physiological use', Anal. Chem., Vol. 52, 1980, pp. 864-869.

5. M. Bacci, M. Brenci, G. Conforti, R. Falciai, A.G. Mignani and A.M. Scheggi, 'Thermochromic transducer optical fibre thermometer', Applied Optics, Vol. 25, No. 7, 1986, pp. 1079-1082.

6. B.D. MacCraith, 'Enhanced evanescent wave sensors based on sol-gel derived porous glass coatings', Sensors and Actuators B, Vol. 11, 1993, pp. 29-34.

7. R.A. Lieberman, L.L. Blyler and L.G. Cohen, 'A distributed fibre optic sensor based on cladding fluorescence', J. Lightwave Technology, Vol. 8, No. 2, 1990, pp. 212-220.

8. Q. Zhou, M.R. Shahriari, D. Kritz and G.H. Sigel Jr., 'Porous fibre-optic sensor for high-sensitivity humidity measurements', Anal. Chem., Vol. 60, 1988, pp. 2317-2320.

9. S. McCabe and B.D. MacCraith, 'Novel mid-IR LED as source for optical fibre evanescent wave gas detection', Electronic Letters, Vol. 29, No. 19, 1993, pp. 1719-1720.

10. N.J. Harrick, 'Internal Reflection Spectroscopy', Harrick Scientific Corporation, 1987.

11. F.M. Mirabella Jr and N.J. Harrick, 'Internal Reflection Spectroscopy: Review and Supplement', Harrick Scientific Corporation, 1985.

12. C.J. Brinker and G.W. Scherer, 'Sol-gel Science', Academic Press, New York, 1990.

13. L.C. Klein, 'Sol-gel Technology for Thin Films, Fibres, Preforms, Electronics and Specialty Shapes', Noyes Publications, New Jersey, 1988.

14. B.D. MacCraith, J.F. McGilp, B. O'Kelly and V. Ruddy, 'A Waveguide Sensor', PCT Patent Application No. PCT/GB92/00428, 1992.

15. G. Stewart and B. Culshaw, 'Optical waveguide modelling and deign for evanescent field chemical sensing', Optical and Quantum Electronics, Vol. 26, 1994, pp. S249-S259.

16. L. Yang, S.S. Saavedra, N.R. Armstrong and J.Hayes, 'Fabrication and characterisation of low-loss, sol-gel planar waveguides', Anal. Chem., Vol. 66, 1994, pp. 1254-1263.

17. L. Yang and S.S. Saavedra, 'Chemical sensing using sol-gel derived planar waveguides and indicator phases', Anal. Chem., Vol. 67, 1995, pp. 1307-1314.

18. R. Zusman, C. Rottman, M. Ottolenghi and D. Avnir, 'Doped sol-gel glasses as

chemical sensors',. J. Non-Crystalline Solids, Vol. 122, 1990, pp. 107-109.

19. O. Lev, B.I. Kugavskaya, Y. Sacharov, C. Rottman, A. Kuselman, D. Avnir and M. Ottolenghi, 'Photometric sensors based on sol-gel porous glass doped with organic reagents', Proc. SPIE Vol. 1716, Intl. Conf. on Monitoring of Toxic Chemicals and Biomarkers', 1992, pp. 357-366.

20. L.M. Ellerby, C.R. Nishida, F. Nishida, S.A. Yamanaka, B. Dunn, J.S. Valentine and J.I. Zink, 'Encapsulation of proteins in transparent porous silicate glasses prepared by the sol-gel method', Science, Vol. 255, 1992, pp. 1113-1115.

21. B.C. Dave, B. Dunn, J.S. Valentine and J.I. Zink, 'Sol-gel encapsulation methods for biosensors', Anal. Chem., Vol. 66, No. 22, pp. 1120A - 1127A.

22. I. Strawbridge and P.F. James, 'The factors affecting the thickness of sol-gel derived silica coatings prepared by dipping', J. Non-Crystalline Solids, Vol. 86, 1986, pp. 381-393.

23. G.E. Badini, K.T.V. Grattan, A.W. Palmer and A.C.C. Tseung, 'Development of pH-sensitive substrates for optical sensor applications', Springer Proceedings in Physics, Vol. 44, 1989, pp. 436-442.

24. B.D. MacCraith, V. Ruddy, C. Potter, B O'Kelly and J.F. McGilp, 'Optical waveguide sensor using evanescent wave excitation of fluorescent dye in sol-gel glass', Electronic Letters, Vol. 27, No. 14, 1991, pp. 1247-1248.

25. J.Y. Ding, M.R. Shahriari and G.H. Sigel Jun., 'Fibre optic pH sensors prepared by sol-gel immobilisation technique', Electronic Letters, Vol. 27, No. 17, 1991, pp. 1560-1562.

26. R.A. Dunbarr, J.D. Jordan and F.V. Bright, 'Development of chemical sensing platforms based on sol-gel-derived thin films: origin of film age vs performance trade-offs', Anal. Chem., Vol. 68, No. 4, 1996, pp. 604-610.

27. R. Blue and G. Stewart, 'Fibre-optic evanescent wave pH sensing with dye doped sol-gel films', Int. J. Optoelectronics, Vol. 10, No. 3, 1995, pp. 211-222.

28. B.D. MacCraith, G. O'Keeffe, C. McDonagh and A.K. McEvoy, 'LED-based fibre optic oxygen sensor using sol-gel coating', Electronic Letters, Vol. 30, No. 11, 1994, pp. 888-889.

Chapter 2 Evanescent Wave Sensing

2.1 Introduction

The evanescent wave is a consequence of total internal reflection and can be generated at the interface between any two dielectric materials. The sensing method investigated in this thesis involves the interaction of the evanescent wave in an optical fibre with an absorbing medium (analyte) in contact with the core of the optical fibre. In an optical waveguide, light is totally reflected at the interface between an optically dense medium of refractive index n_1 and an optically rare one of refractive index n_2, when the angle of refraction is larger than a critical angle θ_c. The relationship between the two refractive indices and θ_c is given by:

$$\text{Sin } \theta_c = n_2 / n_1 \qquad (2.1)$$

Light is not instantaneously reflected when it reaches the interface. Rather, light penetrates to some extent into the optically rare phase. More precisely, the amplitude of the electric field does not drop abruptly to zero at the boundary but has a tail that decreases exponentially in the direction of an outward normal to the boundary. This phenomenon is referred to as an evanescent wave.

Newton [5] was one of the first to note the existence of the evanescent field. He observed that total internal reflection in a prism could be frustrated by bringing a second prism close to the point of total reflection. The properties of the evanescent wave were not discussed in detail until 1933, when Taylor [6] outlined the potential of the evanescent wave for spectroscopic and refractive index measurements. Taylor differentiated between the frustrated total reflection (FTR) observed by Newton and attenuated total reflection (ATR) which is the reduction of the reflected light intensity as a result of absorption in the rarer medium. However, it was not until the early 1960's that the publications of Fahrenfort [7] and Harrick [8] sparked off a flurry of research into ATR spectroscopy. These authors reported the practical use of the evanescent wave as a spectroscopic tool.

The sensitivity of ATR is normally much less than conventional direct absorption spectroscopy because the interaction occurs at the point of total internal reflection over a relatively short path length. Increasing the number of interaction points increases the

sensitivity of ATR in an analogous way to increasing the path length in direct absorption. Optical fibres and waveguides are ideal for ATR spectroscopy because light propagates by means of total internal reflection with a high number of reflections per unit length. Two distinct approaches can be applied in evanescent wave sensing, as discussed in section 1.3, namely direct spectroscopy and reagent-mediated sensing. The work described in this thesis is based on the latter approach and uses absorption-based dyes and multimode optical fibres.

This chapter outlines the theory of evanescent wave sensing using multimode fibres. It begins by showing how the evanescent wave can be generated in the case of refraction and reflection at a dielectric interface. The two distinct ways in which perturbation of the evanescent field can result in a reduction of the reflected optical power are outlined. These are FTR and ATR. The specific case of evanescent wave spectroscopy using multimode fibres is covered in section 2.4 Particular attention is paid to issues affecting the sensitivity of the evanescent wave.

2.2 The evanescent field

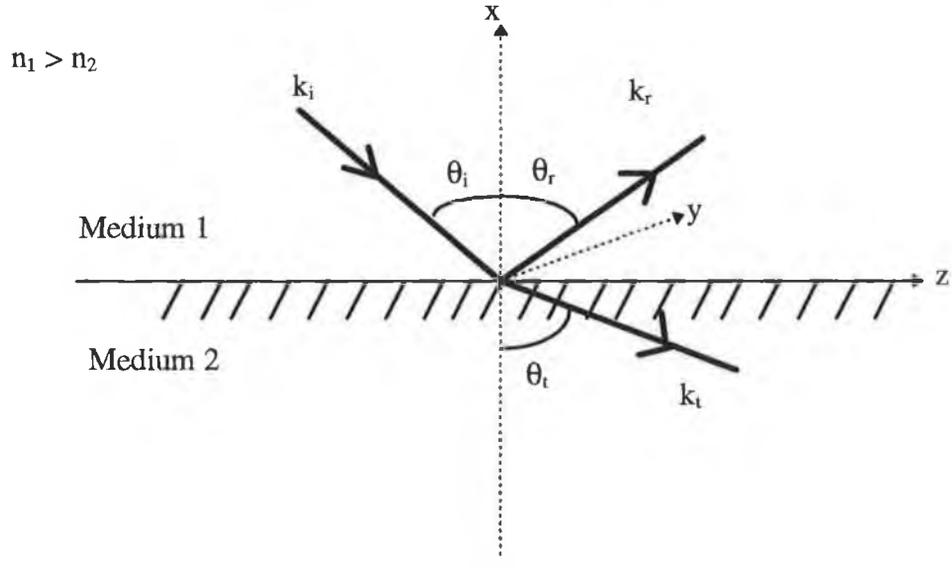

Figure 2.1 Refraction and reflection at a dielectric interface

The simplest case to consider is the reflection and refraction of plane waves at the interface between dielectric media of different refractive indices n_1 and n_2, where $n_1 > n_2$. When an electromagnetic wave strikes the interface, the wavefront is both

reflected and transmitted across the interface. This is illustrated in Figure 2.1. In order to obtain a mathematical description of what occurs at the interface, it is convenient to take the simple case of linear, isotropic, homogeneous and non-magnetic dielectric media. Using Maxwell's equations to consider the boundary conditions between two dielectric interfaces, it can be shown that the tangential components of the electric field **E** and magnetic field **H** must be continuous across the dielectric interface [1,2].

The incident, reflected and transmitted waves may be represented by the following equations:

$$\mathbf{E}_i(\mathbf{r}) = A_i e^{-i(\mathbf{k}_i \cdot \mathbf{r})} \qquad (2.2)$$

$$\mathbf{E}_r(\mathbf{r}) = A_r e^{-i(\mathbf{k}_r \cdot \mathbf{r})} \qquad (2.3)$$

$$\mathbf{E}_t(\mathbf{r}) = A_t e^{-i(\mathbf{k}_t \cdot \mathbf{r})} \qquad (2.4)$$

where A is the electric field amplitude, **k** is the wave propagation vector of the plane wave, the components of **r** specify the co-ordinate point at which the field is observed.

Each wave propagation vector may be resolved into its cartesian components k_x, k_y and k_z where x, y and z are oriented as in Figure 2.1. The interface is defined as the yz plane at x = 0. Without loss of generality, the incident wave may be limited to the xz plane such that $k_y = 0$ [1]. Application of the boundary condition for the tangential **E** field requires

$$A_{iz} e^{-ik_{iz}z} + A_{rz} e^{-ik_{rz}z} = A_{tz} e^{-ik_{tz}z} \qquad (2.5)$$

This equation must be satisfied for all z, i.e. all points on the interface. A nontrivial solution requires that the propagation vectors k_{iz}, k_{rz} and k_{tz} must be equal. The z components of the propagation vectors may be rewritten in terms of the angles they make with respect to the surface normal, which in this case is the x direction, i.e. angles θ_i, θ_r and θ_t. Using the relation $k_m = 2\pi n_m/\lambda_0$ where n_m is the refractive index of the medium and the subscript m denotes medium 1 and 2,

$$k_{iz} = k_1 \sin\theta_i \qquad (2.6)$$

$$k_{rz} = k_1 \sin\theta_r \qquad (2.7)$$

$$k_{tz} = k_2 \sin\theta_t \qquad (2.8)$$

Using $k_{iz} = k_{rz} = k_{tz}$ a number of important relationships may be derived. Firstly

$$\theta_i = \theta_r \qquad (2.9)$$

i.e. the reflected and incident angles measured with respect to the normal are equal. Furthermore, using the relation $k_m = 2\pi n_m/\lambda_0$ and equating equations 2.7 and 2.8, it can be shown that

$$n_1 \sin\theta_i = n_2 \sin\theta_t \qquad (2.10)$$

which is commonly known as Snell's law.

Total internal reflection occurs at the interface between two media where n_2 is less than n_1. As the angle of incidence, θ_i, is increased, the transmitted angle θ_t also increases. There is a critical angle of incidence, θ_c, for which $\theta_t = 90°$. For incidence angles greater than this critical angle, no light propagates into medium 2. Equation 2.1 describes the relation between the critical angle and the refractive indices of the two media. At angles of incidence greater than θc, the x component of the transmitted propagation constant becomes complex and the transmitted electric field exponentially decays in the x-direction. The transmitted wave is evanescent and does not propagate away from the dielectric boundary.

The equation of the transmitted wave polarized in the xz plane is given by

$$\mathbf{E}_t = A_t e^{i\left(\mathbf{k_t}.\mathbf{r} - \omega t\right)} \qquad (2.11)$$

where the propagation vector $\mathbf{k}_t$ is given by

$$\mathbf{k}_t = k_{tz} + k_{tx} = k_t \sin\theta_t + k_t \cos\theta_t \qquad (2.12)$$

Using Snell's law, the x and z components of the propagation vector of the transmitted wave can be described in terms of the angle of incidence and the refractive indices of medium 1 and 2. Therefore

$$k_{tz} = k_2 n_{12} \sin\theta_i \qquad (2.13)$$

$$k_{tx} = k_2\left(1 - n_{12}^2 \sin^2\theta_i\right)^{\frac{1}{2}} \qquad (2.14)$$

$$= k_2 n_{12}\left(\sin^2\theta_c - \sin^2\theta_i\right)^{\frac{1}{2}} \qquad (2.15)$$

where $n_{12} = n_1/n_2$ and similarly $n_{21} = n_2/n_1$.

For incident angles θ_i greater than the critical angle, θ_c, where $\theta_c = \sin^{-1}(n_{21})$, the x component k_{tx} of the propagation constant is complex and may be written as $i\gamma$ where γ is real. The transmitted wave electric field is then given by

$$\mathbf{E}_t = A_t e^{i\left(k_{tx}x + k_{tz}z - \omega t\right)} \qquad (2.16)$$

$$= A_t e^{i\left(k_2 n_{12}\sin\theta_i z - \omega t\right)} e^{-\gamma x} \qquad (2.17)$$

where

$$\gamma = k_2\left(n_{12}^2 \sin^2\theta_i - 1\right)^{\frac{1}{2}} \qquad (2.18)$$

γ is known as the decay constant and can take positive or negative solutions. The solutions are physically constrained such that the product γx is positive. Otherwise the field would increase exponentially with distance into the second medium. This solution describes a non-propagating electric field which decays exponentially in medium 2. The exponentially decaying field is called the evanescent field.

An important parameter often used to characterise the evanescent wave is the field penetration depth d_p which is defined as the distance required for the field to drop to 1/e or 37% of its valve at the interface. It is given by

$$d_p = \frac{1}{\gamma} = \frac{\lambda_0}{2\pi n_2\left(n_{12}^2 \sin^2\theta_i - 1\right)^{\frac{1}{2}}} \qquad (2.19)$$

$$= \frac{\lambda_0}{2\pi n_1\left(\sin^2\theta_i - \sin^2\theta_c\right)^{\frac{1}{2}}} \qquad (2.20)$$

where k_2 has been written in terms of the free space wavelength λ_0.

The factors that determine the penetration depth are (i) the wavelength of the incident light, (ii) the angle of incidence θ_i of the wave at the dielectric interface and (iii) the refractive indices n_1 and n_2 at the dielectric interface. Section 2.4 describes in more detail how the penetration depth can be increased for the case of evanescent wave sensing using multimode fibres.

2.3 Evanescent wave interactions

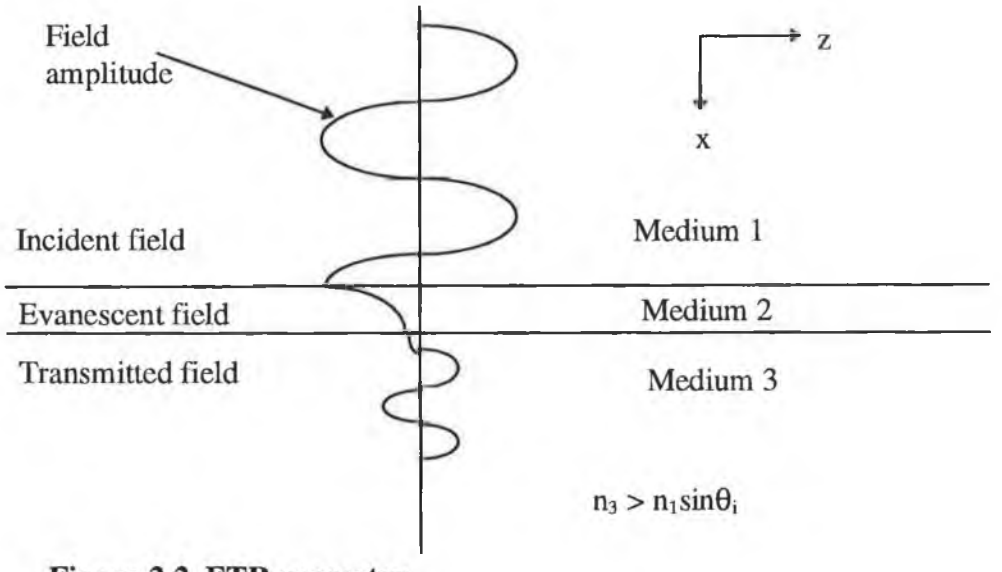

Figure 2.2 FTR geometry

There are two distinctly different methods of coupling to the evanescent wave and extracting energy from it and thereby resulting in a reduction in the intensity of the reflected optical power. These are frustrated total reflection (FTR) and attenuated total reflection (ATR) [3]. Figure 2.2 shows the geometry for FTR. A lossless dielectric with a refractive index n_3 overlaps the exponentially decaying field in medium 2. If $n_3 > n_1 \sin\theta_i$, where θ_i is the angle of incidence of the wavefront, then the evanescent condition is not satisfied and k_z in medium 3 is real. Therefore the wave propagates in medium 3. This reduces the intensity of the reflected wave and the total reflection condition is said to be frustrated. By controlling the distance between medium 1 and 3, or the angle of incidence of the plane wave, the amount of transmitted and reflected light may be adjusted [3]. FTR is, for example, used in prism-coupling to an optical waveguide [4].

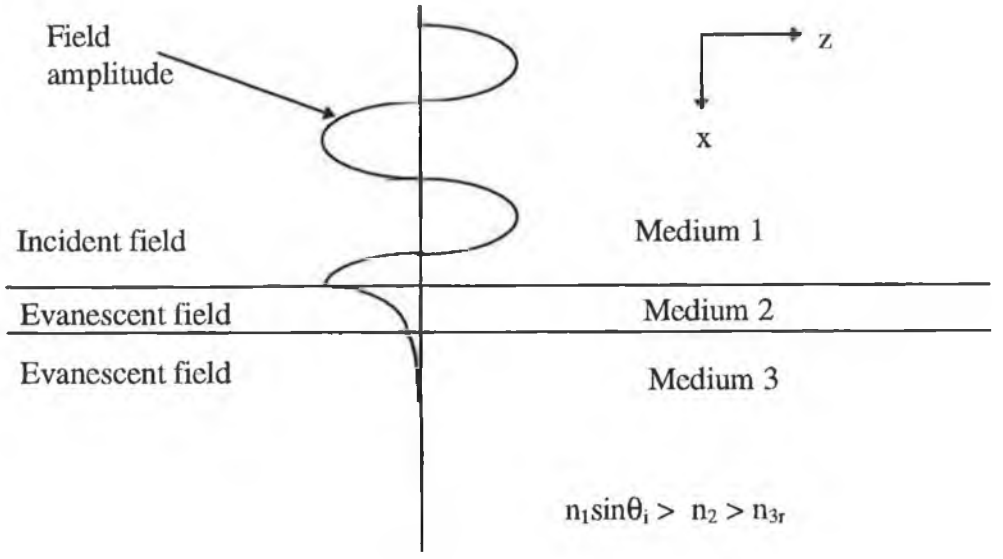

Figure 2.3 ATR geometry

The case for ATR is illustrated in Figure 2.3, where medium 3 is replaced with an absorbing medium with a complex refractive index n_3, with real component $n_{3r} < n_1 \sin\theta_i$. The field in medium 3 is evanescent. The reflected power is attenuated as the lossy medium absorbs a portion of the optical power through interactions with the evanescent field. Power absorbed is a function of the absorption coefficient of the material and the depth of penetration of the evanescent field in the medium. An absorbing spectrum of medium 3 can be recorded using the ATR effect. ATR spectroscopy is normally performed with no separating medium 2 as the field in medium 3 in this configuration is also evanescent and the depth of penetration greater without the intervening medium.

2.4 Fibre optic evanescent wave spectroscopy

2.4.1 Introduction

Chemical analysis based on evanescent wave interactions at the surface of a waveguide and using ATR spectroscopy is a well established laboratory technique [3]. The technique, as described above, relies on the penetration of the evanescent wave of the totally internally reflected ray into an absorbing sample medium. The amount of

absorption depends on both the amplitude of the evanescent field in the sample medium and the number of reflections within the waveguide-sample cell. The former increases dramatically for incident angles approaching the waveguide-sample critical angle, and the latter is inversely proportional to the waveguide thickness. Optical fibres are ideal as ATR cells because they can be of very small width, long length and they transmit light by total internal reflection. They consist of a thin central glass core surrounded by a cladding of slightly lower refractive index, as shown in Figure 2.4. Within the core, the refractive index profile can be uniform or graded, while the cladding index is typically uniform [10]. The two situations are referred to as step-index and graded-index fibres respectively. The step-index fibres can be further divided into single mode or multimode fibres. By removing some or all of the cladding and replacing it with an absorbing material, e.g. a doped sol-gel film, the guided light in the fibre may be attenuated. In this way fibre-based ATR can be performed.

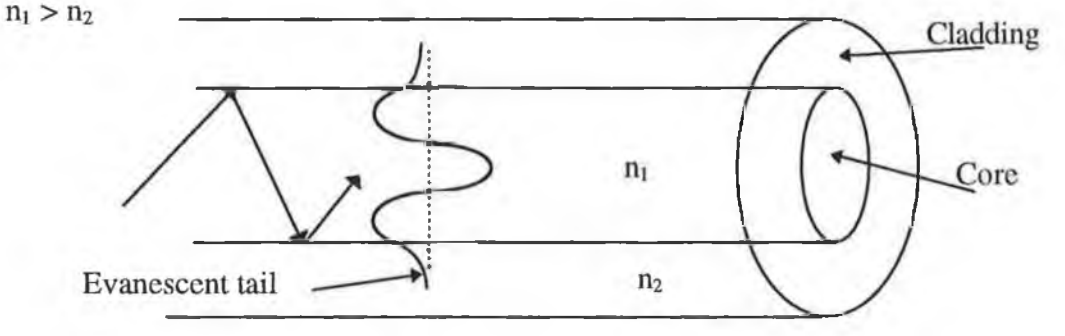

Figure 2.4 Optical fibre showing total internal reflection and typical electric field amplitude

When considering absorption of the evanescent wave, the quantity of the evanescent power which can interact with the analyte is a critical parameter [23]. In the case of optical fibre evanescent wave sensors this quantity is closely related to the fraction, r, of the total guided power that resides in the cladding region, i.e.

$$r = \frac{P_{clad}}{P_{tot}} \qquad (2.21)$$

This fraction is determined to a large extent by the fibre V-number [11] , which is given

by

$$V = \frac{2\pi}{\lambda_0}\rho NA \qquad (2.22)$$

where ρ is the fibre core radius, NA is the numerical aperture $\left(\left(n_1^2 - n_2^2\right)^{\frac{1}{2}}\right)$, and n_1 and n_2 are the refractive index of the core and cladding, respectively. The V-number or normalised frequency of a fibre combines in a useful manner the information about three important design variables for the fibre, namely, the core radius ρ, the relative refractive index difference Δ and the operating wavelength λ. Gloge [11] has shown that the value of r for weakly guiding ($n_1 \cong n_2$) multimode fibres in which all modes are propagating is given by:

$$r = \frac{4\sqrt{2}}{3V} \qquad (2.23)$$

This was later corrected by Payne and Hale [12] to:

$$r = \frac{4}{3V} \qquad (2.24)$$

Although many evanescent wave sensors do not comply with the weakly guiding condition, this expression gives an indication of the fraction of power available for evanescent wave sensing. Values of r less than 1% are typical in multimode evanescent wave sensors.

Many factors affect the sensitivity of an evanescent wave sensor. From the discussion above r is maximised for low V-numbers, i.e. single-mode or low mode fibres. However it is more common to use highly multimode fibres ($V \gg 1$) in evanescent wave sensors because of their much higher power throughput and ease of handling. From section 2.2 and equation 2.20 it can be seen that to increase the evanescent absorption, the penetration depth of the evanescent wave should be increased. Another factor that affects the sensitivity is the number of reflections at the interface in the sensing region. It is noted from equation 2.20 that the penetration depth increases as the angle of incidence, θ, approaches the critical angle θ_c of the sensing region. Thus the penetration depth can be increased by launching only those rays which make angles (θ) slightly greater than but close to the critical angle, while the number of reflections can be increased by choosing a smaller diameter fibre. The mechanism used

to increase evanescent absorption is tapering of the fibre [18]. Selectively launching rays which make an angle close to θ_c [17] can be achieved by using an annular beam mask to block low order modes in the fibre. This increases the fraction of light absorbed and hence the sensitivity. This method was used in the work described in this thesis and is outlined in detail in section 4.5.

A number of studies [13,14,15,16] has been carried out by different groups to model evanescent wave spectroscopy using multimode fibres. In general these show the factors that affect the power transmitted by an optical fibre and how this is related to launch conditions and evanescent wave absorption. In the discussion below the model developed by Ruddy et al. [14,17] and expanded by Gupta et al. [18,19] is outlined and the factors affecting evanescent wave sensitivity are highlighted. The model developed by these authors is based on meridional rays in the fibre. Meridional rays are those which cross the fibre axis between reflections as distinct from skew rays which spiral around the fibre without crossing the axis [10].

2.4.2 Theoretical model

Absorption of power in a fibre due to attenuation of the evanescent wave in the cladding may be characterised by an evanescent absorption coefficient γ which is related to the bulk absorption coefficient α by the expression [21]

$$\gamma = r\alpha\left(\frac{n_2}{n_e}\right) \qquad (2.25)$$

where r, the fraction of the optical power carried by the cladding, is given by equation 2.23, and n_2 and n_e are the sample and effective refractive index, respectively. The effective index $n_e = n_1 \sin\theta$ (see figure 2.5), and is a means of characterising a mode in a fibre. If weakly guiding n_2/n_e is about equal to 1. Ruddy et al. [17] related the evanescent absorption coefficient to the bulk absorption coefficient for the general case of non-weakly guiding fibres and this is outlined below.

The power transmitted by an optical fibre whose cladding has been replaced by an absorbing medium may be written in the form [20]

$$P(z) = P(0)\exp(-\gamma z) \qquad (2.26)$$

where z is the distance along the unclad fibre, P(0) is the power transmitted in the absence of an absorbing species and γ is the evanescent absorption coefficient and can be written as [20]

$$\gamma = NT \qquad (2.27)$$

where N is the number of reflections per unit length and T is the Fresnel transmission coefficient at the interface between a lossless core and lossy cladding. The refractive index of the lossy cladding is given by n_2 - ik, where $\alpha = 4\pi k/\lambda_0$ is the bulk absorption coefficient of the cladding material. In the case of meridional rays in a weakly guiding ($n_1 \sim n_2$) fibre of normalised frequency parameter V, the relationship between the evanescent absorption coefficient γ and bulk absorption coefficient α for a lossy cladding has been shown to be [20]

$$\frac{\gamma}{\alpha} = \frac{1}{V}\left(\frac{\theta_z}{\theta'_c}\right)^2 \frac{1}{\sqrt{1-\left(\theta_z/\theta'_c\right)^2}} \qquad (2.28)$$

where θ_z is the angle the ray makes with the core axis and θ'_c is the complementary critical angle ($\cos^{-1} n_1/n_2$) as illustrated in Figure 2.5. Equation 2.28 is accurate for bound meridional rays whose direction is not close to the critical angle. Ruddy et al. [17] modified this expression to cater for non-weakly bound modes. Removing this condition and allowing all value of $\theta_z < \theta'_c$ the value of T is shown to be

$$T = \frac{\alpha\lambda n_2 \sin\theta_z}{\pi n_1^2 \sin^2\theta'_c \sqrt{\cos^2\theta_z - \cos^2\theta'_c}} \qquad (2.29)$$

Using $N = \tan\theta_z/2\rho_e$ for a fibre of core radius ρ, and effective radius ρ_e ($\rho_e = \rho + d_p$, where d_p is the penetration depth), and equation 2.27, the ratio of the evanescent to bulk absorption coefficients then reduce to

$$\frac{\gamma}{\alpha} = \frac{\lambda n_2 \cos\theta\cot\theta}{2\pi\rho n_1^2 \cos^2\theta_c \sqrt{\sin^2\theta - \sin^2\theta_c}} \qquad (2.30)$$

where θ is the angle between the ray and the normal to the interface ($\theta = \pi/2 - \theta_z$) and θ_c

is the critical angle for the two media ($\sin^{-1}n_2/n_1$). The value of γ/α derived in equation 2.30 reduces to 2.28 in the weakly guiding case of $n_1 \sim n_2$ for angles not close to the critical angle.

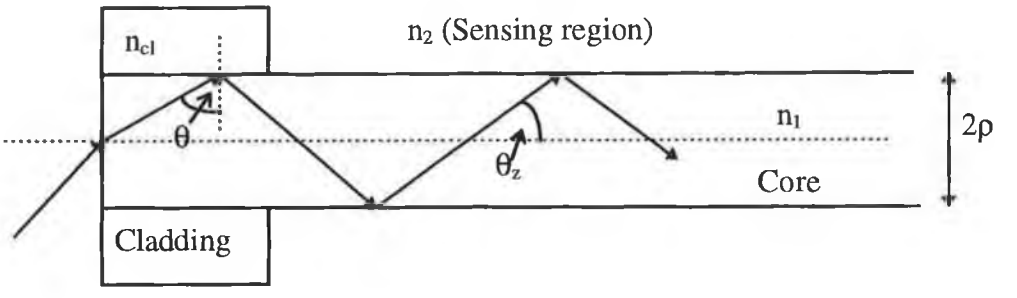

Figure 2.5 Representation of a meridional ray in the fibre

Gupta et al. [18] expanded equation 2.30 to take account of the power distribution of the rays at the launch end of the fibre. If the light is launched into the fibre from a collimated source using a microscope objective such that the beam is focused onto the fibre end-face at the axial point, then [18]

$$p(\theta) \propto \frac{n_1^2 \sin\theta\cos\theta}{\left(1 - n_1^2\cos^2\theta\right)^2} \qquad (2.31)$$

where $p(\theta)$ represents the power distribution of the rays. These authors then defined an effective evanescent absorption coefficient for rays launched into the sensing region for the angles (with respect to the normal to the core-cladding interface) in the range $\theta_1 < \theta < \theta_2$ as given by

$$\gamma_{eff}(\theta_1,\theta_2) = \int_{\theta_1}^{\theta_2} p(\theta)\gamma(\theta)d\theta \Big/ \int_{\theta_1}^{\theta_2} p(\theta)d\theta \qquad (2.32)$$

Therefore, combining equations 2.31 and 2.32 gives:

$$\gamma_{eff}(\theta_1,\theta_2) = \int_{\theta_1}^{\theta_2} \frac{\sin\theta\cos\theta}{\left(1 - n_1^2\cos^2\theta\right)^2}\gamma(\theta)d\theta \Big/ \int_{\theta_1}^{\theta_2} \frac{\sin\theta\cos\theta}{\left(1 - n_1^2\cos^2\theta\right)^2}d\theta \qquad (2.33)$$

Gupta used equation 2.33 in the following two cases [18,19], namely for a uniform core and for a tapered fibre core. The work described in this thesis used only a uniform core fibre and only this case is considered here. In the case of uniform core fibre, and substituting $\gamma(\theta)$ from equation 2.30, equation 2.33 becomes

$$\gamma_{eff}(\theta_1,\theta_2) = \frac{\alpha\lambda n_1\left[1 - n_1^2\left(\cos^2\theta_1 + \cos^2\theta_2\right) + n_1^4\cos^2\theta_1\cos^2\theta_2\right]}{\pi\rho\left(n_1^2 - n_2^2\right)\left(\cos^2\theta_1 - \cos^2\theta_2\right)} \int_{\theta_1}^{\theta_2} \frac{\cos^3\theta d\theta}{\left(1 - n_1^2\cos^2\theta\right)^2\left(n_{12}^2\sin^2\theta - 1\right)^{\frac{1}{2}}} \quad (2.34)$$

where $n_{12} = n_1/n_2$.

If all bound rays in the fibre are allowed to propagate in the sensing region then $\theta_1 = \sin^{-1}(n_{cl}/n_1)$ and $\theta_2 = 90°$, where n_{cl} is the refractive index of the cladding of the fibre used for the sensor. If only selected rays are allowed to propagate using an annular beam mask at the launch end of the fibre [17,18], then θ_1 is equal to or greater than $\sin^{-1}(n_{cl}/n_1)$ while θ_2 is typically chosen 2-3° greater than θ_1. Obviously, the index of the absorbing medium should be smaller than that of the fibre cladding otherwise there will be a loss of intensity even if there is no absorption and the condition of ATR is not fulfilled.

Equation 2.34 is useful in predicting the behaviour of an EW fibre sensor. Gupta et al. [18] made calculations for a range of sensor designs, including uniform and tapered fibres. They compared the sensitivity of uniform and tapered fibres and showed the greater sensitivity achieved by tapering. One can achieve very high sensitivity in the case of tapering and selective launching of rays in the fibre [19]. The conclusions from this analysis by Gupta is that the sensitivity of an evanescent wave sensor depends on the launching conditions (θ) of the ray and the radius of the fibre core ρ. The smaller the core radius the larger the value of γ/α. Similarly, if θ approaches θ_c then γ/α increases. This is illustrated here in figure 2.6 which plots $\gamma / (\alpha C)$ versus θ_2, where the integrant in equation 2.34 is assumed to be a constant C. Figure 2.6 uses a ρ value of 300 μm, λ = 600 nm, a θ_1 value of 74.5° (launch microscope objective of 0.4 NA) and θ_2 values

corresponding to various mask angles (see Appendix C). A core refractive index value of $n_1 = 1.457$ and cladding index $n_2 = 1.43$ (sol-gel film) were also used in these calculations. This figure illustrates that as the critical angle is approached, γ/α increases significantly. Selectively launching rays which make an angle close to the critical angle, by using an annular beam mask, should therefore increase the effective evanescent absorption. This is demonstrated experimentally in section 4.5.

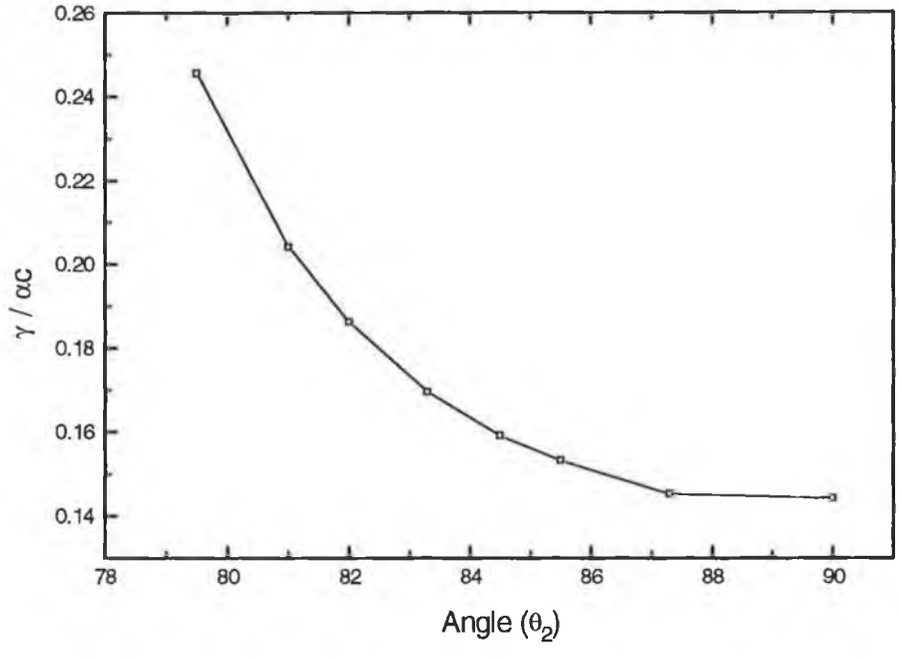

Figure 2.6 Calculated ratio of evanescent absorption coefficient and bulk absorption coefficient versus θ_2

One important feature of the results from Ruddy et al. [17] and Gupta et al. [19] is that the variation of the evanescent absorption coefficient with absorbing analyte concentration is nonlinear in nature. A number of groups [12,22] have investigated this behaviour. Payne and Hale [12] analysed the response of multimode evanescent field optical sensors and how this response deviates from Beer's law. Beer's law describes the attenuation of a beam of light as it passes through a solution of an absorbing chemical compound. The law states that the transmitted optical power P_{out} after passing

through a length L of solution (or absorbing material) is given by

$$P_{out} = P_{in} 10^{-\varepsilon cL} \qquad (2.35)$$

where c is the molar concentration and ε is the molar absorption coefficient. Equation 2.35 can be rewritten as follows:

$$P_{out} = P_{in} \exp(-\alpha L) \qquad (2.36)$$

where the absorption coefficient α is given by

$$\alpha = \frac{\varepsilon c}{\log_{10} e} \qquad (2.37)$$

Equation 2.36 is the familiar exponential absorption law for a bulk material, with α proportional to the concentration of the absorbing compound. This equation is modified in the case of absorption in a multimode fibre to take account of the interaction between the evanescent field and the absorbing material surrounding the fibre to yield the following expression

$$P_{out} = P_{in} \exp(-\alpha r L) \qquad (2.38)$$

where r, as outlined in section 2.4.1, is the total fraction of guided power contained in the evanescent field, and is given by equation 2.24. Payne and Hale [12] noted that there are significant deviations between measured absorbance (defined as $\log_{10}(P_{out}/P_{in})$) and the predictions of equation 2.38. The measured absorbance is much lower than that predicted and often shows nonlinear deviations from Beer's law. The analysis of these authors showed that equation 2.38 is in fact only valid under the special circumstance of continuous coupling between all the fibre modes so as to maintain a uniform distribution of power between all the fibre modes. This situation might arise, for example, as a result of micro-bending along the fibre. However, for short lengths (several centimetres) of straight unclad fibre equation 2.38 is not valid. Each mode of the initially uniform distribution has a different evanescent field and so experiences a different attenuation in the external medium. This means that an initially uniform distribution of modes quickly becomes non-uniform. The result is that the true response of the sensor deviated significantly from equation 2.38. In particularly, equation 2.38 overestimates

considerably the true attenuation [12]. Driver et al. [15] reported a similar behaviour. Higher order modes have a greater effective penetration depth and are quickly lost due to absorption. Therefore, the modal distribution is changing.

2.5 Conclusion

The concept of the evanescent wave and evanescent wave spectroscopy has been introduced. It was shown that the evanescent wave is a consequence of total internal reflection. The advantages of optical fibres as ATR cells was highlighted. A model describing the evanescent wave spectroscopy using multimode optical fibres was outlined. The sensitivity of an evanescent wave sensor was shown to depend on the launch conditions of rays into the fibre and the radius of the fibre core. Sensitivity increases for smaller core fibres and for rays with angles of incidence approaching the critical angle. In section 4.5 the use of annular beam masks to increase the sensitivity of a sensor will be described in detail.

References

1. D.L. Lee, 'Electromagnetic Principles of Integrated Optics', Chapter 3, J. Wiley and Sons, New York, 1986.

2. R.K. Wangsness, 'Electromagnetic Fields', Chapter 25, J. Wiley and Sons, New York, 1979.

3. N.J. Harrick, 'Internal Reflection Spectroscopy', Harrick Scientific Corporation, 1987.

4. R. Ulrich, 'Theory of the prism-film coupler by plane-wave analysis', J. Optical Society of America, Vol. 60, No. 10, 1970.

5. I. Newton, 'Optiks II, book 8', 1817, p.97.

6. A.M. Taylor and A.M. Glover, 'Studies in refractive index I and II', J. Optical Society of America, Vol. 23, 1933, p. 206.

7. J. Fahrenfort, 'Attenuated total reflection: a new principle for the production of useful infrared reflection spectra of organic compounds', Spectrochimica Acta., 1962, p. 698.

8. N.J. Harrick, 'Surface chemistry from spectral analysis of totally internally reflected

radiation', J. Physical Chemistry, Vol. 64, 1960, p.1110.

9. S. McCabe, 'An investigation of evanescent wave gas sensing using zirconium fluoride optical fibres', Ph.D. Thesis, 1994, pp. 18-20.

10. J.M. Senior, 'Optical Fibre Communications, Principles and Practice', 2nd edition, Prentice Hall, 1992.

11. D. Gloge, 'Weakly guiding fibres', Applied Optics, Vol. 10, 1971, pp. 2252-2258.

12. F.P. Payne and Z.M. Hale, 'Deviation from Beer's law in multimode optical fibre evanescent field sensors', Int. J. Optoelectronics, Vol. 8, No. 5/6, 1993, pp. 743-748.

13. P.H. Paul and G. Kychakoff, 'Fibre-optic evanescent field absorption sensor', Appl. Phys. Lett. Vol. 51, No. 1, 1987, pp. 12-14.

14. V. Ruddy, 'An effective attenuation coefficient for evanescent wave spectroscopy using multimode fibres', Fibres and Integrated Optics, Vol. 9, pp. 143-151.

15. R.D. Driver, J.N. Downing and G.M. Leskowitz, 'Evanescent-wave spectroscopy down infrared transmitting optical fibres', Proc. SPIE Vol. 1591 Infrared Fibre Optics III, 1991, pp. 168-179.

16. A. Messica, A. Greenstein and A. Katzir, 'Theory of fibre-optic, evanescent-wave spectroscopy and sensors', Applied Optics, Vol. 35, No. 13, 1996, pp. 2274-2284.

17. V. Ruddy, B.D. MacCraith and J.A. Murphy, 'Evanescent wave absorption spectroscopy using multimode fibres', J. Appl. Phys., Vol. 67, No. 10, 1990, pp. 6070-6074.

18. B.D. Gupta, A. Sharma and C.D. Singh, 'Evanescent wave absorption sensors based on uniform and tapered fibres, a comparative study of their sensitivities', Int. J. Optoelectronics, Vol. 8, No. 4, 1993, pp. 409-418.

19. B.D. Gupta, C.D. Singh and A. Sharma, 'Fibre optic evanescent field absorption sensor: effect of launching condition and the geometry of the sensing region', Optical Engineering, Vol. 33, No. 6, 1994, pp. 1864-1868.

20. A.W. Synder and J.D. Love, 'Optical Waveguide Theory', Chapman and Hall, London, 1983, pp. 120-133.

21. N.S. Kapany and J.J. Burke, 'Optical Waveguides', Academic Press, New York, 1972.

22. V. Ruddy, 'Nonlinearity of absorbance with sample concentration and path length in evanescent wave spectroscopy using optical fibre sensors', Optical Engineering, Vol. 33, No. 12, 1994, pp. 3891-3894.

23. B.D. MacCraith, 'Enhanced evanescent wave sensors based on sol-gel derived porous glass coatings', Sensors and Actuators B, Vol. 11, 1993, pp. 29-34.

Chapter 3 The Sol-gel Process

3.1 Introduction

The sol-gel process is a chemical synthesis technique for preparing gels, glasses and ceramic materials [1]. The method has received considerable attention because it possesses a number of desirable characteristics. It enables one to prepare glasses at far lower temperatures than is possible by using conventional melting techniques. Compositions which are difficult to obtain by conventional means because of volatilisation, high melting temperatures or crystallisation problems can be produced. In addition the sol-gel method is a high-purity process which leads to excellent homogeneity. Finally, the sol-gel process is adaptable to producing bulk pieces as well as films and fibres [1,2].

The first paper on sol-gel optics was published in 1845 by M. Ebelman, a French chemist, who noticed that silica esters hydrolyse slowly in the presence of moisture to give hydrated silica. He concluded that such a process could be used for the production of optical materials [3]. While the first observation of the sol-gel process was made about 150 years ago, it is only in the last 20 years that the process has been used to produce a large array of different materials including bulk glasses, fibres, monoliths and thin films [2].

The bulk of the work carried out in sol-gel research has concentrated on silica and silica-based systems. This is because of the glass forming ability of silica, as well as the traditional dominance of silica-based materials in the application of ceramics. A large number of other elements has been studied including titania, vanadium, and aluminium [4].

The preparation of materials by the sol-gel process generally involves the use of metal alkoxides which undergo hydrolysis and condensation polymerisation reactions to give gels. The process for silica fabrication typically involves a metal alkoxide (e.g. tetraethylorthosilicate, TEOS), water, a solvent and frequently a catalyst, which are mixed together to achieve homogeneity on a molecular scale.

3.2 Hydrolysis and Condensation Reactions

3.2.1 Overview of general reactions

A sol is a colloidal system where particles or large molecules (1-500 nm diameter) are dispersed in liquid [4]. A gel is a interconnected, rigid network in which the dispersed substance (minimum 1-3 % by weight) forms a continuous, ramifying network that is interpenetrated by a system (usually liquid) [4,9]. Hence, the sol-gel process is the transition of a system of colloidal particles in a solution into a disordered, branched, continuous network, which is interpenetrated by liquid. Gels are usually classified according to the dispersion medium used (e.g. hydrogel or aquagel, alcogel and aerogel for water, alcohol and air respectively) [4].

The sol-gel materials used as sensing substrates are usually in the form of monoliths or thin films. The discussion here in relation to how the sol-gel process in general is affected by different processing parameters will deal primarily with bulk gels (i.e. monoliths). Since only silica-based sol-gels were used in the work described in this thesis, all discussion will concentrate on silica-based materials. The difference between bulk gel materials and thin films will then be discussed. Bulk sol-gel materials used as sensing substrates are usually in the form of monoliths and these are usually xerogels or aerogels. Xerogels are produced when the liquid within the gel is removed by simple evaporation, while aerogels are produced when the liquid within the gel is removed above its critical temperature and pressure (i.e. under supercritical or hypercritical conditions) [1,5].

Silica gels may be prepared from the sol-gel polymerisation of silicon alkoxides (e.g. $Si(OC_2H_5)_4$ or TEOS) [6,7]. Hydrolysis occurs when TEOS and water are mixed in a mutual solvent, usually ethanol.

$$Si(OC_2H_5)_4 + xH_2O \xrightarrow{C_2H_5OH} Si(OC_2H_5)_{4-x}(OH)_x + xC_2H_5OH \qquad (3.1)$$

The intermediates that exist as a result of partial hydrolysis include Si-OH groups, which are called silanols. Condensation may occur between two silanols or a silanol and an ethoxy group to form a bridging oxygen or a siloxane group Si-O-Si. Water or an ethanol molecule is eliminated. An example of the condensation between

two silanols with the elimination of water is given below.

$$Si(OC_2H_5)_{4-x}(OH)_x + Si(OC_2H_5)_{4-x}(OH)_x \rightarrow Si(OC_2H_5)_{4-x}(OH)_{x-1}OSi(OH)_{x-1}(OC_2H_5)_{4-x} + H_2O \quad (3.2)$$

A generalised reaction scheme for the preparation of silicate networks via the sol-gel process is shown in Figure 3.1.[8]

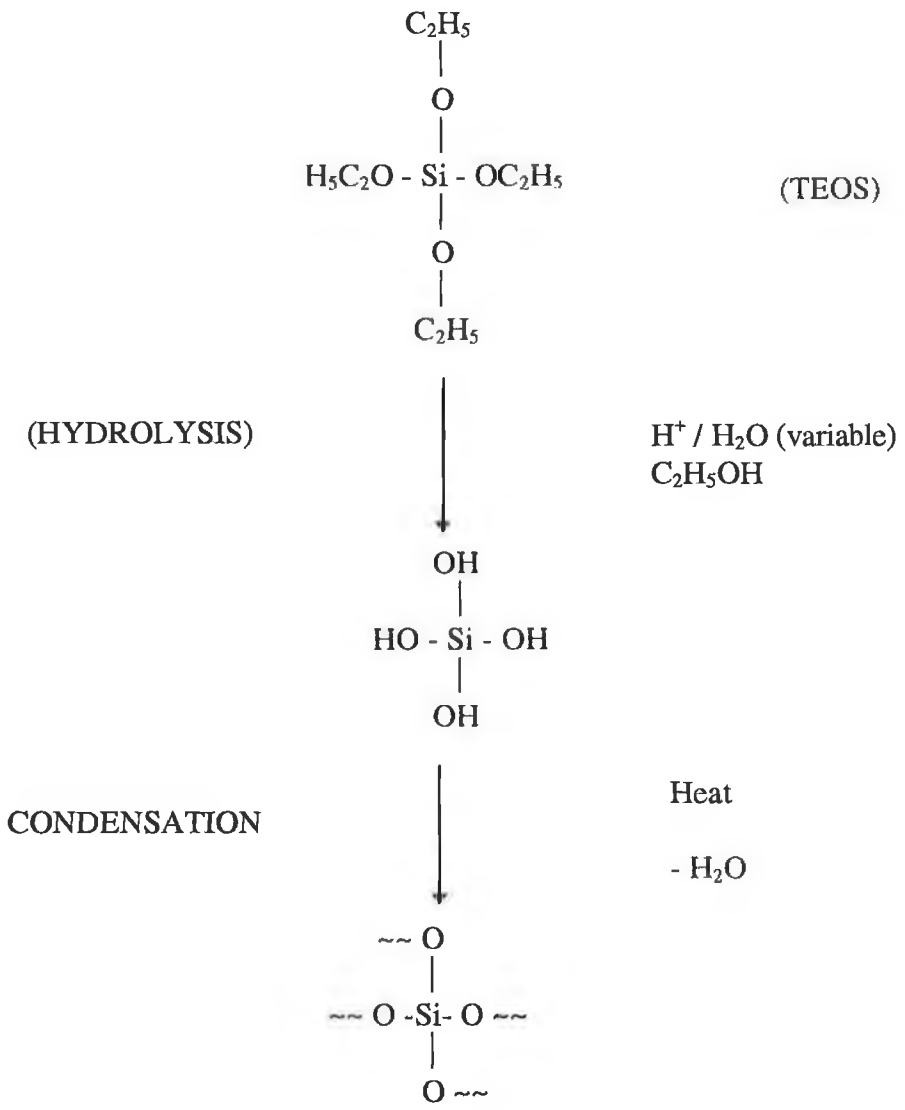

Figure 3.1 Generalised reaction scheme for sol-gel silica

The first step in the sol-gel process is the mixing of the precursor solutions (i.e. metal alkoxide, water and solvent), where hydrolysis and condensation reactions are initialised. Gelation and aging form a solid structure immersed in liquid. Careful drying is used to form a stable sol-gel material. In the following sections a more detailed account of the hydrolysis and condensation reactions for silica sol-gels is presented. The various factors that effect these reactions is well documented in the literature [9,10,11].

3.2.2 Details of hydrolysis and condensation reactions

This section discusses in more detail the hydrolysis and condensation reactions for silica sol-gels with emphasis on the difference in reactions for acid and base catalysis. The formation of silicate gels by the sol-gel process can be described by the 3 general reactions: [1]

Hydrolysis

$$\equiv Si - OR + H_2O \rightleftharpoons \equiv Si - OH + ROH \qquad (3.3)$$

Esterification

Alcohol Condensation

$$\equiv Si - OR + HO - Si\equiv \rightleftharpoons \equiv Si - O - Si\equiv + ROH \qquad (3.4)$$

Alcoholysis

Water Condensation

$$\equiv Si - OH + HO - Si\equiv \rightleftharpoons \equiv Si - O - Si\equiv + H_2O \qquad (3.5)$$

Hydrolysis

where R is an alkyl group, C_xH_{2x+1}. The hydrolysis (eqn. 3.3) reaction replaces alkoxide groups (OR) with hydroxyl groups (OH). Subsequent condensation reactions involving the silanol groups produce siloxane bonds (Si-O-Si) plus the by-products alcohol (ROH) (eqn. 3.4) or water (eqn. 3.5). Under most conditions, condensation commences (eqns. 3.4 and 3.5) before hydrolysis (eqn. 3.3) is complete [1]. Because water and alkoxysilanes are immiscible, a mutual solvent such as alcohol is normally used as a homogenising agent. However gels can be prepared from silicon alkoxide-water mixtures without added solvent, usually when sonication is used, since alcohol produced

as a by-product of the hydrolysis reaction is sufficient to homogenise the initially phase-separated system [12,13]. Alcohol is not simply a solvent, but can participate by the reverse of eqn. 3.3 and 3.4, in esterification or alcoholysis reactions.

Because water is produced as a by-product of the condensation reaction, it can be shown that an R-ratio (i.e. molar ratio of water to alkoxide) of 2 is theoretically sufficient for complete hydrolysis and condensation to yield anhydrous silica as shown by the net reaction: [1]

$$nSi(OR)_4 + 2nH_2O \rightarrow nSiO_2 + 4nROH \qquad (3.6)$$

However even in excess water (R > 2), the reaction does not go to completion. Instead, a spectrum of intermediate species ($[SiO_x(OH)_y(OR)_z]_n$: where $2x + y + z = 4$) are generated.

Hydrolysis and condensation reactions occur at different rates but concurrently and once hydrolysis has occurred, it is unlikely that the two reactions can be separated. Information in the literature suggests that conditions of low water and an acid environment have the same effect on the sol-gel process i.e. the formation of low porous materials [4]. Similarly, the conditions of high water and the presence of alkaline conditions have the same effect on the sol-gel process, i.e. formation of high porous materials [4,10].

When a silica alkoxide (e.g. TEOS) and water are mixed, the hydrolysis and condensation reactions initiate at numerous sites within the TEOS and H_2O solution. Both hydrolysis and condensation may occur by acid- or base-catalysed bimolecular nucleophilic substitution reactions. The acid-catalysed mechanisms are preceded by rapid deprotonation of the -OR or -OH substituents bonded to Si, whereas under basic conditions hydroxyl (OH^-) or silanolate anions ($Si\text{-}O^-$) attack Si directly. Mineral acids and ammonia are generally used as catalysts in sol-gel processing. The mechanisms for acid- and base- catalysis are outlined in detail in Figure 3.2 [1,6], where both the hydrolysis and condensation reactions are outlined.

Hydrolysis and condensation reactions do not occur in isolation from one another and the final material which results derives from a combination of the two reactions. There is a wide range of parameters which affect the properties of the final material and the effects of some of these are discussed in the following sections.

(A) Acid-Catalysed Hydrolysis

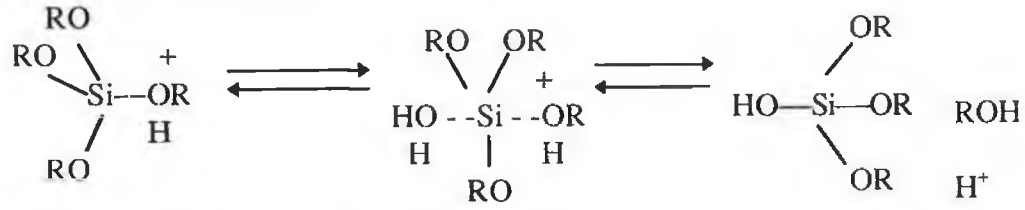

(B) Acid-Catalysed Condensation

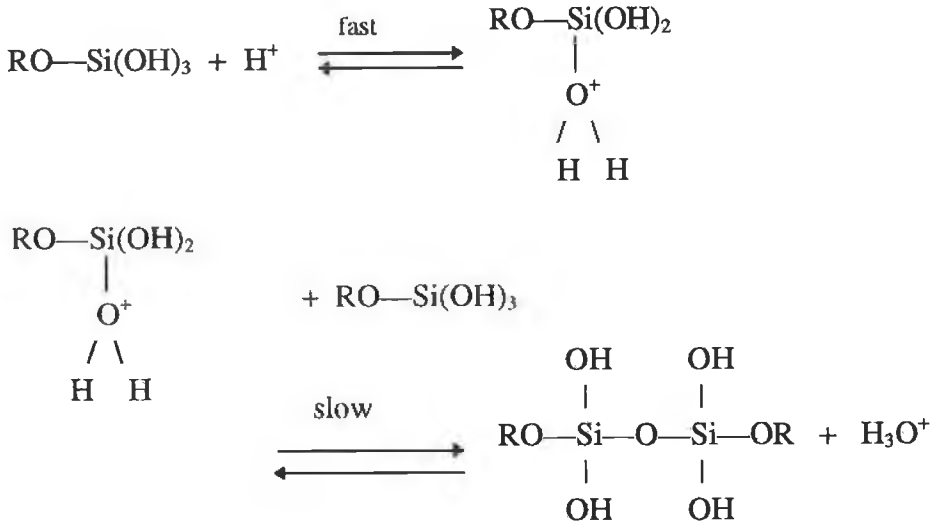

(C) Base-Catalysed Hydrolysis

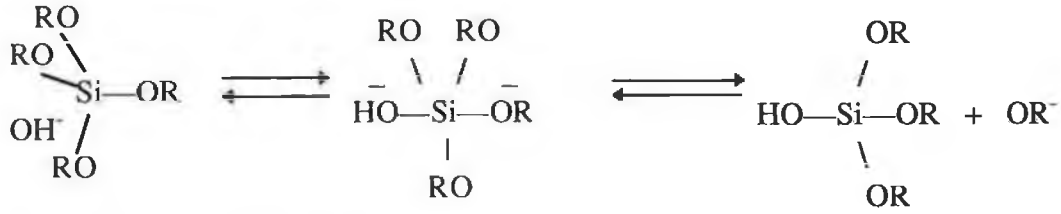

(D) Base-Catalysed Condensation

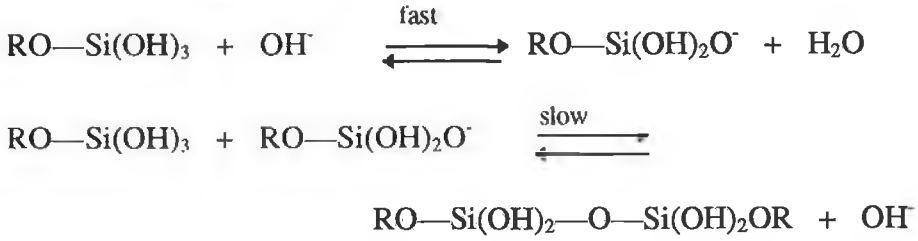

Figure 3.2 : Acid- and Base- Catalysed Hydrolysis and Condensation

3.3 Influence of Processing Parameters on Chemical Reactions

3.3.1 Influence of water and pH

The isoelectric point of silica, at which the electron mobility and the surface charge is zero, occurs at approximately pH =2. This pH value forms the boundary between so-called acid-catalysis of the polymerisation (pH <2) and base-catalysis (pH >2). Acid-catalysis is associated with fast hydrolysis rates and relatively long gel times whereas, under basic conditions, hydrolysis is slow and condensation rates are faster, giving rise to shorter gel times [1]. Silicate gels prepared at low pH (<2) and low water content (<2 moles of water per mole of alkoxide) produce primarily linear polymers with low crosslink density. Additional crosslinks form during gelation and the polymer chains become increasingly entangled. Silicate gels prepared under more basic conditions (pH 5-7) and/ or higher water contents produce more highly branched clusters which behave as discrete species. Gelation occurs by linking clusters together. At still higher pH and excess water content, colloidal silica is formed [10].

The effect of pH on the hydrolysis and condensation reactions can be described qualitatively in Figure 3.3. [4] The rate of hydrolysis is minimum at intermediate pH values, while condensation rates are low at low pH values.

Under conditions of high pH and/ or high water concentrations the rate of hydrolysis is proportional to the concentrations of the base and alkoxide. Gels usually form before all the precursor has been fully hydrolysed. The chemical reason for the occurrence of gelation prior to complete hydrolysis of the precursor molecules is the effect of high pH in stabilising the reaction intermediates. Increasing levels of base lead to a more highly polymerised but less completely hydrolysed gel, i.e. there are species that have undergone a significant amount of hydrolysis and those which have undergone little if any hydrolysis. Those that have undergone hydrolysis are then free to act in a water liberating mechanism generating a highly branched network where the particles continue to grow after the basic gel structure has formed [4]. The material which results is highly branched and highly porous.

For low pH solutions the rate of hydrolysis is proportional to the concentration of the acid, the alkoxide and water. In the low pH systems the rate of hydrolysis is greater than the rate of condensation. Species with very few hydroxyl groups are found

and species which are preferentially hydrolysed are unreacted monomers. This results in a linear growth model and there is little crosslinking [4]. The resulting material is less porous than for base-catalysed case.

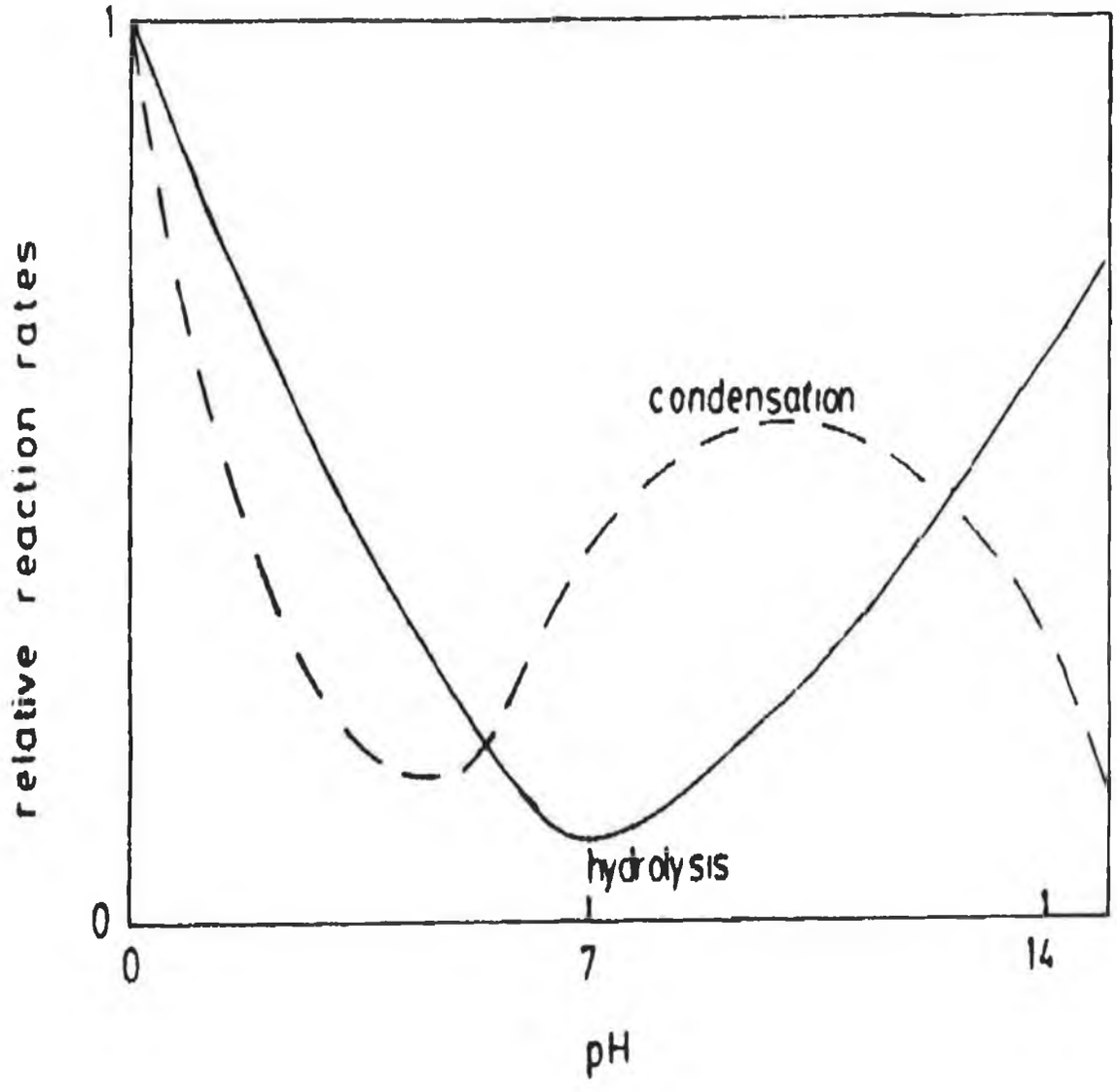

Figure 3.3 pH Dependence of Hydrolysis and Condensation [4]

The behaviour of the rate of condensation as a function of pH was investigated by Coltrain et al [14]. This is shown in Figure 3.4, where the pH dependence of the gel time is used as a measure of the condensation rate (gel time $\propto$ 1/ (average condensation rate)). The effect of water on acid-catalysed silica sol-gel thin films is discussed in Chapter 5.

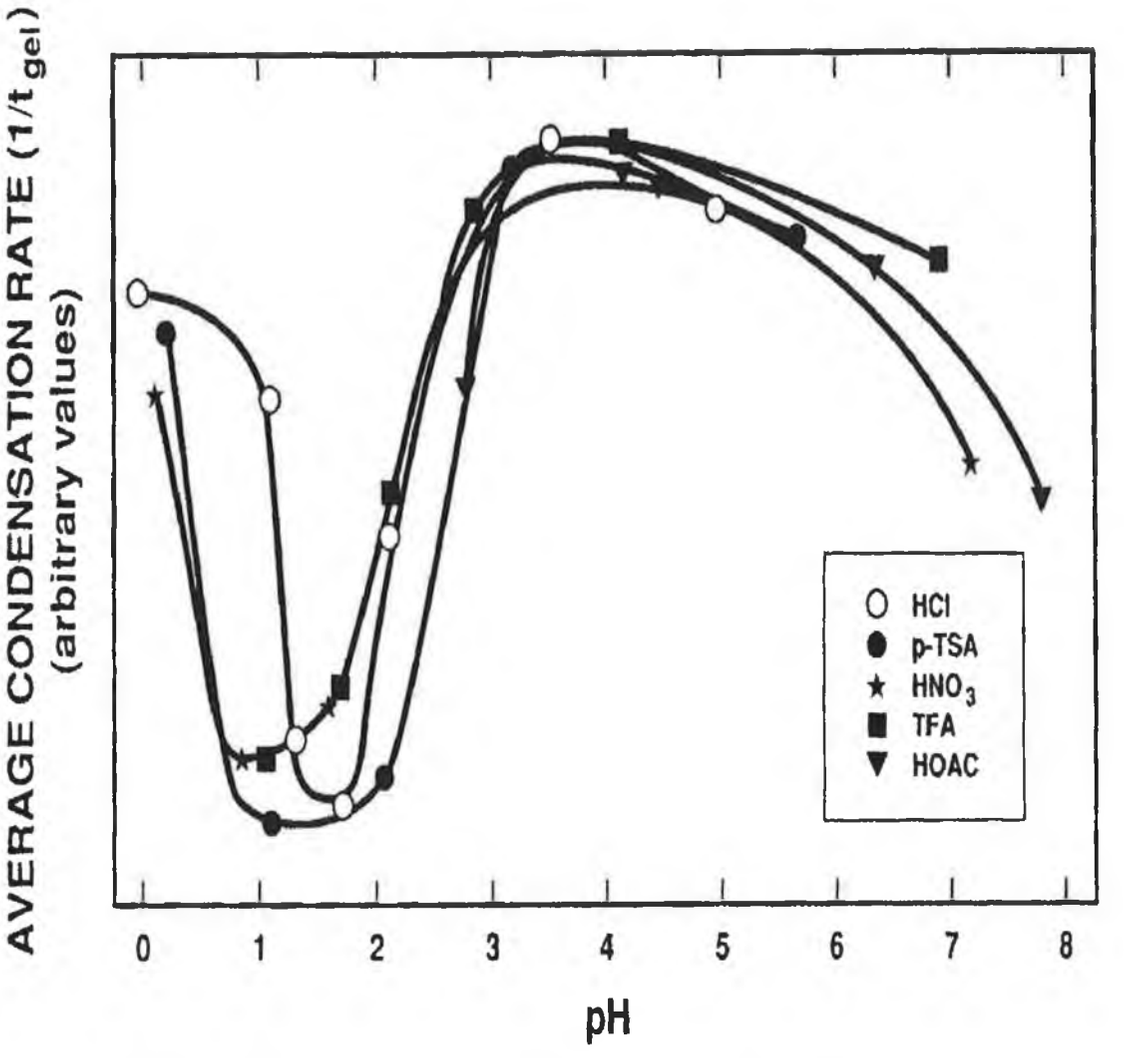

Figure 3.4 : Condensation Rate as a function of pH [14]

3.3.2 Influence of Catalyst

Hydrolysis and condensation rates are enhanced when catalysts are used. As outlined in section 3.2.2 above, the type (acid or base) of catalyst has a major impact on the structure of the sol-gel material formed. The gelation time of sols is also affected by the type of acid catalyst used. Pope and Mackenzie [15] suggested that the variation of the gelling time with the kind of acid cannot be explained by the pH of the starting solution alone, but has to be explained by the differences in the role of the anions such as Cl^-, F^- and CH_3COO^-. The effect of the type of acid catalyst was also studied by Sakka et al. [7].

3.3.3 Influence of Other Chemical Parameters

In the literature several authors have investigated the influence of other parameters, other than those described above, on the hydrolysis and condensation reactions [7,16]. These parameters include the type of solvent and type of alkoxide used in the reaction. The influence of open and closed systems on the reactions is also discussed.

Alcohols are often used as solvents to mix the metal alkoxide and water. However as seen from eqn. 3.3 and 3.4 alcohols also take part in the reactions. An increase in the alcohol content reduces the concentration of metal alkoxide, resulting in the reduction of the polymerisation rate and prolonged gelling times [7].

Systems of silicon alkoxides / alcohol / water solutions catalysed with hydrochloric acid have been studied for different silicon alkoxides which include tetramethylorthosilicate ($Si(OCH_3)_4$, TMOS), tetraethylorthosilicate ($Si(OC_2H_5)_4$, TEOS) and tetrabutylorthosilicate ($Si(OC_4H_9)_4$, TBOS) [4,16]. As the alkyl substituent of the alkoxy group gets larger the rate of hydrolysis decreases. This is due to steric effects on hydrolysis.

Reactions performed in open systems and closed systems show great differences in properties [16]. Gelation is much faster in the open system. This difference is due to (1) solvent evaporation and (2) adsorption of moisture from the atmosphere, both of which increases the net rate of polymerisation.

The discussion of the influence on the hydrolysis and condensation rates have so far concentrated on bulk gels. In a later section of this chapter the special case of thin films will be discussed. In Chapter 5 an extensive characterisation of the sol-gel films used in our sensing applications will be presented. A range of factors is shown to affect the thickness of the sol-gel coatings produced.

3.4 Gelation, Aging and Drying of Gels

3.4.1 Gelation

Once the chemical precursors are mixed together the hydrolysis and condensation reactions are initialised and colloidal particles or a sol is formed. With time the colloidal particles link together to become a three-dimensional network. The

physical characteristics of the gel network depends upon the size of particles and extent of cross-linking prior to gelation [4,9]. Acid-catalysis leads to a more polymeric form of gel with linear chains as intermediates. Base-catalysis yields colloidal gels where gelation occurs by cross-linking of the colloidal particles.

The gelation point of any system, including sol-gel silica is easy to observe qualitatively and easy to define in abstract terms but extremely difficult to measure analytically. As the sol particles grow and collide, condensation occurs and macroparticles form. The sol becomes a gel when it can support a stress elastically. This is typically defined as the gelation point or gelation time, t_g [9]. There is not an activation energy that can be measured, nor can one precisely define the point where the sol changes from a viscous fluid to an elastic gel. This change is gradual as more and more particles become interconnected. The gel point is often described in terms of the sharp increase in viscosity at the transition from a sol to a gel [1,17].

A number of investigations have shown that the time of gelation changes significantly with the sol-gel chemistry [1,16,17]. Gelation time (t_g) varies with size of container, pH, water content, type of alkoxide and counterion. The amount of water for hydrolysis has a dramatic influence on gelation time, as shown in Figure 3.5 [9]. Different authors have studied the sol to gel transition using a variety of methods, including the use of luminescent molecules as probes [10,18], and Raman spectroscopy [7]. Using these techniques the authors were able to monitor the effect of water content, pH effects and thermal effects on the gelation process.

3.4.2 Aging

When a gel is maintained in the pore liquid, its structure and properties continue to change long after the gel point. This process is called aging [9]. During this time, polycondensation continues along with localised solution and reprecipitation of the gel network, which increases the thickness of interparticle necks and decreases porosity. The strength of the gel thereby increases with aging. The reason for doing this is to produce a gel of sufficient strength to withstand the stresses encountered during drying [4].

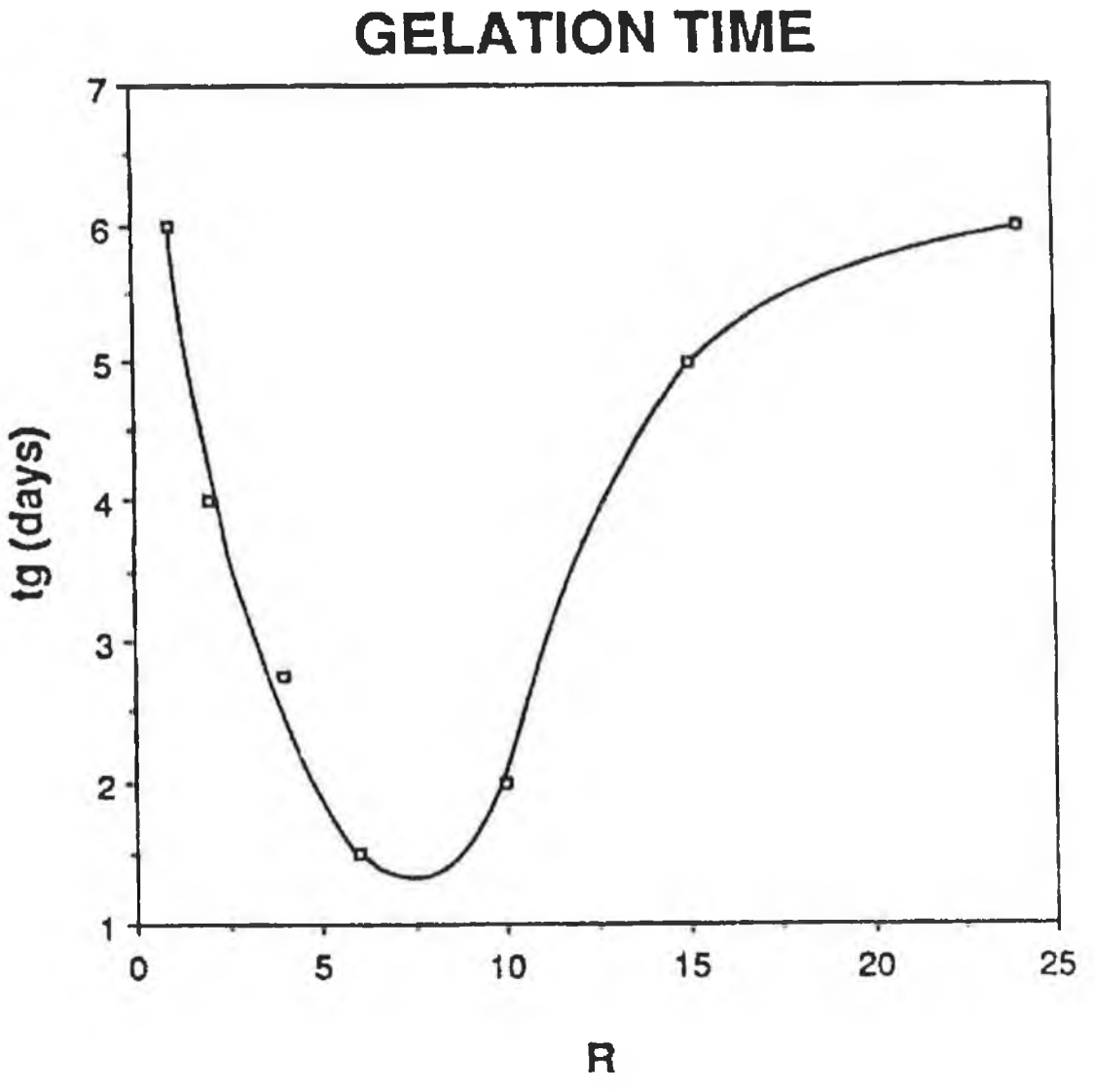

Figure 3.5 Variation of gelation time with R ratio [9]

It should be noted here that the term 'aging' used in section 3.5 on thin films and in Chapter 5 relates to the time of prepolymerisation between sol mixing and coating of samples with the still ungelled sol. In Chapter 5 the effect of different aging times on the properties of sol-gel silica films is described [19].

3.4.3 Drying

In order to use a gel structure it has to be dried. During drying the liquid is removed from the interconnected pore network. If the pores are small (<20 nm) large capillary stresses develop during drying. These stresses may cause the gels to crack

catastrophically unless the drying process is controlled by decreasing the liquid surface chemistry by addition of surfactants or elimination of very small pores, by hypercritical evaporation, which avoids the solid-liquid interface, or by obtaining monodisperse pore sizes by controlling the rates of hydrolysis and condensation [9].

The process of drying of a porous material can be divided into several stages [1,5]. At first the body shrinks by an amount equal to the volume of liquid that evaporates, and the liquid-vapour interface remains at the exterior surface of the body. The second stage begins when the body becomes too stiff to shrink and the liquid recedes into the interior, leaving air-filled pores near the surface. Even as air invades the pores, a continuous liquid film supports flow to the exterior, so evaporation continues to occur from the surface of the body. Eventually, the liquid becomes isolated into pockets and drying can proceed only by evaporation of the liquid within the body and diffusion of the vapour to the outside [1].

Most cracking of a gel during drying occurs at the second stage. A distribution of pore sizes exist in the material and some of the pores empty before others. The pores that empty first (larger pores) stop shrinking at the point of emptying and can only passively shrink under the influence of the nearby saturated pores. The possibility of cracking at this stage is high due to the high stresses and low strain tolerance of the material [1].

Fracture of samples during drying can be prevented by a number of techniques. Aging a gel before drying helps to strengthen the network and thereby reduce the risk of fracture. Surfactants or drying control chemical additives (DCCA) can be added to allow faster drying [1]. Surfactants reduce the interfacial energy and thereby decreases the capillary stress. DCCA's produce gels that are harder and have a larger and more uniform pore size. All these features help to reduce cracking [1].

Other methods of drying gels include supercritical drying and freeze drying. Aerogels are obtained when the liquid within the gel is removed above its critical temperature and pressure. Cryogels are produced from gels in which the liquid phase is first frozen into a solid and then sublimed. The vapour is removed by vacuum pumping [4].

3.5 Preparation of Thin Films

3.5.1 Introduction

One of the important aspects of sol-gel processing is that, prior to gelation, the sol is ideal for preparing thin films by common processes such as dipping, spinning or spraying. Compared to conventional thin film forming processes such as CVD, evaporation, or sputtering, sol-gel film formation requires considerably less equipment and is potentially less expensive [1].

The following sub-sections will look at the differences between the formation of bulk gels and thin films, and the resulting differences in properties. This will be followed by a review of coating processes, with particular attention to dip-coating, the method used in our laboratory.

3.5.2 Differences between bulk gels and thin films

The structural evolution of sol-gel derived thin films differs in many respects from that of bulk sol-gels [1,20].

(1) Films are normally deposited from dilute solutions in which individual solution species are initially weakly interacting or noninteracting. During deposition the rapid increase in concentration (18-36 fold), resulting from evaporation, forces the precursors into close proximity with each other, significantly increasing the reaction rate. Gelation occurs when the condensing network is sufficiently stiff to resist the compressive forces of surface tension. By comparison, in bulk systems the concentration remains constant during gelation and increases only during the drying step.

(2) Concentration-induced gelation imposes a time scale for the sequential stages of film formation which depends on the evaporation rate of the solvent. A competition is established between evaporation (which compacts the structure) and continued condensation reactions (which stiffens the structure, thereby increasing the resistance to compaction). In bulk systems, the gelation and drying stages are normally separated.

(3) Compared to bulk systems, aggregation, gelation, and drying occurs much more rapidly, seconds rather than days or months.

(4) The short duration of the deposition and drying stages causes films to experience considerably less aging (crosslinking) than bulk gels. This generally results in less porous structures.

(5) Fluid flow, due to gravity, evaporation, or angular acceleration (spin-coating), combined with attachment of the precursor species to the substrate, imposes a shear stress within the film during deposition. After gelation, shrinkage due to removal of solvent and continued condensation creates a tensile stress within the film. Such stresses are not present in bulk gels.

3.5.3 Dip Coating of samples

Of the many liquid coating methods available, only three have the capability of laying down very thin layers of precise thickness [21]. These are spin and dip-coating, which are most widely used, and meniscus coating, which is comparatively new. The dip-coating technique is the method used in this work and will be discussed in detail. Planar (glass slides or silicon wafers) and optical fibre substrates were coated using this method. The preparation of samples for coating and the apparatus used for dip-coating of samples will be described in Chapter 4.

In dip-coating the substrate is immersed in a solution and is then withdrawn vertically at a constant speed. In our laboratory the sample is held rigid and the solution, held on a moving stage, is drawn away from the sample. In a review of dip and spin coating, Scriven divided the dip coating process into five stages: immersion, start-up, deposition, drainage, and evaporation [22]. With volatile solvents, such as alcohol, evaporation normally accompanies the start-up, deposition and drainage steps. The different steps are illustrated in Figure 3.6. The moving substrate (or sol-container) entrains liquid in a fluid mechanical boundary layer carrying some of the liquid towards the deposition region (x in Figure 3.6), where the boundary layer splits in two. The inner layer moves upwards with the substrate, while the outer layer is returned to the sol-container. The thickness of the deposited film is related to the position of the streamline dividing the upward- and downward moving layers. A competition between as many as six forces in the film deposition region governs the film thickness and the position of the streamline: (1) viscous drag upward on the liquid by the moving substrate, (2) force of gravity, (3) resultant force of surface tension in the concavely

curved meniscus, (4) inertial force of the boundary layer liquid arriving at the deposition region, (5) surface tension gradient, and (6) the disjoining or conjoining pressure (important for films less than 1 μm thick) [1,22].

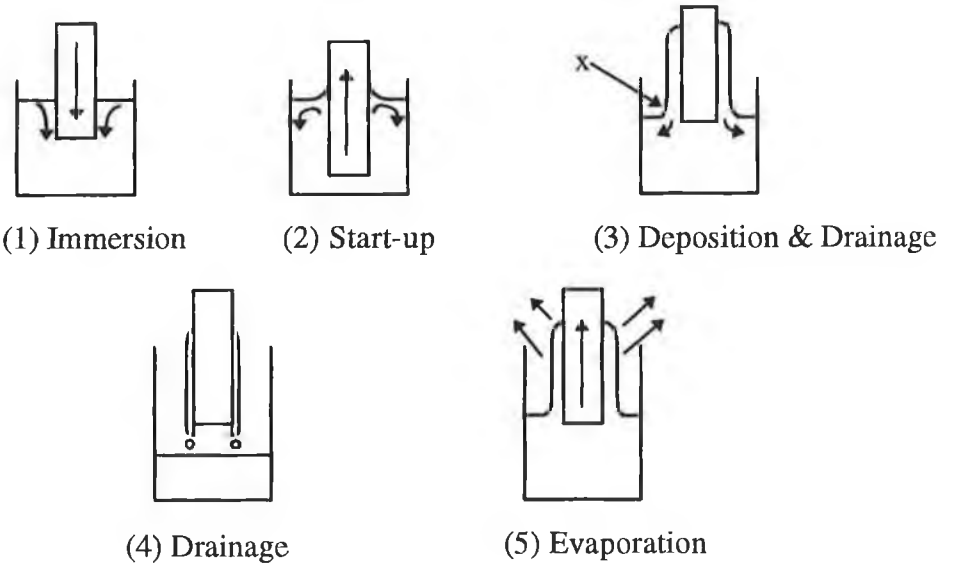

Figure 3.6 Stages of the dip-coating process

When the liquid viscosity (η) and substrate speed (U) are high enough to lower the curvature of the meniscus, then the deposited film thickness (h) is the thickness that balances the viscous drag (∝ηU/h) and gravity force (ρgh), (where ρ is the density of the liquid) :

$$h = c_1(\eta U/\rho g)^{1/2} \qquad (3.7)$$

where the proportional constant, c_1, is about 0.8 for Newtonian liquids [1,22]. When the substrate speed and liquid viscosity are not high enough, as is often the case in sol-gel processing, this balance is modulated by the ratio of viscous drag to liquid-vapour surface tension (γ_{LV}) according to the following relationship:

$$h = 0.94(\eta U/\gamma_{LV})^{1/6}(\eta U/\rho g)^{1/2} \qquad (3.8)$$

or rearranging terms:

$$h = 0.94(\eta U)^{2/3}/\gamma_{LV}^{1/6}(\rho g)^{1/2} \qquad (3.9)$$

To a first approximation, the film thickness is given by the following relationship [21]:

$$thickness \propto \left[\frac{(viscosity)(withdrawal\ speed)}{liquid\ density}\right]^{\frac{2}{3}} \qquad (3.10)$$

If viscosity and density remain constant, the film thickness becomes proportional to the withdrawal speed according to:

$$\text{thickness} \propto [\text{withdrawal speed}]^{2/3}. \qquad (3.11)$$

Many studies have been carried out on the thickness-withdrawal speed relationship and power dependence values ranging from 0.5 to about 0.7 have been reported [23,24,25]. In Chapter 5, a detailed study of dip-coated sol-gel derived coatings, prepared in our laboratory, is presented. Other factors affecting the thickness of dip-coated films include the angle of inclination of the coated surface related to the horizontal line and the concentration of the solution [25].

3.6 Doped Sol-gel Films

The sol-gel process can be used to synthesise a range of materials in different forms ranging from bulk monoliths to thin films. Doping of organic analyte-sensitive reagents into these materials is possible due to the low temperature of the sol-gel processing. The entrapped reagents retain their chemical properties and can react with smaller analyte molecules that diffuse into the porous material. This has been demonstrated by many research groups world-wide [26,27]. For example a range of analytes such as metal ions [28,29], gases such as oxygen and ammonia [30,31,32], and changes in pH [33,34,35] have been detected using doped sol-gel materials. Research has also demonstrated that the sol-gel process can be used to immobilise biomolecules in bulk materials [36,37,38], and more recently thin films [39]. The immobilised biomolecules have been shown to retain many of their characteristics in the sol-gel materials.

Doped sol-gel thin films are more useful configurations for sensors than bulk monoliths for a number of reasons [40]. These include the susceptibility of monoliths to crack when exposed to liquid penetration and the advantage of shorter response times

due to shorter diffusion pathways in thin films. The work described in this thesis used doped sol-gel thin films on optical fibres for pH and ammonia sensing. The preparation of the doped sol-gel films is described as follows. Ethanol is added to an amount of dye in a clean vial. This is stirred using a magnetic bob until the dye is dissolved. Water, whose pH has been adjusted to 1 using hydrochloric acid, is then added. This mixture is stirred for a few minutes and TEOS is then added. The specific amounts of dye, ethanol, water and TEOS added depends on the required dye concentration and the desired water to TEOS ratio (R). In a typical sol a R ratio of 4 is used. The sol mixture is stirred for one hour. Sols are aged for 0-17 hours at 70°C in an oven, depending on the composition of the sol and the film thickness required. After aging, samples are coated with the ungelled sol using by dip-coating at a predetermined withdrawal speed. Samples are then oven-dried at 70°C for 17 hours.

3.7 Ormosils

Ormosils (organically modified silicates) are a relatively new family of materials, prepared by the sol-gel method, with properties that are intermediate between glass and polymers. The introduction in the precursor alkoxide solution of a modified precursor such as an alkylsubstituted ethoxysilane with one or more organic groups attached to the silicon, is a way to incorporate organic components in the material. This has been shown for thin films [41] and bulk materials [42]. Methyltriethoxysilane (MTES, $CH_3(C_2H_5O)_3Si$) for example is one of many organically modified alkoxide precursors that can be used to introduce organic components in a material. The methyl groups bonded to the silicon with a non-hydrolysable covalent bond act as a network modifier. The modification of the structure leads to interesting material properties. Recent reviews [43,44,45] have outlined the properties of ormosils and hybrid organic-inorganic materials in general. Some of the properties of ormosils are outlined below.

The maximum thickness of sol-gel derived films free of cracks is enhanced by introducing an organic component to the material. While the maximum crack-free thickness of films prepared using TEOS is about 0.5 μm [23], films thicker than 2 μm have been prepared using a mixture of MTES and TEOS [41]. Similarly in the preparation of bulk materials it is easier to prepare bulk dry gels without cracks in

inorganic-organic composites [43].

Porosity of materials may be varied by controlling the content and type of the organic groups [43]. Usually the inorganic-organic composite gels are more dense (i.e. less porous) than inorganic gels. For example Innocenzi et al. [41] showed that a higher content of MTES (in a MTES / TEOS mixture) reduced the porosity of films.

An important feature of ormosils compared to traditional sol-gel derived silicates is the effect of the organic groups on the surface properties. Sol-gel derived silica made from $Si(OR')_4$, where R′ is an alkyl group, is very hydrophilic, due to residual Si-OR′ and Si-OH groups. However the use of $RSi(OR')_3$ / $Si(OR')_4$ mixtures (R = alkyl group) results in hydrophobic silica gels [44]. For example the use of MTES replaces the hydrophilic Si-OH groups on the surface with hydrophobic $Si-CH_3$ groups [41]. The structure of MTES - TEOS gels can be characterised using FTIR spectroscopy. The influence of the MTES / TEOS ratio on the content of both $Si-CH_3$ groups and molecular water can be followed using this method.

The introduction of organic groups on the surface can have important implications for the performance of optical chemical sensors using these materials. Recently colleagues at Dublin City University showed that the response of a dissolved-oxygen sensor, based on fluorescence quenching of a ruthenium complex, can be enhanced by using hydrophobic sol-gel derived films using either MTES or ETES (ethyltriethoxysilane) [46]. In the work described in this thesis the effect on the performance of an ammonia gas sensor, using pH indicator dyes, of TEOS and TEOS / MTES films is described.

3.8 Conclusion

The sol-gel process and the parameters that influence the chemical reactions involved, have been described. The preparation of sol-gel derived thin films have been outlined. The influence of different preparation parameters on the properties of sol-gel films is described in more detail in Chapter 5. Finally the important areas of doped sol-gel films and organically modified silicates have been introduced and their uses will be described in detail in later chapters. In the context of fabricating sol-gel thin films for effective entrapment of dye reagents for chemical sensor applications, low water and an

acid environment should be used to ensure low porous materials. Film thickness is expected to vary with coating rate to the power of about 0.67. Ormosil materials should be used where thick films or hydrophobic film surfaces are required.

References :

1. C.J. Brinker and G.W. Scherer, Sol-Gel Science, Academic Press, New York, 1990.
2. L.C. Klein, Sol-Gel Technology for Thin Films, Fibres, Preforms, Electronics, and Specialty Shapes, Noyes Publications, New Jersey, 1988.
3. M. Ebelman, Comptes Rendus Acad. Sci. Fr., vol. 21, 1845, pp. 502.
4. C.C. Harrison, Sol-gel chemistry principles and applications, Tutorial notes, Sira Communications Ltd., Kent, England, May 1993.
5. L.C. Klein, Sol-gel Optics - Processing and Applications, Kluwer Academic Publishers, 1994.
6. A.M. Buckley and M. Greenblatt, 'The sol-gel preparation of silica gels', Journal of Chemical Education, Vol. 71, No. 7, 1994, pp. 599-602.
7. S. Sakka, H. Kozuka, S.H. Kim, 'Various factors affecting the conversion of silicon alkoxide solutions to gels', Ultrastructure Processing of Advanced Ceramics, Wiley, New York, 1988, pp. 159-171.
8. J.E. McGrath, J.P. Pullockaren, J.S. Riffle, S. Kilic and C.S. Elsbernd, 'Sol-gel networks: fundamental chemical studies of hydrolysis, condensation, and polysiloxane toughening of tetraethylorthosilicate (TEOS) systems', Ultrastructure Processing of Advanced Ceramics, Wiley, New York, 1988, pp. 55-75.
9. L.L. Hench, J.K. West, 'The sol-gel process', Chem. Rev. Vol. 90, 1990, pp. 33-70.
10. B. Dunn, J.I. Zink, 'Optical properties of sol-gel glasses doped with organic molecules', J. Mater. Chem., Vol. 1, No. 6, 1991, pp. 903-913.
11. I.C. Tilgner, P. Fischer, F.M. Bohnen, H. Rehage, W.F. Maier, 'Effect of acidic, basic and fluoride-catalysed sol-gel transitions on the preparation of sub-nanostructured silica', Microporous Materials, Vol. 5, 1995, pp. 77-90.
12. L.M. Ellerby, C.R. Nishida, F. Nishida, S.A. Yamanaka, B. Dunn, J.S. Valentine and J.I. Zink, 'Encapsulation of proteins in transparent porous silicate glasses prepared

by the sol-gel method', Science, Vol. 255, 1992, pp. 1113-1115.

13. L. Esquivias and J. Zarzycki, 'Sonogels: an alternative method in sol-gel processing', Ultrastructure Processing of Advanced Ceramics, Wiley, New York, 1988, pp. 255-270.

14. B.K. Coltrain, S.M. Melpolder and J.M. Salva, 'Effect of hydrogen ion concentration on gelation of tetrafunctional silicate sol-gel systems', Ultrastructure Processing of Advanced Materials, Wiley, New York, 1992, pp. 69-76.

15. E.J.A. Pope and J.D. Mackenzie, 'Sol-gel processing of silica II. The role of the catalyst', J. Non-Crystalline Solids Vol. 87, 1986, pp. 185-198.

16. S.Y. Chang and J.A. Ring, 'Map of gel times for three phase region tetraethoxysilane, ethanol and water', J. Non-Crystalline Solids, Vol. 147&148, 1992, pp. 56-61.

17. O. Kinouchi Filho and M.A. Aegerter, 'Rheology of the gelation process of silica gel', J. Non-Crystalline Solids, Vol. 105, 1988, pp. 191-197.

18. V.R. Kaufman and D. Avnir, 'Structural changes along the sol-gel-xerogel transition in silica as probed by pyrene excited-state emission', Langmuir, Vol. 2, 1986, pp. 717-722.

19. C. McDonagh, F. Sheridan, T. Butler and B.D. MacCraith, 'Characterisation of sol-gel-derived silica films', J. Non-Crystalline Solids, Vol. 194, 1996, pp. 72-77.

20. C.J. Brinker, A.J. Hurd, K.J. Ward, 'Fundamentals of sol-gel thin-film formation', from Ultra-Structure Processing of Advanced Ceramics, Wiley, New York, 1988, pp. 223-240.

21. I.M. Thomas, 'Optical coating fabrication', in Sol-gel optics: Processing and Applications, Kluwer Academic Publishers, 1994, pp. 141-158 (edited by L.C. Klein).

22. L.E. Scriven, 'Physics and applications of dip coating and spin coating', in Better Ceramics through Chemistry III, Mat. Res. Soc., Pittsburgh, 1988, pp. 717-729.

23. I. Strawbridge and P.F. James, 'The factors affecting the thickness of sol-gel derived silica coatings prepared by dipping', J. Non-Crystalline Solids, Vol. 86, 1986, pp. 381-393.

24. C.J. Brinker, A.J. Hurd, P.R. Schumk, G.C. Frye and C.S. Ashley, 'Review of sol-gel thin film formation', J. Non-Crystalline, Vol. 147&148, 1992, pp. 424-436.

25. H. Schroeder, 'Oxide layers deposited from organic solutions', in Physics of Thin Films (G. Hass ed.), Vol. 5, 1969, Academic Press, New York, pp. 87-141.
26. D. Avnir, 'Organic chemistry within ceramic materials: doped sol-gel materials', Acc. Chem. Res., Vol. 28, No. 8, 1995, pp. 328-334.
27. L. Yang and S. Scott Saavedra, 'Chemical sensing using sol-gel derived planar waveguides and indicator phases', Anal. Chem. Vol. 67, 1995, pp. 1307-1314.
28. R. Zusman, C. Rottman, M. Ottolenghi and D. Avnir, 'Doped sol-gel glasses as chemical sensors', J. Of Non-Crystalline Solids, Vol. 122, 1990, pp. 107-109.
29. O. Lev, B.I. Kuyavskaya, Y. Sacharov, R. Rottman, A. Kuselman, D. Avnir and M. Ottolenghi, 'Photometric sensors based on sol-gel porous glass doped with organic reagents', SPIE Vol. 1716, 1992, pp. 357-366.
30. B.D. MacCraith, G. O'Keeffe, C. McDonagh and A.K. McEvoy, 'LED-based fibre optic oxygen sensor using sol-gel coatings', Electronics Letters, Vol. 30, No. 11, 1994, pp. 888-889.
31. M.K. Krihak and M.R. Shahriari, 'Highly sensitive, all solid state fibre optic oxygen sensor based on the sol-gel coating technique', Electronic Letters, Vol. 32, No. 3, 1996, pp. 240-242.
32. R. Klein and E. Voges, 'Integrated-optic ammonia sensor', Sensors and Actuators B, Vol. 11, 1993, pp. 221-225.
33. B.D. MacCraith, V. Ruddy and C. Potter, 'Optical waveguide sensor using evanescent wave excitation of fluorescent dye in sol-gel glass', Electronic Letters, Vol. 27, No. 14, 1991, pp. 1247-1248.
34. T.M. Butler, B.D. MacCraith and C.M. McDonagh, 'Development of an extended range fibre optic pH sensor using evanescent wave absorption of sol-gel entrapped pH indicators', Proc. SPIE Vol. 2508, 1995, pp. 168-178.
35. G.E. Badini, K.T.V. Grattan, A.C.C. Tseung, 'Impregnation of a pH-sensitive dye into sol-gels for fibre optic chemical sensors', Analyst, Vol. 120, 1995, pp. 1025-1028.
36. D. Avnir, S. Braun, O. Lev and M. Ottolenghi, 'Enzymes and other proteins entrapped in sol-gel materials', Chemistry of Materials, Vol. 6, No. 10, 1994, pp. 1605-1614.
37. J.I. Zink, J.S. Valentine and B. Dunn, 'Biomolecular materials based on sol-gel

encapsulated proteins', New J. Chemistry, Vol. 18, No. 10, 1994, pp. 1109-1115.

38. U. Narang, P.N. Prasad, F.V. Bright, K. Ramanathan, N.D. Kumar, B.D. Malhotra, M.N. Kamalasanan and S. Chandra, 'Glucose biosensor based on a sol-gel derived platform', Analytical Chemistry, Vol. 66, No. 19, 1994, pp. 3139-3144.

39. B.C. Dave, H. Soyez, J.M. Miller, B. Dunn, J.S. Valentine and J.I. Zink, 'Synthesis of protein-doped sol-gel SiO2 thin films: Evidence for rotational mobility of encapsulated cytochrome c', Chem. Mater., Vol. 7, No. 8, 1995, pp. 1431-1434.

40. B.D. MacCraith, C.M. McDonagh, G.O'Keeffe, A.K. McEvoy, T. Butler and F.R. Sheridan, 'Sol-gel coatings for optical chemical sensors and biosensors', Sensors and Actuators B, Vol. 29, 1995, pp. 51-57.

41. P. Innocenzi, M.O. Abdirashid and M. Guglielmi, 'Structure and properties of sol-gel coatings from methyltriethoxysilane and tetraethyoxysilane', J. Sol-gel Science and Technology, Vol. 3, 1994, pp. 47-55.

42. F. Schwertfeger, W. Glaubitt, U. Schubert, 'Hydrophobic aerogels from $Si(OMe)_4$ / $MeSi(OMe)_3$ mixtures', J. Non-Crystalline Solids, Vol. 145, 1992, pp. 85-89.

43. S. Sakka, 'The current state of sol-gel technology', J. Sol-gel Science and Technology, Vol. 3, 1994, pp. 69-81.

44. U. Schubert, N. Husing and A. Lorenz, 'Hybrid inorganic-organic materials by sol-gel processing of organofunctional metal alkoxides', Chem. Mater., Vol. 7, No. 11, 1995, pp. 2010-2027.

45. P. Judeinstein, C. Sanchez, 'Hybrid organic-inorganic materials: a land of multidisciplinarity', J. Mater. Chem., Vol. 6, No. 4, 1996, pp. 511-525.

46. A.K. McEvoy, C.M. McDonagh and B.D. MacCraith, 'Dissolved oxygen sensor based on fluorescence quenching of oxygen-sensitive ruthenium complexes immobilised in sol-gel-derived porous silica coatings', Analyst, Vol. 121, 1996, pp. 785-788.

Chapter 4 Characterisation System

4.1 Introduction

This chapter outlines in detail the fabrication and characterisation of evanescent wave fibre optic sensors. The aim of this work is the development of fibre optic sensors for ammonia and pH sensing using sol-gel-derived silica and polymer coatings, doped with appropriate analyte-sensitive reagents. The first part of this chapter details the preparation of optical fibre samples and the subsequent dip-coating of these samples with sol-gel-derived films. Issues discussed include the polishing of fibre ends, cleaning and preparation of fibre samples prior to coating and details of the dip-coating apparatus.

The different experimental setups used to characterise the sol-gel coated fibres are then described in detail. Three main systems were used for characterisation, based on either broad-band white light sources or LED sources. Methods of enhancing the sensitivity of these evanescent wave sensors are detailed. These include the effect of the numerical aperture of the launch lens and the use of an annular beam mask to block low order modes in the fibre.

4.2 Preparation of optical fibre samples

4.2.1 Introduction

The optical fibres used as sensor substrates in this work were plastic clad silica (PCS) fibres of core / cladding diameter 600 / 760 μm. This fibre was purchased from Ceramoptec GmbH, Bonn, Germany, and has a numerical aperture (NA) of 0.4. This multimode step index fibre was chosen for the following reasons:

(a) The cladding can be stripped easily from the core by use of a etchant.

(b) The large fibre is more durable and easier to handle than smaller diameter fibres.

(c) The large diameter enables efficient coupling of light into the fibre.

4.2.2 Polishing fibre ends

For efficient coupling of light into the fibres it is necessary that the end-faces are

flat and perpendicular to the optical axis of the fibre. While there are several commercially available fibre optic cleaving tools for smaller diameter fibres, they are not well developed for use with this relatively large diameter PCS fibre. Instead, the fibres were first cut into short lengths and then polished using a Logitech PM2A polishing rig. The fibres were cut into ~ 12.5 cm lengths using a ceramic scissors. This scissors produced less damage to the fibre ends during cutting than a metal one, thus reducing the time required for polishing. About 40 of these fibre pieces were placed in a steel chuck and waxed in place using dental wax. The fibres extend about 4 mm out of the end of the chuck. Caution was taken to ensure that the fibre ends were parallel to the lower face of the chuck. Three of these chucks were then secured in a polishing jig as shown in Figure 4.1. A spirit level was used to ensure all 3 chucks were parallel to the lower face of the polishing jig. The fibres were then ready for polishing.

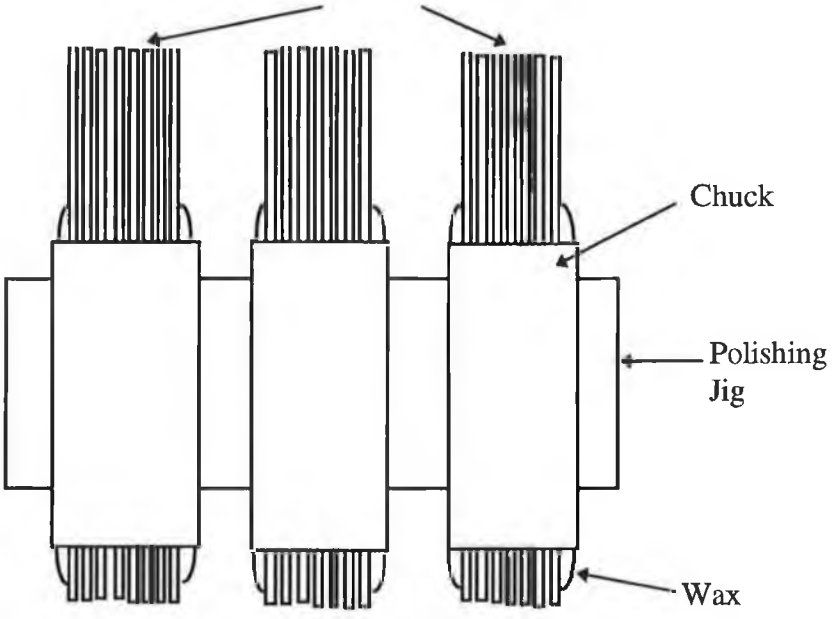

Figure 4.1 Preparation of fibres for polishing

Figure 4.2 shows the outline of the Logitech PM2A polishing rig used in this work. The rig has a choice of two large polishing plates, made of steel and polyurethane, respectively. Each plate was first checked for smoothness using a Logitech flat lapping gauge. The polishing jig was placed on the polishing plate and held in place by a half-circle roller arm [1]. At each end of the half-circle arm is a roller, which allows the jig to rotate on its own axis while it sits on the polishing plate. A

rotating cam system causes the half-circle arm to reciprocate across the plate. This ensures greater uniformity of the finished polished fibres and prolongs the flatness of the plate by preventing troughs forming in the centre of the plate.

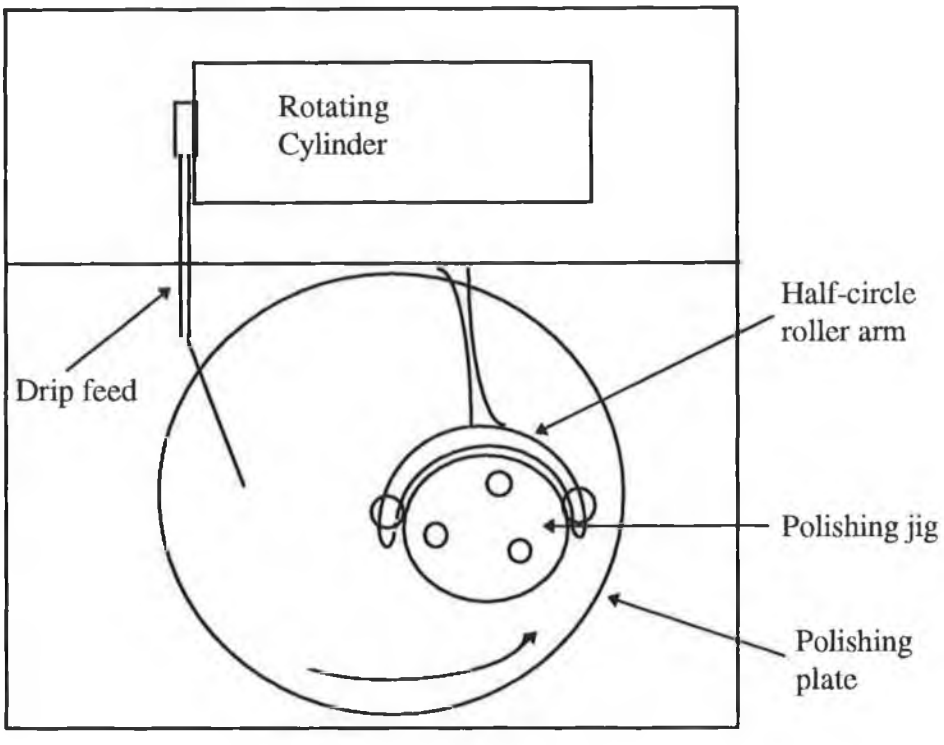

Figure 4.2 Schematic diagram of polishing rig

Polishing fluids were deposited onto the polishing plate using a rotating cylinder mechanism. Various sizes of polishing suspensions were provided by Logitech for use with this polisher. A 9 μm Al_2O_3 suspension was first used until most of the cracks were removed from the fibre end face. This solution was used for a duration of about 3 hours before continuing the process using a 3 μm solution. The 9 and 3 μm solutions were used with the steel polishing plate. This metal plate was replaced by a polyurethane plate for use with a 0.125 μm polishing suspension. After about another 2 hours the fibres were removed from the chucks, inverted and the procedure was repeated for the other end face. The final result was a set of fibres approximately 12 cm in length, with both end faces polished. The quality of the fibre ends was confirmed by microscope examination.

4.2.3 Preparation of samples for coating

An important aspect in preparation of the sensor substrates was the procedure to obtain a clean core surface onto which the sol-gel film was deposited. The fibre was laid on a flat surface and the primary coating was removed from ~ 9 cm of the fibre length using a scalpel, and care was taken not to scratch the core. The silicone cladding was then removed by etching with a commercially available chemical solvent, Optical Fibre Stripper "S" (Lumer, France). This solvent is based on a methylene chloride / sulphuric acid mixture and was developed for the purpose of removal of silicone coatings. The solvent has been shown in a previous study [2] to effectively remove the cladding from PCS optical fibre. The fibres were placed in the Lumer solvent for about 15 minutes and were then washed in water. The fibres were then transferred into methanol and each individual fibre was cleaned with a methanol soaked lens tissue. This procedure was repeated for acetone before finally rinsing the samples in de-ionised water. Prior to dip-coating the substrates were conditioned by soaking in de-ionised water, at 70 °C for 24 hours. This was considered to have the effect of increasing the concentration of silanol groups (SiOH) on the surface of the glass and thereby improving the adhesion of the sol-gel film to the surface.

4.3 Dip-coating of samples

In Chapter 3 an outline of the various steps in the formation of a film by dip-coating was presented. In this section the apparatus used to dip-coat either optical fibre or planar (on glass or silicon) substrates in our laboratory is described in detail. Figure 4.3 shows a schematic diagram of the apparatus used. It consists of a movable stage in which a vial of sol solution is held. The stage was connected to a D.C. motor via a threaded bar. The D.C. motor and thus the movement of the stage was controlled by a BBC micro computer. This sets the direction, duration and speed of movement of the stage. Two stabilising bars (on ball-bearings) through the stage prevent wobble during movement. The dipping apparatus was enclosed within a perspex box, which acts as a draught guard, and was placed on vibration damping mats to ensure that the liquid surface of the sol remains stable during coating. The sample to be coated, either optical fibre or planar substrate, was held fixed and the stage was raised such that a certain

length of the sample was immersed in the sol. The stage was then pulled away at a constant rate. Coating rates ranging from 0.5 mm/sec to about 1.7 mm/sec were used in this work. Typically about a 5 cm length of optical fibre was coated with a sol-gel layer. To prevent coating the end face of the optical fibre, it was covered with an adhesive before coating. This was removed from the fibre tip before drying. After dipping, samples were placed in an oven to dry, typically for 17 hours at 70 °C. Chapter 5 details the effect of different processing parameters on the properties of dip-coated sol-gel films on planar substrates.

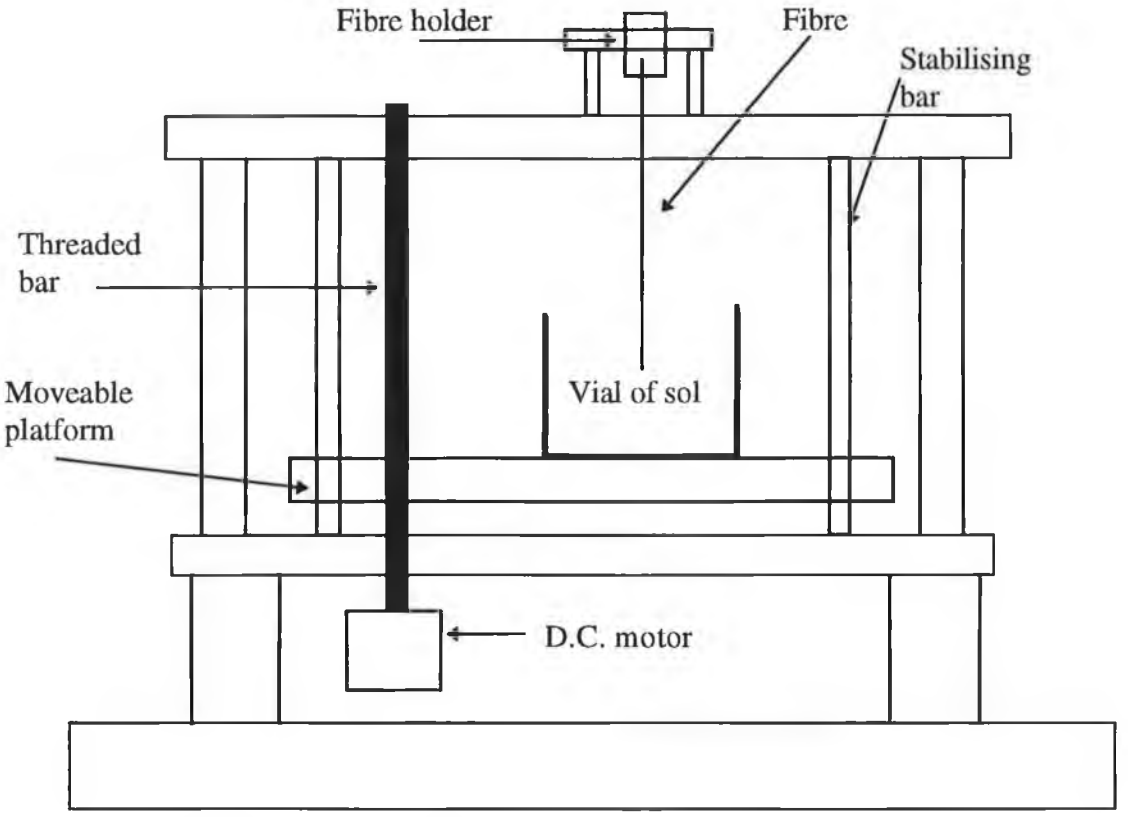

Figure 4.3 Dip-coating apparatus

4.4 Experimental Systems

4.4.1 Introduction

The sensor configuration employed in this work relies on evanescent wave (EW) interactions between the guided radiation in an optical fibre and an analyte-sensitive reagent (i.e. pH indicator) immobilised on the core of the optical fibre. Chapter 2

described the EW theory on which these sensors are based. In this section the different experimental systems used are described in detail. Sections 4.4.2 and 4.4.3 describe systems in which a broad-band white light source is used. In the first system a monochromator is used to disperse the light and a photomultiplier tube (PMT) is used to detect the signal. The second system is based on a miniature fibre optic spectrometer. The advantages of this setup over the previous one are highlighted. The third setup employed in this work used LED sources. The use of LEDs together with a photodiode as detector and a balanced demodulator IC as a lock-in amplifier allowed a compact system to be constructed.

4.4.2 Monochromator / PMT based system

The experimental system using a monochromator to disperse the light from a white light source and a PMT as detector is shown in Figure 4.4. Light from a 50 W tungsten halogen source (in an Optometrics Mini-Chrom Lamp-01 housing) was dispersed in a scanning monochromator (Optometrics Inc., U.S.A., model SDMC1-02), with entrance / exit circular aperture of 1 mm diameter. The emerging beam was collimated using a convex lens of 20 mm focal length, and launched into the optical fibre using a microscope objective, typically of NA = 0.4. The optical signal at the output of the fibre was detected using a Hamamatsu PMT (model R928).

It was outlined in Chapter 2 that it is preferable to launch higher order modes in the fibre to increase evanescent wave absorption. A relatively high NA microscope objective (NA = 0.4 or 0.65) was used for this purpose as shown in Figure 4.4. An annular beam mask, located in the backplane of the microscope objective, was used to block low order modes and increase sensitivity. Section 4.5 details the effect of microscope objectives of different NA and masks of different inner diameter on evanescent absorption.

The coated optical fibre was enclosed in a cell of volume ~ 10 mL . This was mounted on an x-y-z micropositioner, which was used to optimise the coupling between the source and optical fibre. Liquids (e.g. pH buffer solutions) were pumped through the cell containing the optical fibre using a peristaltic pump (Minipuls 3, Gilson, France). When investigating ammonia-gas sensing a different sample cell of volume ~ 60 mL was used. A gas delivery system which used nitrogen gas as a carrier gas and 1% ammonia

in nitrogen as the test gas was setup. By using different mass flow controllers (Unit Instruments, Dublin) with maximum flow rate of 5 litres/min. for nitrogen and 5 cm^3/min. for the ammonia test gas, a range of gas concentrations from 1% to 1 ppm ammonia in nitrogen can be obtained. This gas delivery system is illustrated in Figure 4.5.

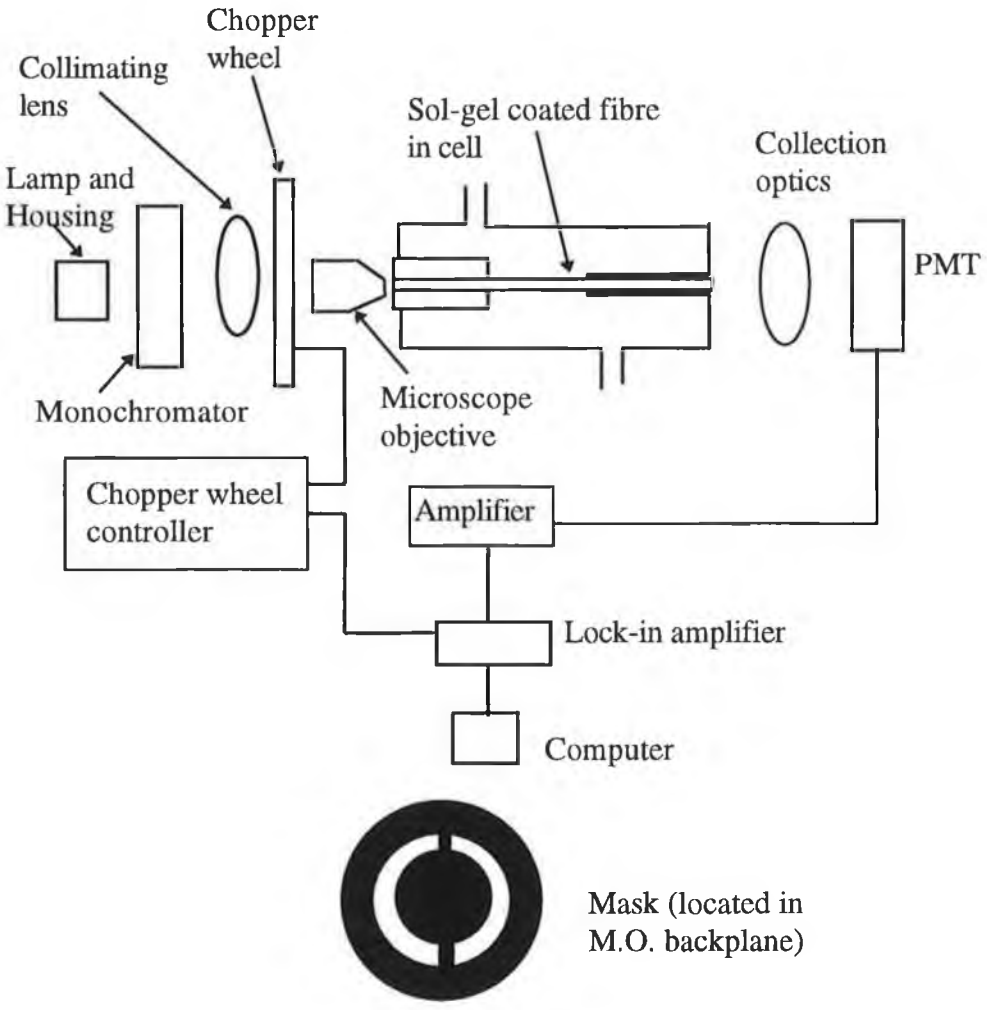

Figure 4.4 : PMT-based characterisation system

The transmitted optical signal was detected by the PMT and amplified by a current to voltage converter whose output was fed to a lock-in amplifier (Stanford Research Systems, model SR510). The use of an optical chopper wheel and lock-in amplifier improved signal to noise levels. Software was written to control a Bytronics multifunction input / output card (model MPIBM3), which converts the analogue signal

from the lock-in amplifier to digital format and this was then passed to the personal computer for analysis.

The monochromator is suitable for the 200-800 nm range and has an effective aperture of f/3.9 and 74 mm focal length. Its resolution for a 1 mm slit is quoted as ~ 7.5 nm. It has built-in upper and lower optical limit switches to prevent the grating from being damaged by collision with the mechanical end stops. The wavelength range that can be scanned was defined by the separation between the two limit switches. For calibration purposes, wavelengths were defined with respect to zero order. This was the point at which all wavelengths were transmitted through the monochromator and as a result zero order was easy to detect as a peak in light intensity. Calibration consists of running the stepper motor down to the lower limit switch, then moving up at one step at a time and recording the signal at each step. The zero order position was found by comparing each signal value with the preceding value. When zero order was found the stepper motor would drive the monochromator to the correct starting wavelength for each scan. This calibration routine was included into the data acquisition software described above. A mercury-cadmium-zinc (HgCdZn) lamp was used to check the calibration of the monochromator.

A typical measurement consists of recording, over a range of wavelengths, I_0, the signal level for an undoped sol-gel coated fibre, which was used as reference. I, the signal level for a fibre coated with an analyte-sensitive coating, was then measured and the evanescent absorbance was calculated according to eqn. 4.1

$$A = \log_{10} (I_0 / I) \qquad (4.1)$$

4.4.3 Fibre optic spectrometer based system

During the course of this work, the monochromator and PMT in figure 4.4 were replaced with a miniature fibre optic spectrometer (Ocean Optics Inc., Florida, U.S.A., model S1000). This is a 38 mm focal length spectrometer with a small 1024 element CCD array detector. Light is dispersed by a grating with 600 lines/mm. In the work described here, two systems were used, one for the uv / visible range (250-750 nm) and the second for the near-infrared region (550-1050 nm). Order blocking filters installed in these systems prevented second order effects. The systems were interfaced to a PC and a range of software options were available. Figure 4.5 shows a schematic diagram

of the characterisation setup using this miniature spectrometer. The gas-mixing setup and the gas cell are included. The launch optics consists of a collimating lens and a 0.4 NA microscope objective. An annular beam mask was again placed in the backplane of the microscope objective. The collection optics consisted of two convex lenses, of 10 and 20 mm focal length, that first collimated the light from the sensing fibre and then launched it into the collection fibre of the spectrometer. The collection fibre was a SMA terminated 400 μm core silica/silica fibre of 0.22 NA. This fibre was a key part of the spectrometer [3], controlling the spectral resolution and signal levels achieved.

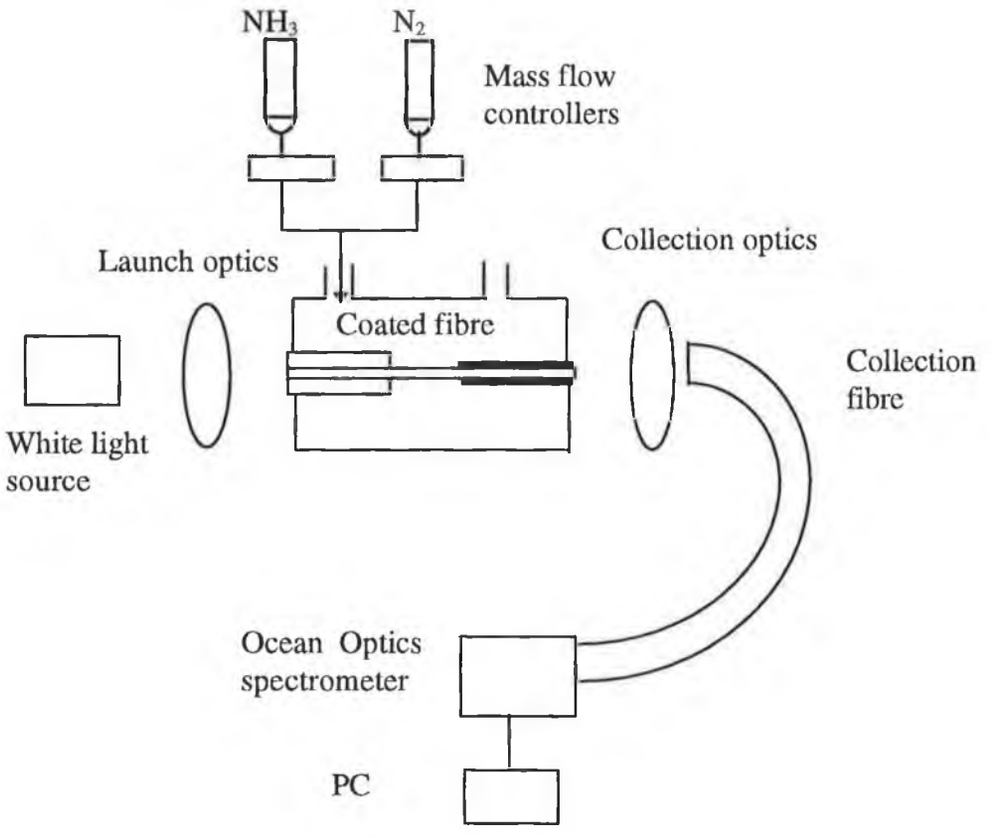

Figure 4.5 Spectrometer-based characterisation system

This experimental arrangement has advantages over the earlier one described in section 4.4.2.

(1) There are no moving parts in the spectrometer based setup, while in the first setup there is a scanning monochromator and an optical chopper wheel.

(2) This setup allows for real-time absorption measurements to be taken. The length of time to update a spectrum, for example an absorption spectrum covering the range λ = 400-700 nm, was typically about 10 seconds in this case as opposed to about 3 minutes in the previous case.

(3) The associated software, provided with the spectrometer, ensures full PC control over the operation of the unit. The gain, integration period (sample frequency) and the number of scans to signal average are some of the parameters that can be varied. Furthermore, included in the software are options for a time-series display [3]. This is of use when investigating the response of a sensor and this can be seen in later chapters.

The spectral resolution of the spectrometer depends on the choice of input fibre diameter and NA, and the grating. Light at a single wavelength is detected by several pixels on the CCD array because of the finite size of the fibre image [4]. The smaller the optical fibre chosen the higher the resolution but at the expense of energy throughput. In the work described here there was a mismatch between the core diameter and NA of the sensing fibre and the collection fibre. The largest fibre available from Ocean Optics for use with this spectrometer was a 400 μm core silica/silica fibre of 0.22 NA. With the collection lenses used, the NA mismatch between the fibres was compensated for but the spot-sizes were not, resulting in a loss in throughput. The collection fibre was mounted on a x-y-z positioner to improve alignment.

A measurement (e.g. absorption spectrum) using the spectrometer involves the collection of 3 types of data, namely 'dark' (the response of the system with no light), 'reference' and 'sample'. Data can be displayed in a number of formats using the associated software. For example data was observed in a normalised mode such as absorbance, where sample data was divided by reference data, or in 'scope' mode where the detector voltage output was displayed. This was useful, for example, in optimising the launch of a fibre sample. The structure seen in scope mode includes detector efficiency, grating efficiency and fibre attenuation, all of which were removed by the normalisation step in the absorbance mode.

4.4.4 LED-based characterisation system

The 2 systems described above have a number of disadvantages associated with the uses of incandescent filament sources:

(1) The physical size of the source makes sensor miniaturisation difficult.

(2) These sources generate a lot of heat.

(3) There are issues of long-term stability of filament sources, and they have high power consumption.

(4) Modulation is typically achieved by mechanical beam choppers.

For these reasons, alternative sources such as laser diodes (LDs) and light emitting diodes (LEDs) have replaced incandescent filament sources in many sensor applications. The added availability of low cost photodiodes, with sufficient sensitivity to replace PMTs, have made possible the construction of small and low cost sensor systems. In a recent review, Taib and Narayanaswamy [5] detailed a number of LED-based systems for chemical sensing. The principal performance characteristics of LEDs are their narrow bandwidth and stability compared to incandescent sources, their small size, low power consumption and long lifetimes. Direct electronic intensity modulation is possible and therefore moving parts are not required.

Commonly available LEDs cover most of the wavelength range from the blue to the near-infrared spectral region. In the work described here, a yellow LED (Radionics # 578-238) with a peak wavelength of 590 nm was used in an optical fibre pH sensor. This LED was chosen on the basis of the spectrophotometric study carried out on the pH sensitive films, which is described in Chapter 6. This is illustrated in Figure 4.6 where the yellow LED output spectrum and the evanescent wave absorption spectra of the pH indicator bromophenol blue, for different pH buffer solutions, are shown. The peak wavelength of the LED closely matches the absorption peak of the deprotonated form of the dye. In a referenced system, a near-infrared LED (DCL Components Ltd., Berkshire, U.K., model L200CWIR850), with peak wavelength of 850 nm, was used as a reference as the dye absorption did not change with pH in this region of the spectrum.

Figure 4.7 shows a schematic diagram of the LED-based characterisation system. Coupling of light by butting the LED directly to the fibre was not very efficient, due to the large beam diameter of the LED at the dome surface relative to the diameter of the fibre. Suggestions in the literature to improve coupling include the use of a microlens

between the LED and fibre [6]. A 10 mm focal length convex lens and 0.4 NA microscope objective were used as launch optics in this setup. There were difficulties in collimating the LED output, due to the plastic dome. In order to improve the quality of the output beam for collimating, the dome was polished very close to the emitting junction. A flat, polished surface perpendicular to the direction of light emission was achieved by the use of different grades of optical polishing paper. The highly diffuse emitting surface that results after polishing required the use of the lenses referred to above to couple light effectively into the fibre.

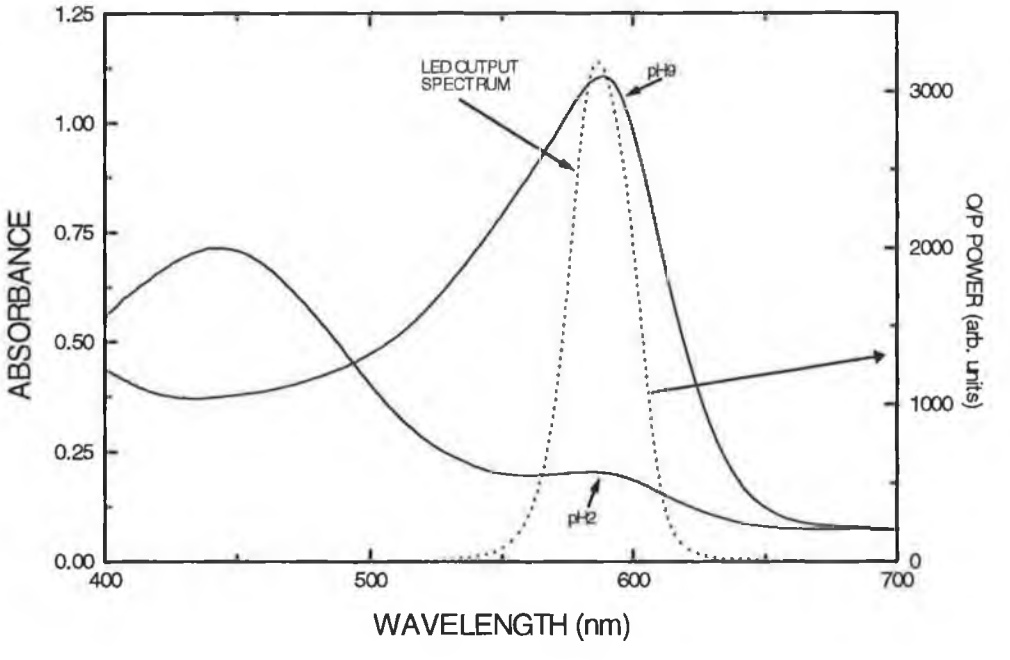

Figure 4.6 Yellow LED spectrum and absorption spectra of bromophenol blue in different pH buffer solutions

In a dual-LED setup, the 2 LEDs were coupled into the same fibre. The reference LED was placed behind the signal LED on the same axis. Good coupling was achieved, exploiting the fact that infrared light is transmitted through the plastic case of the sample LED. Baldini et al. [7] described a similar setup for a dual-LED pH sensor.

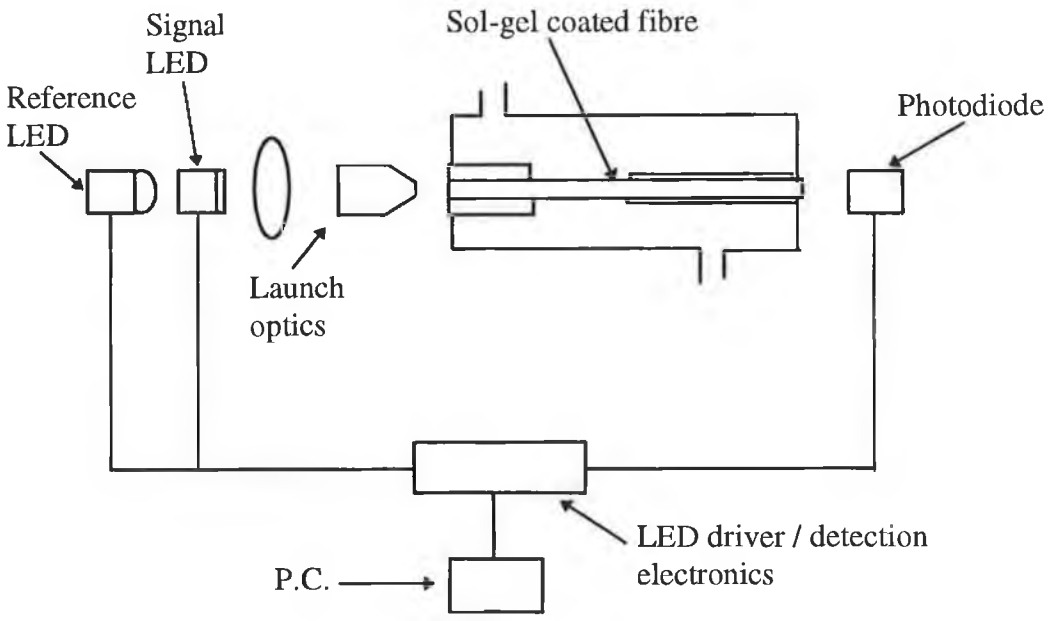

Figure 4.7 LED-based characterisation system

The output signal from the fibre was detected by a photodiode detector. The photodiode used was a Hamamatsu silicon detector (model S2386-45K). In order to discriminate against ambient light and to increase the signal to noise ratio, it was necessary to modulate the LEDs and use lock-in amplification techniques. This was achieved electronically. The modulation circuit consisted of a voltage-to-frequency converter, using an integrated circuit (Analog Devices, AD654). Appendix A illustrates the electronic circuit lay-out of the dual-LED driver circuit. Software controls which LED, signal or reference, is on at a particular time.

Discrimination against ambient light was carried out using the Analog Devices Balanced Modulator / Demodulator (AD630), which can be configured to operate as a lock-in amplifier [8]. The circuit layout of the detection electronics is shown in Appendix B. The D.C. output voltage of the lock-in amplification circuit was fed to the PC, via the Bytronics multifunction I/O card, for analysis. Results obtained using this LED-based pH sensor are described in Chapter 6.

A disadvantage of LEDs is that their output is temperature sensitive. The peak wavelength of the output spectrum shifts to longer wavelengths with increasing temperature by typically 0.3 nm/K [9]. The output intensity also decreases with increasing temperature. Murtaza and Senior [10] detailed these effects and methods of

minimising them. The LED can be operated at a controlled temperature. Alternatively, a fraction of the initial optical signal can be removed from the beam. This fraction can then be used as a reference for the final signal or to determine the feedback in a closed loop control system. This latter method is effective at controlling the output intensity of the LED. The shift in spectral properties can also be compensated for by methods such as wavelength thermal matching (WTM) [10]. When using WTM, a region of minimum variation with temperature on the LED spectrum is used for measurements.

4.5 Sensitivity of evanescent wave sensor

4.5.1 Introduction

Evanescent wave fibre-optic absorption sensors are based on attenuated total internal reflection (ATR) spectroscopy. The technique utilises the absorption of evanescent field penetrating into the cladding region where an absorbing material is placed, e.g. absorbing dye in a sol-gel-derived coating. The penetration depth, d_p, of the evanescent field in the cladding is given by the following expression:

$$d_p = \frac{\lambda}{2\pi n_1\left[\sin^2\theta - (n_2/n_1)^2\right]^{\frac{1}{2}}} \qquad (4.1)$$

where λ is the wavelength of the light launched into the fibre, θ is the angle of incidence to the normal at the core/cladding interface, and n_1, n_2 are the refractive index of the core and cladding, respectively. Chapter 2 discussed the theory of evanescent wave absorption using multimode fibres. This section highlights methods of enhancing the sensitivity of evanescent wave sensors.

To increase the evanescent absorption and, hence the sensitivity of the sensor, the penetration depth should be increased. It is noted from equation 4.1 that the penetration depth increases as the angle θ approaches the critical angle θ_c of the sensing region, where $\theta_c = \sin^{-1}(n_2/n_1)$. Thus the average penetration depth can be increased by launching only those rays which make angles (θ) slightly greater than but close to the critical angle of the sensing region. Another factor which affects the sensitivity is the number of reflections at the interface in the sensing region. The number of reflections

can be increased by choosing an optical fibre of smaller diameter, as discussed in Chapter 2.

In the literature there are two principal mechanisms that have been used to increase evanescent absorption sensitivity in multimode optical fibre sensors. First, the fibre can be tapered so that the radius decreases along the direction of propagation. Gupta et al. [11,12] have reported the advantages of tapered fibres over uniform fibres. As a ray propagates through the taper its angle with the normal decreases and thus the angle of the ray becomes closer to the angle θ_c, thereby increasing the effective evanescent absorption. Furthermore, the number of reflections also increase as the radius becomes smaller and smaller [11]. The other mechanism is to selectively launch only those rays which make an angle close to θ_c. This increases the fraction of light absorbed and hence the sensitivity. A previous study in this laboratory [13] used this method to increase evanescent absorption. A comparison of the sensitivities of the two methods was reported by Gupta et al. [11,12]. These authors concluded [11] that the greatest sensitivity was achieved for a sensor based on selective ray launching in a tapered fibre.

In the work describe here, evanescent absorption sensitivity was increased by selectively launching high order modes in the fibre, using the method described in reference [13]. This technique uses an annular beam mask in the backplane of the launch microscope objective to block low order modes. Section 4.5.3 details the influence of different diameter masks and different NA microscope objectives on the absorption spectrum of an optical fibre coated with a sol-gel-derived film, doped with the pH indicator dye bromophenol blue (BPB). The discussion above highlights the fact that the sensitivity of the sensor is dependent on the modal distribution in the fibre and sensitivity will vary with source / fibre launching conditions. A method to improve the repeatability of launch was investigated and this is described in section 4.5.2 below.

4.5.2 Repeatability of launch

In order to obtain repeatable results from an evanescent wave sensor it is important that the modal distribution in the fibre is the same from one fibre sample to the next. The ability to position the optical fibre at the correct working distance from the

launch microscope objective is critical in achieving this fibre-to-fibre repeatability. Feldman and Uzgiris [14] described a system that attempted to alleviate this problem. In their system a perforated mirror was placed between the launching optics and the proximal end of the fibre probe. A pair of achromat lenses then formed a real, magnified image of the fibre face, which could be viewed using a microscope eyepiece. This system allowed one to accurately adjust the position of the fibre. The PMT based characterisation system described in Figure 4.4. was modified to include a similar imaging system.

The setup used to improve repeatability of launch in our work is shown in Figure 4.8. A glass microscope cover slip was placed at 45° between the collimating lens and microscope objective. The back reflection from the fibre was partly reflected from the cover slip and viewed in the microscope eyepiece. When the fibre was positioned at the working distance of the microscope objective, a bright image was seen in the eyepiece. With a mask in the backplane of the microscope objective, the mask image was visible on the fibre face. The position of the fibre relative to the working distance of the microscope objective was accurately adjusted using this setup. The x-y alignment of the fibre could also be viewed using this system. However due to the bulky nature of this imaging system it is only suitable for laboratory based characterisation systems and, therefore only used in the PMT-based system.

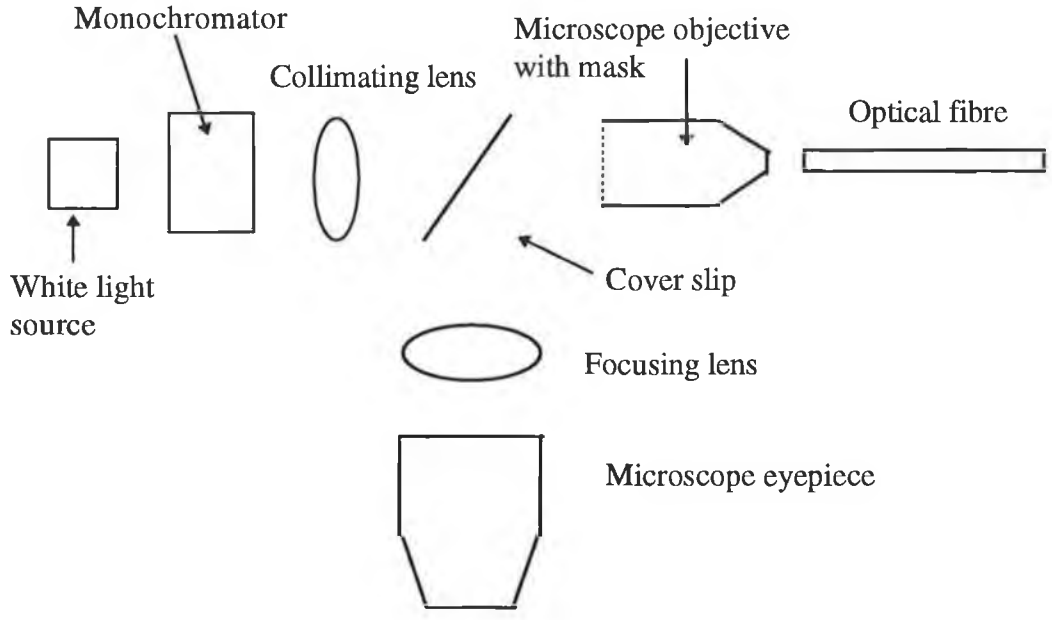

Figure 4.8 Launch imaging system

4.5.3 Annular beam masks

When considering absorption of the evanescent wave, the quantity of evanescent power which can interact with the analyte is a critical parameter. In the case of optical-fibre EW sensors this quantity is closely related to the fraction, r, of the total guided power that resides in the cladding region, i.e.

$$r = P_{clad} / P_{total} \qquad (4.2)$$

Chapter 2 outlined this theory and showed how values of r are maximised for higher order modes. Experimentally, this theory was investigated by placing annular masks of various sizes in the backplane of the launch microscope objective to preferentially excite the higher order modes only. Experiments used the PMT-based characterisation system shown in Figure 4.4. The masks are made of metal and were cut by laser (Dublin Laser Ltd.) to the required size. A series of masks were made, with inner diameter varying from 2 mm to 5 mm. Their outer diameter at 9 mm was greater than the backplane of the microscope objective. The absorbing material used in this study was a sol-gel derived film doped with BPB. The absorption spectrum of BPB / sol-gel on an optical fibre, in air, was measured for masks of different inner diameter, different NA microscope objectives and different sol-gel film thickness. Spectra were artificially normalised to the baseline, (i.e. lowest absorbance value was set to zero) for comparison purposes.

The intensity profile emerging from the microscope objective was first measured. Figure 4.9 shows the experimental setup used to measure this profile. The focal point of the microscope objective was positioned over the centre of a rotation stage. An apertured (~ 1mm) photodiode was mounted on the rotation stage, a set distance away. The monochromator was set to zero order to increase the light intensity. The photodiode was scanned around the output of the microscope objective for various masks in the backplane. The output profile of the 0.4 NA microscope objective, for different masks, is shown in Figure 4.10. The 5 % intensity points were used to determine the range of angles passed by the masks. The data in Figure 4.10 is not fully symmetric around the origin, due to slight misalignment in the setup. For this reason, the average of the 5 % intensity points on both sides of the centre position were taken. Appendix C contains plots of the intensity profile of the three microscope objectives

used in this study, namely 0.25, 0.4 and 0.65 NA. The 5 % intensity angles for various masks are also included. With no mask in place the NA measured for the different microscope objectives corresponded to the expected values.

Figure 4.11 shows how the evanescent absorption spectra of a BPB / sol-gel coated fibre changes for different masks, for a 0.4 NA microscope objective. It can be seen clearly that the larger the inner diameter, the greater the sensitivity, resulting from an increase in r in equation 4.2. The optimal mask size was found to be of 3.5 mm inner diameter. This represented a compromise between optimising evanescent wave absorption and optical throughput of the system.

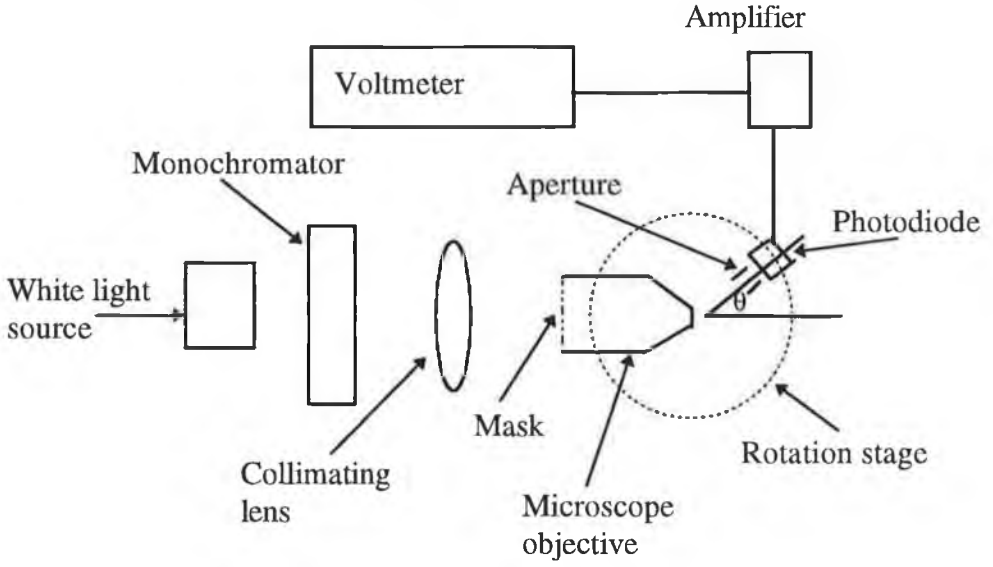

Figure 4.9 Experimental configuration to measure the intensity profile from the microscope objective

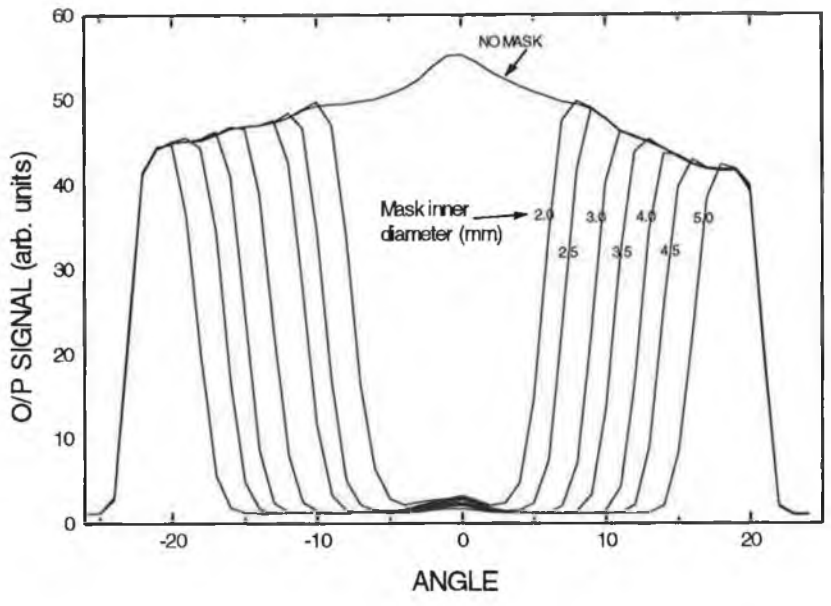

Figure 4.10 Intensity profile of the 0.4 NA microscope objective for various masks

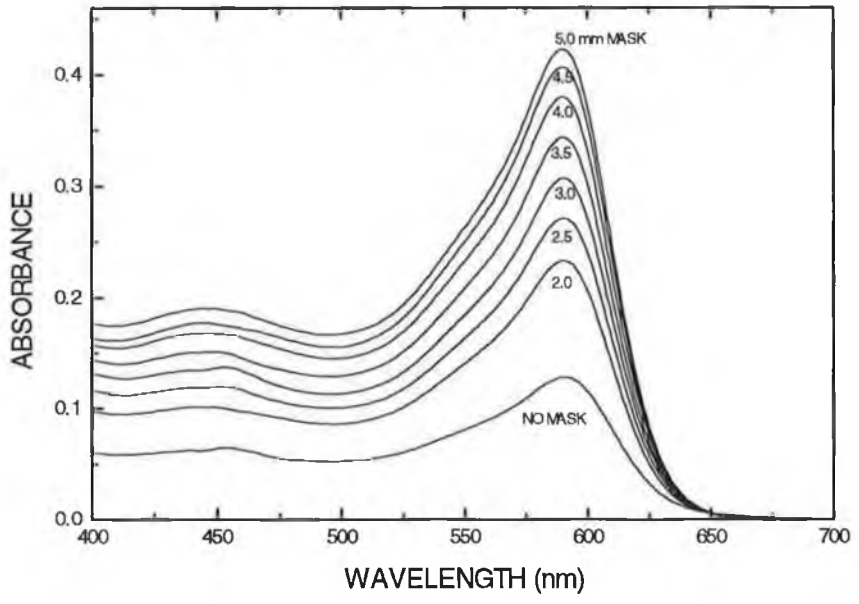

Figure 4.11 Effect of mask diameter on the absorption spectrum of a BPB / sol-gel coated fibre

The influence of the NA of the microscope objective on evanescent wave absorption was also investigated. To increase the ratio r in equation 4.2, higher order modes should be excited in the fibre. This can be achieved by using high NA launch optics. The effect of different NA microscope objectives on the peak absorbance, λ = 590 nm, of a BPB / sol-gel coated fibre is plotted in Figure 4.12, for different mask diameters. Poor sensitivity was achieved for low NA launch optics, e.g. 0.25 NA microscope objective, since mostly low order modes would be excited in the fibre. This would correspond to the case of rays striking the core / cladding interface at angles far removed from the critical angle of the sensing region. From the output profile of the different microscope objectives and masks, the range of incident angles with respect to the normal of the core / cladding interface was calculated. These ranges of values, $\theta(c_1)$ - $\theta(c_2)$, where c_1 and c_2 are the mask angles, are included in Appendix C. Assuming the material surrounding the fibre extends to infinity, the critical angle for a glass core / water interface is approximately 66° and for the case of glass core / sol-gel glass (refractive index 1.43) interface it is ~ 78°. Therefore the light launched from the 0.25

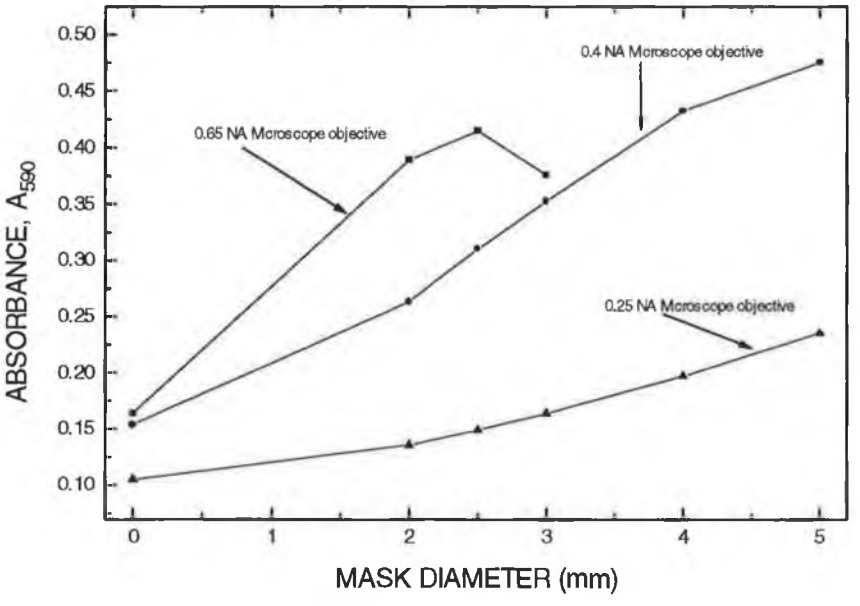

Figure 4.12 Effect of different NA microscope objectives and masks on peak absorption of BPB / sol-gel coated fibre

NA microscope objective ranges at least 6° ($\theta(c_1)$ - $\theta(c_2)$ greater than 84°, Appendix C) above the critical angle in the sol-gel film case. This analysis assumes an infinite material around the optical fibre, while in reality a thin film is the case.

Data relating to the 0.4 and 0.65 NA microscope objectives are also included in Figure 4.12 and Appendix C. Higher NA launch optics result in increased sensitivity as light is launched at angles closer to the critical angle of the sensing region. In the 0.65 NA case, absorbance decreased above a certain mask size for the sol-gel coated fibre. For these masks light is launched below the critical angle of the sensing region.

The above analysis is based on a number of assumptions that need to be clarified further:

(1) The NA of the clad fibre is 0.4. Therefore, using a 0.65 NA microscope objective will launch light above the acceptance angle of the fibre. The short length of cladding and primary coating, which is left on the sensing fibre for handling purposes, will sustain tunnelling modes which are launched into the fibre at angles greater than the meridional numerical aperture permits [13]. Some of these modes may propagate to the sensing region and enhance evanescent absorption.

(2) The analysis above uses a sol-gel film of refractive index 1.43 (see section 5.7 for refractive index measurements on sol-gel films). This analysis assumes the evanescent field is fully contained in the sol-gel film, i.e. a bulk (infinite) material surrounding the fibre. If it is not, a composite effect between the bulk and no film (surrounded by air only) may apply. Equation 4.1 yields a penetration depth of typically a wavelength (600 nm) for the typical example of core and cladding (bulk) refractive indices of 1.46 and 1.43 respectively and for rays striking the core / cladding interface at approximately 2° above the critical angle. Figure 4.13 shows the effect of film thickness on evanescent absorption. Absorption increases with film thickness increase. A measure of the film thickness on the optical fibres themselves was not carried out due to the fibre geometry. A study was carried out on films deposited on silicon wafers and glass slides [15]. It was assumed that the values for planar substrates were the same as for fibres. The film thickness values for the coating rates used in Figure 4.13 are shown in Table 4.1. These values are for undoped films. Doped films are found to have, in

general, thicknesses ~ 100 nm greater than these. From this it can be seen that films coated at low coating rates will not have sufficient thickness to contain the evanescent field i.e. the bulk penetration depth is greater than the film thickness. Films coated at sufficiently high coating rates can have thicknesses close to the typical penetration depth described above and will therefore contain most of the evanescent field. If the absorbance did not change with thickness, this would indicate a fully contained evanescent field. However, as seen in figure 4.13, this is not the case and thicker sol-gel films are required to prevent possible fouling of a sensor. In a recent paper, Blue and Stewart [16] reported that even after 12 coatings (total thickness ~1200 nm) on an optical fibre of a standard pH 1 hydrolysed sol, the evanescent field was still protruding from the sol-gel films. Alternatively, if lower NA launch optics is used (0.25 NA microscope objective in figure 4.12) the evanescent field should be contained by a thinner film due to less higher order modes. However, this approach would result in lower sensitivity.

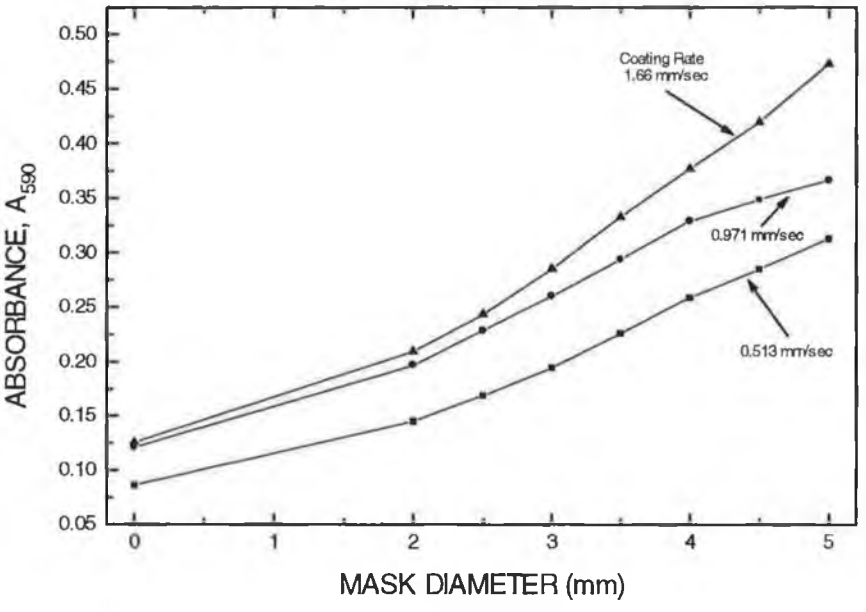

Figure 4.13 Effect of film thickness on evanescent absorbance for different masks (0.4 NA microscope objective)

Coating Rate (mm/sec)	Film Thickness (nm)
0.513	315
0.971	425
1.66	555

Table 4.1 Film thickness for different coating rates

(3) The deprotonated peak (λ = 590 nm) of the BPB / sol-gel coated fibre, in air, was used in this analysis. In Chapter 7, reasons for the large alkaline peak in air are discussed. It is understood that the peak value is related to structural changes of the sol-gel films over time or interactions with the external environment. Therefore, the deprotonated peak could change over time, resulting in poor repeatability in the above results. An absorbing material that does not depend on its external environmental may be a better choice for these measurements.

4.6 Conclusion

In this chapter the fabrication and characterisation of evanescent wave fibre optic sensors were detailed. The preparation and coating of optical fibre samples was described in detail. The different experimental systems used to characterise the sol-gel coated fibres were outlined and their relative advantages discussed. The system based on a miniature fibre optic spectrometer is ideal for laboratory based measurements, while the LED-based system lends itself towards miniaturisation. The sensitivity of these evanescent wave sensors was enhanced by selectively launching higher order modes in the fibre. Furthermore, issues relating to the containment of the evanescent field in the sol-gel film were highlighted.

References

1. 'PMZ Precision Polishing Machine: Operation and Maintenance Instruction Manual', Reference No: BE-01-1-2, Logitech Ltd., Glasgow, Scotland.

2. J.A. Murphy, 'Evanescent wave spectroscopy using multimode optical fibres', M.Sc.

Research Thesis, 1990, Dublin City University.

3. S1000 Fibre Optic Spectrometer: Users Manual, Revision 4, 1994, Ocean Optics Inc., Florida, U.S.A.

4. M.J. Morris, R.A. Walters and G.C. Burke, 'Miniature optical fibre-based spectrometer employing a compact tandem fibre probe', Proc. SPIE Vol. 1796 Chemical, Biochemical, and Environmental Fibre Sensors IV, 1992, pp. 141-149.

5. M.N. Taib and R. Narayanaswamy, 'Solid-state instruments for optical fibre chemical sensors: a review', Analyst, Vol. 120, 1995, pp. 1617-1625.

6. D.R. Gabardi and D.L. Shealy, 'Coupling of domed light-emitting diodes with a multimode step-index optical fibre', Applied Optics, Vol. 25, No. 19, 1986, pp. 3435-3442.

7. F. Baldini, S. Bracci and F. Cosi, 'An extended-range fibre-optic pH sensor', Sensors and Actuators A, Vol. 37-38, 1993, pp. 180-186.

8. Balanced Modulator / Demodulator - Data sheet, AD630, Analog Devices, Norwood, M.A., U.S.A.

9. J.M. Senior, 'Optical Fiber Communications: Principles and Practice', Second edition, Prentice / Hall International Series in Optoelectronics, 1992, pp. 403.

10. G. Murtaza and J.M. Senior, 'Wavelength selection strategies to enhance referencing in LED based optical sensors', Optical Communications, Vol. 112, 1994, pp. 201-213.

11. B.D. Gupta, A. Sharma and C.D. Singh, 'Evanescent wave absorption sensors based on uniform and tapered fibres: a comparative study of their sensitivities', Int. J. Optoelectronics, Vol. 8, No. 4, 1993, pp. 409-418.

12. B.D. Gupta, C.D. Singh and A. Sharma, 'Fibre optic evanescent field absorption sensors: effect of launching conditions and the geometry of the sensing region', Optical Engineering, Vol. 33, No. 6, 1994, pp. 1864-1868.

13. V. Ruddy, B.D. MacCraith and J.A. Murphy, 'Evanescent wave absorption spectroscopy using multimode fibres', J. Appl. Phys., Vol. 67, No. 10, 1990, pp. 6070-6074.

14. S.F. Feldman and E.E. Uzgiris, 'Determination of the kinetic response and absolute sensitivity of a fibre-optic immunoassay', Proc. SPIE, Vol. 2068 Chemical, Biochemical

and Environmental Sensors V, Boston, 1993, pp. 139-144.

15. C. McDonagh, F. Sheridan, T. Butler and B.D. MacCraith, 'Characterisation of sol-gel-derived silica films', J. Non.-Crystalline Solids, Vol. 194, 1996, pp. 72-77.

16. R. Blue and G. Stewart, 'Fibre-optic evanescent pH sensing with dye doped sol-gel films', Int. J. Optoelectronics, Vol. 10, No. 3, 1995, pp. 211-222.

Chapter 5 Characterisation of Sol-gel Films

5.1 Introduction

The optimisation of optical sensors using sol-gel derived films requires a detailed characterisation of film properties. Commercially viable sensors require films which have long-term stability and reproducible behaviour. To this aim, a comprehensive characterisation of film properties was carried out [1]. Film properties were monitored as a function of various processing parameters, and the results were interpreted in terms of the chemical reactions involved in the sol-gel process.

This chapter deals with the characterisation of sol-gel derived silica films coated on silicon and glass slide substrates as described in Chapters 3 and 4. Furthermore, a review of methods of sol-gel film characterisation is given. The films were dipcoated from sols prepared using TEOS, water at pH 1 (using HCl as catalyst) and ethanol. The film parameters measured were thickness, refractive index, temporal stability and film quality. These were monitored as a function of dip-speed, water : precursor ratio (R), sol aging time and time after drying. R was varied from 2 to 7, while sol aging time was varied from 0 hours to gelation. Film thickness was measured using the three methods described in section 5.2, ellipsometry, interferometric microscopy and spectral transmission. All thickness values quoted were averaged over six measurements with a standard deviation of approximately 20 nm. The final section in this chapter concerns the properties of ormosils, prepared using the precursor MTES. Their properties are compared with those of TEOS based films.

Film thickness was the parameter which revealed most about the effect of different processing parameters. It is related to the viscosity of the sol and coating speed as described by equation 3.10. In the development of optical sensors, film thickness can affect the response time of a sensor due, for example, to slower diffusion into a thicker film. Furthermore in the case of evanescent wave interactions in an optical fibre sensor, it is desirable to have a film of sufficient thickness to contain most of the evanescent field and thereby prohibit interactions with the material outside the film.

5.2 Methods of characterisation of sol-gel films

5.2.1 Introduction

A detailed characterisation of film properties is required in order to optimise sol-gel-derived films for use in optical chemical sensors. Parameters of importance include thickness, refractive index, porosity and optical quality of the films [1,17]. For example, film thickness affects the response time of a sensor. Film thickness can also be used to follow the influence of different processing parameters in the sol-gel process [10,11]. Fourier transform infrared (FTIR) spectroscopy is a useful technique that provides information on the chemical structure of films [6]. Information on film porosity can be obtained from refractive index measurements and from studies of leaching from or adsorption into the film of probe molecules of different sizes [11,18]. The following sections outlines the methods used, in our laboratory, to measure thickness and refractive index of sol-gel derived films. These methods are ellipsometry, interferometric microscopy and spectral transmission.

5.2.2 Ellipsometry

Ellipsometry consists of measuring and interpreting the change of polarisation state that occurs when a polarised light beam is reflected at non-normal incidence from a film surface [19]. An ellipsometric measurement involves irradiating the surface of a sample at a known angle of incidence with a collimated beam of monochromatic light having a known, controllable state of polarisation, and determining the difference between the states of polarisation of the incident and reflected beams [20]. The ellipsometer used in this work is a Rudolph Research AutoEL-III, which is a nulling ellipsometer.

The electric fields of the incident beam and reflected beam can each be resolved into two orthogonal linearly-polarised components, one (the 'p' component) with its electric field vector parallel to the plane of incidence, and the other (the 's' component) with its electric field vector normal to the plane of incidence. The p and s components of each beam may have different phases and amplitudes. The state of polarisation of a beam is determined by the relative amplitude (amplitude ratio) of the p and s components and by the relative phase (phase difference) between the p and s components. When a collimated beam of monochromatic polarised light is reflected

from a surface, there will generally occur changes in the relative phases and the relative amplitudes of the p and s components. These changes determine two angles, Δ (DELTA) and Ψ (PSI) which are related by

$$\rho = \tan\Psi e^{i\Delta} \qquad (5.1)$$

where ρ is the ratio of the complex reflection coefficients r_p and r_s [19,20]. Both Δ and Ψ are angles, where Ψ may have any angle between 0° and 90°, and Δ may have any angle between 0° and 360°. The angles Δ and Ψ determine the thickness and refractive index of the sample.

A schematic diagram of the ellipsometry setup is shown in Figure 5.1 and consists of a laser, polariser, analyser, compensator and detector. A measurement consists of setting the incident-beam and reflected-beam axes at some desired angle of incidence with respect to the sample (at 70° for the AutoEL III). The polariser and analyser are alternately rotated until the intensity of the reflected beam (as measured by a photodetector after passage through the analyser) is reduced to a minimum. At this null condition the angles of the polariser and analyser are determined. These angles at null are convertable by means of linear equations into the polarisation parameters Δ and Ψ [20].

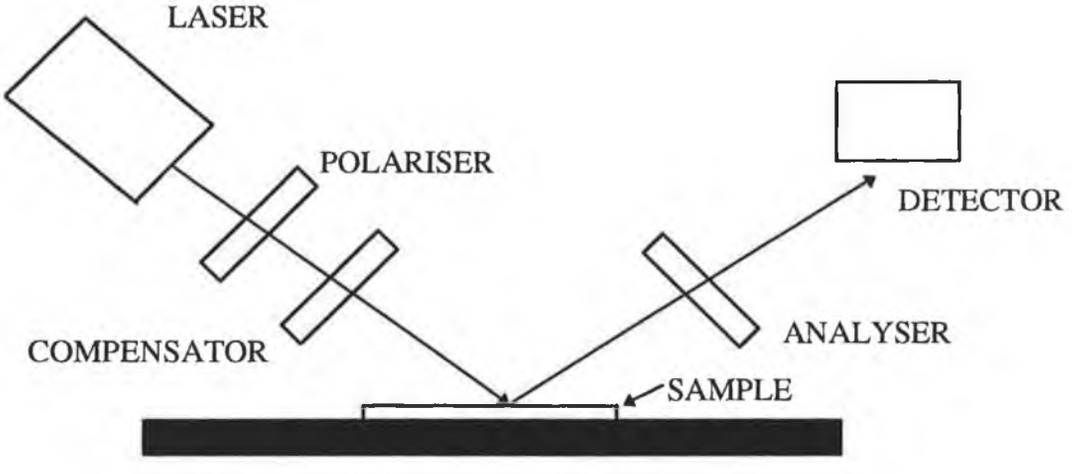

Figure 5.1 Ellipsometry setup

For the case of a transparent film on a reflecting substrate (i.e. sol-gel silica film on a silicon substrate), Δ and Ψ are functions of the incident angle, the wavelength of

light, the refractive index of the ambient medium, as well as the real and imaginary refractive index of the substrate and the sample thickness and refractive index. Since some of these parameters are known the software incorporated within the ellipsometer determines the sample thickness and refractive index.

When the optical path length of the light traversing the film reaches one wavelength (or 2,3,... etc.), Δ and Ψ are the same as for no film at all. In other words Δ and Ψ are cyclic functions of film thickness, and the cyclic function reaches the starting point (completes one cycle) when the optical path length (refractive index times physical path length in transparent film) is an integral multiple of the light wavelength. The full cycle thickness T can be calculated from

$$T = \frac{\lambda}{2\left[\left[(n_f)^2 - n_{ex}^2 \mathrm{Sin}^2(\mathrm{PHI})\right]\right]^{\frac{1}{2}}} \qquad (5.2)$$

where n_f is the film refractive index, n_{ex} the external index and PHI the angle of incidence (70°) [20]. The full cycle thickness is typically about 290 nm for our sol-gel films (n_f = 1.43). Because of this cyclic behaviour an independent measure of thickness is needed and is discussed below.

5.2.3 Interferometric Microscopy

The second method used to measure sol-gel film thickness was interferometric microscopy. This method is based on two-beam interferometry [21]. A two-beam interferometer functions by dividing a beam of coherent light into two beams of approximately equal intensity, directing one beam onto a reference mirror and the other onto the specimen, and measuring the optical path difference between the resulting two reflected light waves. This was performed here using a Mirau interference objective lens in a Nikon optical microscope (model 272285). This objective has a reflection reference mirror in the centre of the objective lens, with a half mirror interposed between the objective lens and the specimen. These components are arranged so that an interference pattern will appear if the system is focused upon the specimen.

In order to increase the contrast at the interface of the sol-gel film / bare substrate, the film and substrate were coated with a very thin layer of a reflective

material such as aluminium. This was achieved using vapour deposition in an Edwards Auto 306 vapour deposition chamber. When the interference objective is focused at the film / substrate interface a shift in fringes across the interface, due to the difference in height of the film and substrate, is observed. Figure 5.2 shows a schematic diagram of the fringe shift, while in Figure 5.3 a photograph of an actual fringe shift is shown. An estimate of the film thickness (t) is found from the fringe shift (N) multiplied by $\lambda/2$ where λ is the wavelength of the light used. This behaviour can be summarised by equation 5.3:

$$t = N(\lambda/2) \qquad (5.3)$$

Therefore a fringe shift of one would correspond to a film thickness of about $\lambda/2$.

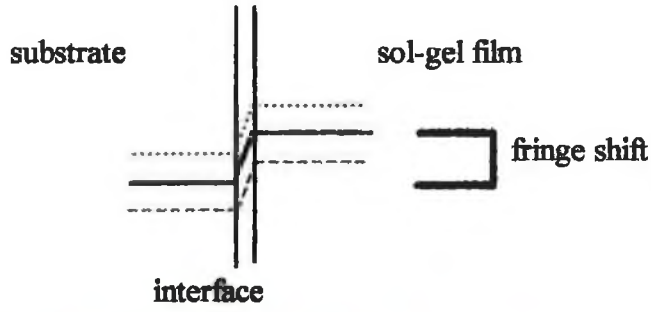

Figure 5.2 Fringe Shift Schematic

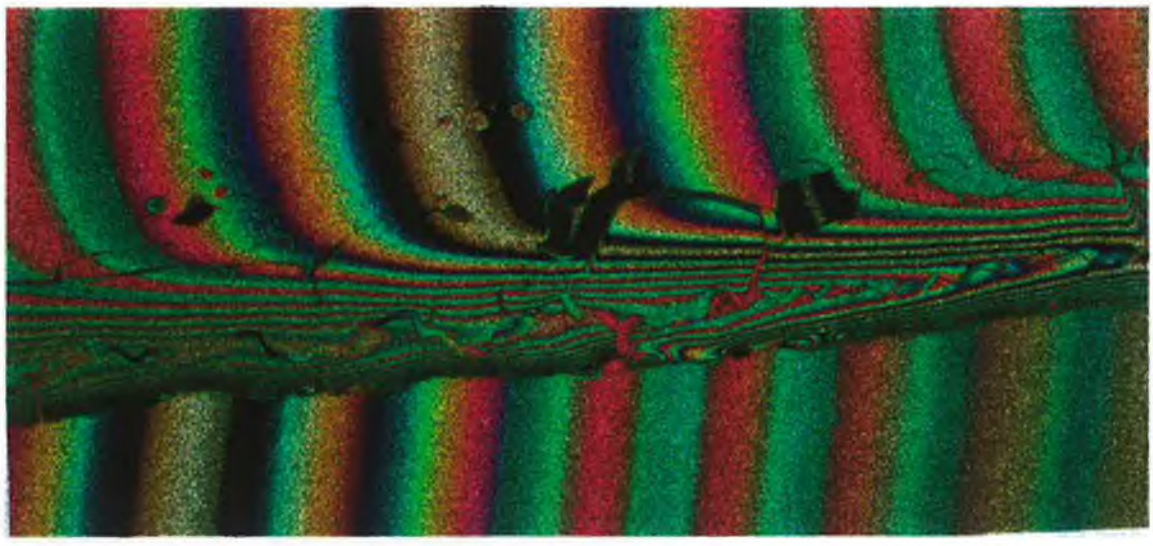

Figure 5.3 Fringe Shift

5.2.4 Spectral Transmission

The thickness and refractive index of a sol-gel film can also be determined by measuring the transmission spectra of samples in a spectrophotometer [22,23]. The

theoretical analysis, shown below, is based on the reflectance and transmission of light by a single non-absorbing film, bound on either side by semi-infinite non-absorbing layers [19,24]. The approach considers the division of a beam incident on a film into reflected and transmitted parts. Such division occurs each time the beam strikes an interface so that the transmitted and reflected beams are obtained by summing the multiply-reflected and multiply-transmitted elements. This situation is illustrated in figure 5.4 for a typical case of an air (n_0)-film (n_1)- glass (n_2) system which could represent a sol-gel film on a glass substrate.

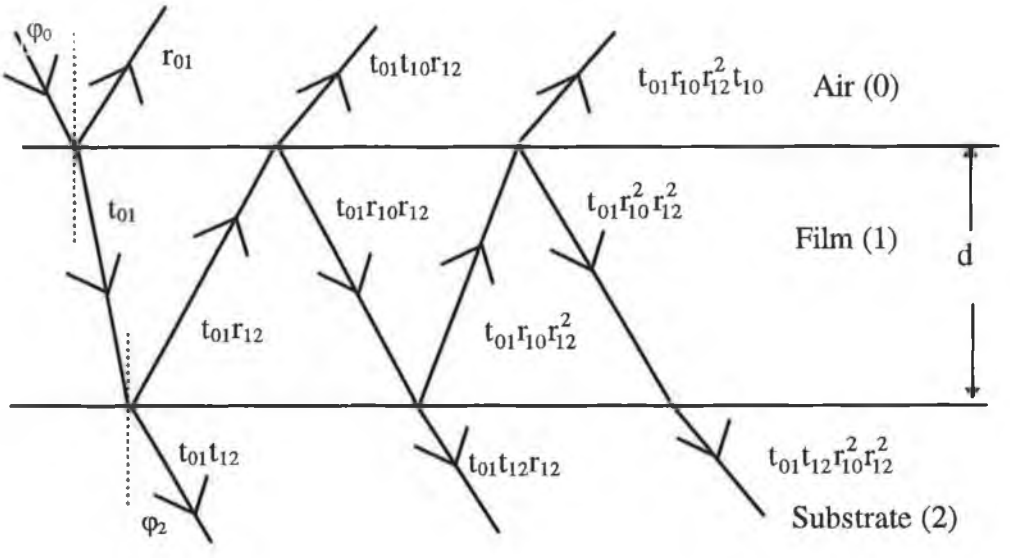

Figure 5.4 Reflection and Transmission of Light at an Air - Film - Glass System

A plane wave incident in medium 0 (at angle φ_0) will give rise to resultant reflected wave in the same medium and to a resultant transmitted wave (at the angle φ_2) in medium 2 (the substrate). In the case of the reflected wave the first three reflected rays have amplitudes given by, $r_{01}, t_{01}t_{10}r_{12}, t_{01}t_{10}r_{10}r_{12}^2$ (see figure 5.4). The change in phase of the beam on traversing the film, δ_1, is represented by:

$$\delta_1 = \frac{2\pi}{\lambda} n_1 d_1 Cos\varphi_1 \qquad (5.4)$$

The reflected amplitude is thus given by

$$R = r_{01} + t_{01}t_{10}r_{12}e^{-2i\delta_1} + t_{01}t_{10}r_{10}r_{12}^2 e^{-4i\delta_1} + \ldots\ldots \qquad (5.5)$$

whose summation gives

$$R = r_{01} + \frac{t_{01}t_{10}r_{12}e^{-2i\delta_1}}{1 + r_{01}r_{12}e^{-2i\delta_1}} \qquad (5.6)$$

From conservation of energy

$$t_{01}t_{10} = 1 - r_{01}^2 \qquad (5.7)$$

and taking $r_{10} = -r_{01}$, then (5.6) becomes [24]

$$R = \frac{r_{01} + r_{12}e^{-2i\delta_1}}{1 + r_{01}r_{12}e^{-2i\delta_1}} \qquad (5.8)$$

Here R represents the total amplitude of the reflected beams. The corresponding intensity is given by

$$R_{Tot} = RR^* = \frac{r_{01}^2 + r_{12}^2 + 2r_{01}r_{12}Cos2\delta_1}{1 + r_{01}^2r_{12}^2 + 2r_{01}r_{12}Cos2\delta_1} \qquad (5.9)$$

where $r_{01} = \frac{n_0 - n_1}{n_0 + n_1}$, $r_{12} = \frac{n_1 - n_2}{n_1 + n_2}$ for normal incidence.

The phase change δ_1, at normal incidence is given by

$$\delta_1 = \frac{2\pi}{\lambda} n_1 d_1 \qquad (5.10)$$

It can be seen from equation (5.10) that maxima and minima respectively of the reflectance curve occurs at values of n_1d_1 given by

$$n_1 d_1 = (2m + 1)\frac{\lambda}{4} \qquad (5.11)$$

$$n_1 d_1 = (2m + 2)\frac{\lambda}{4} \qquad (5.12)$$

The value of reflectances at these points for the case where the refractive index of the coating is greater than the refractive index of the substrate (i.e. $n_1 > n_2$) is given by

$$R_{min} = \left(\frac{r_{01} + r_{12}}{1 + r_{01}r_{12}}\right)^2 = \left(\frac{n_2 - n_0}{n_2 + n_0}\right)^2 \qquad (5.13a)$$

$$R_{max} = \left(\frac{r_{01} - r_{12}}{1 - r_{01}r_{12}}\right)^2 = \left(\frac{n_1^2 - n_0n_2}{n_1^2 + n_0n_2}\right)^2 \qquad (5.13b)$$

Similarly when $n_1 < n_2$ the reflectance values at the maxima and minima are given by

$$R_{max} = \left(\frac{n_2 - n_0}{n_2 + n_0}\right)^2 \qquad (5.14a)$$

$$R_{min} = \left(\frac{n_1^2 - n_0 n_2}{n_1^2 + n_0 n_2}\right)^2 \qquad (5.14b)$$

Rearranging these equations gives

$$n_{coat}^2 = n_{sub}\left(\frac{1+\sqrt{R}}{1-\sqrt{R}}\right) \qquad (5.15)$$

where n_{coat} and n_{sub} replace n_1 and n_2 respectively, and

R = Reflectance maxima (Transmission minima) for $n_{coat} > n_{sub}$

R = Reflectance minima for $n_{coat} < n_{sub}$.

The optical thickness can also be calculated from the transmission spectra from the position of the interference maxima/minima [23]. The basic condition for interference fringes is

$$2nd = m\lambda \qquad (5.16)$$

From this it follows that the thickness is given by

$$d = \frac{\Delta m}{2n_c\left(\frac{1}{\lambda_1} - \frac{1}{\lambda_2}\right)} \qquad (5.17)$$

where Δm represents the extrema separation and λ_1, λ_2 are the wavelengths at the extrema of interest.

It should be noted that equations (5.15) and (5.17) are of use only for films of thickness at least $\lambda / 4$. Moreover this analysis is based on the reflectance of light from a film deposited onto an infinite substrate, i.e. it does not take into account the reflectance off the back of a finite glass substrate used in practice. The transmission can be modified to take this into account as follows [23]

$$T_{corr} = \frac{T_{orig}}{1 - r_{01}^2 T_{orig}} \qquad (5.18)$$

where $T_{corr} = 1 - R_{corr}$ and $r_{01}^2 = 0.0422$ for glass of n = 1.517

The accuracy of the film thickness as measured by the last two methods, spectral transmission and interferometric microscopy, is limited for typical sol-gel coatings of thickness 400 nm as reported here due to poor contrast in fringes or broad transmission peaks. However these methods can still be used to remove the ambiguity as a result of cyclic behaviour in ellipsometry measurements (i.e. the number of ordinates to add). Thus these three methods together can be used to determine the thickness of a sol-gel film.

5.3 Film thickness as a function of coating rate

The theory and application of dip-coating of samples was outlined in detail in Chapters 3 and 4. This section illustrates the effect of varying the coating rate on film thickness for TEOS-derived films prepared using different R values. Previous studies of the dependence of film thickness on coating rate [2,3] have reported slope values of between 0.5 and 0.67 for plots of log (thickness) versus log (coating rate). Theory predicts either a slope of 0.5 or 0.66 [2,3,4] depending on assumptions related to surface tension and viscosity dependence.

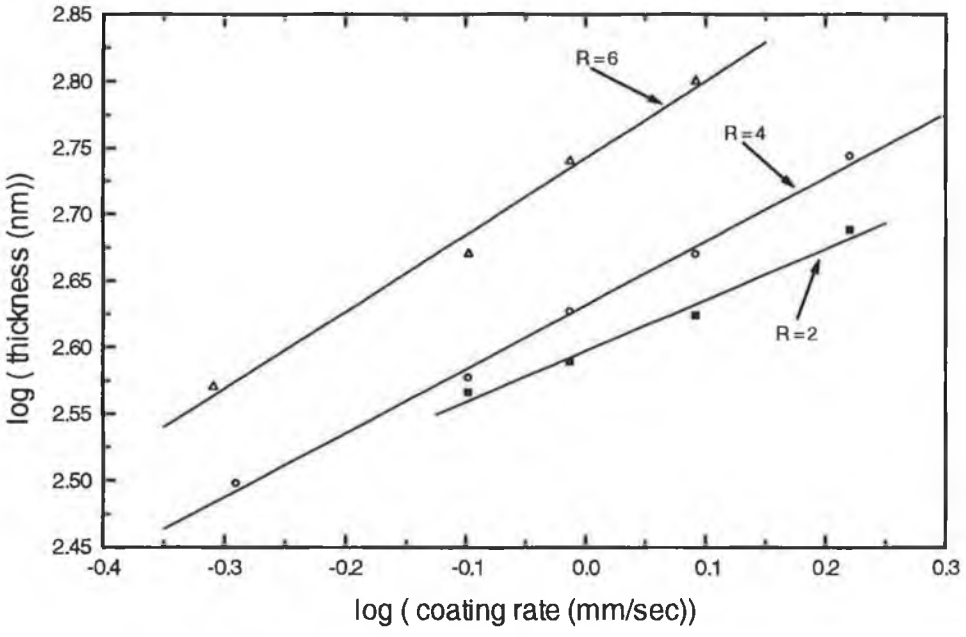

Figure 5.5 Log (thickness) versus Log (coating rate) for R = 2,4 and 6 films

Figure 5.5 plots log (thickness) versus log (coating rate) for TEOS-derived silica films prepared at pH 1 and R values of 2,4 and 6 [5]. Sols were aged for 5 hours before coating in each case. Films prepared at R = 4 and 6 yield a slope of 0.5-0.6, while the slope in the R = 2 film case is ~ 0.4. These results are consistent with those of previous studies except for the R = 2 films. In this case deviations from the predicted behaviour, which assumes Newtonian viscosity, could be due to the relatively small amount of water in the sol preparation, and its effect on the hydrolysis and condensation reactions. This behaviour is consistent with other anomalous results for the R = 2 films which are described below.

The effect of coating rate on thickness can be more easily illustrated by Figure 5.6. This figure shows thickness versus coating rate for R = 4 films prepared after different sol aging times. Coating rates ranging from 0.5 to 1.66 mm/sec were used in this study. In the case of 5 hours aging, films of thickness of ~ 310 nm to ~ 550 nm can be prepared by variation of the withdrawal speed over this range. A plot of log

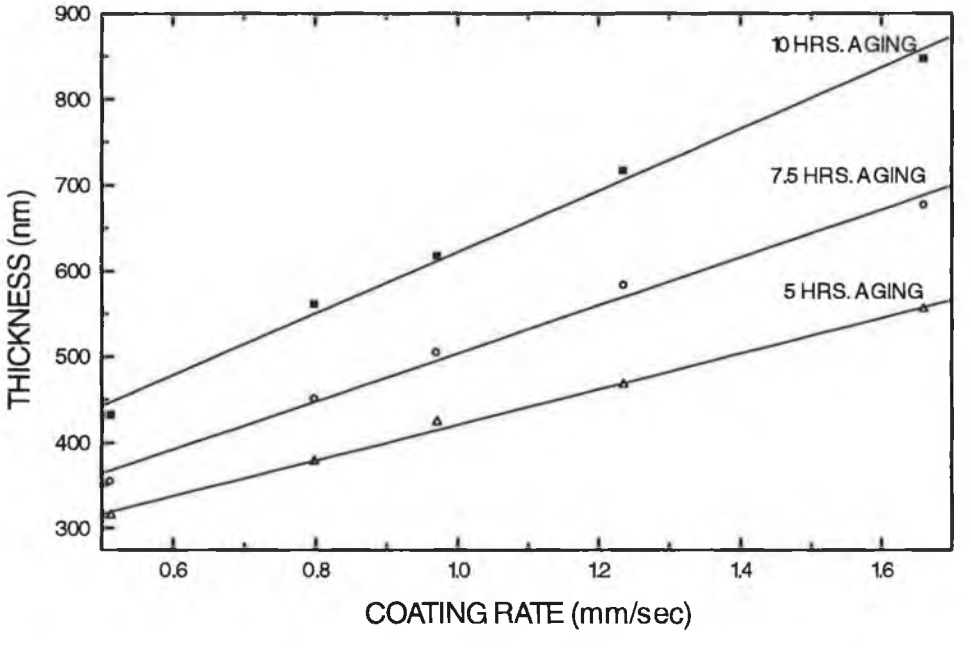

Figure 5.6 Thickness versus coating rate for TEOS (R = 4) films

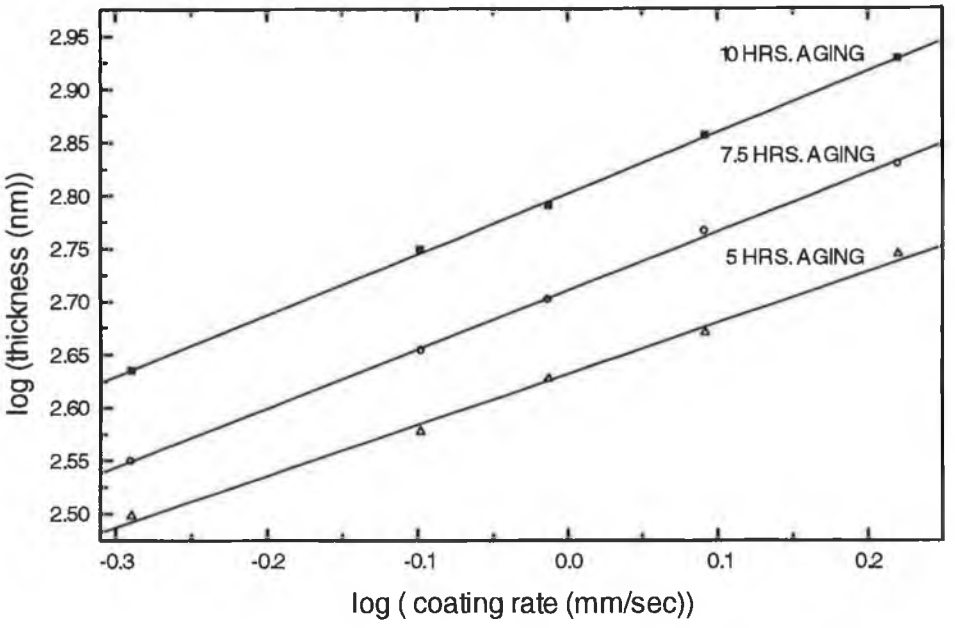

Figure 5.7 Log (thickness) versus Log (coating speed) for R = 4 films

(thickness) versus log(coating rate) for the data in Figure 5.6, is shown in Figure 5.7. Slope values ranged from 0.49 (5 hours aging) to 0.57 (10 hours aging). This increase in slope with aging time could be due to aggregation in the sol and concentration dependence of the viscosity due to evaporation.

5.4 Film thickness as a function of aging time

Aging or pre-polymerisation of the sol causes aggregation due to hydrolysis and condensation reactions, resulting in an increase in viscosity. Aging for too long a period or at too high a temperature leads to gelation before coating. Figure 5.6 shows the effect of sol aging on TEOS-derived films prepared at pH 1 and R = 4. Thickness increased for increasing aging time. This result agrees with other studies [6]. As discussed in section 3.5.3 thickness is proportional to sol viscosity and consequently the viscosity increase that results from the hydrolysis and condensation reactions during aging [7], causes the thickness increase with aging time.

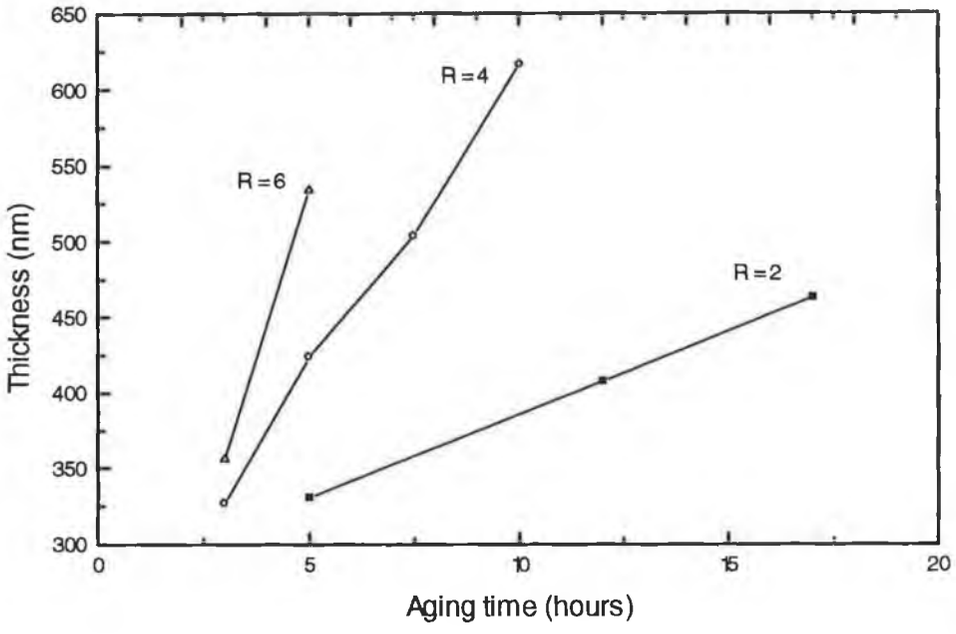

Figure 5.8 Film thickness as a function of aging time for R = 2,4 and 6

Figure 5.8 shows film thickness as a function of aging time for R = 2,4 and 6. In this work, sols were aged at 70 °C and aging times were varied for sols of different R values. Withdrawal speed was fixed at 1 mm/sec. In all cases thickness increased with aging, although the rate of increase is much slower in the R = 2 case.

5.5 Influence of water : precursor ratio (R) on film thickness

In section 3.3.1 the influence of the molar ratio of water to precursor on the hydrolysis and condensation reactions, and the corresponding structural evolution of sol-gel materials was outlined. In this section the influence of R (molar ratio of water : TEOS) on film properties is discussed. Films were fabricated at sol pH of 1 (i.e. pH of added water), dipped at 1 mm/sec and aged for 5 hours at 70 °C. R values were varied between 2 and 7. Figure 5.9 shows the dependence of thickness on R for these films. It is clear that increasing R leads to an increase in film thickness. At pH = 1, hydrolysis is

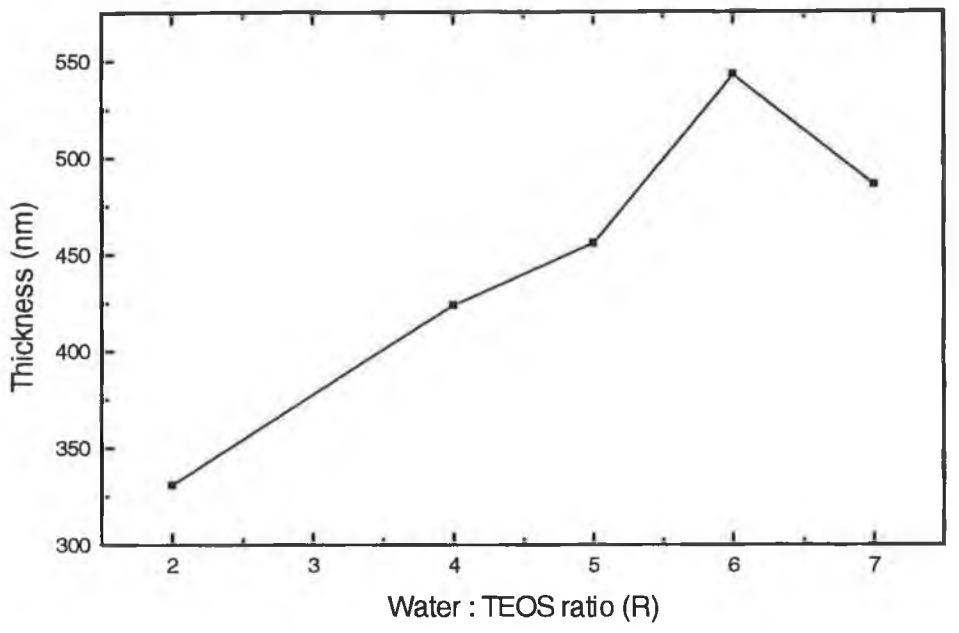

Figure 5.9 Film thickness as a function of R value

relatively fast compared to condensation and, as R is increased, the extra water promotes hydrolysis and is consumed [8]. Thicker films result from this increased hydrolysis. As R is increased further to the point at which there is excess water over that required for hydrolysis at a given sol pH, the excess water serves to dilute the sol. This reduces the relative silica content and gives rise to longer gel times and thinner films [9]. In this work, this point was reached above R = 6. Almeida [6] also observed this behaviour for films prepared at pH = 2.5, where film thickness decreased with increasing R value.

The R value of a sol has a large influence on the length of sol aging before gelation takes place, i.e. the gelation time. Table 5.1 shows the gelation time at 70 °C for R = 2,4 and 6. The point of gelation was qualitatively determined as the time at which the sols did not flow under gravity. Increasing the R value, decreases the gelation time. The effect of increasing R is to increase the rates of the hydrolysis and condensation rates [7]. For R = 2, the relatively small amount of water is rapidly consumed by the hydrolysis reactions. Further water for hydrolysis must be produced

by the slow condensation reactions under these processing conditions of pH = 1 and low water content. This results in long gelation time, as shown in Table 5.1 and slow increase in film thickness with aging time, as shown in Figure 5.8.

R Value	Gelation Time (hours)
2	170
4	13
6	7

Table 5.1 Gelation time as a function of R

5.6 Film stabilisation time

It is clear from the discussions above that R = 2 films differ in many ways from higher R value films. Another anomaly between R = 2 and R = 4 films is in the area of temporal behaviour of film thickness. Figure 5.10 shows the temporal evolution of film thickness, after coating and oven drying at 70 °C for 17 hours, for films fabricated at R = 2 and R = 4. The R = 2 films were aged for 17 hours while the R = 4 films were aged for 5 hours, hence the larger initial thickness in the R = 2 case. Included in Figure 5.10 are data for samples stored in desiccator and ambient conditions. It is clear that the films fabricated at the higher R value stabilise in a much shorter time, when stored in ambient conditions. The thickness of the R = 2 films decreased gradually over about 50 days, while in the R = 4 film case thickness had stabilised within 20 days. This difference in behaviour is attributed to incomplete hydrolysis in the R = 2 films, even though R = 2 is the stochiometric water : precursor ratio. It is clear from the literature that, even at relatively high R values, unhydrolysed nonomers can be present in the gel [8]. The result of this incomplete hydrolysis for films is that after coating, hydrolysis continues to take place during the drying process. This gives rise to a continuously evolving microstructure leading to a gradual decrease in film thickness. The continuing hydrolysis is facilitated by exposure to moisture in the atmosphere.

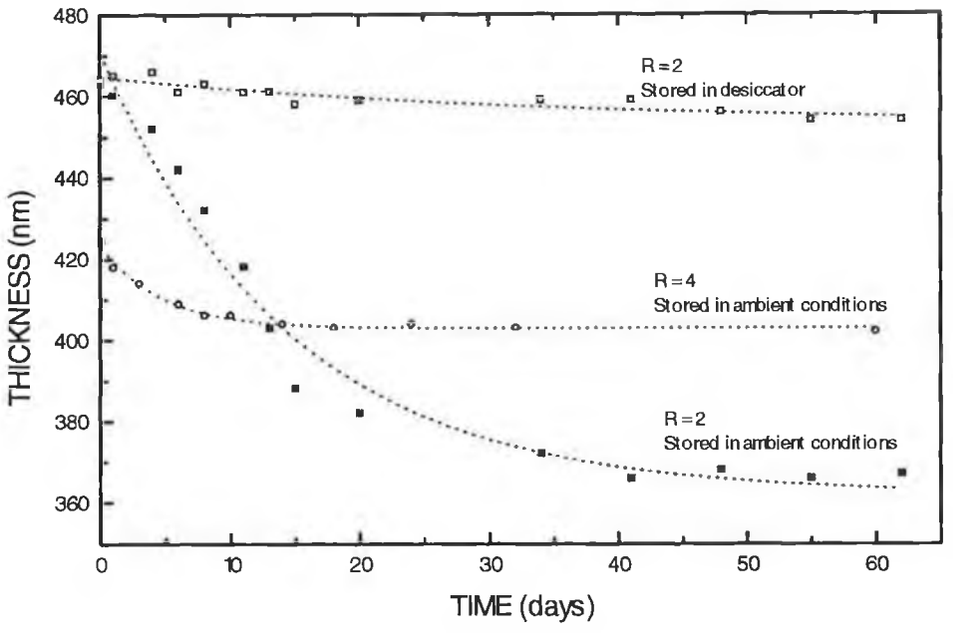

Figure 5.10 Temporal evolution of film thickness at R = 2 and R = 4

In order to investigate the above behaviour further, R = 2 films were stored in a desiccator shortly after oven drying. Their thickness was monitored over time, and compared with those of films stored under ambient conditions, as shown in Figure 5.10. Thickness of films stored in the desiccator changed little from their initial values. When these samples were removed from the desiccator and stored under ambient conditions, thickness began to decrease gradually following the same pattern as films stored in ambient conditions after oven drying. These measurements support the theory of continuing hydrolysis in the presence of atmospheric moisture for films fabricated at low R values. These results have implications for sensors employing these films. Sensors using R = 2 films would have to be fabricated at least 2 months before use to ensure repeatable behaviour. An evolving microstructure is likely to have a strong influence on sensor response.

5.7 Surface quality of sol-gel films

The optical quality of sol-gel-derived films was monitored using an optical microscope (Nikon Optiphot). It was observed in this study that the length of aging of a

sol before coating and the thickness of a film affected the optical quality of films. The quality of films deteriorated when coated close to gelation. As shown in Table 5.1, gelation time decreased with increasing R value. Films coated close to gelation were prone to cracking, resulting in a "crazy-paving" type appearance. This effect on film quality appears to be more related to aging time than thickness. Using the R = 4 films from Figure 5.6 as example, this behaviour will be outlined. Sol aging of 5 hours at 70 °C resulted in good quality films over the range of coating speeds, i.e. thickness range of 310-550 nm. In the case of sol aging for 7.5 hours, quality films were only observed for films coated below approximately 1 mm/sec withdrawal speed, or ~ 500 nm thickness. Above this coating rate quality deteriorated with cracking of films visible under the microscope. Poor quality films were observed at all coating speeds, 430-850 nm thickness range for sol aging of 10 hours. As thickness increased, the extent of film cracking also increased. A similar behaviour was observed for R = 6 films coated close to gelation, i.e. after 5 hours aging with gelation time of ~ 7 hours. In these films it is assumed that due to the extent of particle aggregation and cross-linking, the sol is not suitable for film coating close to the gel point. Therefore in order to obtain good quality homogeneous films, moderate sol aging relative to the gel time should be carried out. Coating rates used should ensure that film thickness is not >> 500 nm.

For high R value sols, aging was necessary to obtain good quality films. For R = 2 and R = 4 good quality films were obtained without aging, while at R = 6 aging was required. In the R = 6 case, if no aging was carried out, the film did not adhere well to the substrate. Matos et. al. [10] observed a similar result for films prepared from a pH 2.5 sol. A certain length of aging was required before good quality films were obtained by spin-coating in their case. The length of aging time required increased when the R value was increased from 2 to 4. They concluded that insufficient condensation in the bulk sol was probably the reason why uniform films could not be prepared before a certain length of sol aging.

5.8 Refractive index and porosity measurements

The refractive index of sol-gel films is a very important parameter to measure experimentally. In the design of evanescent wave fibre optic sensors, film refractive

index must be lower than the refractive index of the fibre optic core, to provide the necessary conditions for light-guiding. Film refractive index is also related to the porosity of the films and has been used by many groups [6,11] to estimate the porosity of sol-gel films.

In the work described here, refractive index of sol-gel films was measured by ellipsometry. Furthermore, by means of the Lorentz-Lorenz relationship [12], one can estimate the porosity of the films from the refractive index according to:

$$\frac{n_f^2 - 1}{n_f^2 + 2} = V_s \frac{n_s^2 - 1}{n_s^2 + 2} \qquad (5.19)$$

where n_f is the film refractive index, V_s is the volume fraction solids, and n_s is the refractive index of the solid skeleton. Porosity (P) is related to the volume fraction (V_s) by:

$$V_s = 1 - P \qquad (5.20)$$

Figure 5.11 shows the temporal evolution of film refractive index of the R = 2 and R = 4 films, stored in ambient conditions, whose thickness evolution was described in Figure 5.10. Some scatter in the refractive index values is observed. A slightly higher refractive index value was measured for the R = 4 films. A film refractive index of 1.43 would correspond to a porosity of ~ 5 %, according to equations (5.19) and (5.20).

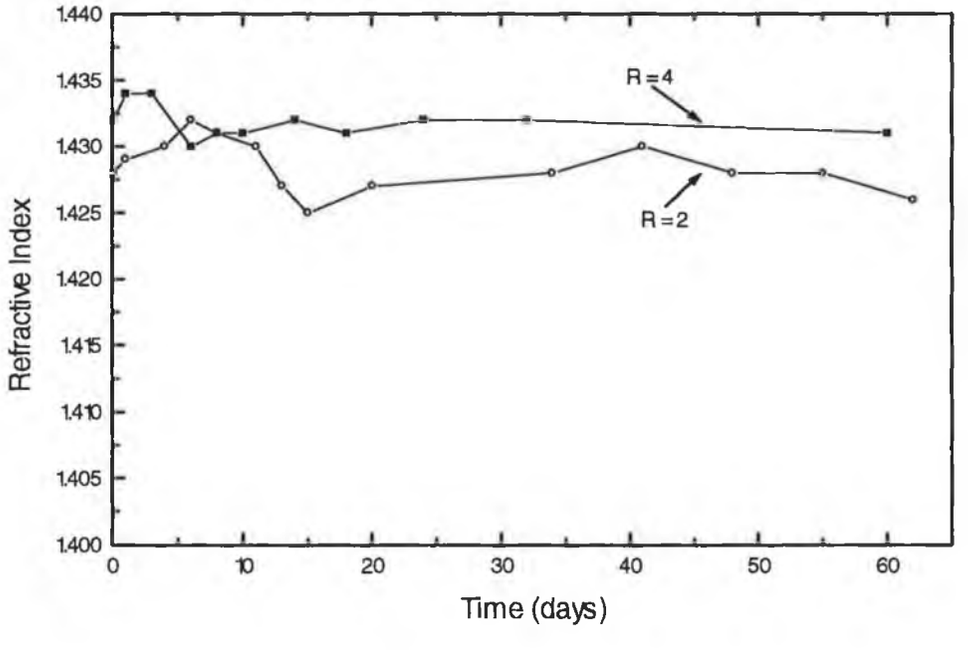

Figure 5.11 Temporal evolution of film refractive index for R = 2 and R = 4

The thickness of the R = 2 films (see Figure 5.10) decreased by ~ 20 % over time, and therefore one would expect the porosity of the films to decrease resulting in a corresponding increase in refractive index. However it is clear from Figure 5.11 that there is no correlation with thickness evolution. From the literature it is clear that the use of equation (5.19) to relate film refractive index and porosity must be handled with caution. Almeida [6] noted that with equation (5.19) one generally obtains estimates for the film porosity which are too high compared with the values obtained from nitrogen adsorption isotherms. Vorotilov et al. [13] reported that for spin-coated sol-gel silica films that showed a 10 % shrinkage following heat treatment, the variation in the refractive index was insignificant in contrast to the film shrinkage. They concluded that the reason for this inconsistency was the high hydroxyl/water content of the films, that has greater impact on the refractive index of sol-gel films than their porosity.

From the above discussion, the refractive index of sol-gel silica films used in this work cannot be strictly considered as characteristic of the film porosity and direct techniques of porosity measurement are needed. The refractive index could be affected by incomplete hydrolysed species in the low R value samples. Frye et al. [14] used a surface acoustic wave (SAW) technique for measuring gas adsorption-desorption isotherms to measure porosity. However, direct measurements of film porosity was not carried out in the work reported here because of the unavailability of such techniques. Information about the relative pore size of sol-gel films prepared using different processing parameters can be estimated from the behaviour of films doped with molecules of a range of sizes. For example the leaching of dyes of different sizes from sol-gel films, when immersed in aqueous solution, is described in Chapter 6.

5.9 Ormosils

The general properties of ormosils (organically modified silicates) was outlined in section 3.7. Ormosils described in this work were prepared from the precursor MTES. The introduction of organic into the material results in films whose thicknesses stabilise quickly after preparation. This is illustrated in Figure 5.12 for a MTES-based film prepared at pH 1 and R = 4, and coated at 1.66 mm/sec [15].

The use of the MTES precursor changes the surface properties of the sol-gel silica films. The hydrophilic Si-OH groups on the surface are replaced with hydrophobic Si-CH_3 groups [16]. These changes can be characterised using FTIR spectroscopy as shown in Figures 5.13 and 5.14 for TEOS and MTES-based films respectively. The FTIR spectra were recorded in the range 4000-500 cm^{-1} for sol-gel films coated on silicon wafers.

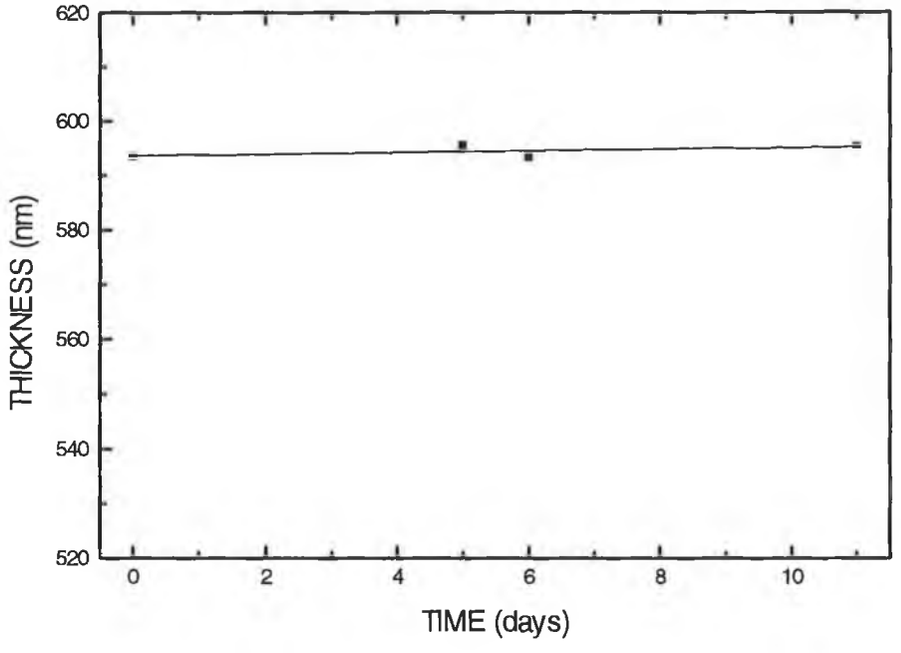

Figure 5.12 Temporal evolution of MTES-based film thickness

The structure of MTES-based films is characterised by the presence of Si-CH_3 groups (bands at 1265 cm^{-1} and 3000 cm^{-1}) [16]. These bands increase in intensity with increasing MTES content of the films. The peak at approximately 1070 cm^{-1} is the primary Si-O-Si peak. The wide band at 3400 cm^{-1} present in the samples is assigned to molecular water (O-H stretching). There could also be contributions from hydrogen bonded internal silanols (3640 cm^{-1}) and free surface silanols (3740 cm^{-1}). Innocenzi et al. [16] observed that these water bands decreased with increasing MTES content. However their results are for films that were dried at 300 °C and higher. In our samples the main water band at 3400 cm^{-1} does not appear to be very different for the MTES and

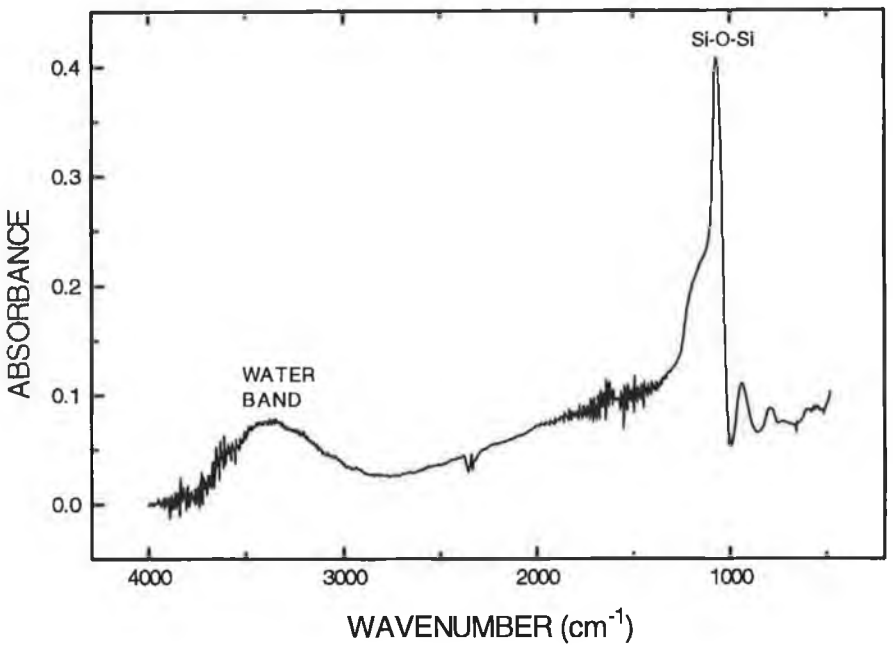

Figure 5.13 FTIR spectrum of TEOS-based sol-gel film

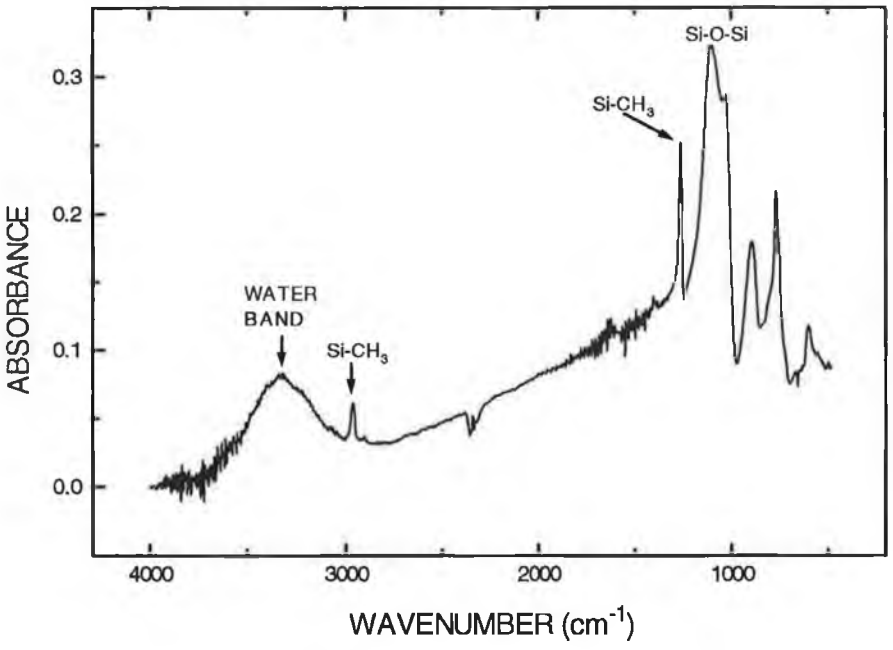

Figure 5.14 FTIR spectrum of MTES-based sol-gel film

TEOS-based films. The shoulder at ~ 3600 cm^{-1} decreases in the MTES case. The exact structural contribution to this feature is unknown. In Chapter 7 the effect of introducing organic constituents into a film is described in relation to an ammonia gas sensor.

5.9 Conclusion

A detailed account of the characterisation of the sol-gel films prepared at our laboratory was presented. Film properties such as thickness and temporal stability were monitored as a function of dip-speed, water : precursor ratio (R), sol aging time and time after dipping. Film thickness was found to increase with sol aging time, increasing R value and increasing dip-speed. Film behaviour was interpreted in terms of the dependence of the hydrolysis and condensation rates on the different processing parameters. Anomalies for R = 2 films, over higher R value films, were identified and included a slower rate of film thickness increase with aging time and a long period of time (~ 50 days) to achieve film stability. A typical optimum sol-gel thin film recipe as identified from this study, using TEOS as precursor and pH1 water, required an R value of at least 4 to ensure a short period of time to temporal stability. In the R=4 case, an aging time of 5 hours and a coating rate of 1 mm/sec gives good quality films (thickness less than 500 nm).

References

1. C. McDonagh, F. Sheridan, T. Butler and B.D. MacCraith, 'Characterisation of sol-gel-derived silica films', J. Non-Crystalline Solids, Vol. 194, 1996, pp. 72-77.

2. I. Strawbridge and P.F. James, 'The factors affecting the thickness of sol-gel derived silica coatings prepared by dipping', J. Non-Crystalline Solids, Vol. 86, 1986, pp. 381-393.

3. C.J. Brinker, A.J. Hurd, P.R. Schunk, G.C. Frye and C.S. Ashley, 'Review of sol-gel thin film formation', J. Non-Crystalline Solids, Vol. 147&148, 1992, pp. 424-436.

4. H. Schroeder, 'Oxide layers deposited from organic solutions', in Physics of Thin Films (G. Hass editor), Vol. 5, 1969, Acamemic Press, New York, pp. 87-141.

5. F. Sheridan, 'Characterisation and optimisation of sol-gel-derived thin films for use in optical sensing', Masters of Sciences Thesis, 1995, Dublin City University.

6. R.M. Almeida, 'Sol-gel silica films on silicon substrates', Int. J. Of Optoelectronics, Vol. 9, No. 2, 1994, pp. 135-142.

7. C.J. Brinker and G.W. Scherer, Sol-gel Science, Academic Press, New York, 1990.

8. J.C. Pouxviel, J.P. Boilet, J.C. Beloeil and J.Y. Allemand, J. Non-Crystalline Solids, Vol. 89, 1987, pp. 345.

9. L.C. Klein, Ann. Rev. Mater. Sci., Vol. 15, 1985, pp. 27.

10. M.C. Matos, A.R. Carvalho, R.M. Almeida and L.M. Ilharco, 'Influence of processing parameters on the thickness of sol-gel silica films', Proc. SPIE, Sol-gel Optics II, Vol. 1758, 1992, pp. 77-82.

11. M.A. Fardad, E.M. Yeatman, E.J.C. Dawnay, Mino Green and F. Horowitz, 'Effects of H_2O on structure of acid-catalysed SiO_2 films', J. Non-Crystalline Solids, Vol. 183, 1995, pp. 260-267.

12. Reference 7, p. 803.

13. K. Vorotilov, V. Petrovsky and V. Vasiljev, 'Spin coating process of sol-gel silicate films deposition: effect of spin speed and processing temperature', J. Sol-gel Science and Technology, Vol. 5, 1995, pp. 173-183.

14. G.C. Frye, A.J. Ricco, S.J. Martin and C.J. Brinker, 'Characterisation of the surface area and porosity of sol-gel films using SAW devices', in Better Ceramics Through Chemistry III (edited by C.J. Brinker, D.E. Clark and D.R. Ulrich), 1988, pp. 349-354.

15. Unpublished data, Vincent Murphy, School of Physical Sciences, Dublin City University, Ireland.

16. P. Innocenzi, M.O. Abdirashid and M. Guglielmi, 'Structure and properties of sol-gel coatings from Methyltriethoxysilane and Tetraethoxysilane', J. Non-Crystalline Solids, Vol. 3, 1994, pp. 47-55.

17. S. McCulloch, G. Stewart, R.M. Guppy and J.O.W. Norris, 'Characterisation of TiO_2-SiO_2 sol-gel films for optical-chemical sensor applications', International J. Optoelectronics, Vol. 9, No. 3, 1994, pp. 235-241.

18. T.M. Harris and E.T. Knobbe, 'Assessment of porosity in sol-gel silica thin films by dye adsorption', J. Materials Science Letters, Vol. 15, 1996, pp. 153-155.

19. R.M.A. Azzam and N.M. Bashara, Ellipsometry and Polarised Light, North-Holland Physics Publishing, 1987.

20. Rudolph Research AutoEL-III Ellipsometer, Condensed operating instructions.

21. H. Homatsu, 'Interferometry: Principles and applications of two-beam and multiple-beam interferometry', Nikon Technical Bulletin.

22. S.N. Dixit, I.M. Thomas, B.W. Woods, A.J. Morgan, M.A. Henesian, P.J. Wegner and H.T. Powell, 'Random phase plates for beam smoothing on the Nova laser', Applied Optics, Vol. 32, No. 14, 1993, pp. 2543-2554.

23. V. Murphy, Degree in Applied Physics Final year project report, 'Sol-gel thin film characterisation', Dublin City University.

24. O.S. Heavens, Optical properties of thin solid films, Dover Publications, New York, 1965.

Chapter 6 pH Sensing

6.1 Introduction

The experimental results obtained from the investigation of an optical fibre pH sensor using evanescent wave absorption of sol-gel entrapped pH indicators are presented in this chapter. This chapter is concerned with the measurement of pH in an aqueous environment, while Chapter 7 deals with ammonia-gas sensing using pH indicator dyes. A range of sulfonephthalein colourimetric indicators, immobilised in sol-gel films, were investigated. Particular attention was given to the difference in behaviour of the immobilised dyes compared with solution. Methods of extending the range of the optical pH sensor are also outlined. Furthermore, a detailed study of dye leachability from sol-gel thin films is described in detail.

The first section of this chapter outlines pH indicator theory. Following this, the experimental results obtained for a range of pH indicators in sol-gel films is presented. Section 6.4 deals with co-immobilisation of indicators to extend the pH range of the sensor. A LED-based sensor, based on the spectrophotometric study of section 6.3 is then presented. Finally, in section 6.6, a range of issues affecting the leaching of pH indicators from sol-gel silica films is detailed.

6.2 pH indicator theory

Optical pH sensors are based on pH-dependent changes of the optical properties (absorbance, reflectance, fluorescence) of a thin reagent layer, attached to the tip or surface of an optical light guide through which these changes are detected [1,2]. The reagent layer usually contains a dye which reacts reversibly with the protons of the sample. In a typical sensor, the pH dependent absorption [3,4] or fluorescence [5,6] is monitored and related to pH. The work described in this chapter uses absorption-based reagents to measure pH.

pH is defined as [2]:

$$pH = -\log\left(a_{H^+}\right) = -\log\left(f_{H^+}\left[H^+\right]\right) \qquad (6.1)$$

where $a_{H}+$, $[H^{+}]$ and $f_{H}+$ are the activity, concentration and activity coefficient of the hydrogen ions, respectively. The activity is essentially the effective concentration. Activity and concentration are related by the activity coefficient (a fraction < 1). The activity coefficient depends on the ionic strength of the solution and approaches unity for infinitely dilute solutions. In very dilute solutions, pH can be related directly to the concentration of the hydrogen ion [2]. Activities compensate for the attraction which ions may exert on one another as well as the incomplete hydration of ions in solutions that are too concentrated.

Acid-base indicators are weak acids that change colour upon protonation or deprotonation of the indicator molecule [7]. The pH of a solution may be determined spectrophotometrically by measuring the concentration ratio of the undissociated (protonated) indicator species, HA, to the dissociated species (deprotonated) A^{-} [8]. This can be expressed in terms of the acid-base equilibrium of the indicator as:

$$HA \longleftrightarrow H^{+} + A^{-} \qquad (6.2)$$

The dissociation constant of this equilibrium is given by the mass-action law [1]:

$$K_{c} = \frac{[A^{-}][H^{+}]}{[HA]} \qquad (6.3)$$

where K_{C} is the concentration constant of the acid-base dye, and [HA] and $[A^{-}]$ are the concentrations of the acid and base form of the dye, respectively. The concentration constant K_{C} is related to the thermodynamic constant K_{a} of a weak acid by the individual activity coefficients f_{x} of the reaction partners:

$$K_{a} = K_{c}\frac{f_{A^{-}}.f_{H^{+}}}{f_{HA}} \qquad (6.4)$$

When expressed in logarithmic form, the activity-based Henderson-Hasselbalch equation is obtained as

$$pH = pK_{a} + \log\frac{[A^{-}]}{[HA]} + \log\frac{f_{A^{-}}}{f_{HA}} \qquad (6.5)$$

where pK_a is $-\log K_a$.

By taking the involvement of water molecules in the dissociation into account, equation 6.5 becomes [2]

$$pH = pK_a + \log\frac{[A^-]}{[HA]} + \log\frac{f_{A^-}}{f_{HA}} - \log a_{H_2O} \qquad (6.6)$$

where a_{H_2O} is the activity of water.

Equation 6.6 represent most of the factors that affect the pH response of an acid-base indicator. Janata [9] noted that nearly all papers describing optical pH sensors ignore the third and fourth terms in equation 6.6. He notes that this can be tolerated for very dilute aqueous solutions, where the activity coefficients tend to unity, and water is in a larger molar excess.

The effect of the environment on the dissociation equilibrium of the indicator is characterised by the ratio of the activity coefficients i.e. the third term in equation 6.6 [9,18]. These effects include the change in ionic strength and is important where the ionic strength is high. The fourth term in equation 6.6 represents the logarithm of the activity of water and becomes important when the ionic strength of the aqueous solution exceeds approximately 4 M or when dealing with mixed organic/aqueous solvents [9].

In spite of these difficulties, optical sensing of pH has some attractive features. There is no reference electrode required as in electrochemical measurements and in general they benefit from the advantages of optical fibre sensors as described in section 1.2. The ionic strength dependence decreases the accuracy at which the pH of an unknown solution can be determined [8].

From the above discussion it is seen that optical measurements are a function of the concentration of the acid and base forms of the indicator, i.e. term 2 in equation 6.6. Since the degree of dissociation of the indicator dye is a function of pH, the latter can be determined by measuring the relative concentrations of both forms of the dye e.g. by absorption. The measured absorbance is related to the concentration of the different

forms of the indicator, [HA] and [A^-], by assuming the Lambert-Beer law [11] i.e. absorbance directly proportional to concentration. The relation between pH and absorbance is given by [4,8]

$$pH = pK_a + \log\left(\frac{A - A_{min}}{A_{max} - A}\right) \qquad (6.7)$$

where A_{max} is the absorbance at a pH high enough to ensure complete dissociation of the indicator, A_{min} is at a low enough pH for the indicator to be totally undissociated, and A is the absorbance at any given pH. pK_a is the dissociation constant of the indicator. Equation 6.7 ignores the effect of the last two terms in equation 6.6.

The first absorbance-based fibre-optic pH sensor described in detail was developed by Peterson et al. [10] for the physiological pH range 7.0 to 7.4. While this pH range has been studied in many reports [4,6] because of its medical applications, other pH ranges are of interest for industrial applications. Some disadvantages of optical pH sensors are the narrow pH range of the indicator, typically within +/- 1.5 pH units of the indicator pK [7,11] and their decreasing precision when the difference between the measured pH and the pK of the dye increases [11]. The range of an optical pH sensor can be increased by using multiple dyes [12] and this issue is discussed in section 6.4.

A wide range of immobilisation methods for pH indicators has been reported in the literature. Examples of host matrices include controlled pore glass [3], cellulose [13] and sol-gel glass. Sol-gel immobilisation of indicators was the method used in this work because of the advantages of the process as outlined in Chapter 3. The sol-gel method has been used by a number of groups for pH sensing [14,15,16,17]. A feature of immobilisation, common to virtually all the methods above, is that the properties of the immobilised dye vary from those of the indicator in solution. A shift in the pK of the indicator is the most common feature and this is detailed in section 6.3 below.

The sulfonephthalein colourimetric indicators were chosen because of their sharp colour change and their high colour intensity that ensure better sensitivity [7]. Indicators from this family have been used in numerous studies [3,10,14] and show good results

when immobilised in a range of matrices. In most cases the base form of the dye is monitored because its optical density is greater than that of the acid form, thus providing a better optical sensitivity to pH change [10].

6.3 Sol-gel-based pH sensor

6.3.1 Introduction

The fibre optic spectrometer-based characterisation system, described in section 4.4.3, was used to characterise the fibre optic pH sensors in terms of evanescent absorbance variation. Different pH buffer solutions in the range pH 2-11, prepared from Hydrion buffers (Aldrich Chemicals), were flowed using a peristaltic pump through the liquid cell containing a sol-gel coated fibre. The sulfonephthalein indicators investigated were bromophenol blue (BPB), bromocresol green (BCG), bromocresol purple (BCP) and bromothymol blue (BTB). These indicators differ from one another with respect to their pK values, i.e. the pH value of maximum colour change [7,19]. This is due to different substituent groups on the indicator molecule [7].

These indicators were immobilised in silica sol-gel films as described in Chapters 3 and 5. The sol-gel films were prepared using tetraethylorthosilicate (TEOS), ethanol and pH1 water at a R-value of 4 and an aging time of 5 hours at 70°C. R = 4 films were chosen because of the anomalies associated with R = 2 films, which are described in Chapter 5. Furthermore, R = 4 films were less prone to leaching than R = 2 films and this is discussed in detail in section 6.6. The sol-gel films were coated at 1 mm/sec coating rate on unclad optical fibres as described in Chapter 4. The concentration of the indicator in the sol-gel thin films is difficult to define exactly. However, there exists a number of possible methods to characterise it, e.g. molarity with respect to the total precursor solution in the sol, or molarity with respect to TEOS. The former was used throughout these results. In a typical preparation, an indicator concentration of about 2 mMol / Litre was used.

6.3.2 Absorption spectra of indicators in sol-gel

Evanescent wave (EW) absorption spectra obtained from fibres coated with sol-gel doped with BPB and BTB are shown in figures 6.1 and 6.2 respectively. Similar

spectra were obtained for BCG and BCP. As the pH of the buffer solutions surrounding the coated fibres is increased, the evanescent absorbance of the alkaline form of the indicator increases. The absorbance of the acid form decreases with increasing pH, but shows a smaller relative change than the alkaline form. BTB has a higher pK value than BPB [7] and therefore shows greater response to higher pH values.

To illustrate the effect of the pK of the dye on the pH range of the indicator, i.e. the range over which most significant absorbance changes can be observed as a function of pH, the absorbance of the alkaline form of the indicator was plotted against pH for the four indicators. These data are shown in figure 6.3. For comparison purposes and to compensate for variations such as lamp fluctuation during the scans, absorbance at the peak λ of the alkaline form minus a baseline absorbance, i.e. $A_{peak} - A_{ref}$, was plotted. The baseline absorbance was chosen at a wavelength where the absorbance varied negligibly with pH. For example, in the BPB case the absorbance at any wavelength above about $\lambda = 680$ nm could be used as reference as shown in figure 6.1.

The pK of an indicator can be estimated as the pH at the point of inflection of a sigmoidal curve fit to absorbance versus pH data [1]. In figure 6.3 sigmoidal curve-fits to the data for the four indicators are shown. A number of features can be observed from these data. The pK of the indicators in solution increase in the following order, BPB < BCG < BCP < BTB. In sol-gel the same trend is followed, although the pK and range of the indicators are different to those in solution. The difference between immobilised indicators and indicators in solution are examined in more detail in section 6.3.3 below. In figure 6.3 the pH range covered was pH 2-11. From the shape of its sigmoidal curve and from figure 6.2, BTB in sol-gel may well respond above this range, i.e. above pH 11, since the sigmoidal curve was still increasing.

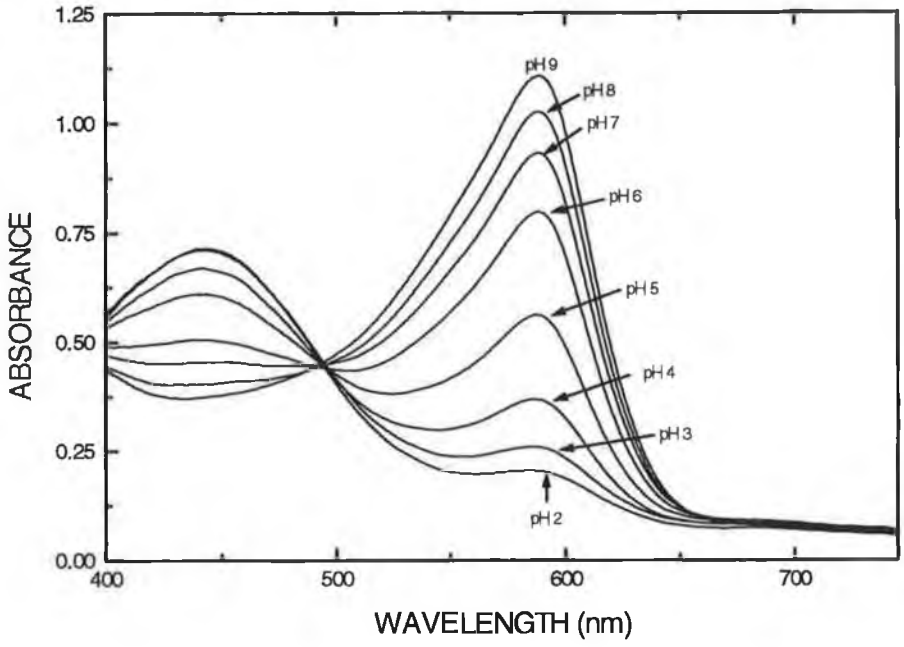

Figure 6.1 EW absorption spectra of BPB in sol-gel

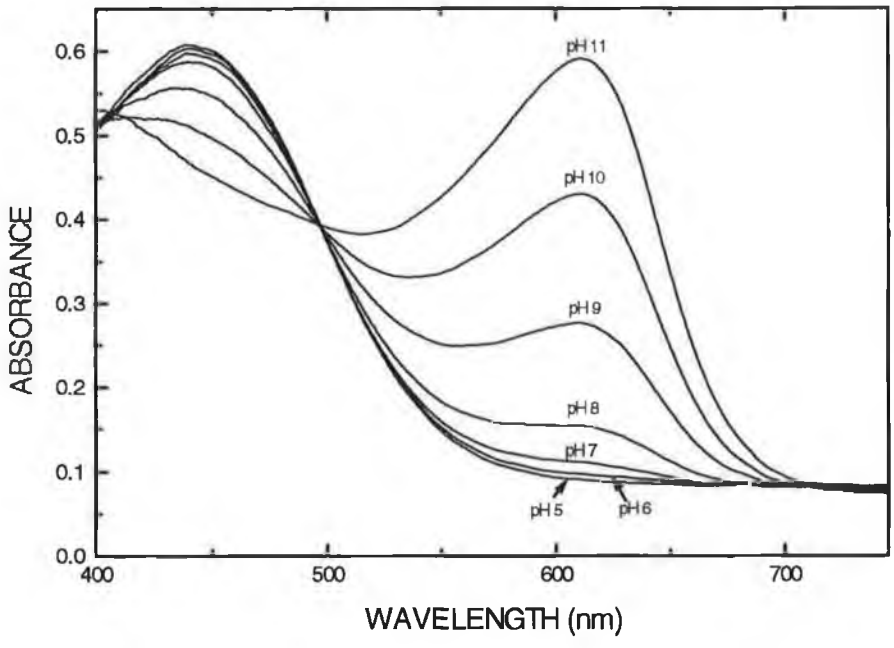

Figure 6.2 EW absorption spectra of BTB in sol-gel

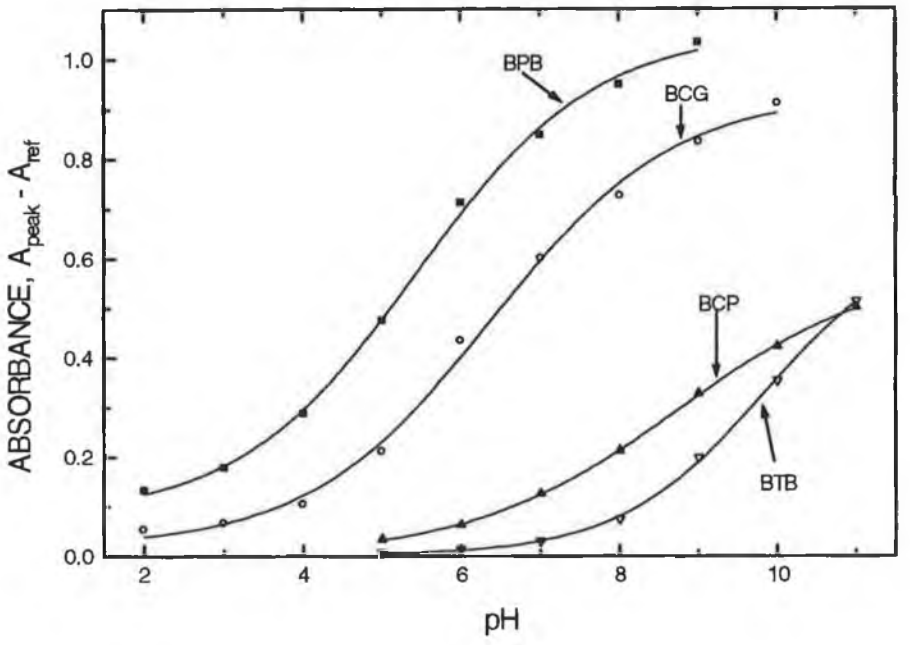

Figure 6.3 pH response of the different indicators

6.3.3 Effect of immobilisation on indicator properties

It is interesting to compare the behaviour of the indicators in solution to that in sol-gel. This is illustrated by the differences exhibited between figure 6.1 for BPB in sol-gel and figure 6.4 for BPB in solution. In solution the pK of BPB is 4.1 [7] and the range of the dye is from about pH3 to pH5, with smaller changes outside this range. In sol-gel the pK of BPB was measured to be about 5.4 and the range of the dye is about pH 3-7. Therefore the process of immobilisation has resulted in a shift in the pK of the dye and a broadening in the pH range of the dye. Table 6.1 summarises this behaviour and shows the pK and range of the 4 dyes in solution and sol-gel. In all cases the pK of the dyes increased on immobilisation. In the case of BCP and BTB the increase in pK is particularly large and the operational range of the dye is shifted considerably from that in solution. BCP, for example, has a range of about pH 5-7 in solution, while in sol-gel this range is approximately pH 6-11. A similar trend was observed for BTB.

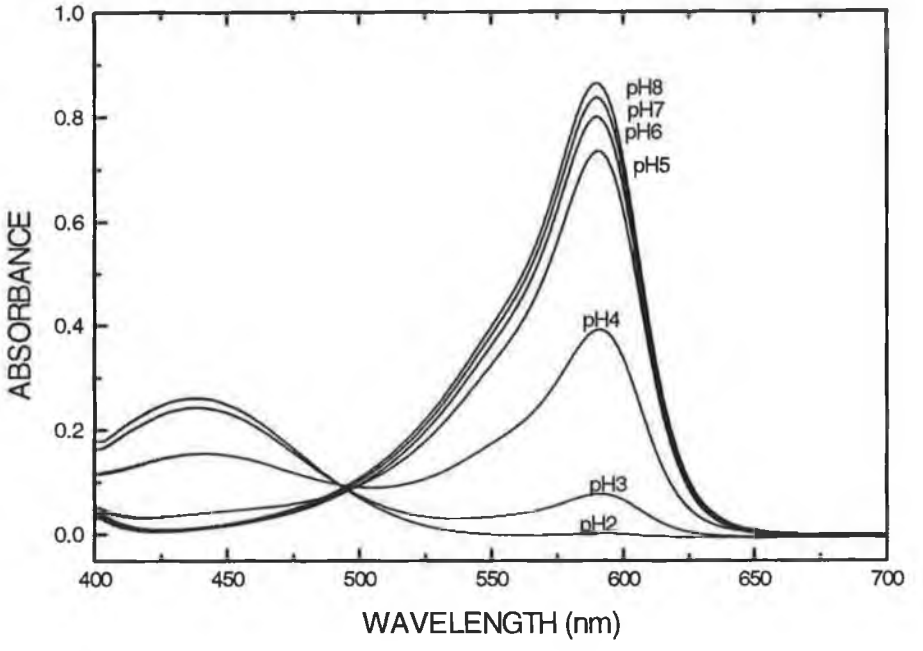

Figure 6.4 Absorption spectra of BPB in solution

Indicator	pK (solution) [7]	pK (sol-gel)	pH Range (solution) [7]	pH Range (sol-gel)
BPB	4.1	5.4	3.0 - 4.6	3 - 7
BCG	4.9	6.5	3.8 - 5.4	4 - 9
BCP	6.4	8.7	5.2 - 6.8	6 - 11
BTB	7.3	9.8	6.0 - 7.6	8 - 11
BPB + BCP		6.6		3 - 11

Table 6.1 pK and range of indicators in solution and sol-gel

The shift in the pK of the indicators is a common feature of immobilisation and has been reported for a number of matrices including polymers [20], controlled pore glass [21] and sol-gel glasses [16,17]. A broadening of the pH range has also been reported [17,21]. Yang and Saavedra [17] reported a doubling in the range of BCP when immobilised in a sol-gel glass film. The broadening is considered to be due to a

distribution of the dye molecules over slightly different sites in the sol-gel resulting in a distribution in the values of the dye dissociation constant [17,21]. This broadening effect can be used to extend the range of pH sensors and this issue is discussed in more detail in section 6.5.

6.3.4 Sensor response and range

The range of a pH sensor depends on which of the indicators is chosen and this is summarised in table 6.1. It should be noted that these indicators can be used for measurement beyond this range with a sacrifice in the accuracy of the measurement. From table 6.1 and figures 6.2 and 6.3, it is observed that some of the indicators, e.g. BCP and BTB, respond to pH values above pH 9. However, problems can be encountered for pH sensing at high pH values when using sol-gel silica glass. For example, over time sol-gel silica films will be susceptible to alkaline attack at high pH. This is caused by hydrolysis of the SiO_2 network at high pH [22]. Blue and Stewart [42] overcame this problem by inclusion of zirconium in the sol-gel matrix. Furthermore, as will be discussed in section 6.6, increased dye leaching may occur at high pH values due to the increased solubility of sulfonephthalein dyes at high pH.

In order to determine the response time of the sensor films to changes in pH, the absorbance of the alkaline form of the dyes was monitored over time using a time-series display function of the Ocean Optics spectrometer [23]. The peak absorbance referenced against a non-absorbing wavelength, i.e. A_{peak} - A_{ref}, was plotted over time. This is illustrated in figures 6.5 and 6.6, which shows the step response to pH of BPB (pH 3-6 range) and BCP (pH 6-10 range), respectively. Both plots show high values of signal-to-noise ratios and good repeatability over the length of the scans. Longer term repeatability is controlled to a large degree by the leaching of dye from the sol-gel films and this issue is covered in section 6.6.

The T_{90} response time, or the time to reach 90 % of the absorbance change, for the BPB film was measured to be about 40 seconds for a change from pH 3 to pH6 and about 20 seconds for a pH 6 to pH 3 step. In the BCP case, the response time was about 30 seconds for both the pH 6 to pH 10 step and the reverse step. These results indicate the rapid diffusion of protons in and out of the sol-gel matrix. Moreover, these

response times includes the delivery time of new solution and the time for the pH solution in the cell to reach equilibrium after a step change in pH.

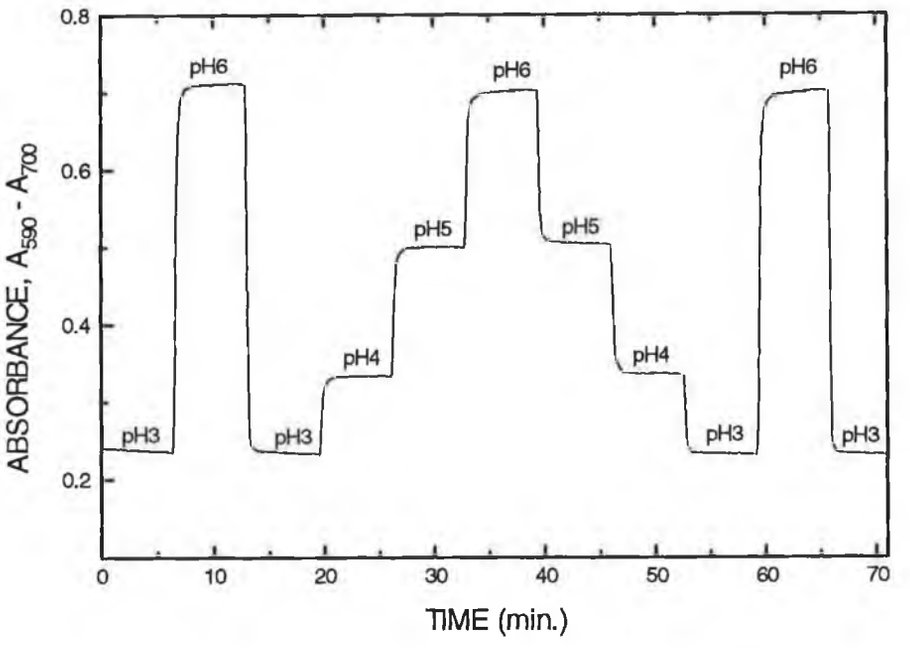

Figure 6.5 Response of BPB to pH

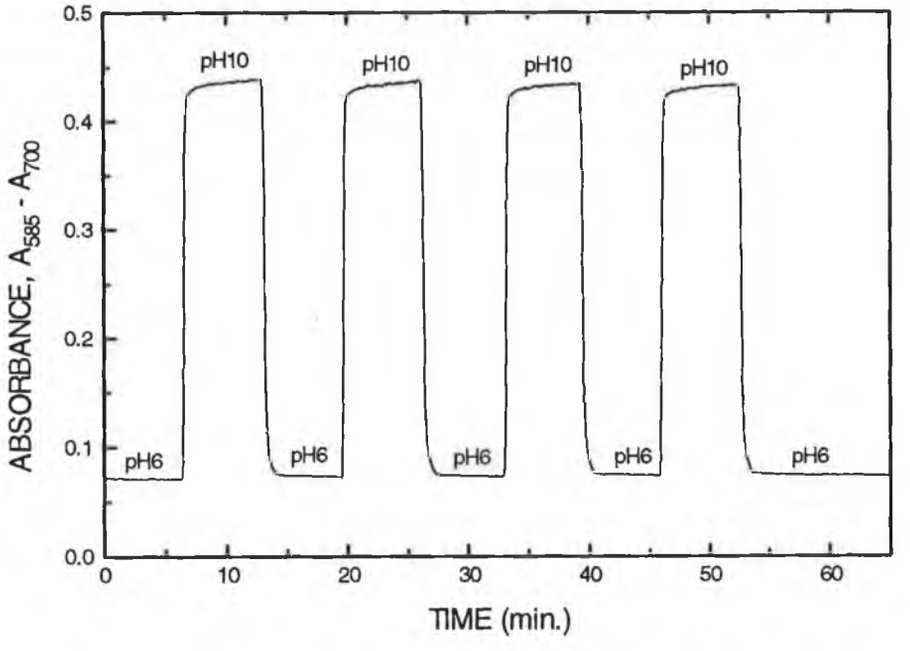

Figure 6.6 Response of BCP to pH

6.4 Extending range of sensor

6.4.1 Introduction

A disadvantage of many optical pH sensors is their limited dynamic range, usually within about +/- 1.5 pH units of the indicator pK. This is illustrated in figure 6.4, which shows the absorption spectra of BPB in solution for different pH buffer solutions. From this graph it is clear that the useful pH range of BPB in solution is only about 2 pH units. This problem can be lessened somewhat by using multiple indicators with different pK [11,25] or by the inherent broadening of the pH range of an indicator when immobilised in certain supports [12,17,21]. This broadening, as discussed in section 6.3, resulted in at least a doubling of the pH range of the indicators when immobilised in sol-gel glass.

The second method to extend the range of the pH sensor is to use multiple dyes. This method has been described in detail by, among others, Boisde et al. [11] and Peterson et al. [27,28]. Multiple dyes can be used to cover a broad pH range in two ways [27]. One way is to use different dyes with different pK's and different spectra, i.e. different peak absorption wavelength. The change in absorption over a short pH range can be observed for each dye, at its particular absorption peak, and combined to cover the whole range. However this method involves complex spectral interpretation. Alternatively, for a dye mixture where the two dyes have similar absorption spectra (i.e. approximately the same wavelength of maximum absorption) with slightly different pK's, then the linear range can be extended by an appropriate combination of the dyes [25,27]. This method uses simpler instrumentation than the previous case since only one measurement wavelength is required.

The development of a multiple indicator system for pH measurements, while a straightforward concept, can be difficult experimentally. Many different combinations of indicator concentrations and measurement wavelengths must be explored to maximise the sensitivity of the pH measurements. Some authors [26,28] have used a mathematical model that describes the visible spectra of sulfonephthalein indicators as a function of pH. The model facilitates selection of optimal measurement wavelengths and concentrations for multiple indicator systems. The principle of using multiple indicators to extend the pH range is demonstrated in section 6.4.2 for BPB and BCP.

6.4.2 Co-immobilisation of indicators

The range of the optical pH sensor was extended by co-immobilisation of BPB and BCP in a sol-gel silica glass film. A 50-50 mixture of dye (~ 1 mMol / Litre for each dye) was used in a R = 4 sol-gel film, prepared as previously described. Figure 6.7 plots the absorption spectra of films in which these two dyes are co-immobilised for different pH buffers between pH 2-11. The pH range of the dye mixture is illustrated in figure 6.8 which plots absorbance versus pH. The range extends approximately from pH 3-11, i.e. measurement over about 8 pH units. The pK of the dye mixture at 6.6 is intermediate between the individual dye pK's of 5.4 (BPB) and 8.7 (BCP). This sensor is essentially benefiting from the double effect of multiple dyes and broadening on immobilisation. The above sections have dealt with a spectrophotometric study of a range of sol-gel immobilised indicators. In the next section the results of a LED-based pH sensor, the design of which is based on the above study, is presented.

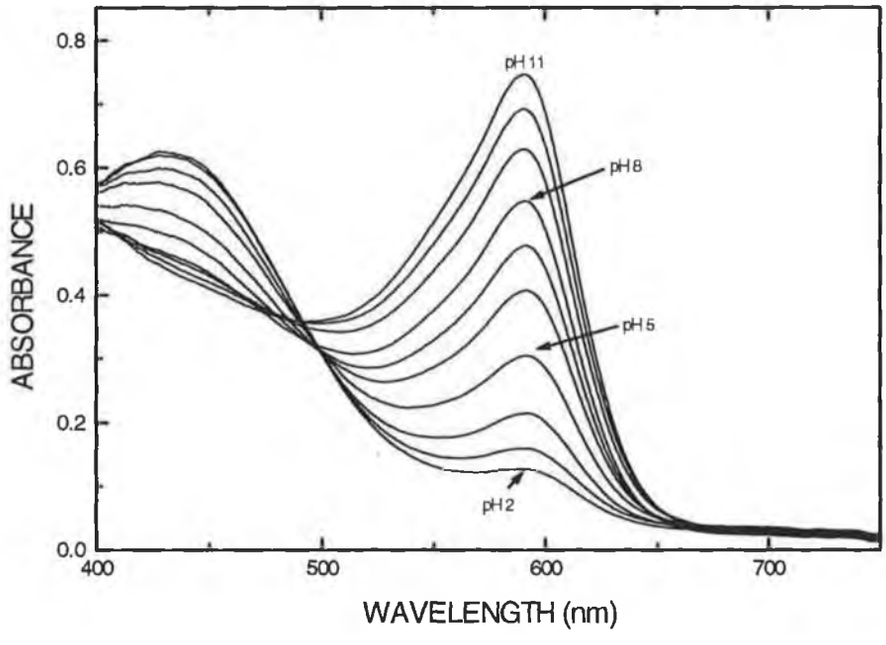

Figure 6.7 Absorption spectra of BPB and BCP co-immobilised in a sol-gel film

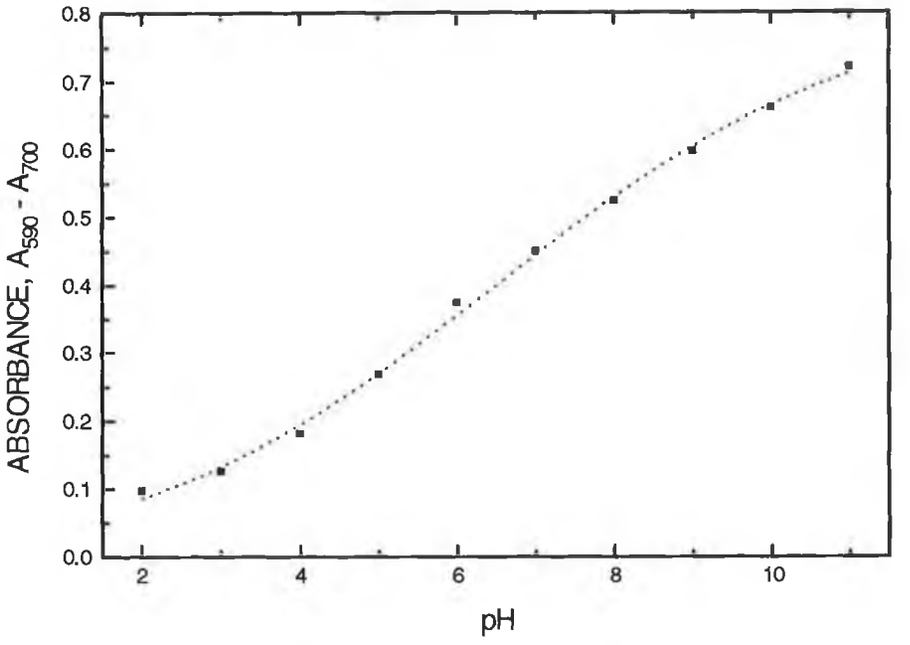

Figure 6.8 Response curve for co-immobilised BPB and BCP

6.5 LED-based pH sensor

In order to reduce the cost and size of the measurement system and to take advantage of solid-state optoelectronic components [24], a LED-based characterisation system was constructed. Section 4.4.4 details this setup and its advantages. Its principle of operation is demonstrated here for BPB. The measurement LED used was a yellow LED, with a peak wavelength of 590 nm, whose output spectrum closely matches the absorption band of the alkaline form of BPB as shown in figure 4.6. A near-infrared LED, with a peak wavelength of 850 nm, was used for reference purposes as absorption did not change significantly with pH in this region of the spectrum.

Figure 6.9 shows a typical response of a BPB film to a step change in pH when using the measurement LED only, i.e. no referencing. Good repeatability and reasonable signal-to-noise levels are observed. A typical response curve for BPB, over the range pH 2-7, for the single LED-based sensor is shown in figure 6.10. A near-linear response in the transmitted intensity was observed over the pH 3-6 range with smaller changes outside this range.

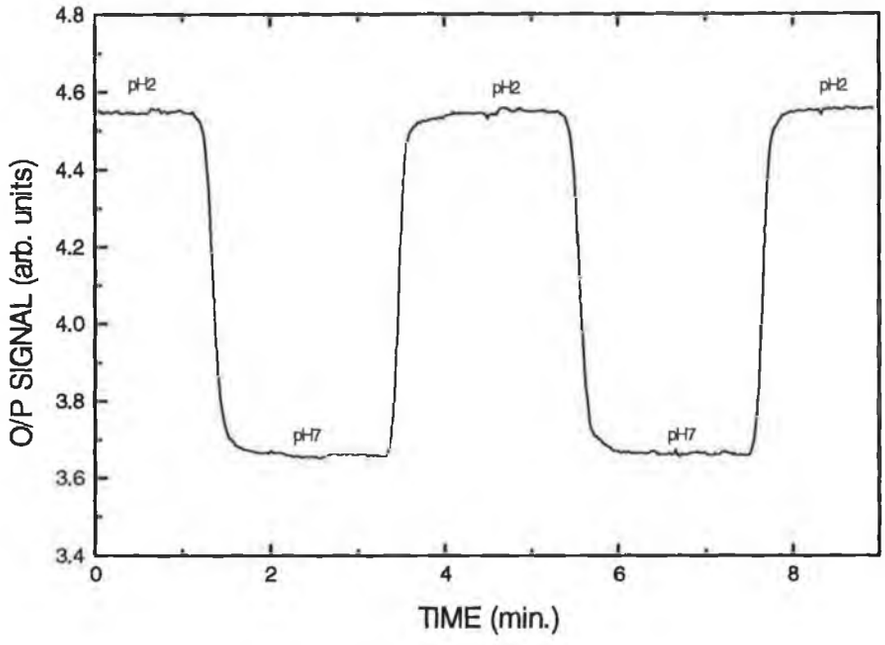

Figure 6.9 Time response of LED based pH sensor

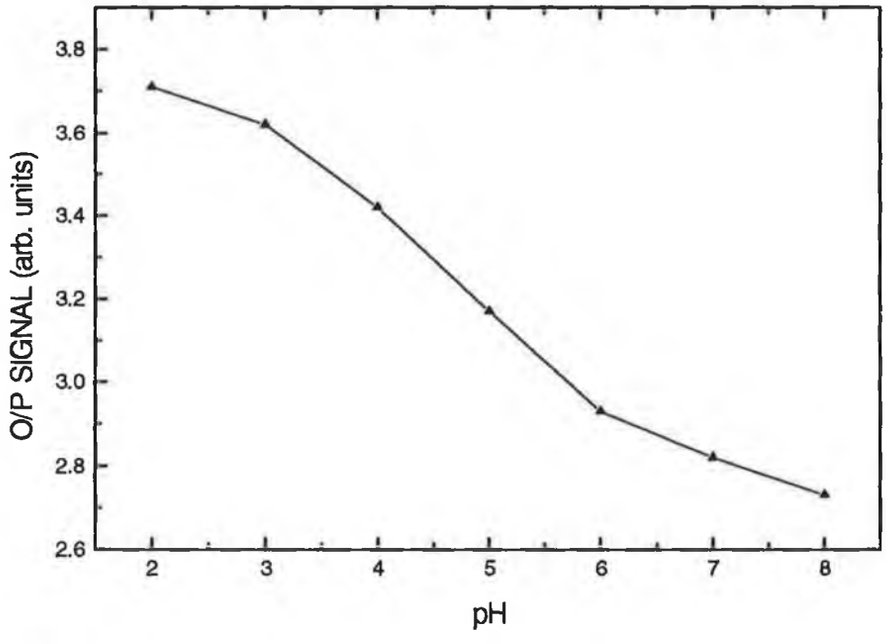

Figure 6.10 Response curve of single-LED system for BPB

In a dual-LED based system, the logarithm of the ratio of the reference to measurement signals of the LEDs was monitored over time. This is illustrated in figure 6.11, which shows the response of a BPB film for pH2 and pH8 buffer solutions. The data shows good repeatability. The software used to control the detection electronics (Appendix B) required greater signal averaging than in the single-LED case. This was due to difficulties in launching the two LEDs into the same fibre. While good coupling was achieved for the signal LED, the reference LED (behind the signal LED on the same axis) was more difficult to couple. The measured signals from the two LEDs were adjusted (by varying the applied voltage) so that for a coated fibre in a low pH solution these signals were about equal and therefore the logarithm of the ratio of the signals about zero. Furthermore, the sensitivity, i.e. the signal change for a step change in pH, was also lower in the LED-based systems due to difficulties in launching higher order modes in the fibre and the fact that no mask was used. This was due to difficulty in collimating the output of the LEDs for launch into the fibre.

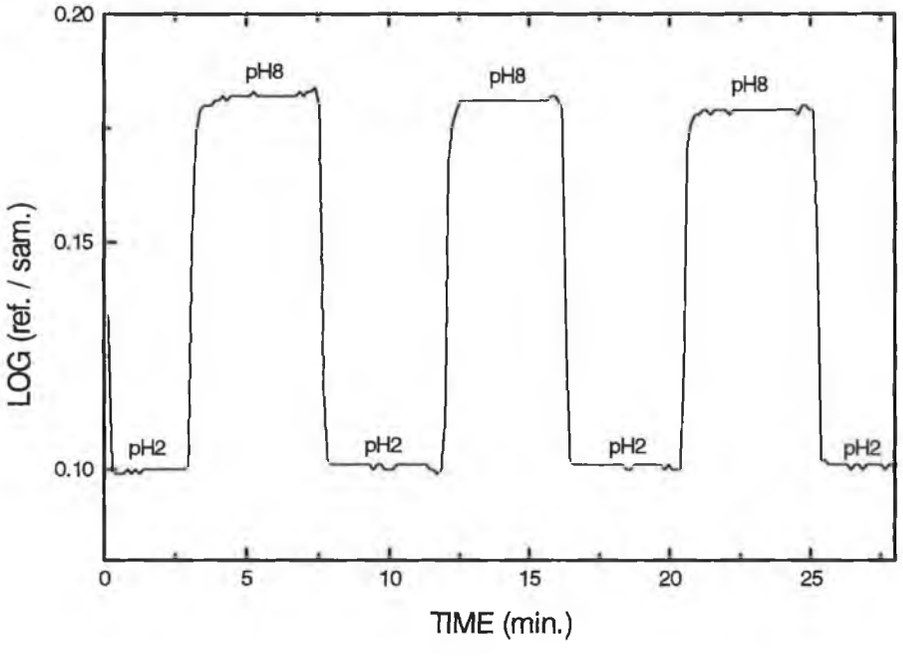

Figure 6.11 Time response of dual-LED based pH sensor

A dual LED-based system is an attractive approach for the development of a sensor since any fluctuations in power supply and aging of the detector are equally

applicable to both signal and reference wavelengths and therefore can be eliminated from the measurements. Furthermore, the use of modulated sources discriminates against ambient light. However, other methods are required, to that described above, to repeatably launch the light from the two LEDs into the one fibre.

6.6 Dye leachability study

6.6.1 Introduction

Doped sol-gel matrices which act as sensors in aqueous and other solvent environments, should be resistant to leaching of the dopant, especially for applications which require continuous monitoring. However, because the physical dimensions of the dopant molecules may in some cases be comparable to the pore diameter of the sol-gel glass and since the dopant is not in general covalently bound, some fraction of the dopant may be leached into solution. Careful tailoring of the sol-gel process is required to prevent or minimise this leaching. A number of reports on the leaching of reagents from sol-gel monoliths [30] and thin films [17,31,32,33] has highlighted these issues.

Kraus et al. [31] reported that an increase in the prepolymerisation or aging time of the starting sol resulted in an enhanced entrapment of indicator molecules and less leaching. These authors also noted that increasing the time and temperature of the drying step resulted in less leaching. Pre-conditioning of samples, to remove leachable indicator, was carried out by Yang and Saavedra [17]. In the work reported by these authors BCP was immobilised in methytriethoxysilane (MTES)-based sol-gel films that were dried at room temperature. Prior to use as sensors, samples were soaked in buffer solutions for 3 days and approximately 50 % of the indicator was estimated to have leached out [17]. The leaching rate was initially rapid but declined to a negligible rate after about 80 minutes and thereafter the samples were reported to be stable.

Two publications [30,33], in particular, highlighted how careful tailoring of the initial processing parameters in the sol-gel process, resulted in leach-free matrices. Aharonson et al. [30] outlined two solutions to the leaching problem, in the case of tetramethyorthosilicate (TMOS)-based xerogels. In the first case, TMOS polymerisation at high acidity and low water content prevented leaching of reagents (pyrene and pyranine in this case). No leaching was reported for sol-gel glass prepared

at pH1 and an R-value (TMOS : water ratio) of 2 or 4. However, for R = 2 at pH4 about 2/3 of the reagent was leached out. In an effort to determine why leaching occurred in one case and not the other, the authors [30] used gas adsorption measurements to estimate the surface area and pore size of the different xerogel samples. They concluded that the main feature which changed was the pore-entrance diameter.

A more complicated and less general approach is the synthesis of a sol-gel precursor to which the analyte-sensitive reagent is covalently bound. Sol-gel materials formed from such precursors will not exhibit leaching problems. Aharonson et al. [30] have demonstrated this technique successfully in the case of a trimethoxysilane derivative of methyl red which was used to prepare a material for pH sensing. In this example, one of the methoxy (MeO) groups of TMOS was replaced with the dopant (methyl red) molecule to form a new precursor $(MeO)_3Si$-D, where D is the dopant. This process is less general than sol-gel doping because it requires synthesis of the organic precursor and may alter the sensing features of the dopant. The pK and absorption spectrum of the derivative of methyl red was reported to be quite different than those of methyl red itself [30].

Severin-Vantilt and Oomen [33] investigated silica films prepared using TEOS and heavily doped with rhodamine B (RB). They deduced that the most important parameters that determine the entrapment of RB in silica sol-gel films are the concentration ratio of dye and silica, the concentration ratio (R-value) of water and silica and the acid concentration. For proper entrapment at least an R-value of 4 is required, the acid concentration should be in the order of 1N HCl (pH1) in the water fraction and at minimum 20 silica molecules are required per molecule of RB (i.e. dye concentration not too high) [33].

The sections below outlines a leaching study concerned primarily with BPB entrapped in TEOS-based sol-gel films. The issues investigated include the effect on the rate of leaching of the R-value of the sol, the pH of the leachant solution and the choice of the precursor (TEOS or MTES). The study was carried out on doped sol-gel films on optical fibres as for the pH sensing work described in section 6.3 above. The

absorbance of the alkaline form of BPB (i.e. A_{peak} - A_{ref}) was monitored over time using the time series display function of the Ocean Optics spectrometer [23]. The leachant buffer solution was continuously circulated around the coated fibre for the entire duration of the leaching study. For the purpose of comparing samples prepared using different processing parameters, the absorbance values were normalised i.e. highest absorbance value to 1 and all others scaled with respect to this value. This was performed due to different absolute absorbances resulting from films of different thickness.

6.6.2 Stabilised versus unstabilised films

The first effect investigated was the influence of the age of the film after preparation on leaching. This is illustrated in figure 6.12 which plots the absorbance over time of a BPB doped R = 4 TEOS film prepared using pH1 water, i.e. a pH1 TEOS (R=4) / BPB film. A pH8 buffer solution was used as leachant. An unstabilised film refers to a film about one day old, i.e. one day after oven drying, while the stabilised case refers to films approximately 3 months old. One day old films are unstabilised in that their thickness values are decreasing with time (see figure 5.6). After 3 months all the films investigated in this work, i.e. R = 2,4 and 6, were found to be stable in thickness. It is noted that all samples were stored in ambient conditions after oven drying. The initial pH3 to pH8 step in figure 6.12 was used to assess the quality of the films prior to a detailed leaching study.

It is clear from figure 6.12 that the rate of leaching is slower from stabilised films. Within about 8 hours in the unstabilised films all accessible dye had leached out, while in the stabilised case it took approximately 25 hours for all dye to leach out. At the end of the scans, neither film responded to a change in the pH of the solution surrounding the fibre. The baseline absorbance at the end of the scans was due to experimental conditions where by a small section of the coated fibre was not in contact with the leachant solution. In figure 5.6 the temporal evolution of film thickness for R = 2 and R = 4 films was plotted. This temporal evolution was attributed to continuing hydrolysis of the films after drying, facilitated by exposure to moisture in the atmosphere. The results of figure 6.12 would suggest that, as expected, the pore

features, e.g. pore entrance diameter, also changes with evolving structure over time. This result is shown here for R = 4 films, but was observed in R = 2 and 6 films as well. An implication of this for sensor use is that films cannot be used in aqueous environments directly after preparation as leaching is more pronounced for these films.

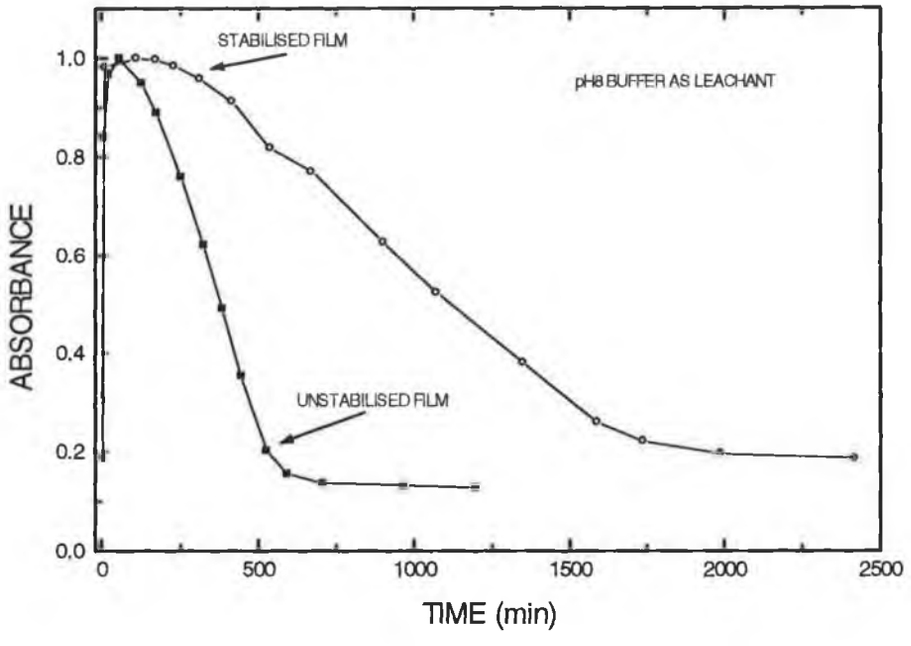

Figure 6.12 Leaching behaviour of stabilised and unstabilised films

6.6.3 Effect of R-value of sol on leaching

Figures 6.13 and 6.14 shows the effect of R-value of the starting sol on leaching for both pH8 and pH6 buffer solutions. This data is for stabilised films prepared using pH1 TEOS (R=x) sols, where x = 2,4 or 6. These illustrate both the effect of the R-value and the effect of the pH of the leachant solution on the rate of leaching. This latter effect is described in section 6.6.4.

From figures 6.13 and 6.14 it is clear that R = 2 films showed the fastest rate of leaching and that leaching decreases with increasing R-value, i.e. rate of leaching decreased in the R-value order 6<4<2. Severin-Vantilt and Oomen [33] reported that sols that are not well hydrolysed (i.e. water content too low with respect to TEOS), resulted in films in which rhodamine B showed increased leaching. They described this effect in terms of the extent of crosslinking in the sol-gel material. At low pH and low

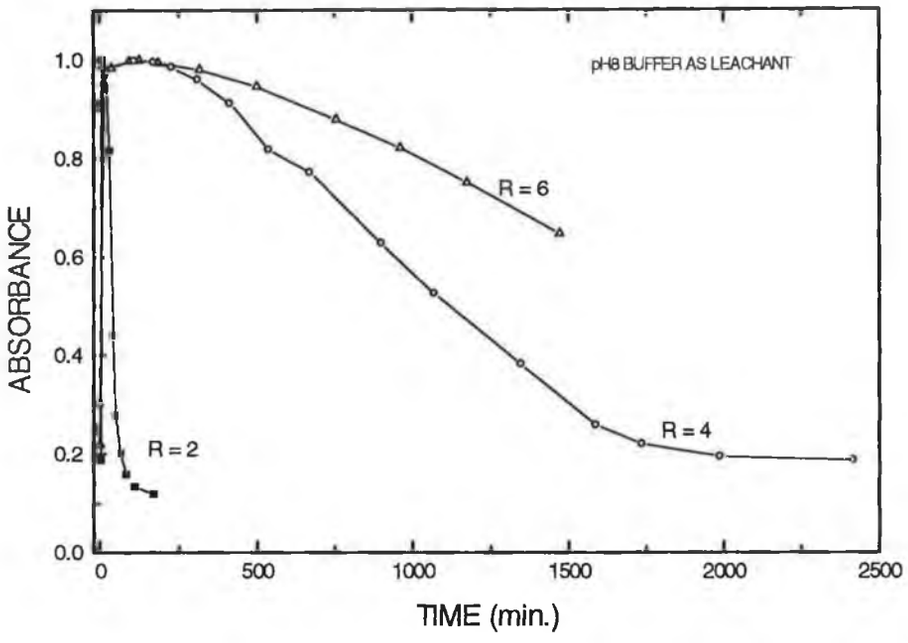

Figure 6.13 Effect of R-value on leaching (pH8 buffer as leachant)

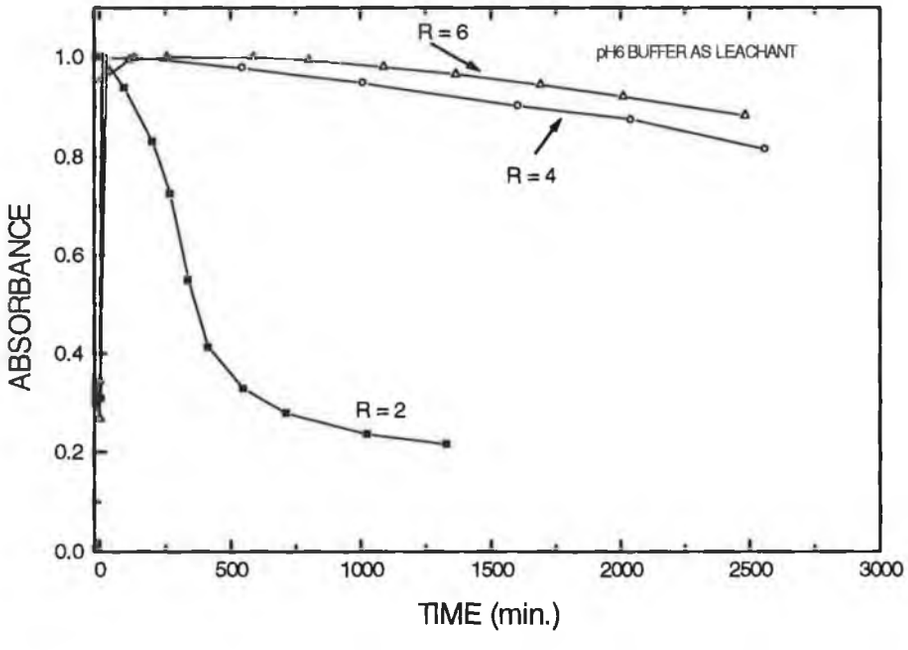

Figure 6.14 Effect of R-value on leaching (pH6 buffer as leachant)

water content a linear chain formation in the sol will occur, but with little crosslinking between chains. Therefore dye molecules are not well incorporated in the sol-gel. At higher water contents, increased hydrolysis results in increased crosslinking and better entrapment. Severin-Vantilt and Oomen [33] deduced that at least a R = 4 value was required for effective entrapment of rhodamine B.

6.6.4 Effect of pH of leachant

It is clear from figures 6.13 and 6.14 that the pH of the leachant solution has a major effect on the rate of leaching of BPB. The rate is much faster in the higher pH buffer case. This is considered to be related to the solubility dependence of BPB on pH. The solubility of BPB should increase at higher pH due to its structure [34] and if the pore size in the sol-gel material is similar to the size of the BPB molecules, then increased leaching may occur. A similar effect was reported by Lacan et al. [32] for fluorescein. In their case, fluorescein was only leachable from a sol-gel film when immersed in a basic pH (i.e. pH9) solution and this was explained in terms of the structure and solubility of the dye. At pH9, fluorescein is a dianion, which is very soluble in water, whereas at acid pH (pH3) it is a neutral molecule which precipitates in water.

These leaching effects described above, would limit the long-term use of the pH sensors described in sections 6.3 and 6.4. An advantage cited for these sensors was their extended range. However, this broadening was towards the high pH range, especially in the BCP and BTB cases, and therefore the advantage of an extended range could be offset by increased leaching. Leaching is considered to be the issue that most affects the usefulness of doped sol-gel films for pH sensing applications. It is noted that after the leaching study using pH6 buffer as leachant (figure 6.14), the R = 4 and 6 films still responded to changes in pH, while R = 2 films did not. Therefore, R = 4 and 6 films could be candidates for continuous use sensors, if periodic calibration was carried out and if the sensors were used only in moderate pH environments. However, their operational pH range would be seriously diminished.

6.6.5 Effect of pH of sol

A limited study based on the work of Severin-Vantilt and Oomen [33] on the effect of the pH of the sol, i.e. the pH of the added water, on leaching is shown in figure 6.15. This plot shows data for sols prepared at pH1 and pH0.5, using both pH8 and pH6 buffers as leachant. Again the slower rate of leaching was observed when using the pH6 buffer. Comparison of the pH1 and pH0.5 data, shows that there is a slightly greater rate of leaching in the pH0.5 case. In the paper by Severin-Vantilt and Oomen [33], increased leaching was observed for sols prepared at pH0.1 compared with those prepared at pH1. This was considered to be due to the large degree of condensation of the silica particles at these high acidic values. In figure 3.4 [35], a plot of condensation rate as a function of pH, it is clear that the condensation rate increases for pH<1. This increased condensation rate could result in a more porous structure in a similar fashion to that of base catalysed sols [36]. Sol-gel materials were not prepared at higher pH (e.g. pH 3,4) due to the well documented high porosity of these materials [29].

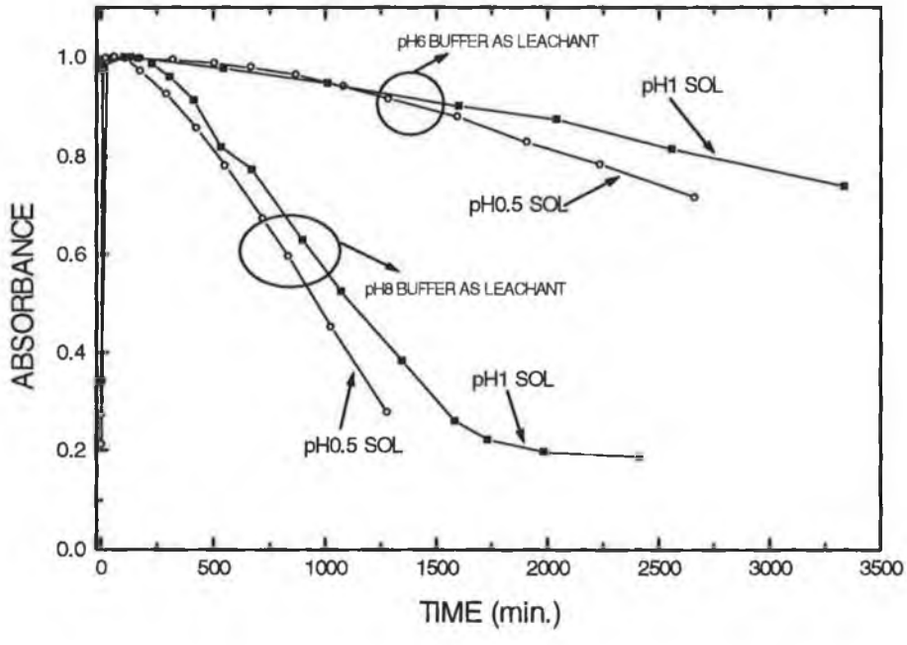

Figure 6.15 Effect of pH of sol on leaching

6.6.6 TEOS versus MTES films

The difference in leaching between standard TEOS and ormosil sol-gel films is shown in figure 6.16 for pH1 TEOS (R=4) and pH1 MTES (R=4) films. pH8 buffer was used as leachant. The rate of leaching was much slower in the MTES case. This could be due to a pore size effect or due to the hydrophobic nature of the ormosil (MTES) film as compared with the hydrophilic TEOS case. Innocenzi et al. [37] showed that a higher content of MTES (in a MTES / TEOS mixture) reduced the porosity of films. It is expected, therefore, that the decreased leaching observed from MTES films is caused at least partly by the smaller pore entrance or steric hindrance effects of the large CH_3 groups on the surface of the pore.

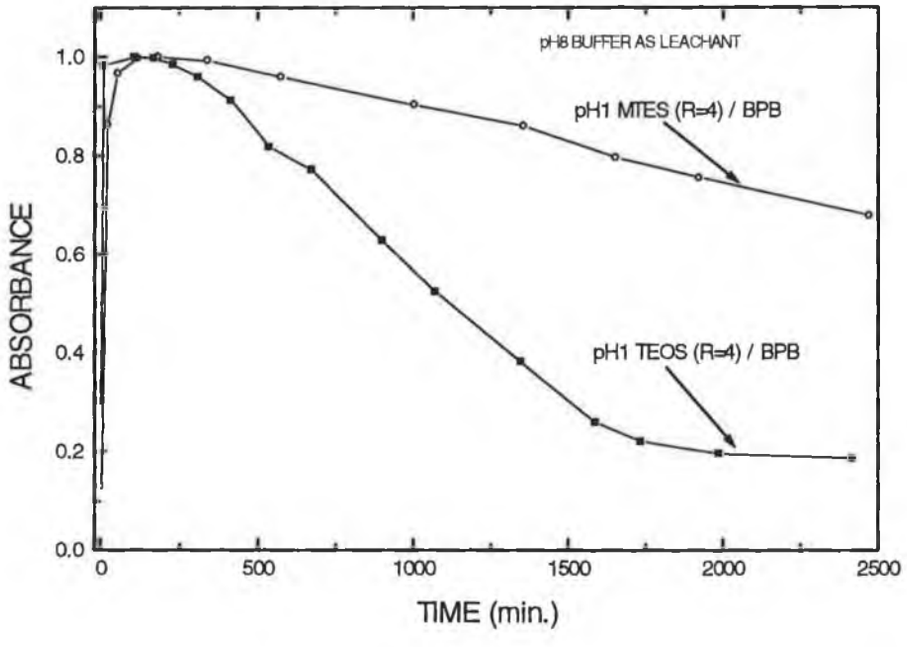

Figure 6.16 TEOS versus MTES films

Furthermore, while the MTES films show slower leaching, their response to changes in pH is very slow. In section 6.3 the response time of BPB in a TEOS film, to a step change in pH (pH 3-6) was about 40 seconds and 20 seconds for the reverse step. In the MTES case the corresponding response times are about 25 and 10 minutes, respectively. Therefore, these MTES films are not suitable for sensing pH due to their slow response. Lacan et al. [32] reported similar observations for the pH response of

fluorescein in TEOS-based films and in ormosil films. The ormosil films showed little evidence of leaching, but the response time to pH was very slow. They considered the difference in response to be related to the physical properties of the material. The ormosil material was dense and hydrophobic, while the TEOS-based films were porous and more hydrophilic.

6.6.7 Effect of molecular size of dye

In the leaching discussion above BPB was used as dopant. If the pore size of the sol-gel material is comparable to that of BPB, then the dye is leached out. Tailoring of the process, as described above, reduced the rate of leaching, but over time some leaching took place in all cases. This would suggest that there is a limit on the effectiveness of tailoring for a given dye species and, furthermore, that a larger dopant molecule should be less susceptible to leaching in the same sol-gel material. This was investigated here for 3 dye reagents, of different molecular size, used for aqueous sensing applications. Table 6.2 details the molecular sizes of the different reagents used. BPB, used for pH sensing as described above, has a molecular size of about 11 angstroms (A). Xylenol orange (XO) is a dye used for the detection of lead (Pb^{2+}) in solution [17]. Chapter 8 details sensing for Pb^{2+} with XO. XO has a molecular size of (15*10) A, i.e. it has a rectangular type structure. The final reagent investigated was a ruthenium complex, Ru[tris(4,7-diphenyl-1,10-phenanthroline)], and is used for gaseous [38] and dissolved oxygen [39] sensing. The molecular size of the reagents was estimated from their structure [34].

Dye	Molecular Size (A)
BPB	11
XO	15 * 10
Ruthenium complex	25

Table 6.2 Molecular size of dopants

Figure 6.17 shows the change in absorbance with time for the 3 reagents in pH1 TEOS (R=4) films, while figure 6.18 shows the region of greatest change expanded. BPB was monitored at λ = 590 nm and a pH6 buffer solution was used as leachant. XO was monitored at λ = 450 nm, the wavelength of peak absorbance in a pH 4.5 buffer solution, which was used as leachant since Pb^{2+} sensing is carried out at this pH. The peak absorption of the ruthenium complex occurs at approximately λ = 450 nm [39], and this was the measurement wavelength used in this case. De-ionised water was used as leachant for this molecule.

Comparing the 3 sets of data in figures 6.17 and 6.18 indicates a large change in absorbance due to leaching in the BPB case and only a small change in the XO and ruthenium complex cases. Moreover, in the XO case, and especially in the ruthenium complex case, most of the change in absorbance occurs over about the first few hours of the study. A slowly varying absorbance in the ruthenium complex case was observed from that time on. The change in absorbance for the XO and ruthenium cases in the initial part of the leaching study could be due to wash off of loosely bound reagent on the surface of the sol-gel film. Other studies [40] have shown little evidence of leaching of this ruthenium complex from TEOS-based sol-gel films. These data have important implications for sensing using sol-gel films. It could indicate that there is a minimum size reagent that will be effectively entrapped in these sol-gel films. After a short conditioning period, films doped with these reagents (XO and ruthenium complex) could give almost leach-free use. This can not be said of the BPB doped films which showed leaching in all films investigated, even where careful tailoring was carried out. Furthermore, an estimate of the relative pore entrance diameter of different sol-gel matrices could be determined from the leaching behaviour of different sized reagents. Harris and Knobbe [41] used the reverse approach to estimate the relative porosity of different sol-gel materials by measuring the extent of dye adsorption into the sol-gel matrix.

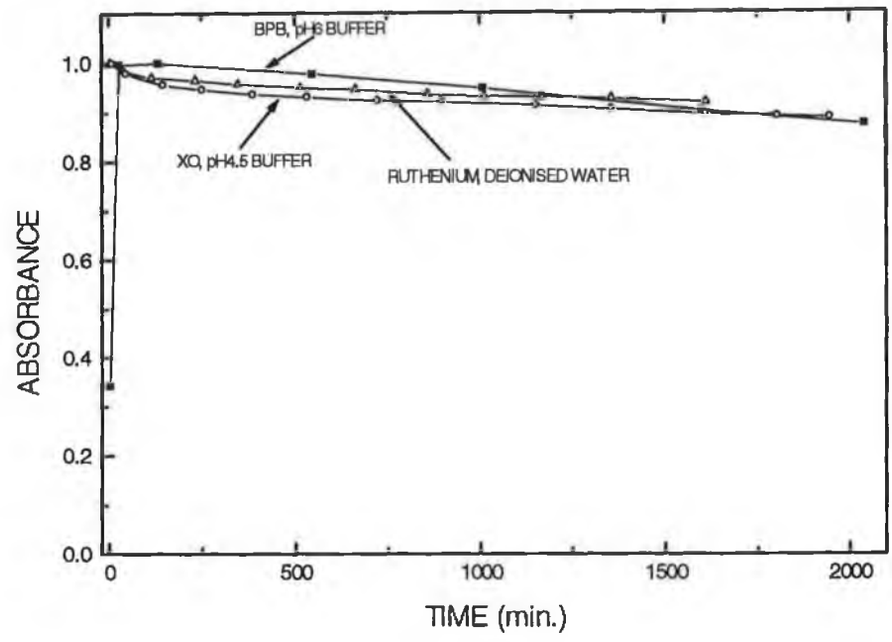

Figure 6.17 Effect of molecular size of dye on leaching

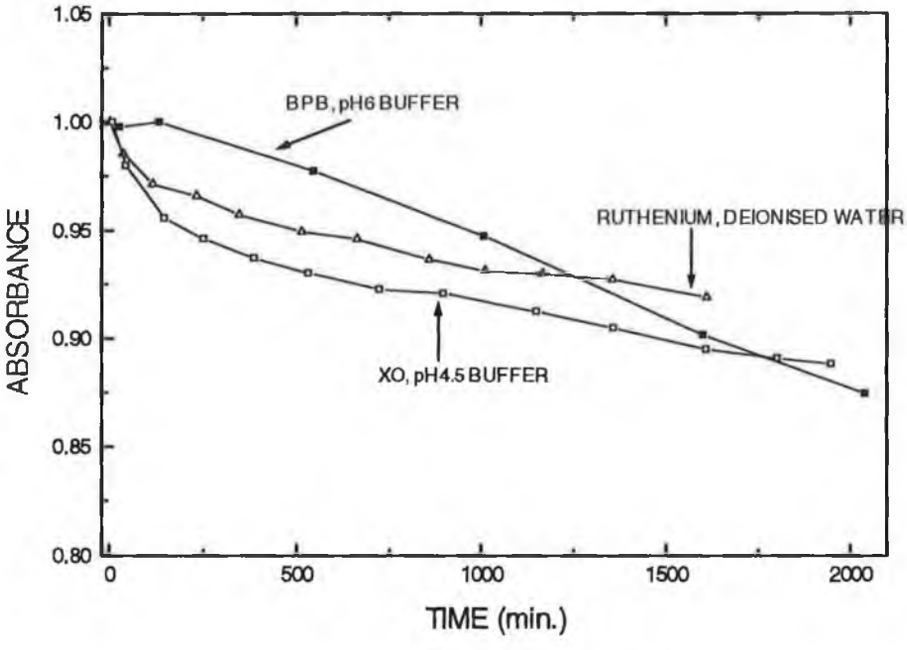

Figure 6.18 Expanded region of figure 6.17

6.7 Conclusion

This chapter outlined the results from optical fibre pH sensors using sol-gel immobilised pH indicators. The properties of the immobilised indicators differ from those in solution, with a shift in pK and a broadening of the pH range the most distinct features. This broadening can be used to extend the range of the sensor. In addition, the range can be extended by co-immobilisation of indicators. A detailed account of the issues affecting the leaching of indicators from sol-gel films was presented. In the BPB case, the most suitable films, from a leaching and response time point of view, for use as pH sensors should be prepared from pH1 TEOS films using an R-value of at least 4. The problem of leaching is the most important consideration in determining the suitability of sol-gel films for pH sensing. The size of standard pH indicators is too small for permanent entrapment in sol-gel films and is likely to restrict their use to short-term or disposable use. Alternatives to this include the search for non-standard pH indicators with large molecular sizes or the modification of the dye to form sol-gel precursors to which the dye is covalently bound. Sol-gel films doped with pH indicators may be more suitable for gaseous-phase measurements (acidic or basic gases).

References

1. M.J.P. Leiner and P. Hartmann, 'Theory and practice in optical pH sensing', Sensors and Actuators B, Vol. 11, 1993, pp. 281-289.

2. O.S. Wolfbeis, 'Fibre Optic Chemical Sensors and Biosensors', Vol. 1, Chapter 8, CRC Press, Boca Raton, Fl., 1991.

3. F. Baldini, S. Bracci and M. Bacci, 'A fibre-optic pH sensor using acid-base indicators covalently bound on control pore glass', Proc. SPIE Vol. 1587 Chemical, Biochemical and Environmental Fibre Sensors III, 1991, pp. 67-73.

4. S. Motellier, M.H. Michels, B. Dureavlt and P. Toulhoat, 'Fibre-optic pH sensor for in situ applications', Sensors and Actuators B, Vol. 11, 1993, pp. 467-473.

5. R.B. Thompson and J.R. Lakowicz, 'Fibre optic pH sensor based on phase fluorescence lifetimes', Anal. Chem., Vol. 65, No. 7, 1993, pp. 853-856.

6. O.S. Wolfbeis, N.V. Rodriguez and T. Weiner, 'LED-compatable fluorosensor for measurement of near-neutral pH values', Mikrochim. Acta., Vol. 108, 1992, pp. 133-141.

7. E. Bishop, 'Indicators', Pergamon Press, Oxford, 1972.

8. T.E. Edmonds, N.J. Flatters, C.F. Jones and J.N. Miller, 'Determination of pH with acid-base indicators: implications for optical fibre probes', Talanta, Vol. 35, No. 2, 1988, pp. 103-107.

9. J. Janata, 'Do optical sensors really measure pH', Anal. Chem., Vol. 59, No. 9, 1987, pp. 1351-1356.

10. J.I. Peterson, S.R. Goldstein, R.V. Fitzgerald and D.K. Buckhold, 'Fibre optic pH probe for physiological use', Anal. Chem., Vol. 52, No. 6, 1980, pp. 864-869.

11. G. Boisde, F. Blanc and X. Machuron-Mandard, 'pH measurements with dyes co-immobilised on optrodes: principles and associated instrumentation', Int. J. Optoelectronics, Vol. 6, No. 5, 1991, pp. 407-423.

12. T.M. Butler, B.D. MacCraith and C.M. McDonagh, 'Development of an extended range optical fibre pH sensor using evanescent wave absorption of sol-gel entrapped pH indicators', Proc SPIE Vol. 2508 Chemical, Biochemical and Environmental Fibre Sensors VIII, 1995, pp. 168-178.

13. A. Holobar, R. Benes, B.H. Weigl, P.O'Leary, P. Raspor and O.S. Wolfbeis, 'Fibre optic and non-fibre optic double-beam pH sensors for use in a flow-through cell', Anal. Methods and Instrumentation, Vol. 2, No. 2, 1995, pp. 92-100

14. J.Y. Ding, M.R. Shariari and G.H. Sigel Jun., 'Fibre optic pH sensors prepared by sol-gel immobilisation technique', Electronic Letters, Vol. 27, No. 17, 1991, pp. 1560-1562.

15. B.D. MacCraith, V. Ruddy, C. Potter, B.O'Kelly and J.F. McGilp, 'Optical waveguide sensor using evanescent wave excitation of fluorescent dye in sol-gel glass', Electronic Letters, Vol. 27, No. 4, 1991, pp. 1247-1248.

16. C. Rottman, M. Ottolenghi, R. Zusman, O. Lev, M. Smith, G. Gong, M.L. Kagan and D. Avnir, 'Doped sol-gel glasses as pH sensors', Material Letters, Vol. 13, 1992, pp. 293-298.

17. L. Yang and S.S. Saavedra, 'Chemical sensing using sol-gel derived planar

waveguides and indicator phases', Anal. Chem., Vol. 67, No. 8, 1995, pp. 1307-1314.

18. Reference 2, Chapter 7.

19. Z. Holzbecher, L. Divis, M. Kral, L. Sucha and F. Vlacil', Handbook of organic reagents in inorganic analysis', Ellis Horwood Limited, Sussex, 1976.

20. G. Boisde, B. Biatry, B. Magny, B. Dureault, F. Blanc and B. Sebille, 'Comparison between two dye-immobilisation techniques on optrodes for the pH-measurement by absorption and reflectance', Proc. SPIE Vol. 1172 Chemical, Biochemical and Environmental Sensors, 1989, pp. 239-250.

21. F. Baldini, S. Bracci and F. Cosi, 'An extended-range fibre-optic pH sensor', Sensors and Actuators A, Vol. 37-38, 1993, pp. 180-186.

22. D. Avnir, S. Braun, O. Lev, D. Levy and M. Ottolenghi, 'Organically doped sol-gel porous glasses: chemical sensors, enzymatic sensors, electrooptical materials, luminescent materials and photochromic materials', Chapter 23, Sol-gel Optics: Processing and Applications, L.C. Klein (editor), Kluwer Academic Publishers, 1994, pp. 539-582.

23. S1000 Fibre Optic Spectrometer: Users Manual, Ocean Optics Inc., Florida, Revision 4, 1994.

24. M.N. Taib and R. Narayanaswamy, 'Solid-state instruments for optical chemical sensors: a review', Analyst, Vol. 120, 1995, pp. 1617-1625.

25. S. Tucker, R. Robinson, C. Keane, M. Boff, M. Zenko, S. Batish and K.S. Street, Jr., 'Colorimetric determination of pH', J. Chemical Education, Vol. 66, No. 9, 1989, pp. 769-771.

26. D.W. King and D.R. Kester, 'Spectral modelling of sulfonephthalein indicators: application to pH measurements using multiple indicators', Applied Spectroscopy, Vol. 44, No. 4, 1990, pp. 722-727.

27. J.I. Peterson and E.J. Netto, 'Design considerations in making a broad-range fibre-optic pH sensor', Proc SPIE Vol. 1886 Fibre Optic Sensors in Medical Diagnostics, 1993, pp. 98-108.

28. E.J. Netto, J.I. Peterson and B. Wang, 'Fibre optic pH sensor for gastric measurements - preliminary results', Proc. SPIE 1886 Fibre Optic Sensors in Medical Diagnostics, 1993, pp. 109-117.

29. B. Dunn and J.I. Zink, 'Optical properties of sol-gel glasses doped with organic molecules', J. Mater. Chem., Vol. 1, No. 6, 1991, pp. 903-913.

30. N. Aharonson, M. Altstein, G. Avidan, D. Avnir, A. Bronshtein, A. Lewis, K. Liberman, M. Ottolenghi, Y. Polevaya, C. Rottman, J. Samual, S. Shalom, A. Strinkovski and A. Turniansky, 'Recent developments in organically doped sol-gel sensors: a microns-scale probe; successful trapping of purified polyclonal antibodies; solutions to the dopant-leaching problem', Mater. Res. Soc. Symp. Proc. Vol. 346 Better Ceramics Through Chemistry VI, 1994, pp. 519-530.

31. S.C. Kraus, R. Czolk, J. Reichert and H.J. Ache, 'Optimisation of the sol-gel process for the development of optochemical sensors', Sensors and Actuators B, Vol. 15-16, 1993, pp. 199-202.

32. P. Lacan, P. Le Gall, J. Rigola, C. Lurin, D. Wettling, C. Guizard and L. Cot, 'Sol-gel derived optical pH sensors', Proc. SPIE Vol. 1758 Sol-gel Optics II, 1992, pp. 464-475.

33. M.M.E. Severin-Vantilt and E.W.J.L. Oomen, 'The incorporation of rhodamine B in silica sol-gel layers', J. Non-Crystalline Solids, Vol. 159, 1993, pp. 38-48.

34. Personal communication with Dr. J.G. Vos, School of Chemical Sciences, Dublin City University.

35. B.K. Coltrain, S.M. Melpolder and J.M. Salva, 'Effect of hydrogen ion concentration on gelation of tetrafunctional silicate sol-gel systems', Ultrastructure Processing of Advanced Materials, D.R. Uhlmann and D.R. Ulrich (editors), J. Wiley and Sons Inc., 1992, pp. 69-76.

36. C.C. Harrison, 'Sol-gel chemistry principles and applications, Tutorial notes', Sira Communications Ltd., Kent, England, May 1993.

37. P. Innocenzi, M.O. Abdirashid and M. Guglielmi, 'Structure and properties of sol-gel coatings from methyltriethoxysilane and tetraethoxysilane', J. Non-Crystalline Solids, Vol. 3, 1994, pp. 47-55.

38. B.D. MacCraith, G.O'Keeffe, C. McDonagh and A.K. McEvoy, 'Led-based fibre optic oxygen sensor using sol-gel coatings', Electronic Letters, Vol. 30, No. 11, 1994, pp. 888-889.

39. A.K. McEvoy, C.M. McDonagh and B.D. MacCraith, 'Dissolved oxygen sensor based on fluorescence quenching of oxygen-sensitive ruthenium complexes immobilised in sol-gel-derived porous silica coatings', Analyst. Vol. 121, 1996, pp. 785-788.

40. Personal communication with A.K. McEvoy, School of Physical Sciences, Dublin City University.

41. T.M. Harris and E.T. Knobbe, 'Assessment of porosity in sol-gel silica thin films by dye adsorption', J. Materials Science Letters, Vol. 15, 1996, pp. 153-155.

42. R. Blue and G. Stewart, 'Fibre-optic evanescent wave pH sensing with dye doped sol-gel films', Int. J. Optoelectronics, Vol. 10, No. 3, 1995, pp. 211-222.

Chapter 7 Ammonia Gas Sensing

7.1 Introduction

Ammonia gas is corrosive, flammable (at high concentrations) and highly toxic. It has many industrial uses especially in the manufacture of fertilisers and plastics, and as a refrigerant gas. The current long-term occupational exposure standard is 25 ppm (maximum exposure in 8 hour period in 40 hour work week) [1]. In this chapter ammonia gas sensing using pH indicators or ammonia-specific reagents, immobilised in sol-gel silica and polymer coatings is detailed. In common with the optical fibre pH sensor described in the previous chapter, this sensor used the evanescent wave absorption configuration. In the next section ammonia gas sensing using pH indicator sulfonephthalein dyes is outlined. Particular attention is paid to the choice of indicator and sol-gel matrix. Furthermore, issues affecting the sensitivity and response time of the sensors are discussed. In section 7.3 ammonia sensing using an ammonia-specific compound, nitrophenylazophenol calix[4]arene, immobilised in a PVC polymer coating is detailed. Finally, in section 7.4, indicators whose absorption maximum occurs in the near-infrared region of the spectrum are described.

This work on ammonia sensing was performed as part of a European COPERNICUS project [2], whose aim was the construction of a distributed sensor for the rapid detection and location of ammonia leaks. Detailed spectroscopic study of short lengths of optical fibre, coated with a range of visible and near-infrared absorbing indicators was carried out as part of this project.

7.2 Ammonia sensing with pH indicators

7.2.1 Introduction

Optical sensors for ammonia in which colourimetric or fluorometric indicators are incorporated in polymer [5,6] or sol-gel [10,11] matrices have received significant research attention. In these systems, ammonia deprotonates the indicator to produce a change in absorbance or emission that is monitored using an optical fibre. An early version of this type of sensor, described by David et al. [3], used a ninhydrin coated

quartz rod, but the response was not reversible. Giuliani et al. [4] achieved reversibility by using a thin film of oxazine perchlorate as the indicator dye. Since then a wide range of indicators and polymer supports have been reported.

pH sensitive acid-base indicators are highly sensitive for ammonia determination. A group of pH indicators commonly used for ammonia sensing are the sulfonephthaleins [5,6,7,9]. These indicators exhibit high extinction coefficients of their base form, are generally stable at room temperature [8], and can be used for precise ammonia measurements at low concentrations. Exposure to ammonia increases the pH of the environment surrounding the indicator. This change in pH is measured as a change in the absorbance of the indicator and is related to the ammonia concentration in the sample. In common with the pH sensing described in the preceding chapter, the absorption band of the base form of the indicator was chosen for analytical measurements because its peak absorption is greater than that of the acid form, and hence provides a better sensitivity to ammonia concentration changes.

The sequence of reaction of ammonia with the dye molecules is a reversible deprotonation of the dye [4,11]. The reaction can be divided into three steps. The first step is the reaction of gaseous ammonia with water to form ammonium hydroxide

$$NH_3(g) + H_2O \leftrightarrow NH_4^+OH^- \qquad (7.1)$$

The second step is the deprotonation of the dye by ammonium hydroxide to give a modified form of the indicator dye and water

$$NH_4^+OH^- + H^+Dye^- \leftrightarrow NH_4^+Dye^- + H_2O \qquad (7.2)$$

The last step is back-reaction to the primary dye and ammonia

$$NH_4^+Dye^- \leftrightarrow H^+Dye^- + NH_3(g) \qquad (7.3)$$

From these equations the importance of water to the reactions is highlighted. This is covered again in section 7.2.5 when the effect of humidity on the ammonia sensor is discussed.

In the work described here, a range of sulfonephthalein indicators immobilised in sol-gel silica coatings on optical fibres was investigated for their sensitivity to ammonia gas. These indicators were bromophenol blue (BPB), bromocresol green (BCG), bromocresol purple (BCP) and bromothymol blue (BTB). The next section outlines the issues affecting the sensitivity of these indicators to ammonia. The optical fibre

spectrometer-based characterisation system, described in section 4.4.3 and used in Chapter 6, was also used in this work. A gas delivery system, shown in figure 4.5, used nitrogen gas as the carrier gas and 1% ammonia in nitrogen as the test gas. Using different mass flow controllers (Unit Instruments, Dublin) with a maximum flow rate of 5 litres/min. for nitrogen and 5 cm^3/min. for the ammonia test gas, a range of gas concentrations from 1% to 1 ppm ammonia in nitrogen was achievable. All other aspects of sample preparation and measurement were as described in previous chapters.

7.2.2 Choice of indicator

This section outlines the issues affecting the sensitivity to ammonia of the four indicators BPB, BCG, BCP and BTB. It is clear from the literature that the pK of the dye has a large effect on its sensitivity to ammonia [5,6,7]. This is related to the difference between the pK of the dye and the pK of the reaction of ammonia with water (equation 7.1) which is quoted as ~ 9.4 [12]. This was observed for sulfonephthalein indicators in polymer coatings by Brandenburg et al. [6] and Mills et al. [7], where dyes of high pK showed poor sensitivity and those of low pK higher sensitivity. Therefore for the four indicators above, whose pK values vary in the order BPB < BCG < BCP < BTB and are shown in table 7.1, the greatest sensitivity was expected for BPB and the lowest for BTB. However, as will be outlined below, the sol-gel immobilised indicators do not follow this expected behaviour.

Indicator	pK (solution) [8]	pK (sol-gel)
BPB	4.1	5.4
BCG	4.9	6.5
BCP	6.4	8.7
BTB	7.3	9.8

Table 7.1 pK of indicators in solution and sol-gel

Figures 7.1 and 7.2 show the absorption spectra of sol-gel immobilised BCP and BPB, respectively, for a range of ammonia concentrations between 0-500 ppm. A dye

concentration of about 2.1 mMol/Litre was used in each case. These plots illustrates an important difference between the two dyes. BCP has a small base peak in the absence of ammonia while BPB has a large one. The change in the absorbance of the base peak referenced against a wavelength where absorbance varied negligibly with ammonia, $A_{peak} - A_{ref}$, over the range 0-100 ppm ammonia, is shown for the four indicators in figure 7.3. As the pK of the dyes decrease, the absorbance of the base peak in the absence of ammonia increases. The lowest sensitivity was observed for BTB, whose pK in sol-gel at 9.8 (see table 7.1) is close to 9.4, the value of the dissociation constant for ammonia in water. For the other three indicators, the sensitivity (change in absorbance from 0 to 100 ppm ammonia) was very similar in the BCP and BCG cases and lower in the BPB case. BPB was expected to have the greatest sensitivity due to its lower pK value. However, as seen in figure 7.2 the absorbance change for BPB with ammonia sits on a large baseline absorbance. This is considered to have an effect in decreasing the sensitivity of BPB. Possible reasons for this large base absorbance peak in the absence of ammonia are outlined below. All four dyes showed greatest sensitivity to ammonia in the low concentration range.

The reason for the large base peak, in the absence of ammonia, in the case of BPB was investigated in detail. Figure 7.4 shows the absorption spectra in air of a fibre coated with BPB/sol-gel, just after oven drying and again after storage in ambient conditions for approximately 2 months. In the first case, a very small base peak was observed while in the latter, the base peak dominates. The increase in base peak was gradual, occurring over about a 2 month period. The exact reason for the base peak is unknown but was considered to be due to structural changes in the sol-gel material over time. The small base peak after oven drying could reflect the low pH of the sol-gel material after preparation (sol prepared using pH1 water). Over time the base form of the dye was deprotonated for samples stored in ambient conditions. For samples that were stored in a desiccator after preparation, a very small change in the base form of the dye was observed over time. This indicates that dry conditions inhibit the observed effect, while the moist ambient conditions facilitate it. In figure 5.6 it was shown that the thickness of sol-gel films decreased over time when stored in ambient conditions. Furthermore, samples stored in a desiccator showed little change in thickness over time.

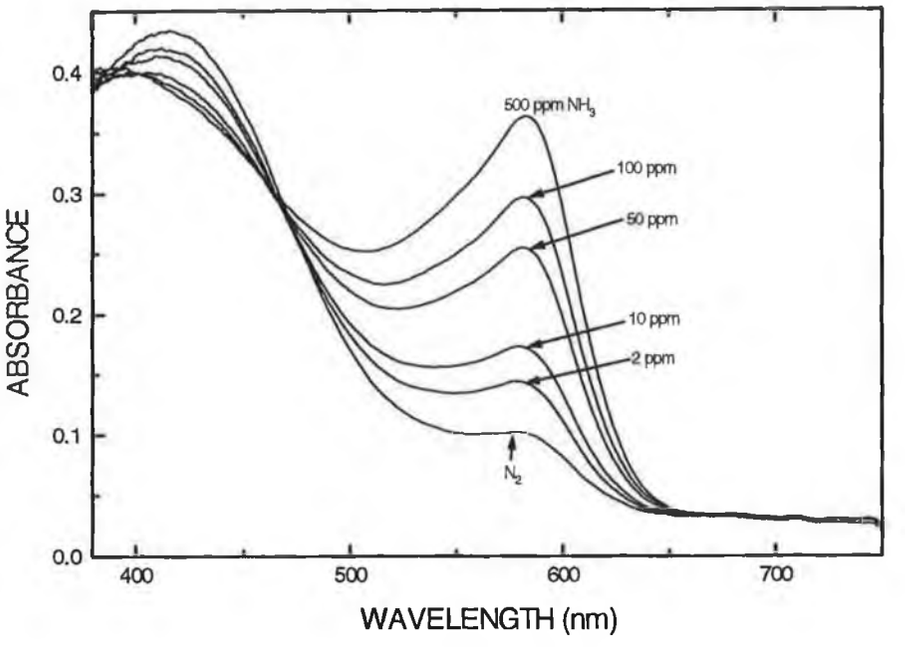

Figure 7.1 Absorption spectra of BCP for different NH_3 concentrations

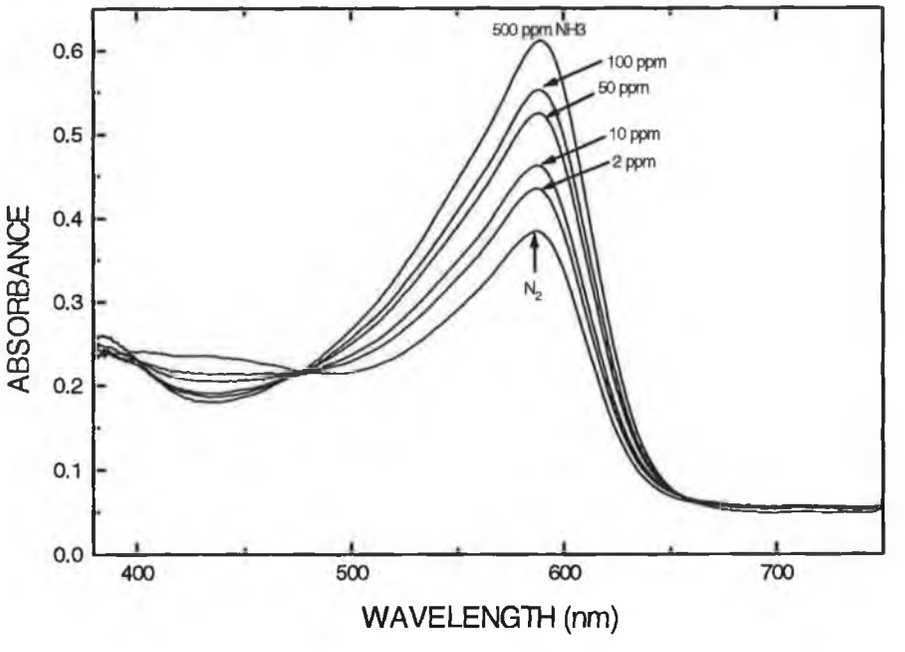

Figure 7.2 Absorption spectra of BPB for different NH_3 concentrations

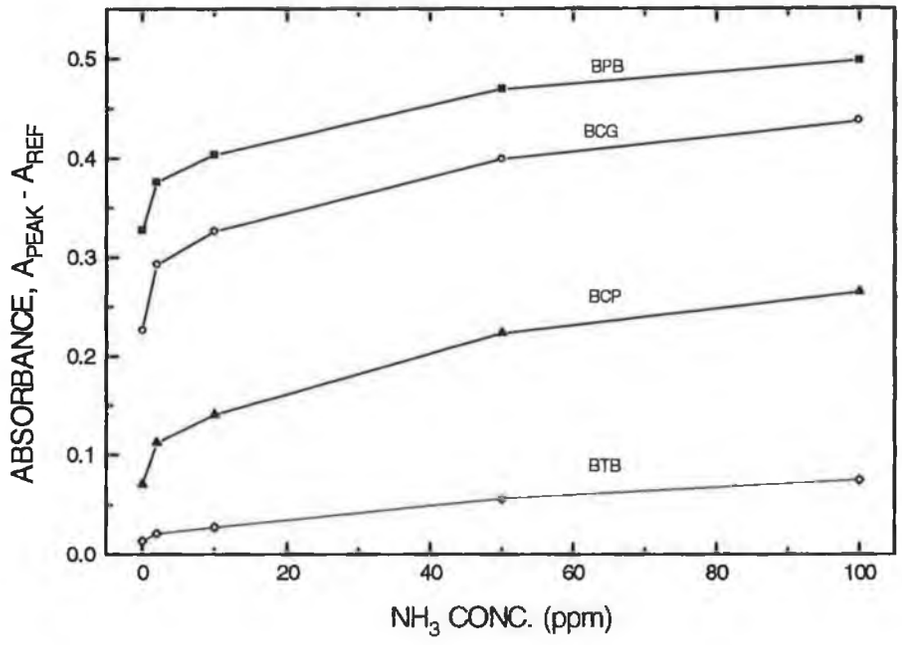

Figure 7.3 Response of the 4 indicators over the range 0-100 ppm NH_3

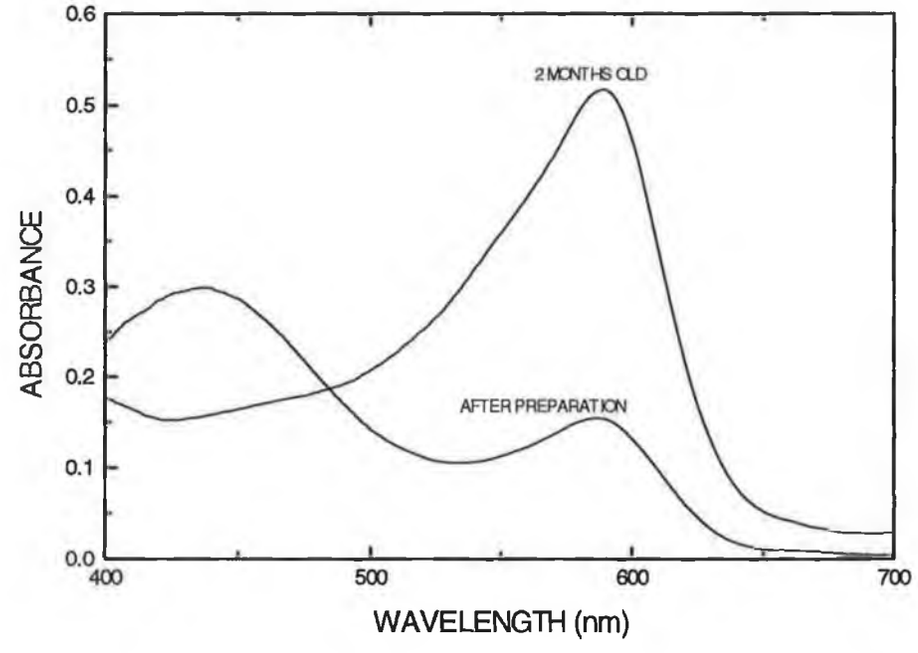

Figure 7.4 Absorption spectra of BPB / sol-gel in air

The structural changes (ambient conditions) could have resulted in an increase in the pH of the sol-gel environment around BPB and this would be reflected in a change in the absorption spectrum of BPB. Moreover, desiccator storage, in preventing structural changes, would prevent the deprotonation of the base form of the dye. The films used in figures 7.1 to 7.3 were all stored in ambient conditions for at least 2 months before measurements were taken. This effect was also investigated for the other three indicator dyes. It was observed that the absorbance of the base form of the dyes scaled with their pK, with low pK dyes (BPB and BCG) showing large base peaks, and high pK dyes (BCP and BTB) showing very small peaks. If the structural changes affected the pH in the sol-gel glass by a fixed amount in all the sol-gel films (independent of dye), then lower pK dyes would be expected to show the greatest change.

An estimate of the effective pH in the sol-gel glass, or the pH seen by the dye, can be obtained from comparing the absorbance of the base form of the dye to the response of the sol-gel film in different pH buffer solutions. For example, comparing the absorbance of the base form of BPB (after 2 months) in figure 7.4 to the response of BPB/sol-gel in different pH buffer solutions, figure 6.1, yielded an effective pH in the sol-gel glass of approximately pH 5-6. BCG yielded a similar result. Furthermore, an effective pH in the sol-gel glass of ~ pH5-6 would help to explain the pK dependence of the base peak in the absence of ammonia. In section 6.3 and table 6.1 it was observed that both BPB and BCG respond strongly to pH around pH6, while BCP and BTB respond only above pH6.

The choice of an indicator for ammonia sensing is strongly influenced by its pK. Dyes with pK too close to the dissociation constant of ammonia in water (9.4) will show lower sensitivity [6,7]. However, in the sol-gel case, indicators with very low pK values (e.g. BPB) may have lower sensitivity to ammonia due to the influence of the pH of the sol-gel glass. In the next few sections the influence of different parameters on the sensor response to ammonia of BCP as indicator are described. BCP was selected as indicator because of its good sensitivity to ammonia (see figure 7.3), its small base peak in the absence of ammonia and its compatibility with the sol-gel immobilisation process.

In general, the criteria for choosing a pH indicator for a particular sensing

application is influenced by the following considerations:

- Sensitivity to the analyte over the range of interest.
- Compatibility with the immobilisation process.
- Selectivity and stability of the indicator.
- Compatibility of the absorbance peak of the indicator with LEDs or laser diodes.

7.2.2 Choice of sol-gel matrix

A number of sol-gel matrices were investigated for immobilising BCP for use as an ammonia sensor. These consisted of TEOS-based and MTES-based sol-gel films and films prepared from a mixture of the two precursors. In all cases a R-value (water/alkoxide ratio) of 4 and water of pH1 was used in the sol preparation. Figure 7.5 shows the absorption spectra of a MTES/BCP film for different ammonia concentrations over the range 0-500 ppm. In figure 7.6 a comparison of the absorbance change, $A_{peak} - A_{ref}$, over the 0-500 ppm ammonia concentration range for the cases of TEOS, MTES, TEOS : MTES (1:1) and TEOS : MTES (1:3) is shown. In all cases a dye concentration of approximately 10.5 mMol/Litre was used. It is clearly seen from these plots that the greatest response was from TEOS-based sol-gel films, with MTES-based films showing very poor sensitivity.

The difference in response between the four cases in figure 7.6 is considered to be caused by the pore surface properties and water content of the films. In the case of TEOS films the surface is hydrophilic due to Si-OH groups. The methyl (CH_3) groups which are present on the surface of the MTES-based films make its surface more hydrophobic. The presence of these methyl groups was confirmed by using FTIR spectroscopy as shown in figure 5.14. Innocenzi et al. [13] observed that the water content of MTES : TEOS films decreased with increasing MTES content, for films dried above 300°C. However from figures 5.13 and 5.14 it was observed that both TEOS and MTES films have a molecular water band associated with them (see section 5.9), although the shape of the water bands was different in the FTIR spectra between the two cases, indicating some difference in properties between the two films. It is not clear

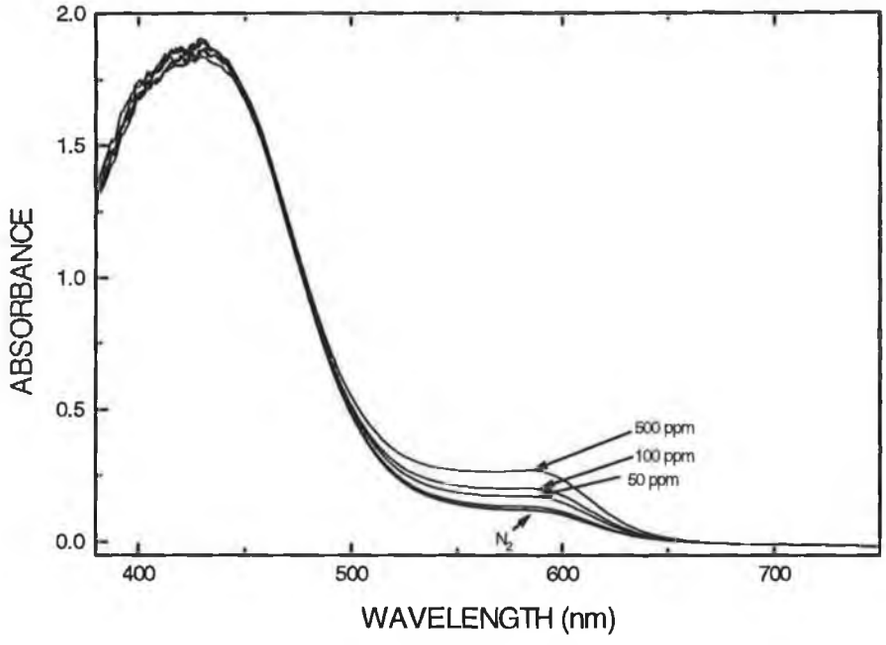

Figure 7.5 Absorption spectra of BCP/MTES in 0-500 ppm ammonia

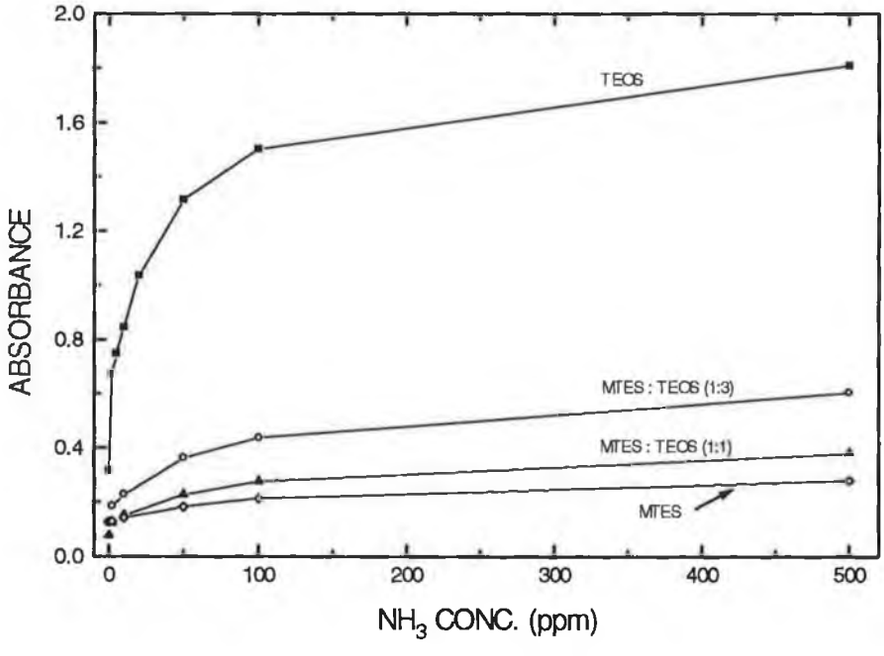

Figure 7.6 Response of BCP in different sol-gel films to ammonia

from these FTIR spectra that the MTES-based films are lower in water than the TEOS-based ones. However, there is evidence from other results (e.g. the uptake of water by the films, section 7.2.5) that this is the case. In equation 7.1 the significance of water to the detection of ammonia is observed. Therefore if there is less water in the MTES film case, the reaction with ammonia would be smaller. In terms of sensitivity TEOS films should be chosen over MTES films. Furthermore, in section 7.2.5 it will be shown that MTES-based films show greater sensitivity to changes in relative humidity than TEOS-based films.

7.2.4 Effect of dye concentration

One method to vary the sensitivity of the sensor is to vary the dye concentration. This effect was investigated for BCP in pH1 TEOS (R=4) sol-gel films in which the dye concentration was varied between about 0.5 to 10.5 mMol/Litre in the starting sol. Figure 7.7 shows the absorption spectra of BCP/sol-gel for different ammonia concentrations, when using the highest dye concentration investigated, i.e. 10.5 mMol/Litre. A comparison of the absorbance change over the 0-500 ppm ammonia range for different dye concentrations is shown in figure 7.8. It is clearly seen that sensitivity increases with increasing dye concentration and that very high sensitivity can be achieved by increasing the dye concentration. The increased absorbance with dye concentration is due primarily to the greater number of sites available for reaction with ammonium hydroxide (see equations 7.1 to 7.3). Assuming Beer's law, absorbance increases as concentration (dye) increases. The increased sensitivity is considered to be caused by a shift to the right of the equilibrium in equation 7.2 with increasing dye concentration.

A number of other observations can be drawn from the above plots. For the four dye concentrations shown in figure 7.8 the shape of the response curve was similar in all cases, with the greatest sensitivity in the 0-100 ppm ammonia concentration range. Smaller sensitivities were observed above this range. Although it was not possible to achieve ammonia concentrations below 2 ppm with the present gas-mixing setup without using large quantities of carrier gas, the large absorbance change for 2 ppm ammonia shown in figure 7.7 indicates that detection of ammonia at concentrations in the sub-ppm range is easily achievable.

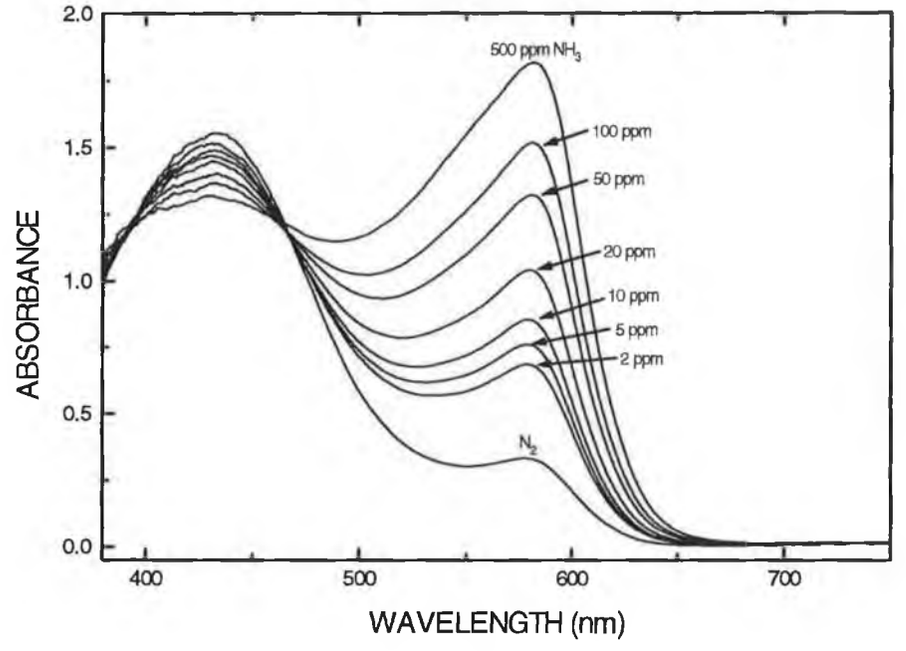

Figure 7.7 Absorption spectra of BCP/TEOS (10 mMol/Litre dye conc.)

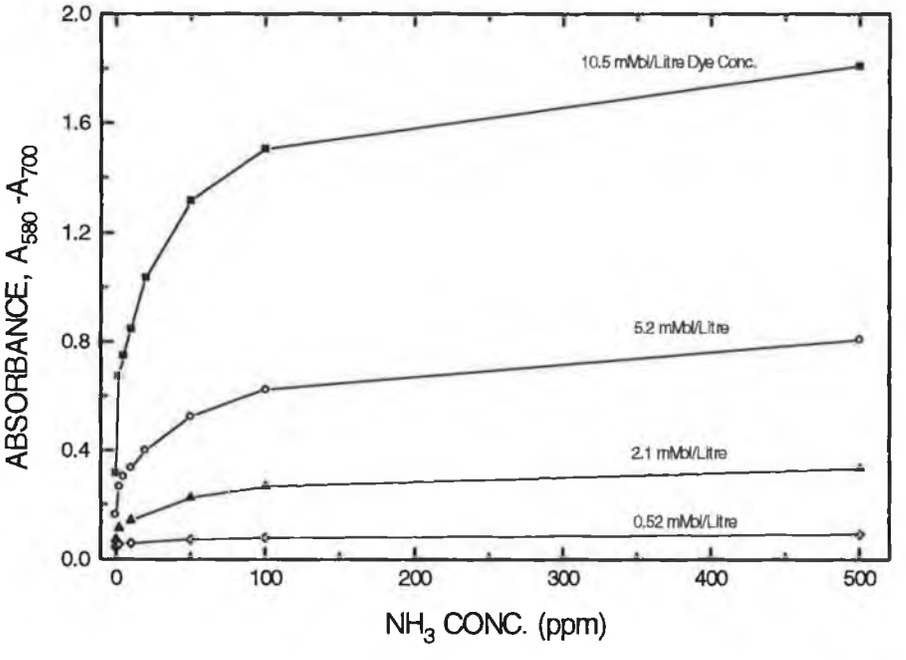

Figure 7.8 Response of BCP for different dye concentrations

7.2.5 Effect of humidity on ammonia sensitivity

All results in this chapter to date were made with dry gases, i.e. relative humidity (RH) about zero. However from equation 7.1 it is clear that humidity could potentially affect sensitivity since one of the primary reactions is that of ammonia with water and RH could affect the amount of water in the sol-gel films. The influence of humidity on ammonia sensitivity has been described in a number of publications [5,6] and can be a major disadvantage of ammonia sensing using pH indicators. In this section the influence of RH on TEOS and MTES-based sol-gel films is discussed.

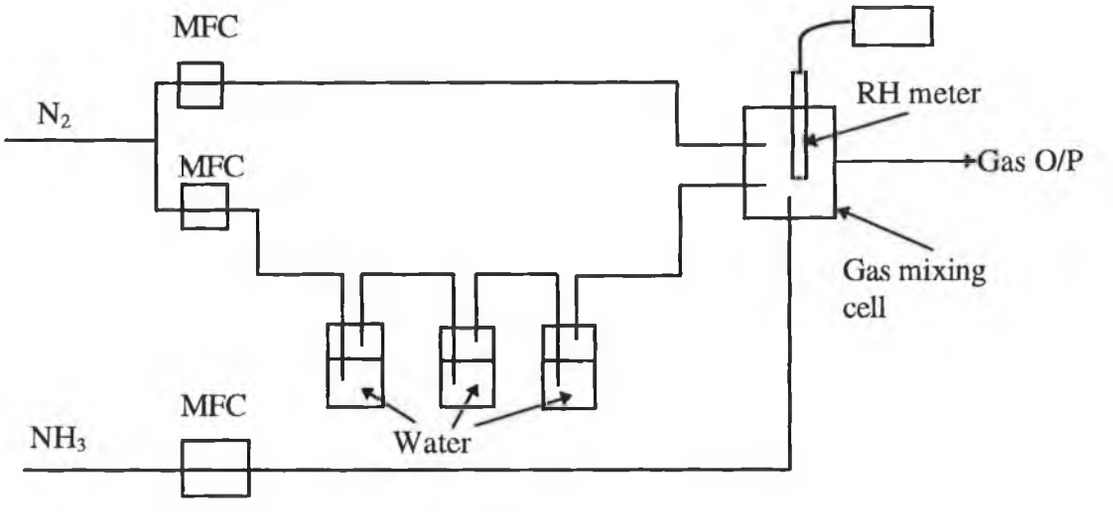

Figure 7.9 Setup for humidifying gases

Figure 7.9 illustrates the setup used to obtain test gases of different RH. This design is based on similar systems described in the literature [11,14]. A nitrogen gas stream was split into two streams, with each directed through a mass flow controller (MFC). One stream was humidified by passage though three gas-washing flasks containing de-ionised water, followed by an empty flask to ensure removal of suspended water droplets. The two nitrogen streams (one humid and one dry) were then passed through a gas mixing cell where they were combined with the ammonia gas stream. The gas mixing cell contained a RH meter (Eirelec Ltd., Dundalk, Ireland, model TH210). Depending on the flow ratio of the two nitrogen streams, it was possible to vary the humidity of the test gas.

Figures 7.10 and 7.11 shows the sensitivity of BCP in TEOS and MTES films, respectively, to 100 ppm ammonia for different RH values. The peak absorbance of the

films was referenced against a wavelength where absorbance changed little with ammonia. In these plots the doped sol-gel films were first exposed to nitrogen gas at 8% RH. Then 100 ppm ammonia gas (8% RH) was introduced into the gas cell containing the fibre. After the absorbance value in 100 ppm ammonia had stabilised, the RH of the gas was varied in steps up to 90% RH. The recovery of the films (100 ppm ammonia to nitrogen) is also included in these figures. The next section will deal in more detail with the issue of response time, while in this section only the change in absorbance due to RH will be considered. Figure 7.12 compares the effect of RH on different sol-gel films exposed to 100 ppm ammonia. The dye concentration in the TEOS case was 2.1 mMol/Litre, while in the MTES and MTES : TEOS (1:1) cases it was 10.5 mMol/Litre. This concentration difference accounts for the difference in the relative absorbance values. Over the range 8-90% RH the 100 ppm ammonia absorbance level changed by about 3% in the TEOS case and about 36% in the other two cases. Only a small difference in absorbance was observed going from 0 to 8% RH. In most typical environments where this sensor could be used, zero or low RH (< 10%) is considered to be uncommon.

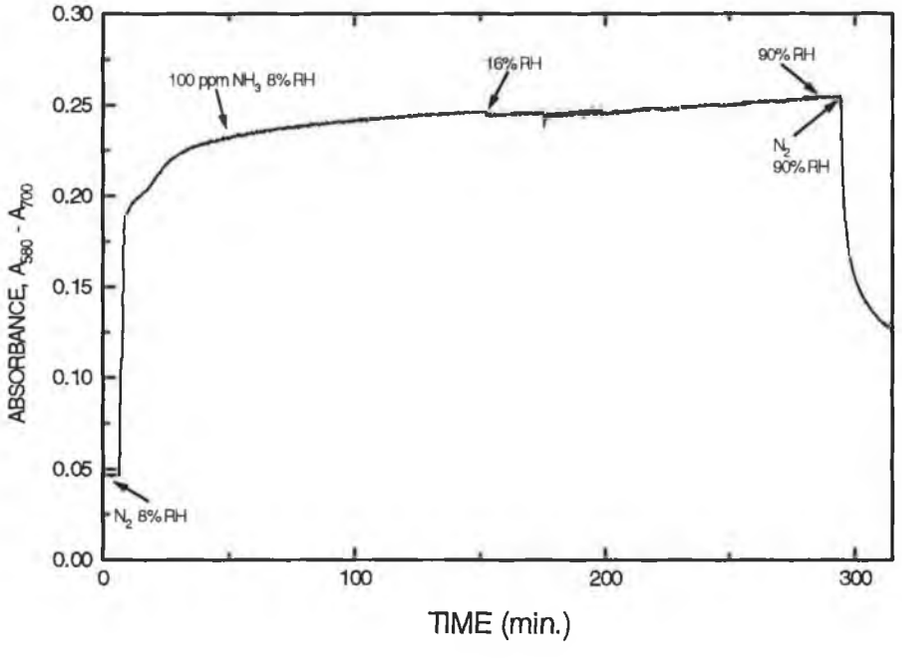

Figure 7.10 Effect of humidity on BCP / TEOS film

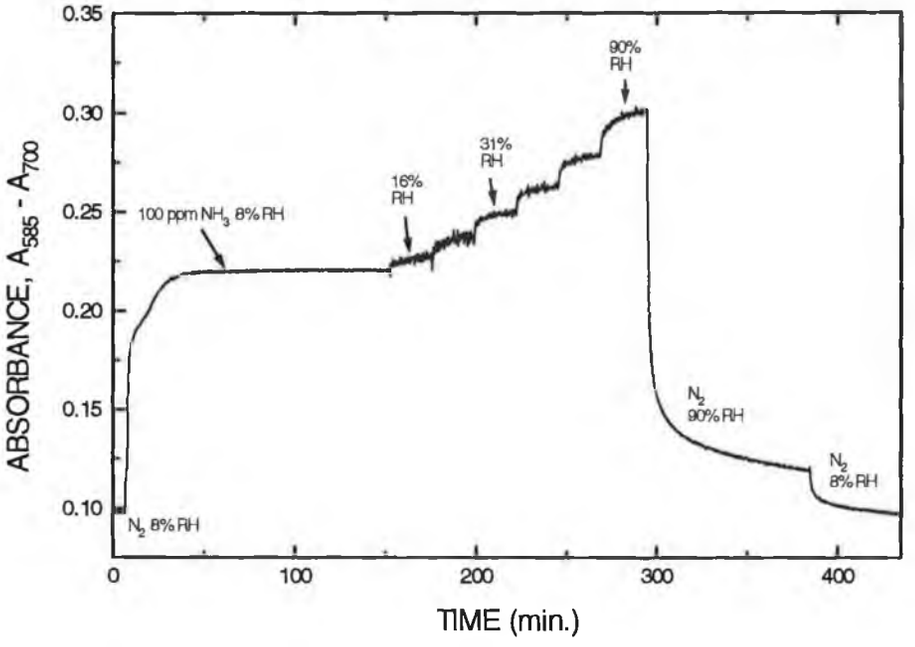

Figure 7.11 Effect of humidity on BCP / MTES film

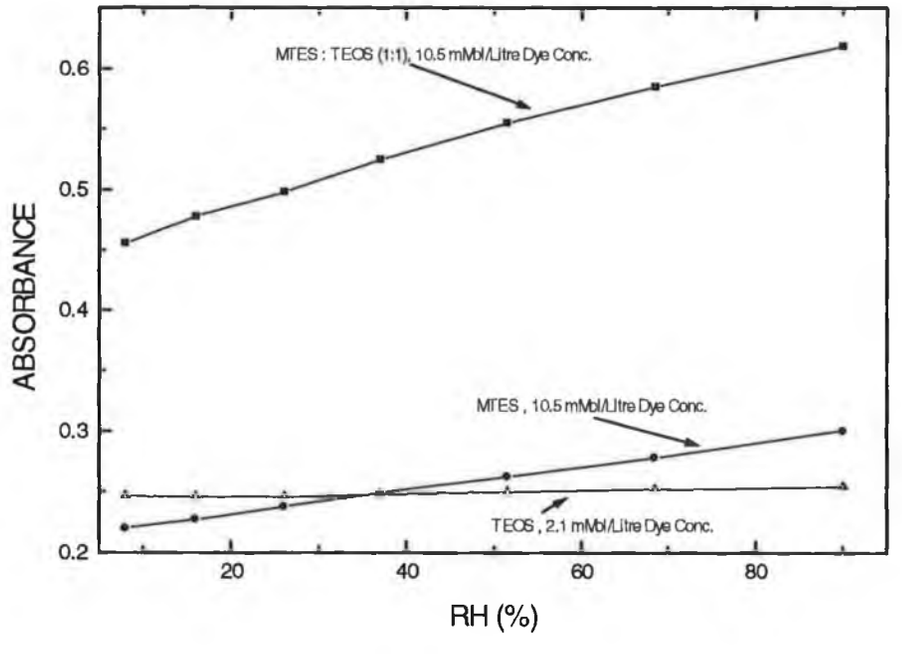

Figure 7.12 Effect of humidity on response of different sol-gel films to ammonia

The data in figures 7.10 to 7.12 illustrate a significant difference in behaviour between TEOS and MTES-based sol-gel films. According to equations 7.1 to 7.3, water is an essential part of the reaction of the dye with ammonia. However in the TEOS case, it is considered that there is sufficient water already in these films for the ammonia reaction to take place and therefore changes in RH have little effect. Klein and Voges [11] reported a similar behaviour for BCP in tetramethylorthosilicate (TMOS)-based sol-gel films. The large effect of RH in the MTES-based film case was considered to be due to an initial small amount of water in these films, which was insufficient for the reaction of ammonia with water. At high RH, however, the increased water content facilitates this reaction.

7.2.6 Response time of sensor

The response and recovery time of BCP to ammonia for different sol-gel films was monitored at the peak wavelength of absorbance using the time display function of the spectrometer. This is illustrated in figure 7.13 for a pH1 TEOS (R=4) film, where the dye concentration was 10.5 mMol/Litre. This plot shows the step response from nitrogen to 100 ppm ammonia and the recovery back to nitrogen. A number of features can be observed from this plot. The initial response to ammonia was fast and was followed by a 'shoulder' (marked * in figure 7.13) on the response curve. Likewise, the recovery from ammonia was also initially fast with a slow tailoff. The response time was much shorter than the recovery time (see also table 7.2). The exact reason for the feature (*) on the response curve is unknown but was observed in all the sol-gel films tested (see figures 7.10 and 7.11). The response behaviour of a film to ammonia can be complicated. Chernyak et al. [10] resolved the time response curve of oxazine-170 (immobilised in a polymethymethacrylate film) to ammonia into two portions, one (exponential) due to a diffusion-controlled reaction and the second (linear) due to reaction with the dye in a situation of a low diffusion rate of ammonia (after initial equalisation of ammonia concentrations inside the film and outside). The slow recovery from ammonia indicates the difficulty in removing ammonia from the water inside the sol-gel film. It could also indicate possible adsorption of ammonia onto the sol-gel pore surface.

Table 7.2 tabulates the response and recovery times of BCP in different sol-gel films and for different RH conditions. The response to and recovery from 100 ppm ammonia was monitored in all cases. $T_{50}(\uparrow)$ and $T_{90}(\uparrow)$ refers to the time for the absorbance to reach 50% and 90% respectively of its full change. $T_{50}(\downarrow)$ and $T_{90}(\downarrow)$ are defined in the same way. For dye concentrations between about 2 and 10.5 mMol/Litre in the starting sol, the response time as defined by $T_{90}(\uparrow)$ and the recovery time, $T_{90}(\downarrow)$, did not vary significantly. It is clear from this data that the overall response and recovery times are long and these films may not be suitable for use where rapid and accurate determination of ammonia is required. However the 50% response and recovery times, $T_{50}(\uparrow)$ and $T_{50}(\downarrow)$ respectively, are quite short. Therefore these films may be suitable for use in an alarm type sensor, where a rapid change in absorbance would indicate the presence of ammonia.

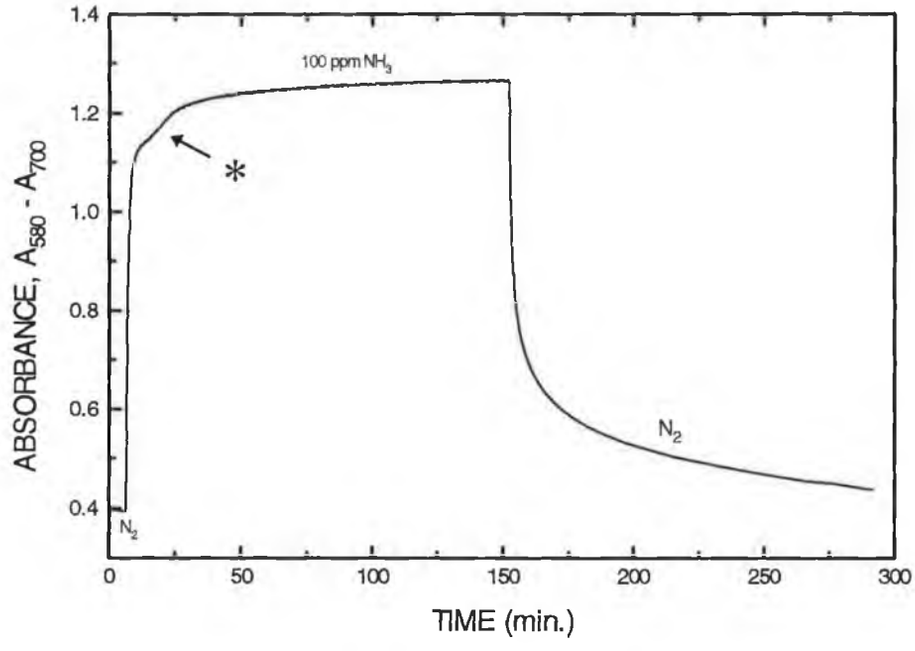

Figure 7.13 Time response of BCP / TEOS film to 100 ppm ammonia

Sol-gel	Dye Conc. (mMol/L)	RH (%)	$T_{50}(\uparrow)$ (min.)	$T_{90}(\uparrow)$ (min.)	$T_{50}(\downarrow)$ (min.)	$T_{90}(\downarrow)$ (min.)
TEOS	2.1	0	0.8	13	2	76
	5.2	0	0.8	14	2	72
	10.5	0	0.9	13.5	2.5	85
MTES: TEOS (1:1)	10.5	0	1.5	18	3	> 175*
	10.5	8	1.5	22		
MTES	10.5	8	1.7	17.5		
	10.5	70	1.6	25	1.5	36.5

(* absorbance has not reached 90% value after this time)

Table 7.2 Response of BCP to ammonia for different sol-gel films

The effect of precursor on response time is also shown in table 7.2. For a MTES : TEOS (1:1) film, the response time $T_{90}(\uparrow)$ is slightly longer than for a TEOS film, but the recovery time is much longer. This study was continued for different humidified gas mixtures. An increase in humidity has only a minor affect on the response time, while it has a large affect on the recovery time in the MTES film case.

Coating rate (mm/sec)	Thickness (nm)	$T_{50}(\uparrow)$ (min.)	$T_{90}(\uparrow)$ (min.)	$T_{50}(\downarrow)$ (min.)	$T_{90}(\downarrow)$ (min.)
0.51	315	0.9	8	1	55
0.971	425	0.8	13	2	76
1.66	555	0.9	11	1.5	72

Table 7.3 Effect of coating rate on response of BCP/ TEOS films

Another issue that can affect response time is the thickness of the sol-gel film due to its effect on diffusion rates. This is illustrated in table 7.3 for films coated at

three different coating rates. The thickness values are for undoped sol-gel films (see section 5.2). BCP-doped films should be thicker than the values quoted here. Films coated at the slowest rate responded and recovered faster than those at higher coating rates. Only a small difference in response and recovery times was observed between films coated at the 0.971 and 1.66 mm/sec coating rates. This data indicates a trend, but there are too few thickness values to make definite conclusions.

7.3 Ammonia sensing with calixarene compounds

7.3.1 Introduction

The pH indicator-based ammonia sensors described in section 7.2 will obviously suffer from cross-sensitivity to other acidic and basic gases. Reports in the literature [6,11] indicate some interference from carbon dioxide, sulphur dioxide and nitric oxide for sulfonephthalein indicator-based ammonia sensors. It is often desirable to have a more ammonia specific sensor. This was investigated using a calixarene compound, nitrophenylazophenol calix[4]arene, immobilised in a polymer coating. This compound was provided by the School of Chemical Sciences, Dublin City University, where a family of these compounds were developed for the detection of metal ions such as lithium or amine gases such as ammonia and trimethylamine [15].

The calixarene compound has a cavity or cup like structure. In a sensing scheme the colour generation in the compound is caused by the deprotonation of the acidic chromophore (—COH) attached near the ligand (L—) polar cavity [16]. The presence of a suitable base causes deprotonation. For example the basic nature of ammonia (NH_3) gas results in the deprotonation of the OH of the chromophore and hence the colour change occurs. This reaction can be described by the following equation

$$L—COH + NH_3 \leftrightarrow L—CO^- + NH_4^+ \qquad (7.4)$$

The specificity to ammonia and other amine gases is considered to be a result of the shape and structure of the compound [16].

7.3.2 PVC polymer coatings

The calixarene compound was immobilised in a polyvinylchloride (PVC) coating. It was not possible to use sol-gel-derived films because the compound was insoluble in ethanol and could not survive the low pH of the sol-gel preparation. In a typical polymer preparation 16 mg of calixarene ligand was mixed with PVC (100 mg), a plasticiser (200 mg) and tetrahydrofuran (THF) which is the common solvent [16]. The function of the plasticiser was to dissolve the ligand in the PVC. Lithium or potassium metal salts in the form of lithium perchlorate ($LiClO_4$) or potassium perchlorate ($KClO_4$) were also added to the PVC cocktail to increase sensitivity for reasons outlined in section 7.3.3.

The refractive index of the PVC coating is affected by the type of plasticiser used. In order to obtain coatings with a refractive index lower than the refractive index of the fibre optic core, and thereby providing the necessary conditions for light-guiding, a range of plasticisers was investigated. These were nitrophenyl octyl ether (2-NPOE), dioctyl phthaline (DOP), dioctyl adipate (DOA), dioctyl sebacate (DOS) and dibutyl sebacate (DBS). The refractive index of PVC polymer coatings, using these plasticisers, were measured on silicon substrates using ellipsometry as outlined in section 5.2.2. The results of this study are shown in table 7.4. Only PVC coatings prepared using DBS as plasticiser gave a refractive index lower than the fibre core index (1.46). PVC / DBS coatings doped with the calixarene compound were used as sensor substrates on optical fibres. Optical fibres were coated and tested as in the sol-gel case described in previous sections.

Plasticiser	Refractive Index
2-NPOE	1.52
DOP	1.51
DOA	1.47
DOS	1.465
DBS	1.45

Table 7.4 Refractive index of PVC coatings using different plasticisers

7.3.3 Sensor response

Figure 7.14 shows the absorption spectra of the calixarene compound in a PVC coating when exposed to different concentrations of ammonia gas. This data is referenced to a scan of the coated fibre in nitrogen. The peak absorption is observed at approximately $\lambda = 490$ nm. The reversibility and response/recovery times of these films is plotted in figure 7.15. A typical response time of about 7 minutes for the $0 \rightarrow 20$ ppm NH_3 step was observed. The poor signal to noise in figure 7.15 and at the low wavelength region ($\lambda < 450$nm) in figure 7.14 is due to low detected signal levels. This is caused by high inherent absorption of the calixarene compound at the low wavelength spectral region in the absence of ammonia. Furthermore, the detection efficiency of the characterisation system is lower at these wavelengths.

In order to increase the sensitivity of the sensor the effect of metal ions was investigated. The presence of 1 mole equivalent of $LiClO_4$ to the calixarene in the PVC coating increased the sensitivity to ammonia by a factor of about ten. This is illustrated in figure 7.16 for the 0-100 ppm ammonia concentration range. The inclusion of the metal cation into the calixarene increases the acidity of the ionisable chromophore, thereby lowering the pK and facilitating proton uptake by NH_3 [16]. The metal salt also shifted the wavelength of maximum absorption from 490 to about 520 nm. The absorbance at $\lambda = 520$ nm versus ammonia concentration is plotted in figure 7.17 and these data indicate the high sensitivity achievable at the low-ppm concentration range.

The influence of metal salts on the sensitivity of the sensor was further investigated by using different quantities of $LiClO_4$ or $KClO_4$ in the PVC coatings. For this purpose two further coatings were prepared, one with 0.5 mole equivalent of $LiClO_4$ and the second with 0.5 mole equivalent of $KClO_4$ to the calixarene. The least sensitivity to ammonia was observed for the coating containing ligand only (i.e. no metal salt), while the greatest sensitivity was observed for the coating containing 1 mole $LiClO_4$. The sensitivity to ammonia of the 4 coatings went as follows

ligand + $LiClO_4$ > ligand + 0.5$LiClO_4$ > ligand + 0.5$KClO_4$ > ligand only.

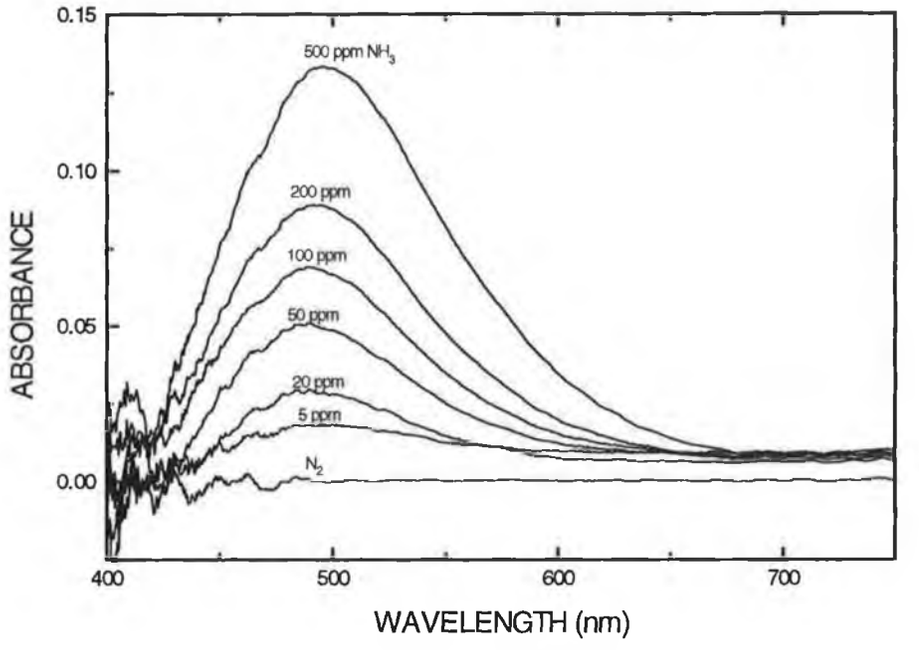

Figure 7.14 Absorption spectra of calixarene / PVC film

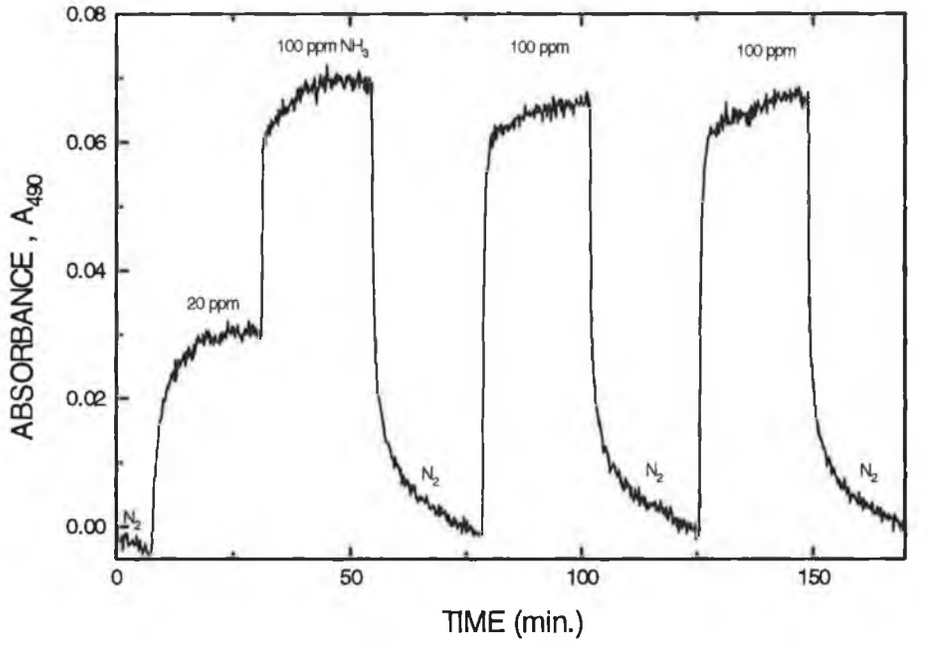

Figure 7.15 Time response of calixarene / PVC film

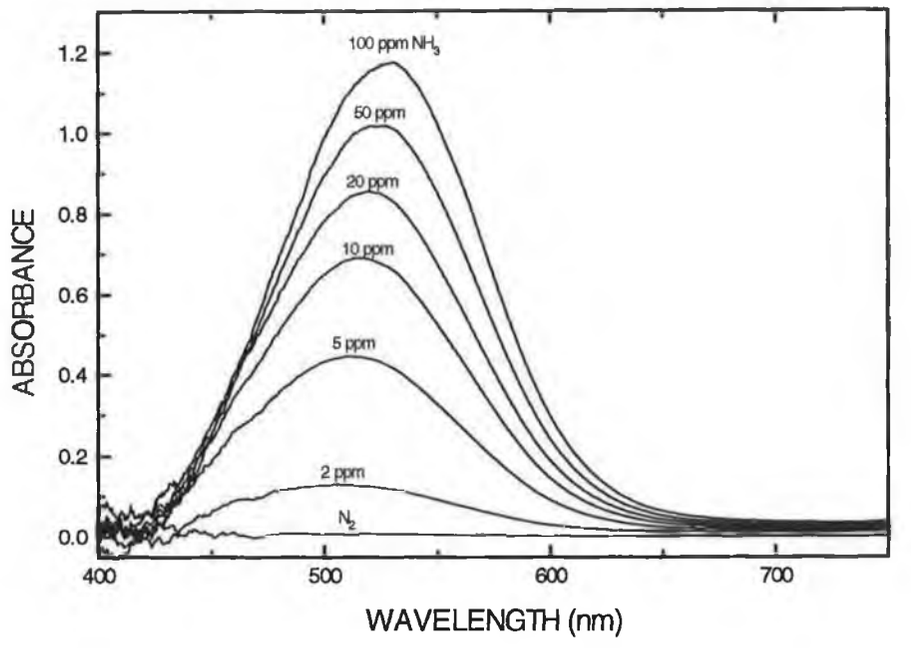

Figure 7.16 Absorption spectra of calixarene / PVC / $LiClO_4$ film

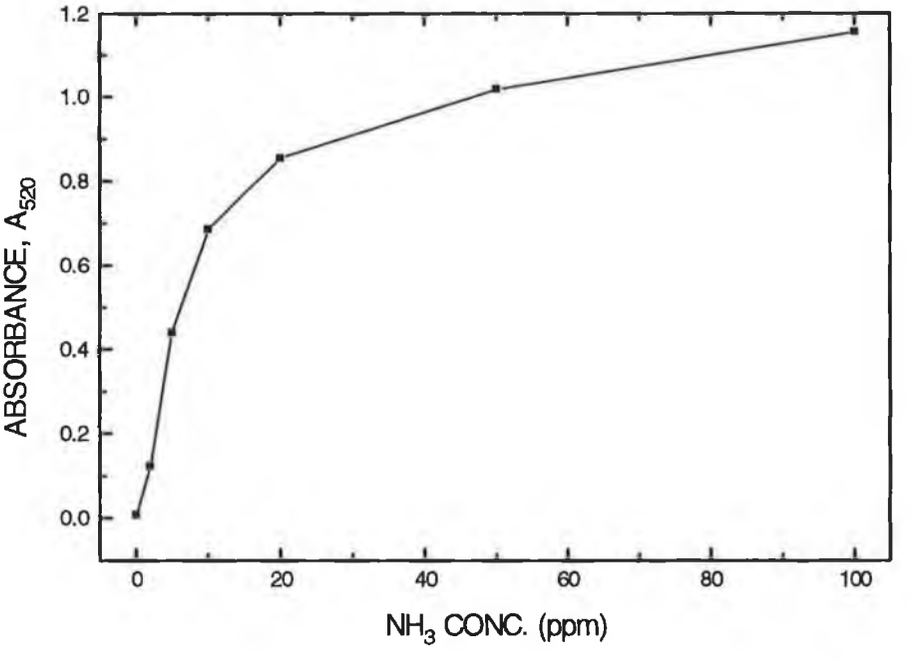

Figure 7.17 Calibration curve for calixarene / PVC / $LiClO_4$ film

These preliminary results indicate that the calixarene compound is a suitable candidate for an ammonia-specific sensor at low concentrations, with sub-ppm detection limits possible. Moreover, these polymer coatings were not optimised in terms of film thickness or lithium salt content. Optimisation of coating parameters should improve both sensitivity and response time to ammonia.

7.4 Ammonia sensing with near-infrared indicators

7.4.1 Introduction

Most of the work on optical chemical sensors is carried out in the visible spectral region where the chemical and optical properties of indicator dyes are well known. However a number of advantages exist in moving to the near-infrared (NIR) spectral region (i.e. λ = 700-950 nm). These include the following:

- Most optical fibres are silica-based and have a minimum optical attenuation not in the visible but in the NIR spectral region. For example the first transmission window of fibre optic telecommunication fibres lies in the 800-850 nm range.
- The most comprehensive range of LEDs and laser sources exist in the NIR region (developed for telecommunication applications)
- The NIR region is of particular interest in biomedical sensing because the absorbance of biological samples is minimal in this region and hence does not interfere with the absorbance of the NIR indicator [18]. Furthermore, the light in this region does not excite parasitic fluorescence in organic media [19].

Despite the above attractive features, indicators absorbing above 650 nm are scarce. This is reflected in the low number of publications appearing on the subject [17,18,19,20]. A problem with the stability of dyes with increasing indicator length (necessary for NIR absorption) is cited as a reason why sensor dyes in this spectral region are scarce [19].

In the work described here a number of NIR absorbing indicator dyes were investigated for ammonia gas sensing. This work was carried out as part of a European COPERNICUS project, whose aim was the construction of a distributed sensor for ammonia. To operate over long lengths of optical fibres, the spectral response of sensing reagents must be matched to the NIR attenuation minimum of the silica-based

fibres used. Short lengths (~ 12 cm) of optical fibres coated with NIR indicator dyes, immobilised in either sol-gel silica or polymer coatings, were characterised for this purpose. An Ocean Optics spectrometer operating in the 550-1050 nm spectral region was used in this work. The indicators for this study were synthesised by the Slovak Technical University, Bratislava, a partner in the COPERNICUS project.

7.4.2 Sensor response

A number of indicators that had peak absorption in the NIR region of the spectrum were investigated. Figure 7.18 shows the absorption spectra of one of these NIR indicators for different ammonia concentrations. This indicator is a copper (Cu^{2+}) based complex and was immobilised in a pH3 TEOS (R=4) sol-gel film. Its peak absorption occurred at about λ = 710 nm. In figure 7.18 the air scan was for static air, while the N_2 and NH_3 scans were for flowing gases. The reason for the change in absorbance going from air to nitrogen is not understood but could be due to the change in the RH of the test gas. In the static air case the RH was about 40%, while in the flowing gas cases it was about 0%. While the dye showed some response to ammonia, its response was very slow (> 60 minutes) and did not show reversibility.

A second indicator investigated was a dimethylaminophenyl cyanine type dye. This dye was first immobilised in a TEOS sol prepared at pH1, but the dye was almost destroyed by the process and showed negligible response to ammonia. A good response was obtained when the dye was immobilised in a TEOS sol prepared at pH3, as illustrated in figure 7.19. The peak absorption for this dye occurred at λ = 790 nm. As seen previously, a large decrease in absorbance in going from static air to flowing nitrogen was observed. While showing a good response to ammonia, this dye had a slow response and incomplete recovery.

The final NIR indicator investigated showed a peak absorption at λ = 850 nm. This dye was also a copper-based dye. The reaction mechanism in the two copper based dyes was a substitution reaction between copper and ammonia. In the other dye case an acid / base type reaction takes place. Attempts were made to incorporate this dye in a sol-gel matrix, but these were unsuccessful. The sol-gel preparation, even at pH3, was too harsh for the indicator. Therefore it was immobilised in a PVC coating. Figure 7.20

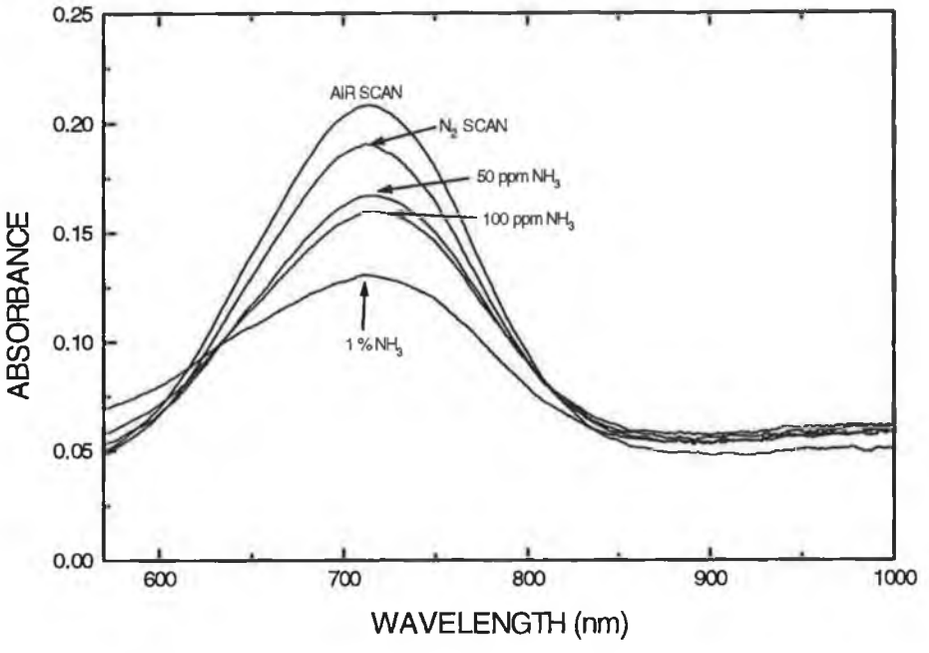

Figure 7.18 Absorption spectra of copper complex in sol-gel film

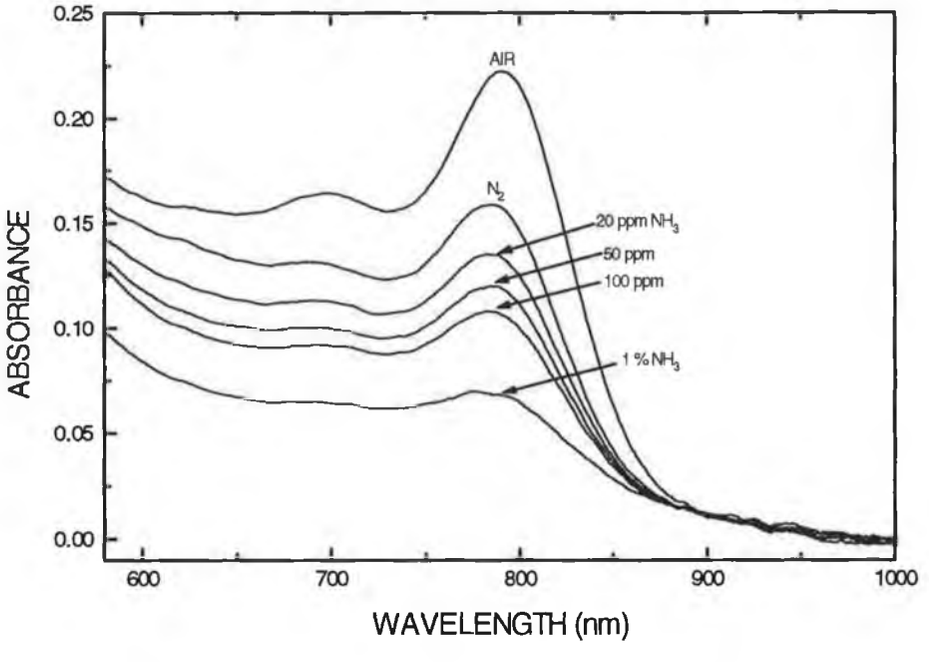

Figure 7.19 Absorption spectra of dimethylaminophenol cyanine dye

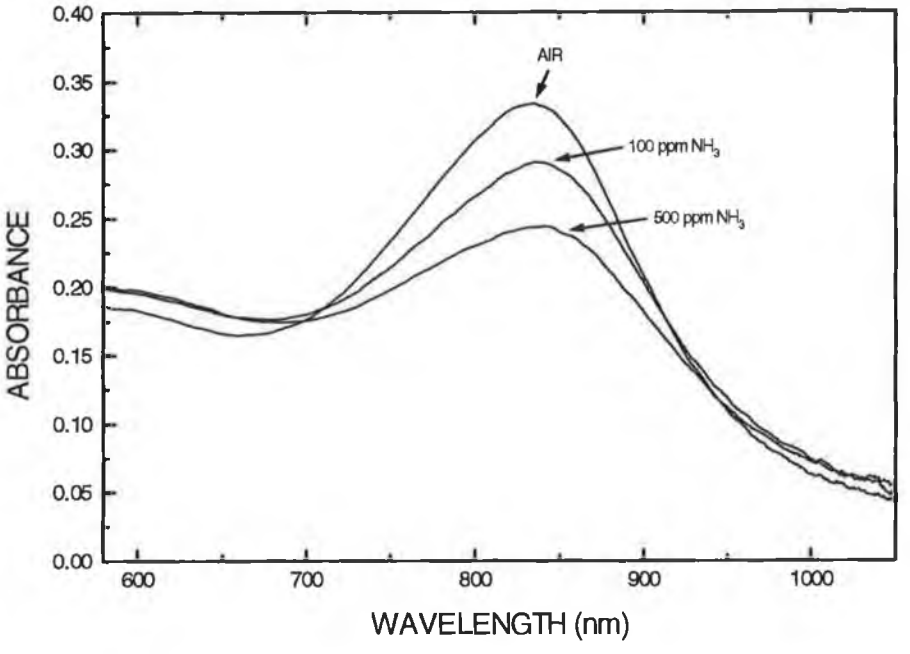

Figure 7.20 Absorption spectra of copper complex in PVC film

shows the absorption spectra. In this case the carrier gas used was air at a RH of about 100%. A very small difference in absorbance between static and flowing air was observed. The response of the dye was again very slow (> 100 minutes) and it showed poor recovery.

The exact reason why the 3 NIR indicators showed slow response and poor recovery is unclear. The recovery could indicate a strong reaction between the indicator and ammonia. This study showed that the sol-gel preparation at low pH is too harsh for some indicators. To advance this work further, more stable NIR indicators and different methods of immobilisation are required.

7.5 Conclusion

This chapter described ammonia sensing using both pH indicators and ammonia-specific indicators. The sensitivity of the sulfonephthalein pH indicators to ammonia was influenced by both their pK and by the nature of the sol-gel matrix. Doped TEOS-based sol-gel films showed much greater response than MTES-based films.

Furthermore, MTES-based films showed much greater sensitivity to RH than the TEOS-based ones. The response time of these films was influenced by RH and the thickness of the sol-gel films.

Ammonia sensing was also demonstrated using an ammonia-specific calixarene compound, immobilised in a PVC coating. The sensitivity of these coatings was greatly increased by the inclusion of a lithium salt in their preparation. Finally, ammonia sensing using NIR absorbing indicators was outlined. Unfortunately, these indicators showed very slow response and poor reversibility.

This chapter highlighted possible sensing schemes for ammonia based on either sol-gel or polymer coatings. The criteria for choosing a pH indicator for a particular application were outlined. Sub-ppm ammonia detection limits are possible in the sol-gel case by choosing a suitable indicator, dye concentration and sol-gel matrix.

References

1. K. Colbow and K.L. Colbow, 'Sensors and monitoring systems in environmental control', Chapter 19, Sensors A Comprehensive Survey, W. Gopel, J. Herse and J.N. Zemel (editors), Vol. 3, VCH Publications, 1991.

2. European COPERNICUS project, 'Rapid detection and location of ammonia leaks', Contract No. CIPA-CT94-0206.

3. D.J. David, M.C. Willson and D.S. Ruffin, 'Direct measurement of ammonia in ambient air', Analytical Letters, Vol. 9, No. 4, 1976, pp. 389-404.

4. J.F. Guiliani, H. Wohltjen and N.L. Jarvis, 'Reversible optical waveguide sensor for ammonia vapours', Optics Letters, Vol. 8, No. 1, 1983, pp. 54-56.

5. Y. Sadaoka, Y. Sakai and M. Yamada, 'Optical properties of sulfonephthalein dyes entrapped within polymer matrices for quantification of ammonia vapour and humidity in air', J. Mater. Chem., Vol. 3, No. 8, 1993, pp. 877-881.

6. A. Brandenburg, R. Edelhauser, T. Werner, H. He and O.S. Wolfbeis, 'Ammonia detection via integrated optical evanescent wave sensors', Mikrochim. Acta., Vol. 121, 1995, pp. 95-105.

7. A. Mills, L. Wild and Q. Chang, 'Plastic colourimetric film sensors for gaseous ammonia', Mikrochim. Acta., Vol. 121, 1995, pp. 225-236.

8. E. Bishop, 'Indicators', Pergamon Press, Oxford, 1972.

9. S.P. Golubkov, N.A. Vasilenko, R.A. Polyrailo, V.S. Kovtan and P.S. Borsuk', Application of pH dyes for ammonia sensing by portable analyser', Proc. SPIE Vol. 1637 Environmental and Process Monitoring Technologies', 1992, pp. 227-232.

10. V. Chernyak, R. Reisfield, R. Gvishi and D. Venezky', Oxazine-170 in sol-gel glass and PMMA films as a reversible optical waveguide sensor for ammonia and acids', Sensors and Materials, Vol. 2, No. 2, 1990, pp. 117-126.

11. R. Klein and E. Voges, 'Integrated-optic ammonia sensor', Sensors and Actuators B, Vol. 11, 1993, pp. 221-225.

12. A. Albert and E.P. Serjeant, 'The Determination of Ionisation Constants, A Laboratory Manual', 3rd edition, Chapman and Hall Ltd., London, 1984, p. 195.

13. P. Innocenzi, M.O. Abdirashid and M. Guglielmi, 'Structure and properties of sol-gel coatings from methyltriethoxysilane and tetraethoxysilane', J. Sol-gel Science and Technology, Vol. 3, 1994, pp. 47-55.

14. S.J. West, S. Ozawa, K. Seiler, S.S.S. Tan and W. Simon, 'Selective ionophore-based optical sensors for ammonia measurement in air', Anal. Chem., Vol. 64, No. 5, 1992, pp. 533-540.

15. M. McCarrick, S.J. Harris and D. Diamond, 'Assessment of a chromogenic calix[4]arene for the rapid colorimetric detection of trimethylamine', J. Mater. Chem., Vol. 4, No. 2, 1994, pp. 217-221.

16. Personal communication with Theresa Grady, School of Chemical Sciences, Dublin City University.

17. G. Patonay, J.M. Zen and T. Czuppon, 'Near-infrared laser diodes in monitoring applications', Proc. SPIE Vol. 1637 Environmental and Process Monitoring Technologies, 1992, pp. 142-150

18. H. Lindauer, P. Czerney, G.J. Mohr and U.W. Crummit, 'New near infrared absorbing acidochromic dyes and their application in sensor techniques', Dyes and Pigments, Vol. 26, 1994, pp. 229-235.

19. H. Lehmann, G. Schwotzer, P. Czerney and G.J. Mohr, 'Fibre-optic pH meter using NIR dye', Sensors and Actuators B, Vol. 29, 1995, pp. 392-400.

20. L.E. Norena-Franco and F. Kvasnik, 'Near-infrared optical detection of acids in atmospheric air by phthalocyanine dyes in polymer films', Analyst, Vol. 121, 1996, pp. 1115-1118.

Chapter 8 Diffusion Study

8.1 Introduction

The response time of a sensor is one of the critical performance parameters of a sensor. Response time is affected by the diffusion of the analyte under test to the region containing the analyte-sensitive reagent and the particulars of the reaction of the reagent with the analyte. For example, in the sensors described in this thesis, analytes diffuse into a porous sol-gel-derived silica film to react with the immobilised analyte-sensitive reagent. Therefore, the particulars of the diffusion process are very important in sensor development and required detailed examination.

The response times of sol-gel based sensors for pH (TEOS-derived films in Chapter 6) and gases like oxygen are very short [1,2]. This suggests rapid diffusion of protons and oxygen in and out of the sol-gel matrix. The behaviour of charged species, such as metal ions, is expected to be quite different, however, and is addressed in the work described here. Arbuthnot et al. [3] reported a very slow complexation rate between zinc ions in solution and a sol-gel film doped with the fluorescent indicator 8-hydroxyquinoline-5-sulfonic acid (HQSA). This effect was presumed to be due to slow diffusion of zinc ions through the porous silica.

Diffusion is considered a random process where matter is transported through a system by a series of random molecular motions [4]. The mathematical model generally used to describe diffusion is known as Fick's first law [4]. It is based on the hypothesis that the rate of transfer of a diffusing species through a unit area of a section is proportional to the concentration gradient measured normal to the section, i.e.

$$F = -D\frac{\partial C}{\partial x} \qquad (8.1)$$

where F is the rate of transfer per unit area of section, C is the concentration of diffusing substance, x is the space coordinate measured normal to the section, and D is called the diffusion coefficient. Fick's second law, considered the fundamental differential equation of diffusion, can be derived from Fick's first law and a mass balance [4], and is given by:

$$\frac{\partial C}{\partial t} = D\frac{\partial^2 C}{\partial x^2} \qquad (8.2)$$

These equations have been used in many studies [4,9] to model diffusion behaviour.

In order to investigate diffusion of metal ions into sol-gel silica films and to assess its potential as a sensor, the reaction of lead with the indicator dye xylenol orange (XO) was studied. Lead (Pb^{2+}) in solution was chosen as a test analyte because of its environmental significance. Lead is one of the most commonly determined heavy metals and because it accumulates in body tissue it follows that strict limits on its presence in drinking water must be imposed. European Union and U.S. EPA standards for lead in domestic water supplies are 240 mMolar (0.05 mg/L Pb) [5].

XO was used as the colourimetric indicator for an evanescent wave absorbance-based lead sensor. XO forms complexes with a variety of metal ions [6,7]. XO belongs to a group of indicators known as metallochromic indicators [7] which are organic dyes containing donor groups that complex a metal ion to yield a chelate differing in colour from the indicator under the same conditions. Metallochromic indicators behave as acid / base indicators and the colour of the free indicator is pH-dependent. Therefore, the colour change during a reaction with a metal is determined by the pH of the solution containing the metal ions. The recommended pH for the reaction of XO with lead is about pH5 [7]. Calibrated lead solutions were prepared by diluting lead standards (Aldrich Chemicals, No. 35,633-6) with acetate buffer of pH4.5, as outlined in the report by Yang and Saavedra [8]. The buffer was prepared by adjusting the pH of a 0.1 molar sodium acetate solution with acetic acid.

The ingress of Pb^{2+} ions into a XO doped sol-gel film, on an optical fibre, can be monitored by real-time evanescent wave absorption. This was used here to observe the difference in behaviour between tetraethoxysilane- (TEOS) and methyltriethoxysilane-(MTES) derived sol-gel films, as described in section 8.2. Evanescent wave spectroscopy has been used in a number of studies of analyte diffusion into polymer coatings [9,10,11,12]. It is an attractive technique for such investigations because it yields data in real time and enables direct evaluation of the sensing film without

interference from the surrounding solution. In the work described here, the relative difference in diffusion into different sol-gel-derived films was estimated from the time response ($T_{90}(\uparrow)$) of the reaction of Pb^{2+} with XO. In some cases reported in the literature [9,13], the time dependent absorbance change was used to determine the diffusion coefficient D, using solutions to Fick's diffusion laws (equations 8.1 and 8.2). In the case of evanescent wave spectroscopy, a model used to estimate D should incorporate the diffusion process inwards through the thin film on the optical fibre and the evanescent field penetration outwards from the interface with the core [11].

Zerda and co-workers have reported extensively on the issues affecting the diffusion of different species (e.g. liquids, metal ions and steroids) into and out of porous sol-gel glass [14,15,16,17]. These authors concluded [15,16] that the diffusion of metal cations (neodymium and erbium) in porous silica was determined by a number of factors. These included the average pore diameter in the sol-gel, the size of the diffusing species, composition of the coordinate sphere of the diffusing species, solvent used, interactions between the surface and the complexes and temperature effects. By increasing the average pore diameter, the rate of diffusion was observed to increase [15]. Erbium with a smaller molecular size than neodymium [16], diffused faster. However, these authors noted that these metal cations do not move as separate species, they diffuse as complexes with water and anions. The composition of the coordination spheres associated with the metal cations was shown to have an important effect in determining the diffusion rate [16]. Furthermore, by modifying the pore surface of the sol-gel glass to reduce the concentration of hydroxyl-groups, the diffusion rate was increased. In the work described here, a preliminary study of the effect of the sol-gel surface properties on the diffusion of Pb^{2+} ions is examined.

8.2 Reaction of Pb^{2+} with XO

The reaction of Pb^{2+} with XO was compared for two sol-gel-derived films, using TEOS and MTES as precursors, respectively. In both cases water of pH1 and a R-value (water/alkoxide ratio) of 4 was used. An equivalent dye concentration of approximately 10.5 mM / litre was used in each case. The time response of the films to 10 mM Pb^{2+} was monitored at the wavelength of maximum absorbance change (i.e. around λ = 580

nm) using the time display function of the spectrometer system. The Pb^{2+} solution was continuously circulated around the coated fibre for the duration of the study. A blank pH4.5 buffer was used as a reference solution.

The absorption spectra in 0 and 10 mM Pb^{2+} solutions and the time response behaviour of pH1 TEOS (R=4) / XO films are shown in figures 8.1 and 8.2, respectively. The spectrum in 10 mM Pb^{2+} was taken after the absorbance had reached a constant value, e.g. after approximately 270 minutes (see figure 8.2). The absorbance at λ = 570 nm increased in the presence of Pb^{2+} ions. Similarly, figures 8.3 and 8.4 shows the absorption spectra and response behaviour, respectively, for a pH1 MTES (R=4) / XO film. As above, the absorbance spectrum in 10 mM Pb^{2+} ions was recorded after the saturation of the absorbance. It is seen clearly from these graphs that that the reaction of Pb^{2+} in TEOS- and MTES-derived films is quite different. The observed differences are as follows:

(1) The most dramatic effect is that the response time is much shorter in the MTES-derived films. An difference by a factor of about 5 in the response time of the two films was observed with the MTES film showing the faster response. This is summarised in table 8.1 which shows the 50% and 90% response times for TEOS- and MTES-derived films. Possible reasons for this behaviour are outlined below.

(2) A larger absorbance change was detected in the TEOS film case, indicating that these films are more sensitive to changes in Pb^{2+} concentration. This is difficult to see from figures 8.1 and 8.3 due to the difference in the absorption band formation in the presence of Pb^{2+}. However, this can be clearly seen from the change in absorbance going from pH 4.5 buffer (0 Pb^{2+}) to 10 mM Pb^{2+} in figures 8.2 and 8.4. In the TEOS film case the change in absorbance was about 0.55, while in the MTES case it was about 0.34.

(3) The wavelength of maximum absorbance change was different in the two film cases. In the TEOS-derived films it occurred at approximately λ = 570 nm, while in the MTES-derived film case, it occurred at λ = 590 nm. This difference in peak absorption wavelength could indicate different environments within the two sol-gel films that perturb the structure of the indicator molecule in different ways. Furthermore, it is clearly seen from figures 8.2 and 8.4 that the absorption band formation in the presence

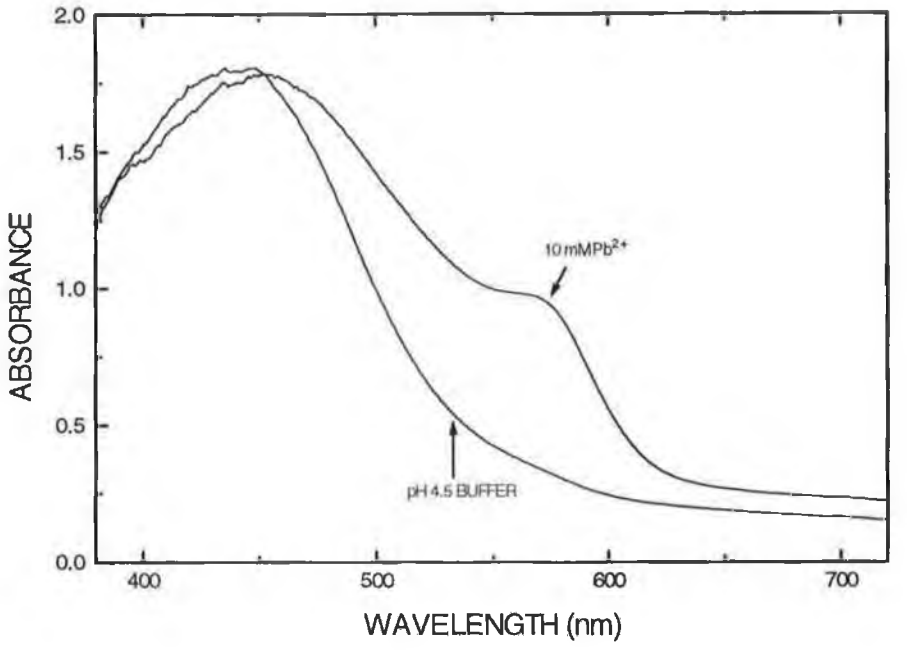

Figure 8.1 Absorption spectra of pH1 TEOS (R=4) / XO film

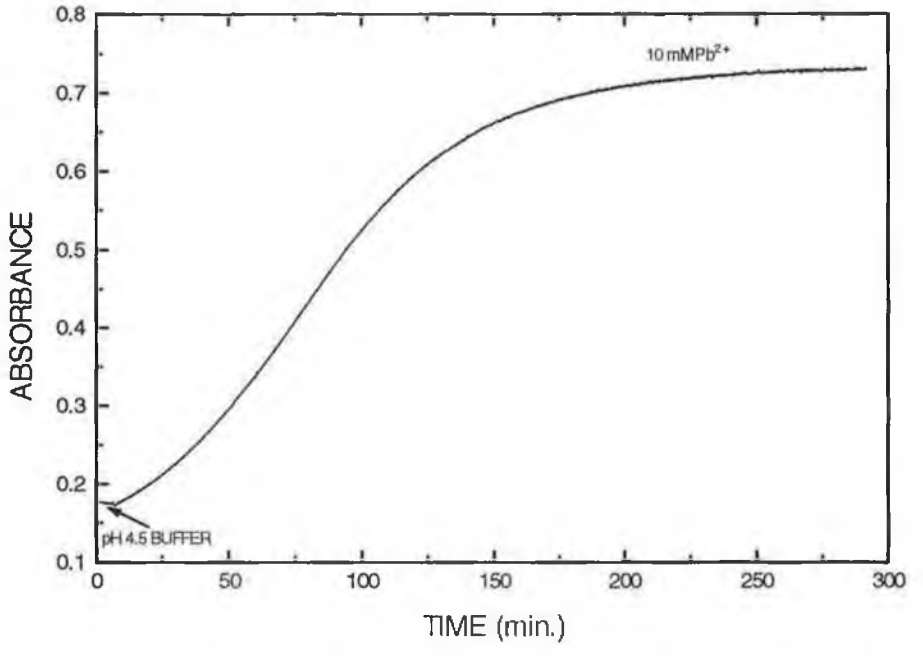

Figure 8.2 Time response of TEOS / XO film to 10 mM Pb^{2+}

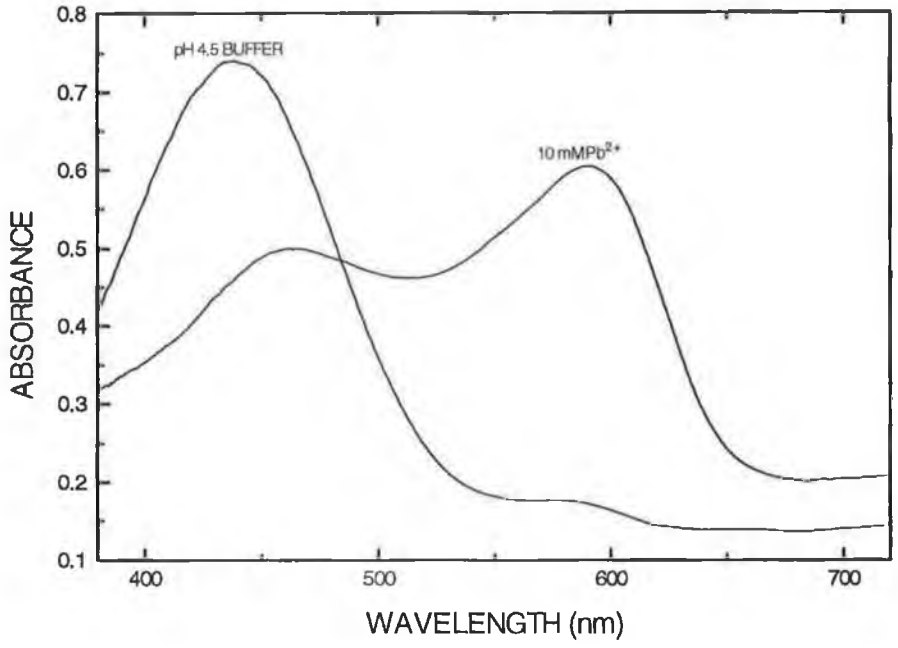

Figure 8.3 Absorption spectra of pH1 MTES (R=4) / XO film

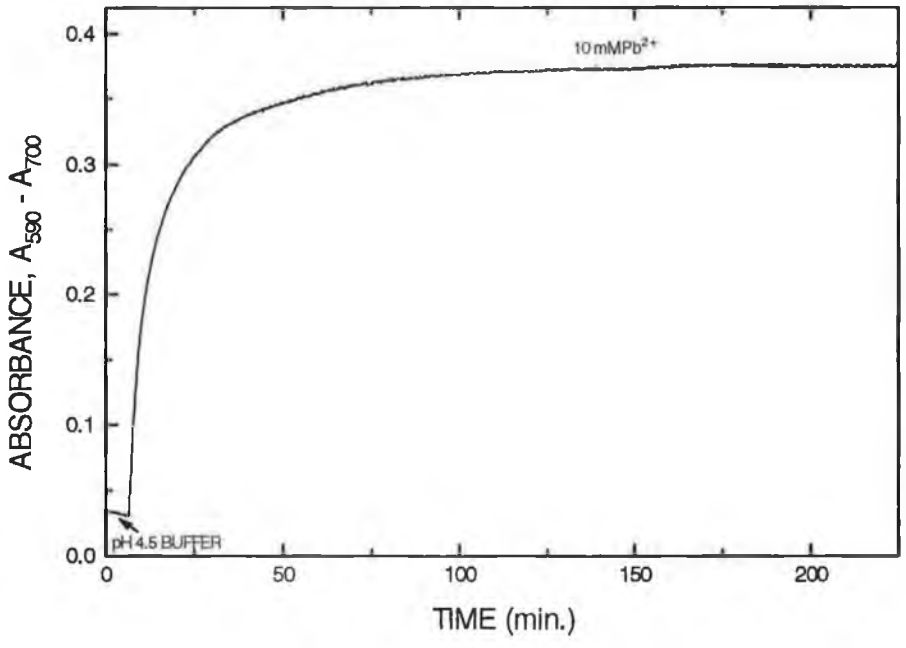

Figure 8.4 Response of MTES / XO film to 10 mM Pb^{2+}

of Pb^{2+} is quite different in the two cases. In the MTES films a clearly defined absorption band forms when XO complexes with Pb^{2+}. In contrast, in the TEOS films only a 'shoulder' forms on the original absorption band.

In order to compare our MTES film behaviour with the data reported by Yang and Saavedra [8], a second MTES-derived film was fabricated based on their procedure. In this film fabrication procedure a 1:1 (w/w) solution of MTES and ethanol was mixed together. The hydrolysis reaction was catalysed by adding 1% (w/w) of concentrated HCl acid, which was the only water added to the sol preparation. The response of these films to Pb^{2+} was very similar to the previous MTES-derived films. An absorbance band formed at λ = 590 nm and the response to Pb^{2+} was fast. Yang and Saavedra [8] also reported a fast response for their MTES-derived films for a reaction with Pb^{2+}. Table 8.1 summaries the data for the 3 sol-gel film cases investigated in this work.

Film Type	$T_{50}(\uparrow)$ (min.)	$T_{90}(\uparrow)$ (min.)	Peak λ (nm)
TEOS (R=4)	89	169	570
MTES (R=4)	5	36	590
MTES*	1.5	15	590

* Film based on procedure in [8]

Table 8.1 Comparing TEOS- and MTES-derived films

Zerda and co-workers [14,16] concluded that of the different parameters affecting diffusion into a sol-gel glass, the most important are surface interactions and geometric restrictions. Increasing the pore size should increase the rate of diffusion. However, Innocenzi et al. [18] reported that films prepared with larger amounts of MTES (in MTES : TEOS mixtures) are less porous. Furthermore, the refractive index of the TEOS- and MTES-derived films were very similar (about 1.43 in each case). Therefore, it is unlikely that the effects outlined above are due to pore size effects and reactions at the surface should be considered.

The TEOS- and MTES-derived films have different surface properties. As outlined in section 5.8, the TEOS-derived films are hydrophilic and are characterised by hydroxyl (OH) groups on the surface. MTES-derived films on the other hand are more hydrophobic, with CH_3 groups on the surface. Therefore, the surface in the TEOS film case is more polar than in the MTES case. The difference in the response behaviour of the two films is likely to be related to electrostatic interactions between the Pb^{2+} ions and the pore surface. Those interactions will clearly be more significant in the TEOS case. While the exact reason for the difference in behaviour the two film cases is unknown, a possible explanation is outlined below.

The polar surface of the TEOS-based film may attract the positively charged Pb^{2+} ions and thereby slow their movement into the pores. This would explain the long response time in these films. In the MTES film case, the more neutral surface would not have the same attraction for the Pb^{2+} and, as observed, would show faster response.

8.3 Conclusion

This chapter outlined a preliminary study of the factors that affect the diffusion of metal ions into a sol-gel silica glass film. The nature of the sol-gel surface is of critical importance. This was demonstrated here for the reaction of Pb^{2+} ions with XO immobilised in different sol-gel films. This study emphasised critical issues in the development of an optical sensor for Pb^{2+} ions in solution. While the greatest sensitivity was observed for TEOS-derived films, the fastest response was observed for MTES-derived films. Apart from surface properties of the sol-gel film, other factors that affect the response time include film thickness and Pb^{2+} concentration.

References

1. T.M. Butler, B.D. MacCraith and C.M. McDonagh, 'Development of an extended range fibre optic pH sensor using evanescent wave absorption of sol-gel entrapped pH indicators', Proc. SPIE Vol. 2508 Chemical, Biochemical, and Environmental Fibre Sensors VII, 1995, pp. 168-178.

2. B.D. MacCraith, G. O'Keeffe, C. McDonagh and A.K. McEvoy, 'LED-based fibre optic oxygen sensor using sol-gel coating', Electronic Letters, Vol. 30, No. 11, 1994,

pp. 888-889.

3. D. Arbuthnot, X.J. Wang and E.T. Knobbe, 'Spectroscopic study of 8-hydroyquinoline-5-sulfonic-acid-doped sol-gel transition metal ion optrode materials', J. Non-Crystalline Solids, Vol. 178, 1994, pp. 52-57.

4. J. Crank, The Mathematics of Diffusion, Second edition, Clarendon Press, Oxford, 1975.

5. P.J. Flanagan, Parameters of Water Quality: Interpretation and Standards, Environmental Research Unit, Dublin, 1988.

6. E. Bishop, Indicators, Pergamon Press, Oxford, 1972, p. 358.

7. Z. Holzbecher, L. Divis, M. Kral, L. Sucha and F. Vlacil, Handbook of Organic Reagents in Inorganic Analysis, Ellis Horwood Limited, Sussex, 1976.

8. L. Yang and S.S. Saavedra, 'Chemical sensing using sol-gel derived planer waveguides and indicator phases', Anal. Chem., Vol. 67, No. 8, 1995, pp. 1307-1314.

9. D.S. Blair, L.W. Burgess and A.M. Brodsky, 'Study of analyte diffusion into a silicone-clad fibre-optic chemical sensor by evanescent wave spectroscopy', Applied Spectroscopy, Vol. 49, No. 11, 1995, pp. 1636-1645.

10. U.E. Spichiger, D. Citterio and M. Bott, 'Analyte-selective optrode membranes and optical evaluation techniques: characterisation of response behaviour by ATR-measurements', Proc. SPIE Vol. 2508 Chemical, Biochemical, and Environmental Fibre Sensors VII, 1995, pp. 179-189.

11. V. Ruddy, S. McCabe and B.D. MacCraith, 'Detection of propane by IR-ATR in a teflon-clad fluoride glass optical fibre', Applied Spectroscopy, Vol. 44, No. 9, 1990, pp. 1461-1463.

12. S.N. Behrens Thomas, H.W. Blanch an D.S. Soane, 'A novel optical method for the measurement of biomolecular diffusion in polymer matrices', Biotechnology Progress, Vol. 5, No. 3, 1989, pp. 126-131.

13. A. Mills and Q. Chang, 'Modelled diffusion-controlled response and recovery behaviour of a naked optical film sensor with a hyperbolic-type response to analyte concentration', Analyst, Vol. 117, 1992, pp. 1461-1466.

14. N. Koone, Y. Shao and T.W. Zerda, 'Diffusion of simple liquids in porous sol-gel glass', J. Phys. Chem., Vol. 99, No. 46, pp. 16976-16981.

15. N.D. Koone and T.W. Zerda, 'Diffusion and optical properties of Nd-doped sol-gel silica glass', J. Non-Crystalline Solids, Vol. 183, 1995, pp. 243-251.

16. N.D. Koone, J.D. Guo and T.W. Zerda, 'Diffusion of Er^{3+} in porous sol-gel glass', submitted to J. Non-Crystalline Solids, 1996.

17. L. Sieminska and T.W. Zerda, 'Diffusion of steroids from sol-gel glass', J. Phys. Chem., Vol. 100, 1996, pp. 4591-

18. P. Innocenzi. M.O. Abdirashid and M. Guglielmi, 'Structure and properties of sol-gel coatings from methytriethoxysilane and tetraethoxysilane', J. Sol-gel Science and Technology, Vol. 3, 1994, pp. 47-55.

Chapter 9 Conclusion

The work presented in this thesis described the optimisation of the sol-gel process for the fabrication of porous silica films and the subsequent development of evanescent-wave absorption-based sensors. Sensors based on coated optical fibres were developed for pH and ammonia.

The sol-gel process and the parameters that influence the chemical reactions involved, have been described. The attractiveness of the sol-gel process over other immobilisation techniques lies primarily in the flexibility and simplicity of the process. A detailed account of the characterisation of the sol-gel films prepared at our laboratory was presented. A range of film properties such as thickness, refractive index and temporal stability were monitored as a function of various processing parameters. These included coating-speed, water : precursor ratio (R), sol aging time and time after drying. Film thickness was found to increase with sol aging time, increasing R-value and increasing coating-speed. These results were interpreted in terms of the dependence of the hydrolysis and condensation rates on the different processing parameters.

This work contributed to the task of choosing optimal fabrication conditions for films used in optical chemical sensor applications. Anomalies identified for R = 2 films, over higher R-value films, included a slower rate of film thickness increase with aging time and a long period of time (~ 50 days) to achieve film stability. An optimal sol-gel film preparation identified by us for chemical sensor applications used TEOS as precursor, a R-value of 4, water of pH1 and a coating rate of 1 mm/sec.

Further characterisation studies covered the areas of dye leaching from sol-gel-derived films and analyte-diffusion into sol-gel films. The leaching of sulfonephthalein pH indicators from sol-gel films was found to be influenced by the age of the sol-gel film (issue of temporal stability), the R-value and pH of the sol, the pH of the leachant solution and the type of sol precursor used. R = 2 films were found to be unsuitable for sensor development in aqueous environments due to rapid leaching. Higher R-value films showed slower rates of leaching. However, some leaching was observed for all the films investigated. This highlighted that other strategies need to be investigated to effectively solve the leaching of dopants from the sol-gel films. The effect of the surface

properties of the sol-gel film on the ingress of metal ions was investigated for the reaction of Pb^{2+} ions with xylenol orange. Film prepared using MTES as precursor showed much faster response than TEOS-derived films.

The development of an optical fibre pH sensor, based on sulfonephthalein indicators entrapped in sol-gel-derived films, was presented. The sol-gel immobilisation affects the operational pH range of the indicators compared with solution values. The pK of the indicators was shifted to higher values. The range of the pH sensor can be extended by two techniques, namely, by the inherent broadening of the range of the indicator on immobilisation and by co-immobilisation of indicators. A pH sensor covering about 8 pH units was achieved by a combination of these two techniques. A response time of about 30 seconds was measured for these pH sensors. The long-term use of these sensors in environments of high pH is not practical due to dye leaching.

In addition to a sensor for aqueous pH, the sensing of gaseous ammonia using pH indicators and ammonia-specific dyes was presented. The sensitivity of a sulfonephthalein indicator for ammonia sensing depended on its pK and on the sol-gel matrix. Indicators of higher pK were found to be more sensitive than low pK indicators. Bromocresol purple was the indicator of choice out of the range investigated. TEOS-derived films resulted in very high sensitivity and a near independence to relative humidity. Meanwhile, MTES-derived films showed very poor sensitivity and were very sensitivity to changes in relative humidity. The lower water content and hydrophobic nature of its surface was considered to be the reason for poor sensitivity in MTES-derived films. A sub-ppm detection limit was possible in TEOS-derived films, especially at high dye concentration. The response time of these films to ammonia was long, typically about 14 minutes for the 90% response time. These films are suitable for use in an alarm type sensor.

An ammonia-specific sensor was investigated using a calixarene-based compound in a PVC polymer coating. A fast and reversible ammonia sensor was possible with this material. The sensitivity was greatly increased by inclusion of a lithium salt in the PVC coating. Ammonia sensing using near-infrared absorbing indicators was also presented. However with the indicators available, the response to ammonia was very slow and was not fully recoverable.

A number of characterisation systems used in this work were outlined and their relative advantages discussed. For laboratory-based measurements a system using a miniature fibre optic spectrometer was ideal, while a LED-based system was suitable for miniaturisation. The evanescent wave sensitivity of these sensors was enhanced by selectively launching higher order modes in the fibre, by using an annular beam mask in the launch optics. This increased the relative fraction of light absorbed and hence the sensitivity.

Possible future work based on the results in this thesis includes the development of a (quasi-) distributed sensor. To implement this successfully, more stable near-infrared indicators and different methods of immobilisation would be needed. For example, sol-gel materials prepared at neutral pH or different polymer supports may be less harsh environments for entrapment of these indicators. Other possibilities for future work could include miniaturisation of the sensors using either a LED or a planar waveguide approach. In order to develop a leach free sensor for aqueous environments, modification of indicators to form covalent bonds within the sol-gel matrix is of importance. Fluorescence-based systems employing lifetime measurements may be more suited to sol-gel-based sensors in aqueous environments as leaching problems are less critical in their case. The issue of containment of the evanescent field is important to prevent fouling, especially in aqueous environments. Thicker sol-gel films need to be investigated for this reason.

List of Publications & Conference Presentations:

Oral Presentation

i) Development of an Extended Range Fibre Optic pH Sensor using Evanescent Wave Absorption of Sol-gel Entrapped pH Indicators. *Chemical, Biochemical, and Environment Sensors VIII*, Munich, 19th - 23th June, 1995.

Poster Presentations

i) Characterisation of TEOS and Liquicoat-Derived Sol-gel Thin Films. *8th Int. Workshop on Glasses and Ceramics from Gels*, Faro, Portugal, September, 1995.

ii) Tailoring of Sol-gel Films for Optical Sensing. *Sensors & their Applications VIII*, Dublin, September, 1995.

iii) Development of a Distributed Fibre Optic Ammonia Sensor. *EUROPT(R)ODE III, 3rd European Conference on Optical Chemical Sensors and Biosensors*, Zurich, 31st March - 3rd April, 1996.

Publications

i) B.D. MacCraith, C. McDonagh, G. O'Keeffe, T. Butler, B. O'Kelly and J.F. McGilp, 'Fibre Optic Chemical Sensors based on Evanescent Wave Interactions in Sol-gel Derived Porous Coatings', *Journal of Sol-gel Science & Technology*, 2, 1-3, 1994, pp. 661-665.

ii) B.D. MacCraith, C. McDonagh, G. O'Keeffe, A.K. McEvoy, T. Butler and F.R. Sheridan, 'Sol-gel Coatings for Optical Chemical Sensors and Biosensors', *Sensors and Actuators B*, 29, 1995, pp. 51-57.

iii) T.M. Butler, B.D. MacCraith and C.M. McDonagh, 'Development of an Extended Range Fibre Optic pH Sensor using Evanescent Wave Absorption of Sol-gel Entrapped pH Indicators', SPIE Proceedings, Munich, 2508, *Chemical, Biochemical, and Environmental Sensors VIII*, 1995, pp. 168-178.

iv) C. McDonagh, F. Sheridan, T. Butler and B.D. MacCraith, 'Characterisations of Sol-gel-Derived Silica Films', *Journal of Non-Crystalline Solids*, 194, 1996, pp. 72-77.

v) B.D. MacCraith, C. McDonagh, A.K. McEvoy, T. Butler, G. O'Keeffe and V. Murphy, 'Optical Chemical Sensors Based on Sol-gel Materials: Recent Advances and Critical Issues', *Accepted for Publication in Journal of Sol-gel Science & Technology.*

Appendix A:

Dual-LED Driver Circuit

IC1 Voltage to Frequency Converter, (AD654, RS# 637-860)

IC2 Comparator, (LM392N, RS# 308-859)

In the configuration shown, the output from IC1 is a square wave of frequency 950 Hz. An individual LED is switched on by applying a 5 volt signal to the base of one of the npn transistors. The control pulse is supplied by the I/O card of the computer. In this way the 2 LED's are modulated at the same frequency and by sending the relevant pulse, the computer selects which LED operates at a particular time.

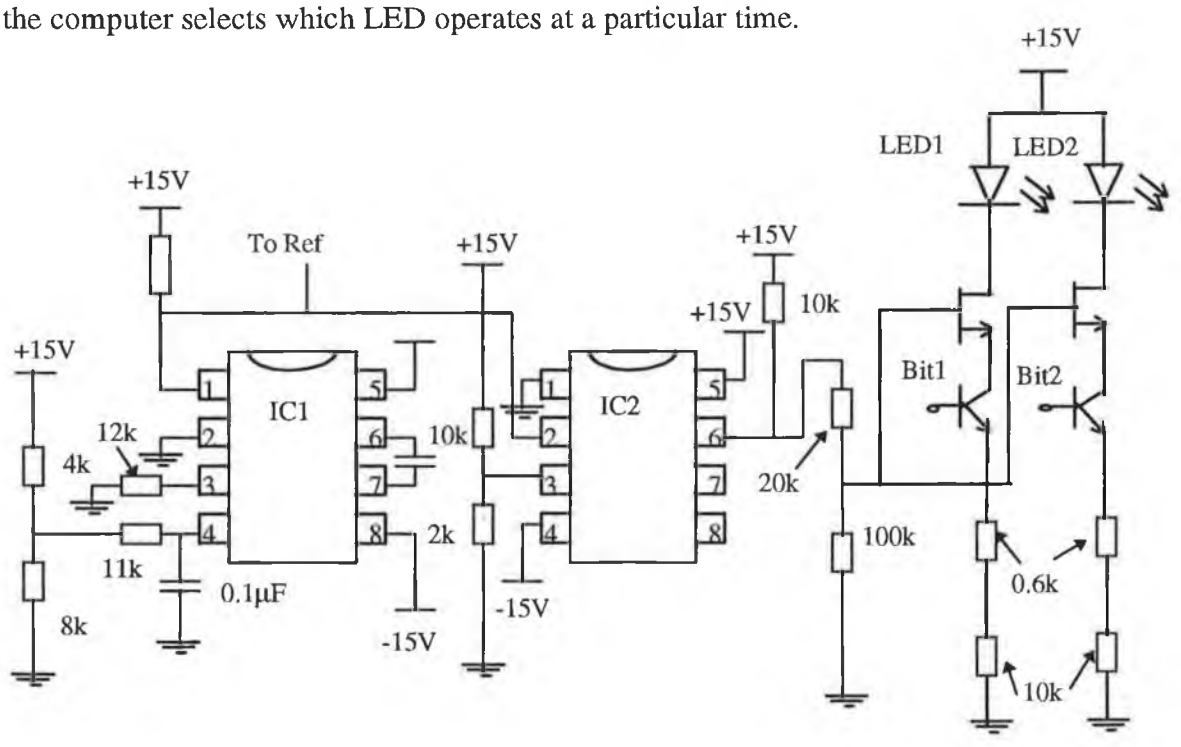

Appendix B:

LED Detection Circuit

IC1 Balanced Modulator / Demodulator, (AD630)

This circuit effectively acts as a lockin-amplifier. The reference for the lockin chip comes from the square-wave generator of the LED driver circuit. The output from the circuit goes, via a buffer, to the ADC of the I/O card of the computer.

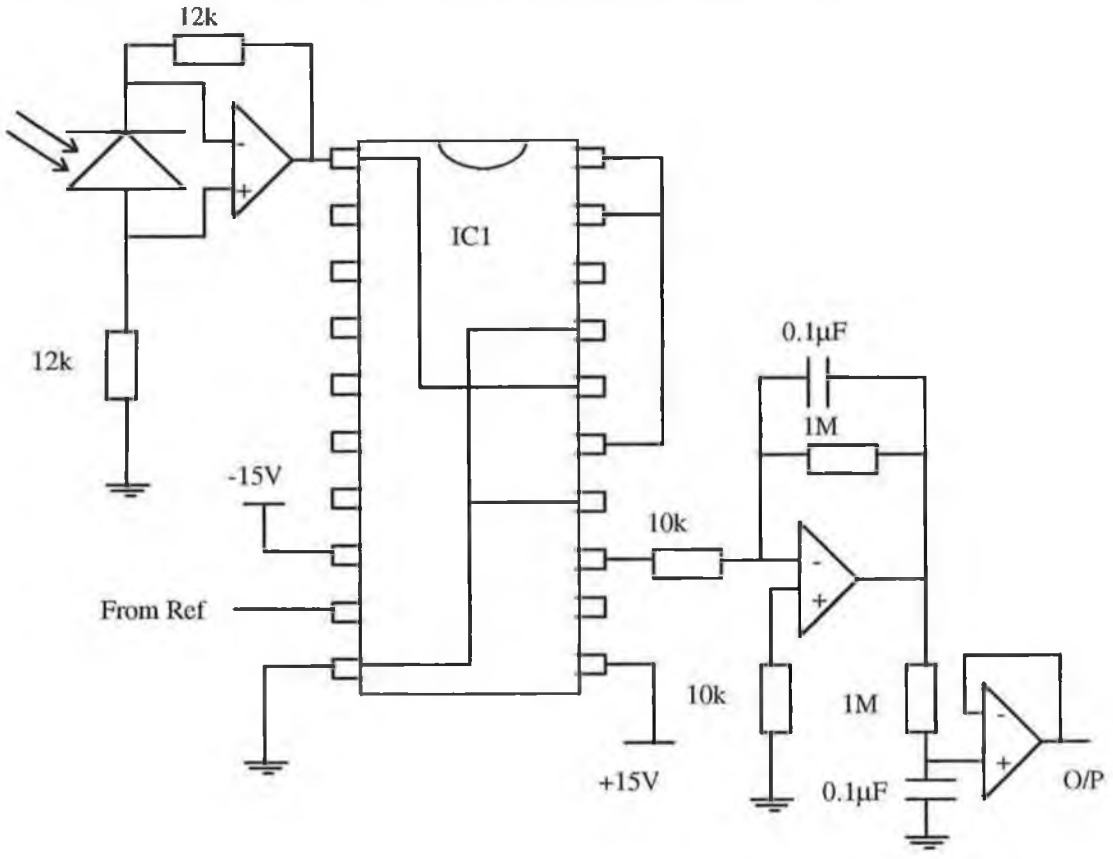

Appendix C:

Intensity profiles of the different microscope objectives

The output intensity profiles of the 3 microscope objectives, namely 0.25, 0.4 and 0.65 NA, with various sized masks in their backplane are shown. Included are the range of angles (c_1 - c_2) at which the masks allow light through the microscope objective. Furthermore, the corresponding range of contact angles ($\theta(c_1)$ - $\theta(c_2)$), which the mask angles would make at a core / cladding interface are calculated.

0.25 NA Microscope objective

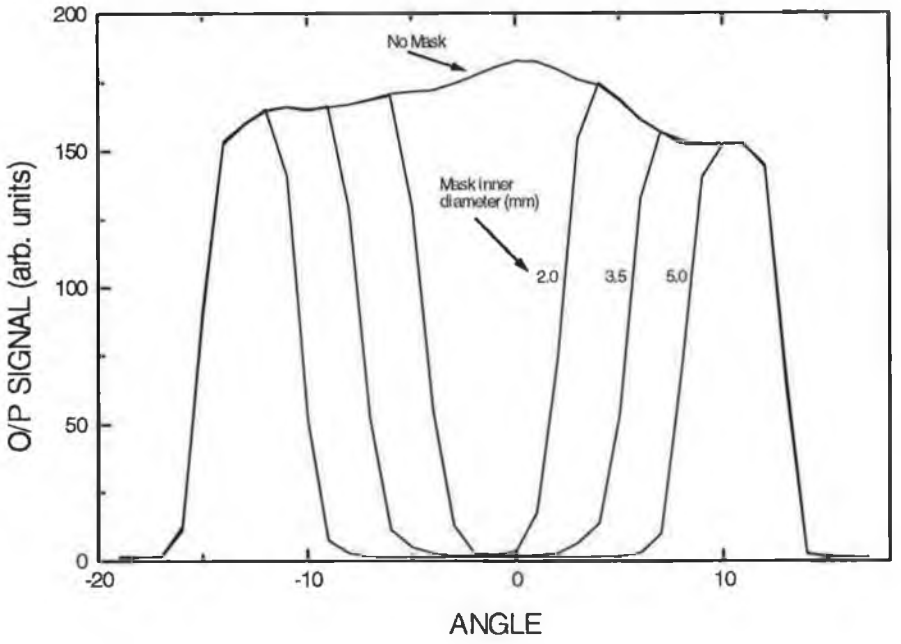

Mask Diameter (mm)	Mask Angles (c_1 - c_2)	$\theta(c_1)$ - $\theta(c_2)$
0	0° - 15°	90° - 80°
2.0	1.5° - 15°	89° - 80°
3.5	4.5° - 15°	87° - 80°
5.0	8.0° - 15°	84.5° - 80°

0.4 NA Microscope objective

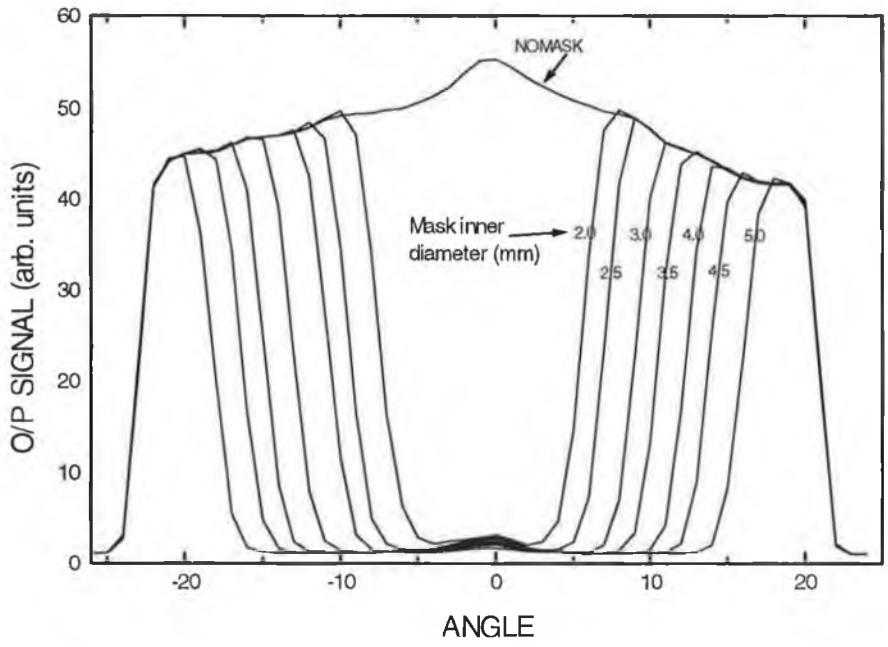

Mask Diameter (mm)	Mask Angles (c_1 - c_2)	$\theta(c_1)$ - $\theta(c_2)$
0	0° - 23°	90° - 74.5°
2.0	4° - 23°	87.3° - 74.5°
2.5	6.5° - 23°	85.5° - 74.5°
3.0	8° - 23°	84.5° - 74.5°
3.5	9.75° - 23°	83.3° - 74.5°
4.0	11.5° - 23°	82.0° - 74.5°
4.5	13.25° - 23°	81° - 74.5°
5.0	15.5° - 23°	79.5° - 74.5°

θ.65 NA Microscope objective

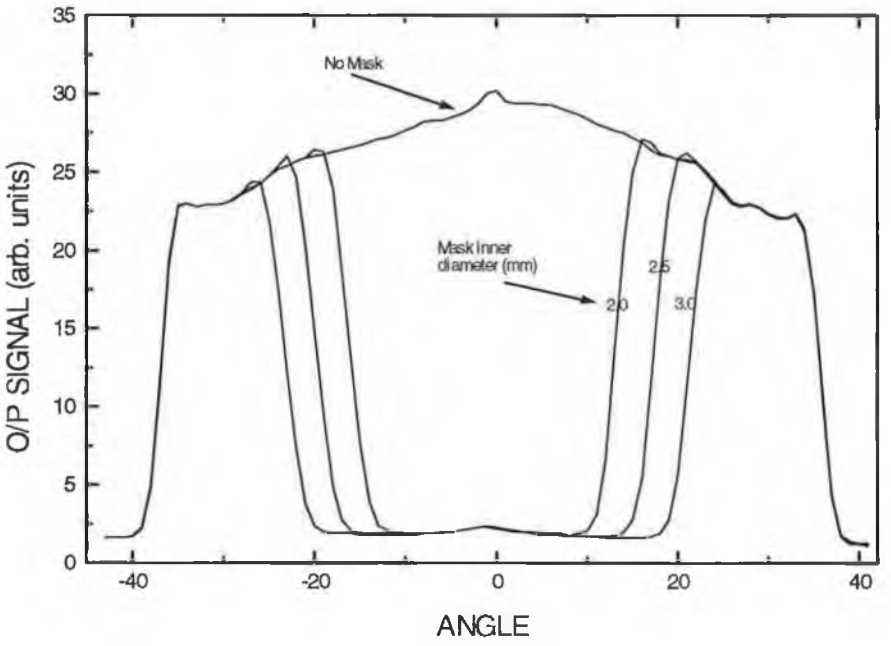

Mask Diameter (mm)	Mask Angles (c_1 - c_2)	$\theta(c_1)$ - $\theta(c_2)$
0	0° - 39.5°	90° - 64°
2.0	10° - 39.5°	83° - 64°
2.5	14.5° - 39.5°	80° - 64°
3.0	18.5° - 39.5°	77.5° - 64°